

Editor
Øivind A. Arntsen

COASTAL TECHNOLOGY – Coast 2008
International Workshop Celebrating
Professor Alf Tørum's 75th Birthday

29-30 May 2008, Trondheim, Norway



PROCEEDINGS



NTNU
Norwegian University of Science and Technology
Department of Civil and Transport Engineering
Coast 2008 Proceedings

PROCEEDINGS

The International Workshop Celebrating
Professor Alf Tørum's 75th birthday

COASTAL TECHNOLOGY – Coast 2008

29-30 May 2008,
Trondheim, Norway

Prepared and published by the
Department of Civil and Transport Engineering, NTNU,
Høgskoleringen 7a,
NO-7491 Trondheim,
Norway

Editor: Øivind A. Arntsen



ABOUT THE WORKSHOP

This is the Proceedings of the International Workshop on Coastal Technology – Coast 2008. The workshop was held in Trondheim, Norway, 29-30 May 2008.

The workshop, organized by the Department of Civil and Transport Engineering, NTNU, invited investigators who have an interest in Coastal Marine Civil Engineering, including Port Engineering and Arctic Marine Civil Engineering, to submit and present a paper during this workshop celebrating Professor Alf Tørum's 75th birthday.

The principal aim of the workshop was to present past and ongoing international research, and address future research needs in fields that have been of large interest for Norway on the above issues, and in which Alf Tørum has made significant contributions.

The workshop received 15 extended abstracts, all of which were reviewed and accepted by the organizing committee. In addition, Alf Tørum gave a presentation on coastal engineering in Norway and 5 invited speakers covered different central fields in coastal technology.

ISBN: 978-82-92506-61-5 Book of Abstracts
and
ISBN: 978-82-92506-62-2 Proceedings (CD)

The International Workshop on Coastal Technology, Coast 2008
Trondheim, Norway
29-30 May 2008

The Book of Abstracts and the CD are published by:
Department of Civil and Transport Engineering
Faculty of Engineering Science and Technology
Norwegian University of Science and Technology, NTNU
NO-7491 Trondheim, Norway.

Copies of the Book of Abstracts including the Proceedings CD can be obtained by contacting Øivind Arntsen at the above address, or by e-mail to: oivind.arntsen@ntnu.no

Front cover photos: Above: Alf Tørum. Below: Trondheim with a view of a bridge over the river Nidelven, the red student center and the Gløshaugen campus. Photo: Jørn Adden.
Back cover photo: The Sirevåg berm breakwater built from January 2000 to July 2001 in southwestern Norway.

© 2008. Department of Civil and Transport Engineering, NTNU.

Printed by Tapir Uttrykk

ORGANIZING COMMITTEE

Associate professor Øivind A. Arntsen
NTNU

Professor Eivind Bratteland
NTNU

Professor Ove Tobias Gudmestad,
NTNU/StatoilHydro

Chief Engineer Eivind Johnsen,
Norwegian Coastal Administration

Professor Sveinung Løset
NTNU

Professor Thomas A McClimans,
SINTEF Fisheries and Aquaculture

CORRESPONDENCE

Coast 2008
Øivind A. Arntsen
Department of Civil and Transport Engineering
Høgskoleringen 7A
NO-7491 Trondheim, Norway
Tel.: +47 73594640
Fax.: +47 73597021
E-mail: coast2008@bygg.ntnu.no

SPONSORS

The Norwegian Coastal Administration
StatoilHydro
NTNU

WEB PAGE

<http://www.ivt.ntnu.no/bat/english/coast2008/>

PREFACE

Professor Alf Tørum received his civil engineering degree from the Norwegian Institute of Technology, NTH, in 1957. He has contributed to the development of safe coastal and offshore structures both in Norway and abroad for more than 50 years.

When the oil industry came to Norway in the late 1960's, persons like Tørum had the scientific expertise to develop the structures needed for the rough North Sea conditions and the international experience and relations needed to interact and establish trust with the foreign oil companies and consultants. Tørum is widely recognized for his contribution to this work and has been a key scientist in this field in Norway.

Presently, at the age of 75, Tørum is fully occupied with the preparation of international standards and text books as well as giving guidance to MSc and PhD students. He is involved in consultancy work for some of the largest and most prestigious civil engineering projects worldwide. His main interest at present is safe harbours and breakwaters and he follows all actual projects with top interest to see where he can contribute. The latest projects have been the Sirevåg breakwater in southern Rogaland County where the significant wave height is estimated to be 7 m. In Russian waters, huge breakwaters may need to be constructed in view of the plans to produce LNG from the arctic offshore gas fields there. Similarly, in shallow waters in the northern Caspian Sea, protection of facilities against moving ice is needed.

With an international contractor market, the need for safe international standards is very important to secure an acceptable safety level for all structures worldwide. Tørum has recently been the convenor for the ISO Standard 21650: Actions from waves and currents on coastal structures.

As a tribute to his 75 year birthday, he is honoured with this seminar at the Norwegian University of Science and Technology (NTNU) in Trondheim.

The field of coastal engineering is still very important in Norway with all the scattered harbours along the rough coast and numerous breakwaters. In case of even rougher sea conditions in the future, the breakwaters may need strengthening and repair and competence in the field is important for Norway.

During the present seminar, papers in the areas that Tørum has contributed during his career have been invited. The fields include breakwaters and coastal structures, design of offshore pipelines (in particular for the near coast area) and water wave kinematics, as well as other subjects of interest for the coastal engineer.

The organizing committee for the Tørum 75 Year Birthday Seminar is honoured to welcome the participants to Trondheim.

The Coast 2008 organizing committee

TABLE OF CONTENTS

	Page
Title page	
About the workshop	
Preface	
Table of Contents	
Session A: WAVE PROPAGATION AND WAVE KINEMATICS	1
Stanislaw R Massel	
Invited lecture: SURFACE WAVE PROPAGATION IN OCEANIC AND COASTAL WATERS	2
Sebastien Fouques and Carl Trygve Stansberg	
COMPARING LAGRANGIAN AND EULERIAN MODELS FOR THE ANALYSIS OF STEEP IRREGULAR WAVES	17
Diana De Padova, Robert A. Dalrymple, Michele Mossa, Antonio F. Petrillo	
LABORATORY EXPERIMENTS AND SPH MODELLING OF REGULAR BREAKING WAVES	29
Session B: SPECIAL TOPICS	39
Alf Tørum	
Alf Tørum's anniversary speech: COASTAL ENGINEERING IN NORWAY - A HISTORICAL REVIEW	40
Iñigo J. Losada	
Invited lecture: WAVE INTERACTION WITH MARINE VEGETATION	83
K.A. Belibassakis, Th.P. Gerostathis & G.A. Athanassoulis	
WAVE - CURRENT - SEABED INTERACTION OVER GENERAL BOTTOM TOPOGRAPHY	84
Kristian Etienne Einarsrud and Iver Brevik	
KINETIC ENERGY APPROACH TO DISSOLVING MULTIPHASE PLUMES	96
Frøydis Solaas and Ivar Fylling	
SENSITIVITY OF SHIP MOTIONS TO SEA BOTTOM MODELLING	108
Lars Petter Røed and Jens Boldingh Debernard	
FUTURE WIND, WAVE AND STORM SURGE CLIMATE IN THE NORTHERN SEAS: A REVISIT	118
Lars Gansel, Thomas McClimans and Dag Myrhaug	
DRAG FORCES ON AND WAKES BEHIND POROUS CYLINDERS	130

TABLE OF CONTENTS (cont.)

	Page
Session C: BREAKWATERS	139
Hans F. Burcharth	
Invited lecture: ASPECTS OF BREAKWATER DESIGN	140
D.Morgan Young and Firat Y. Testik	
WAVE FIELD AND SCOUR CHARACTERISTICS AROUND SUBMERGED VERTICAL AND SEMICIRCULAR BREAKWATERS	141
Thomas A. McClimans	
IMPROVED EFFICIENCY OF BUBBLE CURTAINS	152
Session D: PIPELINES	162
Hermann Moshagen	
Invited lecture: COASTAL ENGINEERING APPLICATIONS ON PIPELINES	163
Øivind A. Arntsen, Alf Tørum and Colin Kuester	
STABILITY AGAINST WAVES AND CURRENTS OF RUBBLE MOUNDS OVER PIPELINES	181
Dag Myrhaug and Lars Erik Holmedal	
STOCHASTIC AND DYNAMIC APPROACHES TO SEABED BOUNDARY LAYER AND SEDIMENT DYNAMICS UNDER IRREGULAR WAVES PLUS CURRENT	193
Raed Lubadd	
EXPERIMENTAL INVESTIGATIONS OF THE EFFICIENCY OF ROUNDSECTIONED HELICAL STRAKES	205
Session E: CHALLENGES IN COLD CLIMATE	219
Sveinung Løset	
Invited lecture: SOME CHALLENGES FOR THE PETROLEUM INDUSTRY IN COLD WATERS	220
Arne Gürtner, Ibrahim Konuk and Sveinung Løset	
NUMERICAL SIMULATION AND FAILURE MODE ANALYSIS OF ICE DRIFT ON ARRANGEMENTS OF ICE PROTECTION PILES	222
Aleksey Marchenko and Christian Ulrich	
ICEBERG TOWING: ANALYSIS OF FIELD EXPERIMENTS AND NUMERICAL SIMULATIONS	235
Ivar Langen, Aleksey Marchenko, and Aleksey Shestov	
HYDROLOGICAL CHARACTERISTICS OF THE STRAIGHT SEPARATING BRAGANZAVÅGEN FROM SVEABUKTA IN VAN MIJEN FJORD	247
Authors Index	257
Keywords Index	258

**Session A:
WAVE PROPAGATION AND WAVE
KINEMATICS**

SURFACE WAVE PROPAGATION IN OCEANIC AND COASTAL WATERS

Stanisław R. Massel

Institute of Oceanology of the Polish Academy of Sciences, Sopot, Poland

ABSTRACT

The up-to-date, current needs and trends in the modelling of surface wave propagation in oceanic and coastal waters are discussed. In particular, the progress made in recent years is demonstrated and the most important contemporary achievements in wave hydrodynamics and application of new modelling techniques are discussed.

INTRODUCTION

The atmosphere and the ocean form a coupled system which exchanges heat, momentum and water at the air-sea interface. The interface, comprising surface waves, is dynamic and masses and energy are continually transferred across it. Due to the high complexity and non-linear nature of surface waves, particularly those that are unsteady, very high and steep, they remain a hydrodynamic process that is still not fully understood. Therefore, in this paper, particular attention is given to the physics of non-linear, steep waves and their modelling. A detailed description of models will not be given, but the governing equations and references to the professional literature will be used to illustrate the structure of particular models. It is useful to distinguish between deep ocean and shallow waters. Thus, the review is organised in two main blocks, dealing with waves in oceanic and shallow waters. In each block, the dominant physical processes are characterised first. To a large extent these processes determine the choice of appropriate mathematical and numerical models. Moreover, special wave events, such as whitecapping, freak waves, tsunami and wave-induced groundwater circulation, are discussed. Knowledge of these events is of special importance for modern oceanic and coastal technology.

WAVES IN OCEANIC WATERS

Energy balance equation

We concentrate more on shallow waters where the interactions between the wave environment, engineering structures and the coast are extensive and more complex. Waves are generated by winds over the deep ocean. They propagate into shallower regions, where they are treated as the forcing terms for many processes there. Deep water waves are highly dispersive. They interact with each other, but the interaction time is finite because each wave propagates with a different phase speed. In practice there is no need for detailed information regarding the phase of ocean waves. Usually knowledge about the distribution of wave energy over wave number space, \mathbf{k} (e.g. wave number spectrum, $F(\mathbf{k}, t)$) or over wave frequency, ω (e.g. wave frequency spectrum, $S(\omega, t)$) is sufficient. In order to develop the governing equations for functions $F(\mathbf{k}, t)$ or $S(\omega, t)$, two methods are usually applied, namely the Hamiltonian approach (Zakharov, 1968) and the Lagrangian approach, proposed by Luke (1967). The resulting energy balance equation takes the form (Janssen, 2004)

$$\frac{\partial N}{\partial t} + \nabla \cdot (C_g N) = S_{in} + S_{nl} + S_{diss}, \quad (1)$$

in which the wave action density $N = \frac{E}{\omega}$, C_g is the group velocity and E is the wave energy.

The right-hand side of the equation describes the spectral input from wind (S_{in}), the net spectral flux of energy action through the wave number k by non-linear wave-wave interactions (S_{nl}) and S_{diss} is the energy loss by wave breaking. In this paper, we restrict ourselves to the S_{nl} and S_{diss} terms only. The generation of ocean waves by wind is still a problem subject to many theories and much controversy. In fact, we are dealing here with an extremely difficult problem of modelling of a turbulent airflow over a surface varying in space and time. The reader should consult Janssen (2004) for an in-depth discussion.

Non-linear wave-wave interaction

Ocean waves are usually regarded as weakly non-linear, dispersive waves, and the effect of non-linearity on wave propagation is a result of a perturbation expansion starting with linear, freely propagating waves. Theoretical and experimental studies provide convincing evidence that regular wave trains in deep water are liable to a number of instabilities which lead to wave breaking without external forcing. A small disturbance in the form of two modes with “sideband” frequencies adjacent to the fundamental frequency will be forced to increase exponentially due to non-linear interaction mechanisms, and primary wave motion becomes unstable (Benjamin-Feir instability). The long-time evolution of the unstable non-linear wave train shows recurrence, known as the Fermi-Pasta-Ulam recurrence phenomenon, with periodically increasing and decreasing modulation. For small steepness, the original three-wave system is almost recovered. When the initial steepness is large enough, strong modulation and demodulation also appears, but the spectral peak is downshifted to a lower sideband, which is known as the frequency downshift phenomenon. Recently it was found that Krasitskii’s modification of the Zakharov evolution equation for the four-wave interaction correctly predicts the major features of the increase of energy in the lower sideband relative to the upper sideband (Krasitskii, 1994; Tulin & Waseda, 1999). The spectral peak downshifting to a lower sideband appears in the absence of breaking, which demonstrates the role of the balance between momentum losses and energy dissipation in the exchange of energy between sidebands. Unfortunately, for a more complicated evolution, analytical solutions of the evolution equations fail and only numerical simulations are possible. In particular, Dold & Peregrine (1986) showed that initial carrier wave steepness $(ak)_0$ differentiates between two modes of behaviour, i.e. recurrence of the initial state without breaking or the rapid onset of breaking. Moreover, they established a connection between a weakly non-linear four-wave interaction process and a truly non-linear wave breaking phenomenon (see also Song & Banner, 2002; Banner & Song, 2002).

The question now arises how the above discoveries may be used to predict waves propagation in practice. In particular, we are interested in a statistical description of the sea surface in terms of the evolution of the energy of an ensemble of waves. Non-linear transfer gives rise to a downshift of the wave number. In order to conserve energy and wave action, considerable amounts of energy are transferred from the region just beyond the location of the spectral peak to the high wave number part of the spectrum. Therefore, the rate of change of the wave number spectrum due to non-linear interactions demonstrates the typical three-lobe structure (Figure 1). It should be noted that in the evolution equation, both resonant and non-resonant wave-wave interactions are included. For short times the evolution of the wave action density N is due to both resonant and non-resonant four-wave interactions. However, the time scale on which non-resonant interactions operate is short, typically of the order of 10 to 20 wave periods. Thus, for wave prediction on the global scale there is only interest in the slow time evolution of the wave

spectrum when only resonant interactions contribute to spectral change. Numerical experiments using the exact non-linear transfer function suggest that the spectra tend to adjust in such a way that the directionally averaged spectra are close to $k^{-5/2}$ (or to $k^{-7/2}$ for the two-dimensional spectrum). This result follows from Kolmogorov's concept of an energy cascade when a constant non-linear energy flux is maintained through the system. Then the Kitaigorodskii (1983) scaling yields the frequency spectrum $S(\omega)$ in the form suggested by Toba (1973)

$$S(\omega) = 2A \left(\frac{\rho_a}{\rho_w} \right)^{1/2} u_* g \omega^{-4}, \quad (2)$$

where ρ_a and ρ_w are the air and water density, respectively, u_* is the friction velocity, g is the acceleration of gravity and A is a constant. The ω^{-4} law is typically valid for frequency range $(1.3 - 3.0) \cdot \omega_p$, where ω_p is the peak frequency of the waves. For frequencies above $3\omega_p$, there are some arguments for the transition of Toba's ($\sim \omega^{-4}$) to Phillips' ($\sim \omega^{-5}$) spectrum.

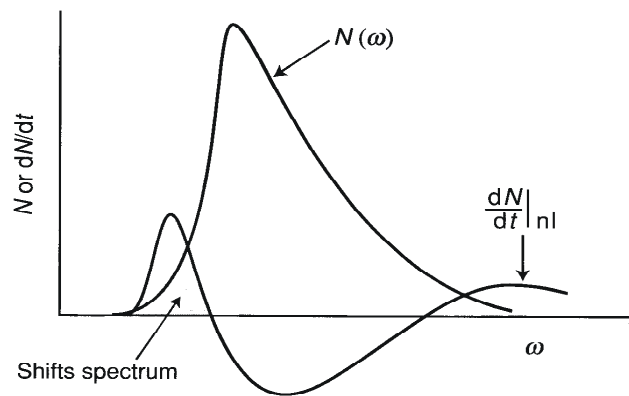


Figure 1 – Three-lobe structure of the spectrum (adapted from Janssen, 2004).

The evaluation of the S_{nl} term in (1) requires an enormous amount of computations. Thus, some form of parameterization of S_{nl} is needed. After several past attempts there is now some consensus that the *discrete interaction approximation* (DIA) developed by Hasselmann *et al.* (1985) offers the best parameterization of S_{nl} . It was incorporated into the well known third-generation prediction model WAM. For more information on the numerical implementation techniques for the energy balance equation, see for example WAMDI (1988), Janssen (2004) or Holthuijsen (2007).

Whitecap coverage and energy dissipation

The energy flow from the atmosphere to the ocean generates an aerodynamically rough ocean surface. If the energy flow is sufficiently strong, at some points of the surface, waves lose their stability and eventually break in the form of whitecaps of various scales. The percentage of whitecap coverage is usually parameterized in terms of the wind speed when this speed is greater than about 4m/s; below this speed, whitecaps are not observed. However, wind speed alone cannot fully parameterize the complex event of wave breaking and subsequent whitecap formation. There are other processes that contribute to wave breaking, for example the wave-wave interaction mentioned above, current-wave interactions and others. The rate of energy supplied by the wind is closely related to the wind stress and the atmospheric stability

conditions. The percentage of sea surface covered by breaking waves can be written in the general form (Massel, 2007)

$$F_{cov} = a \cdot V_{10}^b, \quad (3)$$

where V_{10} is the wind speed in m/s at 10m altitude, a and b are empirical constants, and F_{cov} is in percentage. The experimental data (Monahan, 1971; Stramska & Petelski, 2003; Massel, 2007) indicate that

$$10^{-7} < a < 10^{-5} \quad \text{and} \quad 3.0 < b < 3.75. \quad (4)$$

Whitecaps are evidence that waves are breaking and energy is being dissipated. However, despite great efforts, our knowledge of energy dissipation is still fragmentary. This is mostly due to the absence of good quantitative measures of the distribution of breaking and the rates of energy dissipation in breaking waves. Estimating the amount of energy lost during breaking is a very difficult task despite many experimental and theoretical efforts. Potentially, the energy dissipation would be estimated from the energy budget expressed in the wind-wave evolution models. At present, two such approximate methods are considered, namely: the equilibrium range model (Phillips, 1985; Hanson & Phillips, 1999), and the whitecap model for a fully developed sea (Komen *et al.*, 1984). For a very narrow spectrum, a probability approach (Longuet-Higgins, 1969) is also used. In Tables 1 and 2, adapted from Massel (2007), known experimental data and theoretical estimates of energy loss due to breaking are collected. In the Tables, the following notations are used: C is the dominant phase speed, C_{br} is the phase speed of the breaking waves, θ is the inclination of a breaking wave's forward face, m_n is the spectral moment of order n , γ_l is the numerical constant, $I(s)$ is the spreading function, s is the directional spreading parameter, A_{rms} and A_{br} are the root-mean-square and critical amplitudes, respectively, a_l and $I_A(T)$ are the functions of the period probability density.

Table 1 - Summary of experimental data on wave energy dissipation due to wave breaking (adapted from Massel, 2007).

Quantity	Mathematical expression	Source
Number of breaking waves per wave	$N_b = (4.0 \pm 2.0) \times 10^{-3} \left(\frac{V_{10}}{C} \right)^3$	Thorpe (1993)
Rate of energy loss per unit surface [J/m ² /s]	$E_{dissrate} = (3.0 \pm 1.8) \times 10^{-5} \rho_w \left(\frac{C_{br}}{C} \right)^5 V_{10}^3$	Thorpe (1993)
Rate of energy loss per unit crest length [J/m ² /s]	$E_{dissrate} \sim 0.009 \rho_w \frac{C_{br}^5}{g \sin \theta}$	Duncan (1981)
	$E_{dissrate} \sim 0.0075 \rho_w \frac{C_{br}^5}{g \sin \theta}$	Duncan (1983)
	$E_{dissrate} \sim (3.2 \times 10^{-3} \div 1.6 \times 10^{-2}) \rho_w \frac{C_{br}^5}{g}$	Rapp & Melville (1990)
Rate of total energy dissipation in the equilibrium range [J/m ² /s]	$E_{dissrate} = 4.28 \times 10^{-5} V_{10}^{3.74}$	Hanson & Phillips (1999)

Table 2 - Summary of theoretical formulae for wave energy dissipation due to wave breaking (adapted from Massel, 2007).

Quantity	Mathematical expression	Source
Rate of total energy dissipation in the equilibrium range [J/m ² /s]	$E_{dissrate} = \frac{\gamma_1 \rho_w I(3s)}{16[I(s)]^3 g^3} \times \int_{\omega_p}^{\infty} \omega^{11} S^3(\omega) d\omega$	Hanson & Phillips (1999)
	$E_{dissrate} = 1.59 \rho_w g \frac{m_0 m_2}{m_1} \left(\frac{m_1^4}{g^2 m_0^3} \right)^2$	Komen <i>et al.</i> (1984)
Rate of energy dissipation for extremely narrow spectrum [J/m ² /s]	$E_{dissrate} = 1.59 \rho_w g m_1 \left(\frac{m_1^4}{g^2 m_0^3} \right)^2$	Komen <i>et al.</i> (1984)
Energy dissipation for very narrow spectrum [J/m ² /s]	$E_{diss} = \frac{1}{2} \rho_w g A_{rms}^2 \exp\left(-\frac{A_{br}^2}{A_{rms}^2}\right)$	Longuet-Higgins (1969)
Energy dissipation for two-dimensional probability density $f(A,T)$ [J/m ² /s]	$E_{diss} = \frac{1}{2} \rho_w g \int_0^{\infty} a_1 I_A(T) dT$	Massel (2007)

Extreme steep waves and their kinematics

Modelling of special wave events such as extreme, very steep and rapidly varying waves, as well as freak waves and tsunamis, requires a phase-resolving approach. In particular, freak or giant waves correspond to large-amplitude waves quite surprisingly appearing on the sea surface; see for example the famous “New Year wave” of 26m height recorded at Draupner platform in the North Sea on 1 January 1995. In the literature, various definitions of freak waves are proposed, but usually a freak wave is characterised by the wave height H_{max} , when $H_{max}/H_s > 2$ (H_s is the significant wave height), or by the crest height C_{max} , when $C_{max}/H_s > 1.2$ (Bitner-Gregersen & Hagen, 2004). Accordingly, from the Rayleigh distribution it follows that the probability of extreme wave formation is less than 0.000336 or one wave among 2980 waves.

Non-linear interactions have a pronounced impact on the probability distribution of the surface elevations. In deep water the non-linearities result in focusing and therefore in a tendency to have an increased probability of freak wave events occurring. During the last 30 years, various mathematical models of freak wave phenomena have been intensively developed and many laboratory experiments conducted, and great progress was achieved in the understanding of the physical mechanisms involved (Trulsen & Dysthe, 1997; Onorato *et al.*, 2000, 2001, 2006; Kharif & Pelinovsky, 2003; Kurkin & Pelinovsky, 2004; Bitner-Gregersen & Hagen, 2004). As a result, a number of physical mechanisms have been identified: dispersion enhancement of transient wave groups, geometrical focusing in basins of variable depth, wave-current interactions and non-linear modulational instability. In particular, focusing of frequency modulated wave groups and blocking effect of spectral components on opposing currents is very sensitive to the spectrum width. On the other hand, studies on the influence of randomness of the wind field on the phase coherence and instability of the wave field are based on non-linear models. Numerical simulations of the non-linear Schrödinger and Dysthe equations for JONSWAP type spectra showed that the probability density of wave height substantially depends on the enhancement factor γ and on the Phillips constant α . When the coefficients α and γ increase, the effects of non-linearity become more important and freak waves are more likely to occur (Onorato *et al.*, 2000).

In the first approximation, wind-induced waves can be considered as waves of narrow spectrum when the complex envelope of the sea elevation is described by the non-linear Schrödinger equation (Peregrine, 1983)

$$i\left(\frac{\partial A}{\partial t} + C_g \frac{\partial A}{\partial x}\right) = \frac{\omega_0}{8k_0^2} \frac{\partial^2 A}{\partial x^2} + \frac{\omega_0 k_0^2}{2} |A|^2 A, \quad (5)$$

in which k_0 and ω_0 are the wave number and frequency of the carrier wave. The complex amplitude A is a slowly varying function of x and t . In Figure 2, the formation of a highly energetic wave group in a slowly modulated wave train is shown. Numerical simulation indicates that wave groups appear and disappear in the characteristic time scale of order $[\omega_0(k_0 A_0)^2]^{-1}$.

Due to the fact that freak waves have large amplitude and short duration, the assumption of weak non-linearity and narrow-banded spectrum does not correspond exactly to real data. Substantial improvement in the reconstruction of high amplitude freak waves has been achieved through the extension of the weakly non-linear models by inclusion of higher order terms of wave steepness, wave-induced mean flow and higher-order linear dispersive terms (Dysthe, 1979; Lo & Mei, 1985; Trulsen & Dysthe, 1996; Dysthe *et al.*, 2003).

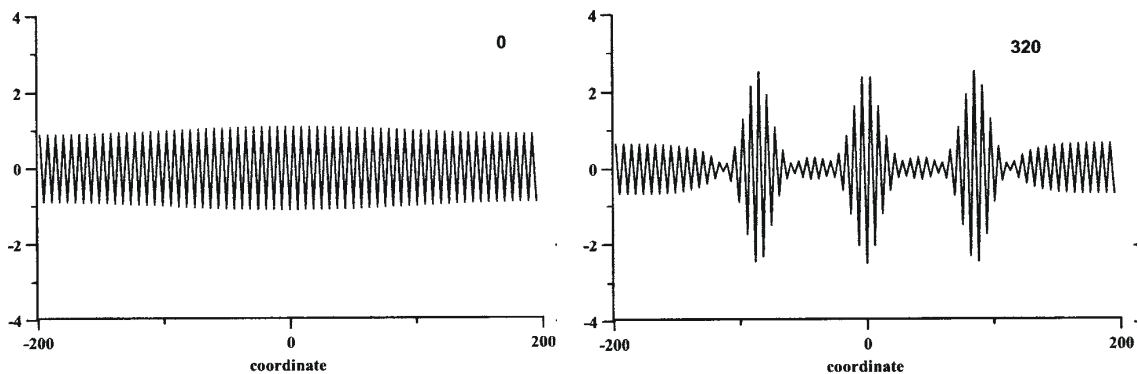


Figure 2 – Formation of a highly energetic wave group $y(x)$ in a slowly modulated wave train. The time (0 at left and 320 at right) is normalised by the fundamental wave period and the coordinate is the phase $2k_0x - \omega_0t$, in which k_0 and ω_0 are the wave number and frequency of the fundamental mode, respectively (adapted from Kharif & Pelinovsky, 2003).

The wave kinematics and loadings due to steep and extreme waves are very important for offshore engineering operations, and offshore structures' and ships' performance. In particular, in determining a design load, an accurate assessment of the maximum water particle velocities beneath the largest wave crest is required for drag force calculations, while the maximum accelerations beneath the steepest section of the wave profile are appropriate for inertial force calculations. The wave models used to determine the water particle kinematics associated with a measured time history of the surface elevation $\zeta(t)$ are traditionally based either on a non-linear regular wave theory (for example a fifth-order Stokes' solution) or on an unsteady linear wave theory (a Fourier transform technique). A fifth-order solution accurately predicting regular waves (Tørum & Gudmestad, 1990; Gudmestad, 1993) is however no longer valid close to the breaking limit for regular waves ($Hk/2 \approx 0.44$) and higher order terms must be included. In the

case of random waves, the near-surface velocities beneath a large wave crests are significantly overestimated due to the fact that the linear theory does not allow the individual wave components to ride over one another, but rather all the components oscillate about the still water level.

To overcome this difficulty, an empirical stretching technique (Wheeler, 1970), best fit of the experimental profile to the fifth-order Stokes profile and two alternative local methods for solving irregular wave problems (Sobey, 1992; Baldock & Swan, 1994) have been proposed. Sobey's solution gives an excellent description of the crest kinematics, but is unable to model the global non-linearities and results in a poor description of the kinematics in the lower layers of the flow. On the other hand, the Baldock & Swan solution is able to model both the local and the global non-linearity, but is limited in terms of the total number of Fourier components that can practically be included, resulting in some underestimation of the near surface kinematics. Also under some circumstances it overestimates the kinematics beneath the still water level. Overall, however, the double Fourier series solution provides both the most accurate and the most reliable estimate of the water particle kinematics for extreme 2D waves (Smith & Swan, 2002).

This is not the case for freak waves and waves which are near breaking, for which the kinematics is not well predicted by any existing theory, and according to Gudmestad (1993) further research is needed. A new fully non-linear unsteady wave model has been recently developed by Clamond & Grue (2001a, b) which offers substantial improvement in the modelling of steep wave kinematics. The model is based on potential theory and assumes the integration of the kinematic and dynamic boundary conditions at the free surface of very steep (freak) waves. The theoretical results compare favourably with a some available sets of experimental data, namely:

- particle image velocimetry for the leading wave of a wave train, focusing waves as well as random waves (Grue *et al.*, 2003) (see Figure 3)
- a set of cases of large waves such as the Draupner wave and the Camille wave with slopes in the range 0.40 – 0.46 (Grue & Jensen, 2006)
- the LDA measurements by Baldock *et al.* (1996).

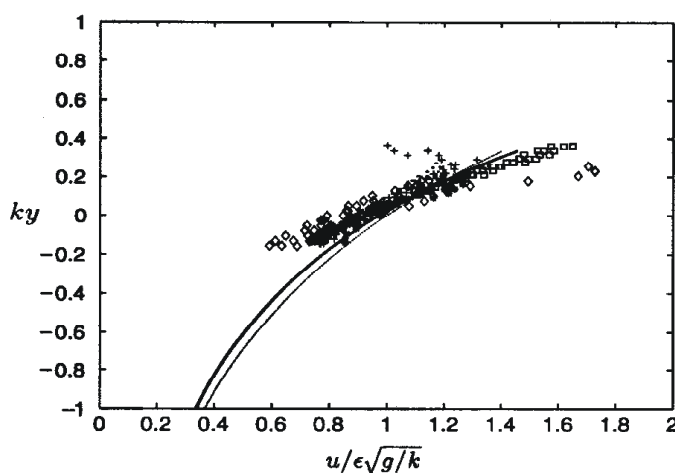


Figure 3 – Comparison of experimental velocity profile with theoretical results (adapted from Grue *et al.* 2003).

Measurements and computations show some deep water waves with a fluid velocity up to 75% of the phase speed. The PIV and LDA data demonstrate excellent agreement with the fully non-linear theory (see for example Figure 3). The experimental data correspond to the JONSWAP spectrum with $\omega_p^2 H_s / 2g = 0.15$ and the range of the wave slope is $0.21 < \varepsilon < 0.34$. These data are compared with the non-linear computations with $s = 0.29$. A surprising result is that the exponential profile e^{ky} compares well with all measurements in deep water. The case of extreme waves propagating at finite water depth and the corresponding kinematics will be discussed in the next section.

Accelerations at the sea surface are required to estimate the inertia forces on offshore installations. Moreover, vertical accelerations at the wave crests are frequently used as a wave breaking criterion (Massel, 2007). A distinction should be made between two accelerations of the water particles. The first acceleration is known as the apparent (or Eulerian) acceleration, while the second one, including the convective terms, is known as real (or Lagrangian) acceleration. In the linearized theory both acceleration definitions are equal, but in steep waves they are different. Very few measurements of the real acceleration below steep waves exist (see for example Bonmarin & Kjeldsen, 2000 and Grue & Jensen, 2006). In particular, Grue & Jensen reported a maximum negative vertical acceleration value of about 1.1g, while the upward vertical acceleration grows to about 1.5g, in the front face of the wave, at the base below the overturning jet of the plunging breakers. The fully non-linear model for accelerations in unsteady waves shows very good agreement with experiments. It was shown that the convective term is of the same order of magnitude and of opposite sign to the local acceleration, and it cannot be neglected when estimating the acceleration and forces (Jensen *et al.*, 2007).

WAVES IN SHALLOW WATERS

Waves in constant water depth

Coastal engineering projects are becoming more complex and near-shore wave models are required to provide results with greater accuracy. In particular, design calculations are needed to assess the applied water loading on structures, the stability and transport of bed material, and the run-up and over-topping of breakwaters. Higher accuracy of models requires the formulation of predictive models in which non-linearities and the unsteady character of the wave field are taken into account.

In deep and intermediate water depths the water particle kinematics and dynamics, corresponding to a measured or predicted time-history of surface elevation $\zeta(t)$, is usually determined according to non-linear Stokes' steady wave theory (Fenton, 1985), while in very shallow water, a non-linear cnoidal theory is more appropriate (Fenton, 1979). In linear models, the unsteadiness and irregular nature of surface waves may be included, but the non-linearity is not. The observed surface elevation is assumed to be a sum of freely propagating wave components, and each of them satisfies the linear dispersion relation. However, this type of solution for near-surface velocities results in significant errors due to high frequency contamination. To reduce this effect, an empirical stretching technique has been proposed by Wheeler (1970). Although this correction overcomes the effects of this contamination, some under-prediction of the velocities remains and there are fundamental problems with satisfying the mass continuity condition and a proper description of the non-linear wave-wave interactions. However, the simplicity of this solution makes it useful in design practice in spite of the fact that the empirical solution does not provide a basis for estimating the kinematics in a non-linear sea state.

For non-linear and unsteady surface waves Longuet-Higgins & Cokelet (1976) in their pioneer study developed an exact method for extreme 2D waves in deep water. They showed that the non-linear free surface conditions can be re-arranged in such a way that a spatial representation of surface elevation and velocity potential Φ are defined at some initial time $t = t_0$, and the entire solution can be time-marched to give values for $\zeta(x)$ and $\Phi(\eta, x)$ at all subsequent times. This procedure has been extended by Dold & Peregrine (1984) for a spatially periodic wave field with no restriction on the water depth. First, they considered six laboratory tests with different periods, corresponding to deep, intermediate and shallow water conditions, and two spectra, i.e. a broad-banded spectrum and a narrow-banded spectrum. These tests have been successfully reproduced by Dold & Peregrine's numerical model for adopted initial conditions. Subsequently, Smith and Swan used these exact numerical calculations, rather than laboratory data, as benchmark data to compare with other prediction models. These comparisons indicate that the fifth-order Stokes' solution or linear random wave theory provides a poor description of the water particle kinematics as they are unable to model the unsteadiness and the non-linearities which are common in extreme wave events. On the other hand, the local Fourier series solution (Sobey, 1992) and the double Fourier series (Baldock & Swan, 1994) provide improved representations of the surface profile and wave kinematics, also for waves propagating in finite water depths.

Fenton (1986) developed an alternative local approximation method for unsteady waves in shallow water. In this method, the local solution is represented by a truncated polynomial series for the complex potential function. The unknown polynomial terms are determined numerically to fit the non-linear free surface conditions using a measured time history of the surface elevation. This procedure is best suited for long waves where the vertical variation in the fluid velocities can be described by a polynomial function. In general, if accurate descriptions of the water particle kinematics is required, particularly close to the water surface, the applied wave models must incorporate the non-linearity and unsteadiness of events.

Wave propagation over gradually varying depth

Effects of refraction and diffraction should be taken into account when water depth is shoaling. If relative wave height and bottom slope are small, non-linearities are weak and the mild-slope equation developed by Berkhoff (1972) and many of its alternative derivations and numerous extensions provide effective tools to predict wave variation for regions of moderate size. However, steep bottom slopes, such as underwater shoals and coral reefs (Lie & Tørum, 1991, Massel, 1993, 1996) require inclusion of higher order terms and possibly wave breaking mechanisms in equation for the wave amplitude ϕ (only the propagating mode is shown):

$$\frac{d^2\phi}{dx^2} + (CC_g)^{-1} \frac{d(CC_g)}{dx} \frac{d\phi}{dx} + [k^2(1+\psi) + i\lambda k] \phi = 0, \quad (6)$$

in which

$$\psi = E_1(kh) \left(\frac{dh}{dx} \right)^2 + E_2(kh) \frac{g}{\omega^2} \frac{d^2h}{dx^2} \quad (7)$$

and $\gamma = \gamma_b + \gamma_f$. The ψ term describes the influence of bottom slope dh/dx and bottom shape d^2h/dx^2 , and the γ term represents energy dissipation due to wave breaking γ_b and bottom friction γ_f , and E_1 and E_2 are the functions of non-dimensional water depth (Massel, 1996). However,

the above model does not satisfy exactly the Neumann condition on a sloping bottom. This means that the velocity field in the vicinity of the bottom is poorly represented and wave energy is not generally conserved. In order to improve the mild-slope representation in the bottom layer, Athanassoulis & Belibassakis (1999) developed the consistent coupled-mode theory in which an additional term, called the sloping-bottom mode, was introduced to satisfy the bottom condition exactly. The equation for wave amplitude then takes the form

$$\varphi(x, z) = \varphi_{-1}(x) \cdot Z_{-1}(z; x) + \varphi_0(x) \cdot Z_0(z; x) + \sum_{n=1}^{\infty} \varphi_n(x) \cdot Z_n(z; x), \quad (8)$$

where $\varphi_0(x) Z_0(z; x)$ denotes the propagating mode and the remaining terms $\varphi_n(x) Z_n(z; x)$ are the evanescent modes. The additional term $\varphi_{-1}(x) Z_{-1}(z; x)$ is the required sloping-bottom mode which provides a proper Neumann condition over a non-horizontal bottom when the function $Z_{-1}(z; x)$ takes the form

$$Z_{-1}(z; x) = h(x) \left[\left(\frac{z}{h(x)} \right)^3 + \left(\frac{z}{h(x)} \right)^2 \right]. \quad (9)$$

The functions $Z_0(z; x)$ and $Z_n(z; x)$ are the classical functions representing the z -dependence of wave motion for propagating and evanescent modes, respectively. The idea was further extended to a 3D environment (Belibassakis *et al.*, 2001) and to second-order Stokes waves over variable bathymetry (Belibassakis & Athanassoulis, 2002).

Run-up of waves on beaches and wave-induced groundwater circulation

Sandy beaches are highly exploited but very dynamic and fragile environments. The beach system is driven by the physical energy induced by waves and tides. The water flow through the beach body is of great importance for introducing water, organic materials and oxygen to the ground environment and for sediment transport and coastal structure stability and modern beach nourishment techniques. Moreover, the water flow through the beach material is able to transport oxygen, and hence help to maintain biological activity in the porous media. For long, non-dispersive waves, the governing equations are usually based on Carrier and Greenspan's transformation (Carrier & Greenspan, 1958) and its various modifications (Pelinovsky, 1996; Belibassakis & Athanassoulis, 2006). They can be supplemented by the effects of dispersion of waves approaching the coast and the effects of dissipation due to wave breaking (Massel & Pelinovsky, 2001). In the simple case when a plane slope joins a horizontal bottom, the surface elevation $\zeta(x, t)$ over the sloping bottom takes the form

$$\zeta(x, t) = \Re \frac{H_i}{2} K_T J_0 \left[\sqrt{\left(1 + \frac{iD_b}{\omega} \right)} \frac{4\omega^2(-x)}{g\beta} \right] \exp(-i\omega t), \quad (10)$$

in which H_i is the incident wave height, K_T is the transmission coefficient, β is the beach slope, D_b is the dissipation factor due to wave breaking and J_0 is the Bessel function of the first kind and zero order.

A controlled, almost full-scale experiment revealed the dual nature of the pore pressure. Beyond the breaker zone, only the fast varying phase-resolving pore pressure component due to the

surface variation is observed, while within the surf zone, the phase-resolving component as well as the slowly varying phase-averaged pore pressure component due to wave set-up are present (Massel, 2001; Massel *et al.*, 2004, 2005). Massel *et al.* (2005) developed an exact closed-form solution for the fast varying pore-pressure component and velocity, which takes into account soil deformations, volume change and pore-water flow. When the stiffness ratio $G/E'_w \geq 100$ (G is the shear modulus of the soil and, E'_w is the apparent bulk modulus of the pore water), the vertical distribution of the pore pressure is very close to the Moshagen & Tørum (1975) solution assuming that the soil is rigid and the fluid is compressible. The apparent bulk modulus depends on the degree of saturation by air, which is very difficult to estimate in experimental conditions. Extensive field measurements carried out by de Rouck & Troch (2002) showed that there was approximately 3% gas in the soil pores. Tørum (2007) argued that in laboratory conditions, the air/gas content can be in the range 3-10%. Figure 4 shows the example of comparison of the theoretical results with the Large Wave Channel experimental tests in Hannover (Massel *et al.*, 2004). The long wave case and three solutions, namely the exact closed-form solution (eq. 34 in the figure), Moshagen & Tørum (1975) solution (eq. 64 in the figure) and the special case of a rigid soil and incompressible water (eq. 55 in the figure), have been adapted. The solution for a partly saturated soil, when $G/E'_w \rightarrow \infty$, is very close to the exact solution and compares well with the experimental data.

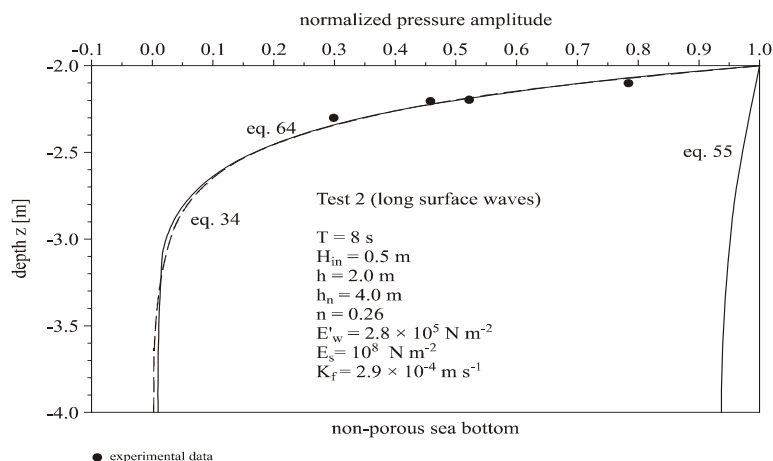


Figure 4 – Attenuation of pore pressure with depth. Comparison of the experimental data and theoretical models (adapted from Massel *et al.*, 2005).

The radiation stress tensor S_{xx} induces a change in the mean water level that exhibits two different horizontal steady pressure gradients. These steady pressure gradients induce two systems of circulation, related to the different gradients' signs (Massel, 2001). For the offshore gradient, the horizontal excess pressure carries the flow in the offshore direction. However, closer to the shore, the pressure gradient is reversed and the resulting flow moves shorewards. The final circulation pattern due to waves run-up on the porous beach is a result of combined the impact of the phase-resolving and phase-averaged pore pressure components.

CONCLUSIONS

When reviewing the modelling techniques of surface wave propagation one striking observation is the increasing variety and complexity of models in which more physical processes are implemented, greater precision and resolution are achieved and extended ranges of applicability are demonstrated. In particular, substantial progress has been made in the modelling of freak waves. Estimated velocities and forces induced by these events can help improve the design of

ships and offshore structures. In coastal waters, more processes have to be taken into account than in oceanic waters. The modified mild-slope equation approach offers a more accurate description of wave propagation over a sloping bed. However, highly non-linear phenomena such as wave breaking and wave run-up require new theoretical ideas and more precise experimental data. In general, the proper selection of any model should be based first of all on a proper understanding of the physical processes to be modelled. Finally, in order to estimate the applicability of particular models, a comparison with high quality experimental data, collected in nature or in laboratory conditions, is necessary.

REFERENCES

- Athanassoulis, G.A. & Belibassakis, K.A. 1999. A consistent coupled-mode theory for the propagation of small-amplitude water waves over variable bathymetry regions. *J. Fluid Mech.*, 389: 275-301.
- Baldock T.E. & Swan, C. 1994. Numerical calculations of large transient water waves. *Applied Ocean Res.*, 16: 101-112.
- Baldock, T.E., Swan, C. & Taylor, P.H. 1996. A laboratory study of non-linear surface waves on water. *Phil. Trans. R. Soc. London, A* 354: 1-28.
- Banner, M.L. & Song, J.B. 2002. On Determining the onset and strength of breaking for deep water waves. Part II. Influence of wind forcing and surface shear. *J. Phys. Oceanogr.*, 32: 2559-2570.
- Belibassakis, K.A., Athanassoulis, G.A. & Gerostathis, T.P. 2001. A coupled-mode for the refraction-diffraction of linear waves over steep three-dimensional bathymetry. *Applied Ocean Res.*, 23: 319-336.
- Belibassakis, K.A. & Athanassoulis, G.A. 2002. Extension of second-order Stokes theory to variable bathymetry. *J. Fluid Mech.*, 464: 35-80.
- Belibassakis, K.A. & Athanassoulis, G.A. 2006. A coupled-mode technique for the run-up of non-breaking dispersive waves on plane beaches. *Proc. 25th Intern. Conf. Offshore Mech. and Arctic Eng.*, Hamburg, OMAE 2006 - 92162: 1-8.
- Berkhoff, J.C.W. 1972. Computation of combined refraction-diffraction. *Proc. 13th Coastal Eng. Conf.*, 1: 471-490.
- Bitner-Gregersen, E.M. & Hagen, Ø. 2004. Freak wave events within the second order wave model. *Proc. Offshore Mech. and Arctic Eng.*, OMAE 2004-51410.
- Bonmarin, P. & Kjeldsen, S.P. 2000. Some geometric and kinematic properties of breaking waves. In: Olagnon, M. & Athanassoulis, G.A. (Eds). *Rogue Waves*. Editions Ifremer, Brest, 169-180.
- Carrier, G.F. & Greenspan, H.P. 1958. Water waves of finite amplitude on a sloping beach. *J. Fluid Mech.*, 4: 97-109.
- Clamond, D. & Grue, J. 2001a. A fast method for fully non-linear water wave computations. *J. Fluid Mech.*, 447: 337-355.
- Clamond, D. & Grue, J. 2001b. On efficient numerical simulations of freak waves. *Proc. of 11th Intern. Offshore and Polar Eng. Conf.*, Stavanger.
- de Rouck, J. & Troch, P. 2002. Pore water pressure response due to tides and waves based on prototype measurements. *PIANC Bull.*, 110: 9-31.
- Dold, J.W. & Peregrine, D.H. 1984. Steep unsteady waves: an efficient computational scheme. *Proc. 19th Intern. Conf. Coastal Eng.*, 1:955-967.
- Dold, J.W. & Peregrine, D.H. 1986. Water-wave modulation. *Proc. 20th Intern. Conf. Coastal Eng.*, 1:163-175.
- Duncan, J.H. An investigation of breaking waves produced by a towed hydrofoil. *Proc. R. Soc. London, A* 377: 331-348.

- Duncan, J.H. 1981. 1983. The breaking and non-breaking wave resistance of a two-dimensional hydrofoil. *J. Fluid Mech.*, 126:331-348.
- Dysthe, K.B. 1979. Note on a modification to the non-linear Schrödinger equation for application to deep water waves. *Proc. R. Soc. London, A* 369: 105-114.
- Dysthe, K.B., Trulsen, K., Krogstad, H.E. & Socquet-Juglard, H. 2003. Evolution of a narrow-band spectrum of random surface gravity waves. *J. Fluid Mech.*, 478: 1-10.
- Fenton, J.D. 1979. A high-order cnoidal wave theory. *J. Fluid Mech.*, 94:129-161.
- Fenton, J.D. 1985. A fifth order Stokes' theory for steady waves. *J. Waterway, Port, Coastal and Ocean Eng.*, 111: 216-234.
- Fenton, J.D. 1986. Polynomial approximation and water waves. *Proc. 20th Coastal Eng. Conf.*, 1: 193-207.
- Grue, J., Clamond, D., Huseby, M., & Jensen, A. 2003. Kinematics of extreme waves in deep water. *Applied Ocean Res.*, 25: 355-366.
- Grue, J. & Jensen, A. 2006. Experimental velocities and accelerations in very steep wave events in deep water. *European J. Mechanics B/Fluids*, 25: 554-564.
- Gudmestad, O.T. 1993. Measured and predicted deep water wave kinematics in regular and irregular seas. *Marine Structures*, 6: 1-73.
- Hanson, J.L. & Phillips, O.M. 1999. Wind sea growth and dissipation in the open ocean. *J. Phys. Oceanogr.*, 29: 1633-1647.
- Hasselmann, S., Hasselmann, K., Allender, J.H. & Barnett, T.P. 1985. Computations and parameterizations of the non-linear energy transfer in a gravity wave spectrum. Part 2: parameterizations of the non-linear energy transfer for application in wave models. *J. Phys. Oceanogr.*, 15: 1378-1391.
- Holthuijsen, L.H. 2007. *Waves in oceanic and coastal waters*. Cambridge Univ. Press. Cambridge, 387 pp.
- Janssen, P. 2004. *The interaction of ocean waves and wind*. Cambridge Univ. Press. Cambridge, 300 pp.
- Jensen, A., Clamond, D., Huseby, M., & Grue, J. 2007. On local and convective acceleration in steep wave events. *Ocean Eng.*, 34: 426-435.
- Kharif, C. & Pelinovsky, E. 2003. Physical mechanisms of the rogue wave phenomenon. *Eur. J. Mech. B/Fluids*, 22: 603-634.
- Kitaigorodskii, S.A. 1983. On the theory of the equilibrium range in the spectrum of wind-generated gravity waves. *J. Phys. Oceanogr.*, 13: 816-827.
- Komen, G.J., Hasselmann, S. & Hasselmann, K. 1984. On the existence of a fully developed wind-sea spectrum. *J. Phys. Oceanogr.*, 14: 1271-1285.
- Krasitskii, V.P. 1994. On reduced equations in the Hamiltonian theory of weakly non-linear surface waves. *J. Fluid Mech.*, 272: 1-20.
- Kurkin, A.A. & Pelinovsky, E.N. 2004. *Freak waves: facts, theory and modelling*. Techn. Univ. of Nizhny Novgorod, 157 p. (in Russian).
- Lie, V. & Tørum, A. 1991. Ocean waves over shoals. *Coastal Eng.*, 15: 545-562.
- Lo, F. & Mei, C.C. 1985. A numerical study of water-wave modulation based on a high-order non-linear Schrödinger equation. *J. Fluid Mech.*, 173: 683-707.
- Longuet-Higgins, M.S. 1969. On wave breaking and the equilibrium spectrum of wind-generated waves. *Proc. R. Soc. London, A* 310; 151-159.
- Longuet-Higgins, M.S. & Cokelet, E.D. 1976. The deformation of steep surface waves on water. I. A numerical method of computation. *Proc. R. Soc. London, A*350: 1-26.
- Luke, J.C. 1967. A variational principle for a fluid with a free surface. *J. Fluid Mech.*, 27: 395-397.
- Massel, S.R. 1993. Extended refraction-diffraction equations for surface waves. *Coastal Eng.*, 19: 97-126.

- Massel, S.R. 1996. *Ocean Surface Waves: their Physics and Prediction*. World Scientific Publ. Singapore, 491 pp.
- Massel, S.R. 2001. Circulation of groundwater due to wave set-up on a permeable beach. *Oceanologia*, 43(3): 279-290.
- Massel, S.R. 2007. *Ocean Waves Breaking and Marine Aerosol Fluxes*. Springer. New York, 323 pp.
- Massel, S.R. & Pelinovsky, E.N. 2001. Run-up of dispersive and breaking waves on beaches. *Oceanologia*, 43(1): 61-97.
- Massel, S.R., Przyborska, A. & Przyborski, M. 2004. Attenuation of wave-induced groundwater pressure in shallow water. Part 1. *Oceanologia*, 46(3): 383-404.
- Massel, S.R., Przyborska, A. & Przyborski, M. 2005. Attenuation of wave-induced groundwater pressure in shallow water. Theory. *Oceanologia*, 47(3): 291-323.
- Monahan, E.C. 1971. Oceanic whitecaps. *J. Phys. Oceanogr.*, 1: 139-144.
- Moshagen, H. & Tørum, A. 1975. Wave induced pressure in permeable sea beds. *J. Waterways, Harbors and Coastal Eng.*, 101(1): 49-57.
- Onorato, M., Osborne, A.R., Serio, M., & Damiani, T. 2000. Occurrence of freak waves from envelope equations in random ocean wave simulations. In: Olagnon, M. & Athanassoulis, G.A. (Eds). *Rogue Waves*, Editions Ifremer Brest, 181-192.
- Onorato, M., Osborne, A.R., Serio, M., & Bertone, S. 2001. Freak wave in random oceanic sea states. *Phys. Rev. Letters*, 86: 5831-5834.
- Onorato, M., Osborne, A.R., Serio, M., Cavaleri, L., Braudini, C., & Stansberg, C.T. 2006. Extreme waves, modulational instability and second order theory: wave flume experiments on irregular waves. *European J. Mechanics B/Fluids*, 25: 586-601.
- Pelinovsky, E.N. 1996. *Tsunami Waves Hydrodynamics*. Institute of Applied Physics, Nizhiny Novogorod, 274 pp (in Russian).
- Peregrine, D.H. 1983. Water waves, non-linear Schrödinger equations and their solutions. *J. Math. Soc., Ser. B.*, 25: 16-43.
- Phillips, O.M. 1985. Spectral and statistical properties of the equilibrium range in wind-generated gravity waves. *J. Fluid Mech.*, 156:505-531.
- Rapp, R.J. & Melville, W.K. 1990. Laboratory measurements of deep-water breaking waves. *Phil. Trans. R. Soc. London, A* 331: 735-800.
- Smith, S.F. & Swan, C. 2002. Extreme two-dimensional water waves: an assessment of potential design solutions. *Ocean Eng.*, 29: 387-416.
- Sobey, R.J. 1992. A local Fourier approximation method for irregular wave kinematics. *Applied Ocean Res.*, 14: 93-105.
- Song, J.B. & Banner, M.L. 2002. On Determining the onset and strength of breaking for deep water waves. Part I: Unforced irrational wave groups. *J. Phys. Oceanogr.*, 32: 2541-2558.
- Stramska, M. & Petelski, T. 2003. Observations of oceanic whitecaps in the north polar waters of the Atlantic. *J. Geophys. Res.*, 108(C3): 3086.
- Thorpe, S.A. 1993. Energy loss by breaking waves. *J. Phys. Oceanogr.*, 23: 2498-2502.
- Toba, Y. 1973. Local balance in the air-sea boundary process. On the spectrum of wind waves. *J. Oceanogr. Soc. Japan*, 29: 2009-2020.
- Tørum, A. 2007. Wave induced pore pressure – air/gas content. *J. Waterways, Port, Coastal, Ocean Eng.*, 133(1): 83-86.
- Tørum, A. & Gudmestad, O.T. (Eds). 1990. *Water wave kinematics*. Kluwer Academic Publ., Dordrecht, 771 p.
- Trulsen, K. & Dysthe, K.B. 1996. A modified non-linear Schrödinger equation for broader bandwidth gravity waves on deep water. *Wave Motion*, 24: 281-289.
- Trulsen, K. & Dysthe, K. 1997. Freak Waves – A three-dimensional wave simulation. *Proc. 21 Symp. on Naval Hydrodynamics*. Nat. Academy Press, 550-560.

- Tulin, M.P. & Waseda, T. 1999. Laboratory observations of wave group evolution including breaking effects. *J. Fluid Mech.*, 378: 197-232.
- WAMDI group: Hasselmann, S., Hasselmann, K., Bauer, E., Janssen, P.A.E.M., Komen, G.J., Bertotti, L., Lionello, P., Guillaune, A., Cordone, V.C., Greenwood, M., Reistad, L., Zambresky, L. & Ewing, J.A. 1988. The WAM model: a third generation ocean wave prediction model. *J. Phys. Oceanogr.*, 18: 1775-1810.
- Wheeler, J.D. 1970. Method for calculating forces produced by irregular waves. *Proc. Offshore Techn. Conf.*, Houston, 1: 71-82.
- Zakharov, V.E. 1968. Stability of periodic waves of finite amplitude on the surface of a deep fluid. *J. Appl. Mech. Tech. Phys.*, 9: 190-194.

COMPARING LAGRANGIAN AND EULERIAN MODELS FOR THE ANALYSIS OF STEEP IRREGULAR WAVES

Sébastien Fouques¹ and Carl Trygve Stansberg¹
¹Norwegian Marine Technology Research Institute AS (MARINTEK)
Trondheim, Norway

ABSTRACT

Two different approaches for the surface and kinematics description of steep ocean waves are reviewed and compared. One is the Lagrangian description, which considers the motion of individual labelled fluid particles. The other is the more commonly used Eulerian description where the wave properties at fixed positions in space are analyzed. For both approaches, first- and second-order solutions are investigated. They were studied earlier in Fouques et al. (2005, 2006), and Stansberg et al. (2008). One fundamental difference between the two descriptions is that in the Eulerian modelling, a second order solution is required to reproduce steepened crests and flat troughs, while in the Lagrangian model, this property already arises in the linear solution.

This comparative investigation makes use of numerical case studies as well as experimental wave tank recordings. In the latter case, numerical reproductions are benchmarked against the actual measurements. Differences in the two approaches are discussed, both from a theoretical point of view and as observed from case study examples.

INTRODUCTION

There exists two main approaches in fluid mechanics to describe the motion of a fluid. In the Eulerian formulation, one expresses the unknowns of the problem, which may be the fluid velocity and the pressure, as functions of earth-fixed space variables x , y , and z . In the Lagrangian approach, the fluid is described through a collection of individual particles, and one looks for the properties of each of them, such as its position and velocity, as well as the pressure in its vicinity. The unknowns are therefore written in terms of so-called Lagrangian variables, which serve to continuously label the fluid particles (Lamb, 1932).

As far as ocean wave modelling is concerned, the Lagrangian formalism has received less attention than its Eulerian counterpart. A review of some various attempts and discussions can be found in Fouques (2005). Still, it is an interesting fact that some typical steep wave properties such as the sharpening of the crests and the flattening of the troughs, horse-shoe patterns in three-dimensional wave groups, or the steepening of the wave front are already captured at lower orders in the Lagrangian approach (Fouques et al., 2005).

Governing equations for the fluid motion will not be presented here. These equations include the conservations of mass and momentum, as well as free-surface and bottom boundary conditions, and they can be found for example in Fouques et al. (2005) for the Lagrangian approach, and in Sharma and Dean (1981) for the Eulerian one. However, it can be noticed that when using the Lagrangian point of view, the free surface conditions are linear whereas the mass and momentum conservations are not. In the Eulerian approach, the Laplace equation is linear whereas the free surface conditions are not. This suggests that there will be two different kinds of limitations when deriving first- and second order approximated solutions. In the Eulerian

formalism, fluid properties are only known up to the mean water level $z = 0$, while the free surface is accurately determined in the Lagrangian one. However, since the mass conservation is not exactly fulfilled in approximated solutions based on the latter approach, some water may simply disappear from the surface in steep waves, whereas this does not occur with sinusoidal Eulerian waves.

This paper compares these two approaches using both simple numerical case studies and measured wave data. First- and second-order solutions for irrotational gravity waves in deep water are considered. The first part investigates the differences between the Eulerian and Lagrangian solutions for simple regular waves. Further, long-crested bichromatic waves are discussed. Eventually, the last part of the paper deals with the reconstruction of a measured wave time series using both approaches.

REGULAR WAVES

Eulerian solutions

The regular wave solution obtained in deep water by solving the Eulerian equations of motion can be written up to the third-order as

$$\eta(x, t) = \eta_1 + \eta_2 + \eta_3, \quad (1)$$

with

$$\eta_1 = a \cos(\Psi) \quad (2a)$$

$$\eta_2 = \frac{1}{2} k a^2 \cos(2\Psi) \quad (2b)$$

$$\eta_3 = \frac{3}{8} k^2 a^3 \cos(3\Psi), \quad (2c)$$

where $\Psi = kx - \omega t$ is the wave phase, x the horizontal space coordinate, k the wave number, ω the wave frequency, t the time variable, and a the wave amplitude. Here, η_1 , η_2 , and η_3 denote the first, second, and third order contributions, respectively. At the first and second orders, the wave frequency and the wave number are bound through the dispersion relation $\omega^2 = kg$, where g denotes the acceleration of the gravity. At the third order, the dispersion relation becomes $\omega^2 = kg(1 + a^2 k^2)$ so that the phase velocity increases together with the wave amplitude.

Lagrangian solutions

The corresponding Lagrangian solution is given as the horizontal and vertical positions of the surface particles $\tilde{x}(\alpha, t)$ and $\tilde{z}(\alpha, t)$, respectively. Here, α is a horizontal labelling parameter for the particles, such as the position of the particles at rest. Up to the second order, the irrotational regular solution in deep water reads (Fouques et al., 2005):

$$\tilde{x}(\alpha, t) = \alpha + \tilde{x}_1 + \tilde{x}_2 \quad (3a)$$

$$\tilde{z}(\alpha, t) = \tilde{z}_1 + \tilde{z}_2 \quad (3b)$$

with

$$\tilde{x}_1 = -a \sin(\tilde{\Psi}) \quad (4a)$$

$$\tilde{z}_1 = a \cos(\tilde{\Psi}) \quad (4b)$$

for the linear part, and

$$\tilde{x}_2 = a^2 \omega k t \quad (5a)$$

$$\tilde{z}_2 = \frac{1}{2} k a^2 \quad (5b)$$

for the second order one. Here, the wave phase $\tilde{\Psi} = k\alpha - \omega t$ is no longer a function of the Eulerian coordinate x , but it depends on the particle label α . The deep water dispersion relation for the first- and second-order Lagrangian solutions is identical to the Eulerian one, viz. $\omega^2 = kg$.

Comparison of the linear wave profiles

The linear Lagrangian wave profile is a trochoid with sharper crests and broader troughs than its Eulerian sinusoidal counterpart, as depicted in Figure 1 and Figure 2. It is obtained by horizontally “compressing” the original sinusoidal wave \tilde{z}_1 at the crests and “stretching” it in the troughs, so that the Lagrangian and Eulerian wave heights are equal. Consequently, the mean water level in the Lagrangian solution is negative, which is related to the fact that the mass conservation is fulfilled at the first order only. However, as the wave amplitude gets infinitely small, the two wave profiles become identical.

Figure 2 shows a comparison of the local wave slope defined as the derivative of the surface elevation with respect to the Eulerian coordinate x for the linear Lagrangian and Eulerian solutions. It can be seen that the former show slightly steeper waves than the latter. However, the location of the steepest point is dramatically moved towards the wave crests in the Lagrangian wave compared to the Eulerian one, for which the slope curve is sinusoidal with maxima located at the midpoint between the crest and the trough.

By solving $x = \alpha + \tilde{x}_1$ for α and inserting in \tilde{z}_1 , it is possible to rewrite the Lagrangian wave profile in term of the Eulerian coordinate x and compare with the linear Eulerian solution. As noticed by Kinsman (1965), it is a remarkable fact that the first order Lagrangian solution already matches the third-order Stokes wave as given in Equations (1) and (2a)-(2c).

Comparison of the non-linear waves profiles

Unlike the second-order Eulerian solution, in which harmonics with double frequency are required to render the sharper crests, the second-order Lagrangian wave profile is identical to the linear one apart from a vertical translation of $ka^2/2$ in order to fulfill the mass conservation.

As illustrated in Figure 1 and Figure 3, the wave height and the crest height obtained from the second-order Eulerian and Lagrangian solutions are equal. The third-order Stokes wave has shallower troughs and higher crests, but as mentioned above, its shape is identical to the first- and second-order Lagrangian solution up to the third-order. The main difference between the black and the solid red curves in Figure 1 is therefore the total wave amplitude, the third-order wave being more energetic because of additional harmonics.

Figure 3 shows the local slope of the second-order Lagrangian and Eulerian regular waves, as well as the one from the third-order Stokes wave. It should be noted that the slope of the second-order Lagrangian solution is identical to the slope of the linear Lagrangian one shown in Figure 2 because the former is merely obtained by a vertical translation of the latter. One can see that the second-order Eulerian wave is somewhat steeper than its Lagrangian counterpart. However, as the order of the Eulerian solution increases, the location of the maximum steepness moves

towards the wave crest in space and gets closer to the steepest point in the linear and second-order Lagrangian solutions.

As mentioned by Pierson (1961), the horizontal surface current with velocity $a^2\omega k$ (and with exponential vertical decay) is similar to the one obtained from the second order Stokes drift and it is needed to fulfill the irrotational flow condition. In addition, since the Lagrangian phase $\tilde{\Psi}$ depends on the Lagrangian coordinate α and not on the horizontal position x , this surface drift results in a second order alteration of the wave crest velocity, which equals

$$\tilde{V}_c = \frac{\omega}{k}(1 + k^2 a^2). \quad (6)$$

This additional second order crest velocity term in the second-order Lagrangian solution is twice as large as the one obtained from the alteration of the dispersion relation in the third-order Eulerian solution (Pierson, 1961).

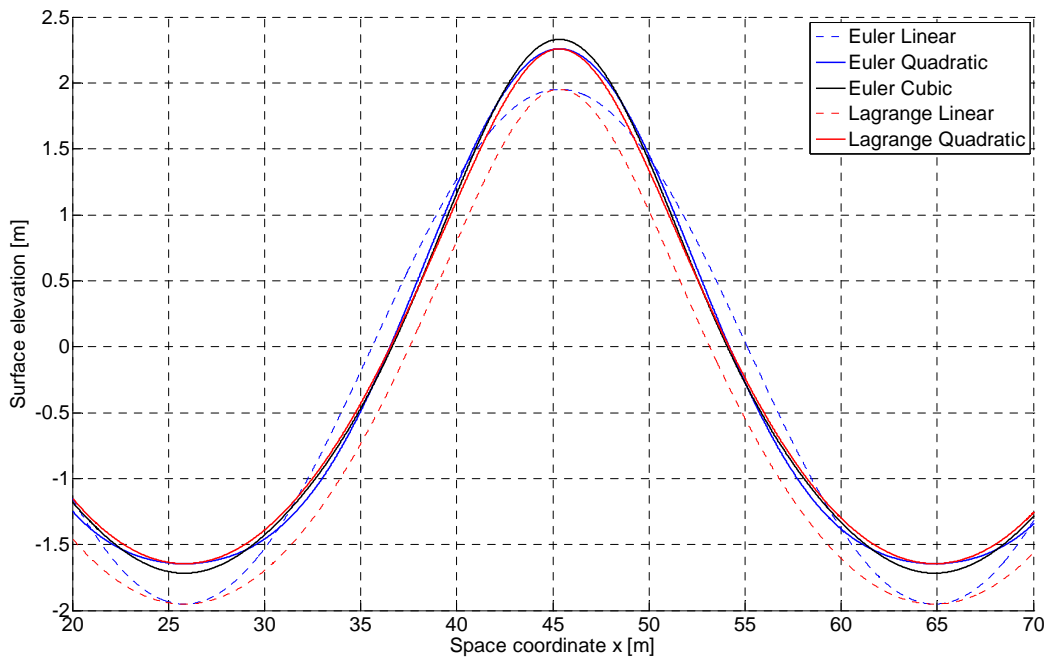


Figure 1: Comparison of regular wave profiles (period $T=5s$ and steepness $k.a=0.31$) for the first-, second- and third-order Eulerian solutions, as well as the first- and second-order Lagrangian solutions. Dotted lines: linear solutions. Solid lines: second and third order solutions.

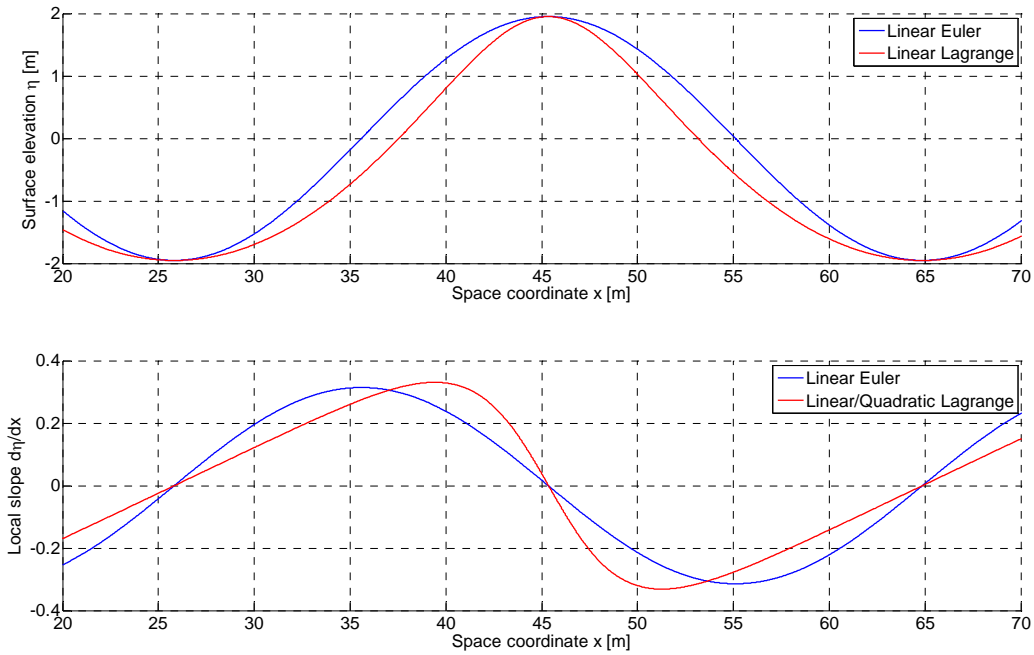


Figure 2: Comparison of regular wave slopes (period $T=5s$ and steepness $k.a=0.31$) for the linear Eulerian and Lagrangian solutions. Top: wave profiles. Bottom: corresponding local wave slope.

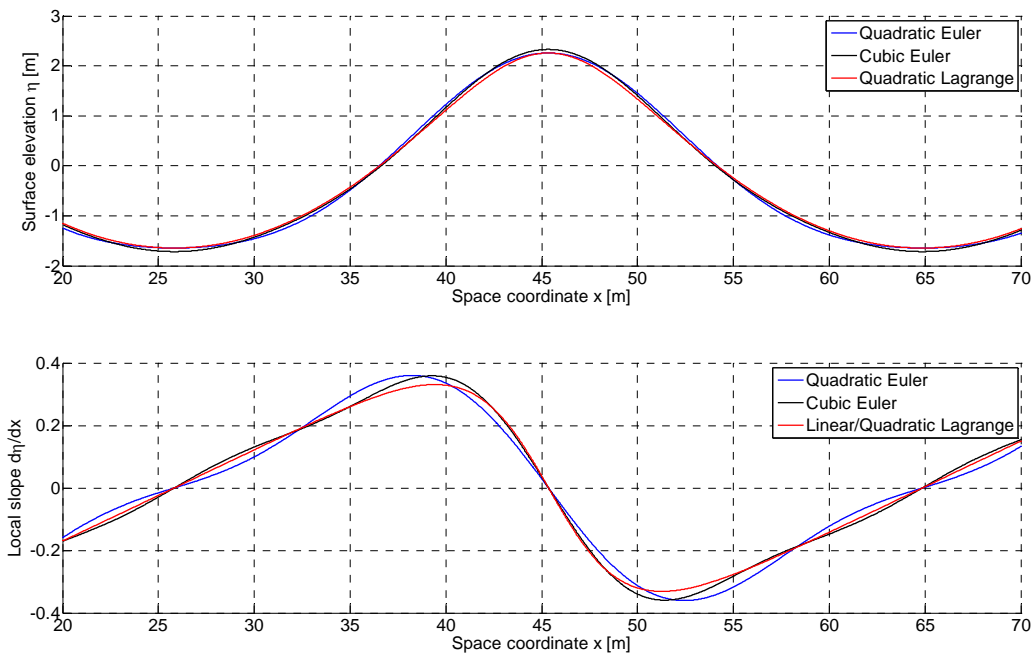


Figure 3: Comparison of regular wave slopes (period $T=5s$ and steepness $k.a=0.31$) for the second-order Eulerian and Lagrangian solutions, as well as the third order Eulerian solution. Top: wave profiles. Bottom: corresponding local wave slope.

Horizontal particle velocity under wave crests

Another parameter of interest is the particle velocity in the wave. In this section we will compare the horizontal particle velocity under the wave crest u for the first- and second-order Eulerian and Lagrangian regular waves.

Using the first order Eulerian solution, u is known only up to the mean water level $z = 0$ and it reads

$$u_{E1} = a\omega \exp(kz) \text{ for } z \leq 0. \quad (7)$$

Further, since the second order velocity potential is zero for regular waves in deep water, the second-order velocity u_{E2} is also zero for $z \leq 0$. Over the mean water level and up to the top of the crest $z = a + ka^2/2$, u_{E2} can be obtained from a Taylor expansion of the first order horizontal particle velocity u_{E1} (Stansberg et al., 2008), viz.

$$u_{E2} = a\omega kz \text{ for } 0 \leq z \leq a + ka^2/2 \quad (8)$$

The total horizontal velocity under the crest is then equal to the sum $u_{E1} + u_{E2}$. It should be noticed that the expression of u_{E2} given above also contains third-order terms for $z \geq a$.

With the Lagrangian approach, flow parameters such as the particle velocity can be determined up to the free-surface. Thus the Lagrangian linear horizontal particle velocity under the crest u_{L1} can be written as (Fouques et al., 2006)

$$u_{L1} = a\omega \exp(k\delta) \quad (9a)$$

at

$$z = \delta + a \exp(k\delta). \quad (9b)$$

Here δ is the vertical Lagrangian coordinate equal to zero on the free surface. Similarly, at the second order we obtain that the total horizontal velocity reads

$$u_{L1} + u_{L2} = a\omega \exp(k\delta) + a^2\omega k \exp(2k\delta) \quad (10a)$$

at

$$z = \delta + a \exp(k\delta) + \frac{1}{2}ka^2 \exp(2k\delta). \quad (10b)$$

Figure 4 shows a comparison of the four above-mentioned horizontal velocity profiles. It can be noticed that the Eulerian and Lagrangian linear solutions provide the same maximum velocity, but this value is reached at $z = 0$ in the former and at the surface in the latter. The Lagrangian solution is in this way similar to the Wheeler stretching method (Stansberg et al., 2008).

The total velocity profiles including first- and second-order contributions are plotted up to the top of the crest. From Figure 4, one can see that the Lagrangian solution gives smaller horizontal particle velocities than its Eulerian counterpart, but it should be noted that third-order terms are included in equation (8). The velocity from the Eulerian solution at the top of the first order crest $z = a$ is the same as the velocity from the Lagrangian one at the top of the second order crest $z = a + ka^2/2$, and it is equal to $a\omega + a^2\omega k$. Once again, the Lagrangian velocity profile is obtained by stretching the Eulerian one, this time from $z = a$ to $z = a + ka^2/2$.

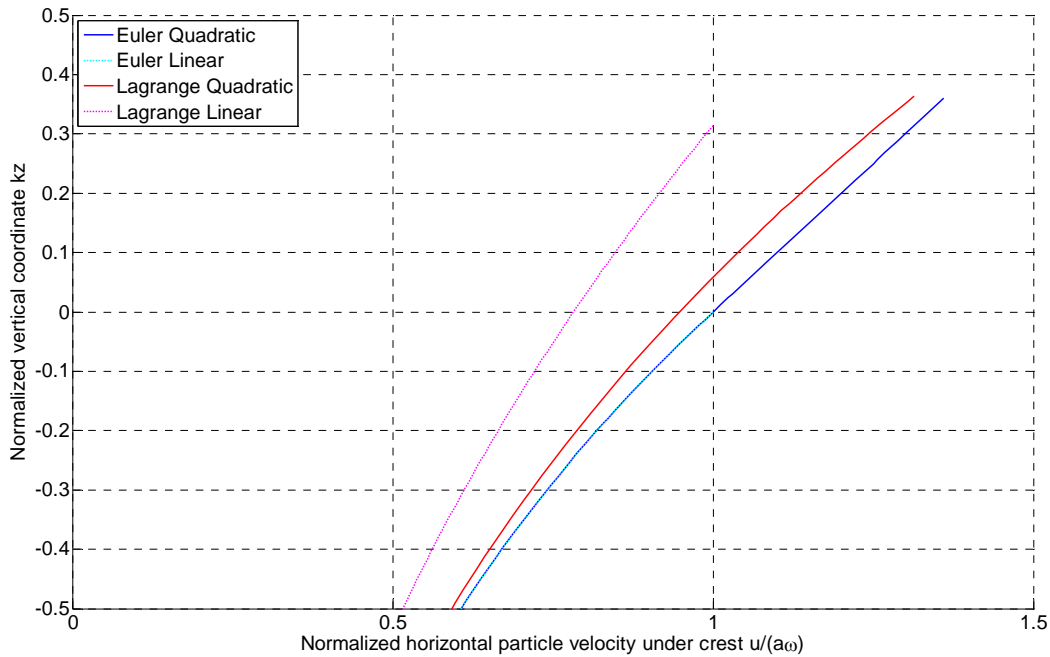


Figure 4: Normalized horizontal particle velocity under the wave crest versus normalized vertical position (same case as in Figure 1).

BICHROMATIC WAVES

In this section, we consider the interaction of two regular waves with amplitudes a_1 and a_2 , and wave numbers k_1 and k_2 . In addition, we assume that $k_1 > k_2$ and that the two wave numbers are close to each other so that the interference pattern shows beatings.

Eulerian solutions

The first order Eulerian solution is simply the sum of two sine waves, viz.

$$\eta_1 = a_1 \cos \Psi_1 + a_2 \cos \Psi_2 \quad (11)$$

with $\Psi_i = k_i x - \omega_i t + \varphi_i$ for $i = 1..2$, with the dispersion relation $\omega_i^2 = k_i g$, and where the φ_i are constant phase terms.

The corresponding second-order solution shows both sum- and difference-frequency terms:

$$\begin{aligned} \eta_2 = & \frac{1}{2} a_1 a_2 [(k_1 + k_2) \cos(\Psi_1 + \Psi_2) - (k_1 - k_2) \cos(\Psi_1 - \Psi_2)] \\ & + \frac{1}{2} a_1^2 k_1 \cos(2\Psi_1) + \frac{1}{2} a_2^2 k_2 \cos(2\Psi_2). \end{aligned} \quad (12)$$

Lagrangian solutions

The first order Lagrangian solution for bichromatic waves can be written as (Pierson, 1961):

$$\tilde{x}_1 = -a_1 \sin \tilde{\Psi}_1 - a_2 \sin \tilde{\Psi}_2 \quad (13a)$$

$$\tilde{z}_1 = a_1 \cos \tilde{\Psi}_1 + a_2 \cos \tilde{\Psi}_2 \quad (13b)$$

with $\tilde{\Psi}_i = k_i \alpha - \omega_i t + \varphi_i$ for $i = 1..2$.

At the second order, no sum-frequency terms are present in the solution, so that the corresponding particle displacement reads (Fouques et al., 2006)

$$\tilde{x}_2 = a_1 a_2 \sin(\tilde{\Psi}_1 - \tilde{\Psi}_2) \times \left[-\frac{k_1^2 + k_2^2 + (k_1 + k_2)\sqrt{k_1 k_2}}{k_1 - k_2} + \sqrt{k_1}(\sqrt{k_1} + \sqrt{k_2}) \right] + (a_1^2 k_1 \omega_1 + a_2^2 k_2 \omega_2) \times t \quad (14a)$$

$$\tilde{z}_2 = a_1 a_2 \cos(\tilde{\Psi}_1 - \tilde{\Psi}_2) \times \left[k_1 + k_2 + \sqrt{k_1 k_2} - \sqrt{k_1}(\sqrt{k_1} + \sqrt{k_2}) \right] + \frac{1}{2} a_1^2 k_1 + \frac{1}{2} a_2^2 k_2. \quad (14b)$$

Comparison

Figure 5 shows a comparison of the Eulerian and Lagrangian surface elevations corresponding to the linear and second-order solutions for bichromatic waves in deep water. It can be seen that the crest height of the Eulerian and Lagrangian solutions are quite similar at the second order, the former being still slightly higher. The maximum local slope however is a little larger in the second order Lagrangian solution. Figure 6 shows the second-order contributions \tilde{x}_2 and \tilde{z}_2 to the particle displacement together with the first- and second-order Lagrangian wave profiles. One can notice that the second-order Lagrangian surface is lifted up in the wave group, which is the opposite result compared to the set-down observed in the second-order Eulerian solution. Still, this second-order set-up compensates for the set-down in the linear Lagrangian solution, which is due to the horizontal “compression” of the wave crests and the “stretching” of the wave troughs.

A more striking feature is the phase shift that occurs in the second-order Lagrangian solution. This is due to the second-order slowly varying motion with phase $\tilde{\Psi}_1 - \tilde{\Psi}_2$ in equations (14a) and (14b), and which is plotted in Figure 6. Fluid particles are slowly flushed towards the center of the wave group, which results in an increase of the surface elevation due to mass conservation. Actually, this feature is similar to what happens in a regular Lagrangian wave where fluid particles are flushed towards the wave crest, but on a much larger horizontal crest. The \tilde{x}_2 values corresponding to second-order displacement waves may be very large because of the denominator in equation (14a). Since the Lagrangian phase terms $\tilde{\Psi}_i$ depend on the particle label α , and not on the Eulerian coordinate x , the crests appear to be translated towards the center of the wave group. Consequently, the crest velocity decreases as the crests travel through the wave group. Here again, the alteration of the crest velocity in the second-order Lagrangian solution is a property similar to the third-order Eulerian one.

In addition, second-order horizontal displacement waves are responsible for a steepening of individual wave fronts as they travel through areas with large and negative \tilde{x}_2 horizontal gradient, corresponding to large \tilde{z}_2 values (see Figure 6). In irregular waves, this may lead to a steepening of individual wave fronts as they travel through wave groups and as would do nearly breaking waves (Fouques et al., 2006).

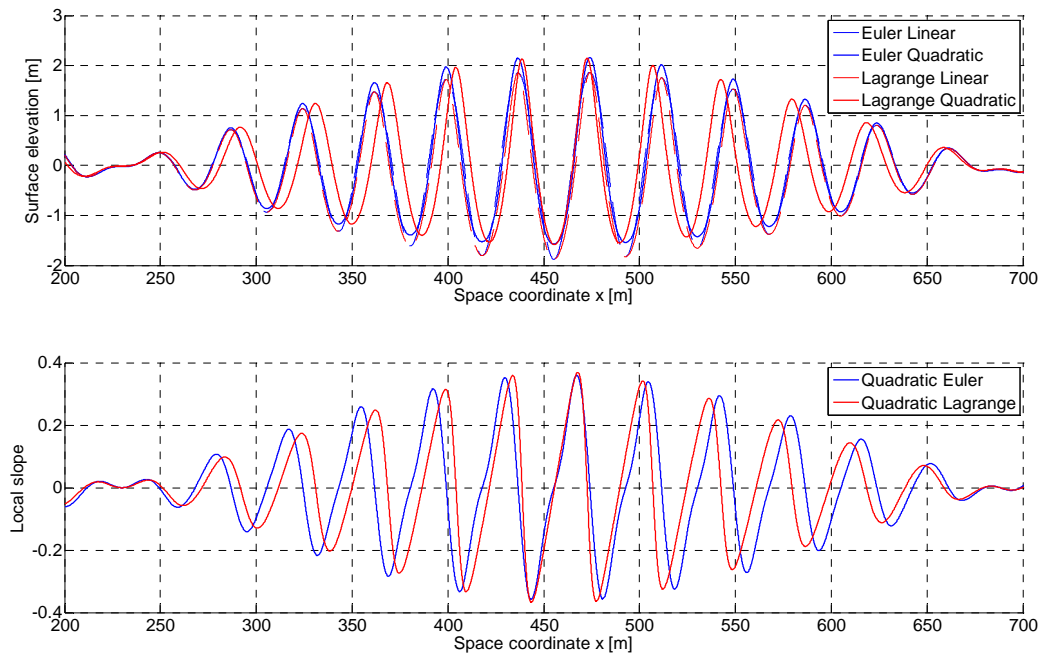


Figure 5: Comparison of first- and second-order Eulerian and Lagrangian solutions for bichromatic waves. Waves periods $T_1 = 5s$ and $T_2 = 4.8s$. Wave steepness $k_1 a_1 = 0.157$ and $k_2 a_2 = 0.157$. Top: surface elevation. Bottom: corresponding local slope.

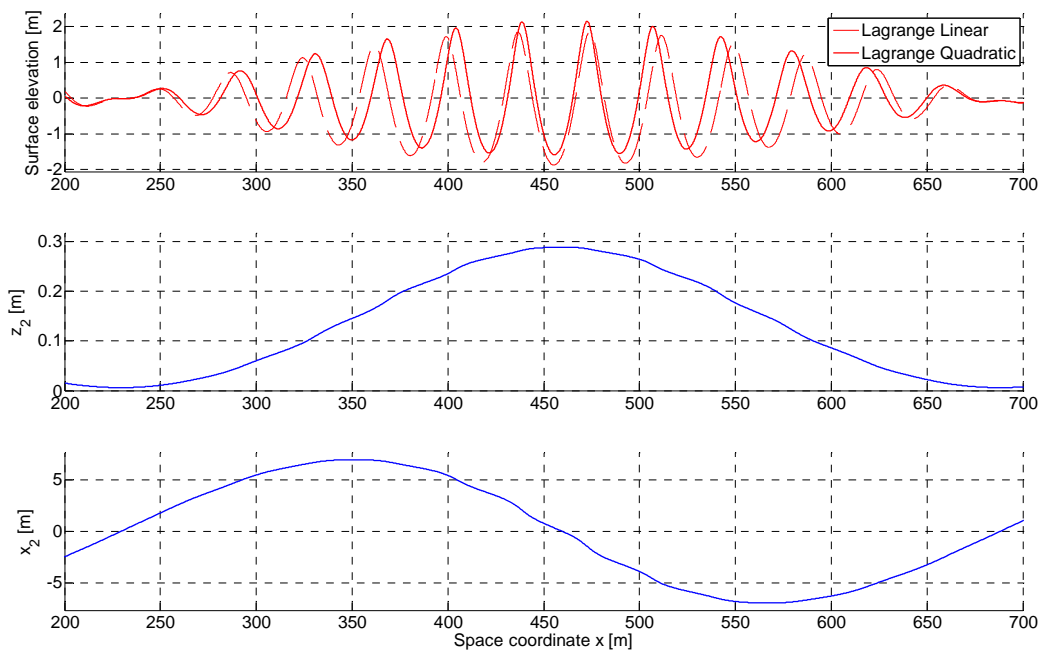


Figure 6: Second order particle displacements z_2 (middle) and x_2 (bottom) versus Lagrangian wave profile (top) in bichromatic waves with close frequencies. Same wave parameters as in previous figure.

MEASURED IRREGULAR WAVES

In this section we present some results from an ongoing research work that deals with the reconstruction of the surface elevation time series and related wave kinematics parameters from wave point measurements. Linear and second-order Eulerian and Lagrangian irregular wave models are considered. A mathematical description of these models can be found for example in Sharma and Dean (1981) and in Fouques et al. (2006). The black curve in Figure 7 is an excerpt from a time-series of a very steep and energetic wave event measured in Marintek's ocean basin, which was also among those investigated previously in Stansberg et al. (2008). A unidirectional Jonswap spectrum with scaled significant wave height and spectral peak period $H_s = 20m$ and $T_p = 20s$, respectively, was used to generate the 3-hour storm in model scale 1:55.

In order to reconstruct the surface elevation, the linear "free" wave components have first to be extracted from the measured time series. This was done by using the same low-pass filtering of the spectral tail and cut-off criterion as described in Stansberg et al. (2008). The obtained linear components were then used as inputs to both the Eulerian and Lagrangian wave models. Furthermore, Lagrangian wave models provide the position of fluid particles, which fluctuates horizontally with time. To be able to determine the surface elevation at a fixed location as a function of time, the positions of several particles located around the point of interest were calculated and the surface elevation interpolated at the wanted location.

Figure 7 shows the various reconstructed surface elevation time series along with the initial measured one. Corresponding time derivatives are given in Figure 8 and a close up of Figure 7 is provided in Figure 9. As shown above for regular and bichromatic waves, the wave reconstructed by the linear Lagrangian model looks thinner compared to the linear Eulerian one because the nonlinear mass conservation is not fulfilled exactly. However, its general shape appears to be closer to the measured wave. The wave height is similar in both linear models. In addition, it can be seen that the modelling of the crest height is improved in both approaches when adding second-order contributions, but it still remains lower than the measured crest height. The time derivative of the surface elevation provided in Figure 8, and which is directly related to the wave slope, shows the strong front-back asymmetry of the wave. This asymmetry is much better reproduced by the second-order Eulerian model compared to the linear one. Hardly any improvement is shown when using a second-order Lagrangian model instead of the first order one, except that some artificial secondary oscillations near the peak region are seen to be avoided in the Lagrangian models. Moreover, the two wave troughs preceding and following the large wave are not deep enough in the second-order Lagrangian reconstruction. This may be related to instabilities due to very large second-order horizontal particle displacements (see equation 14a) and the limited duration of the time series used to compute the linear wave components (2048 points). Such phase shift effects shown in the second-order Lagrangian models do not occur until the third-order in Eulerian models.

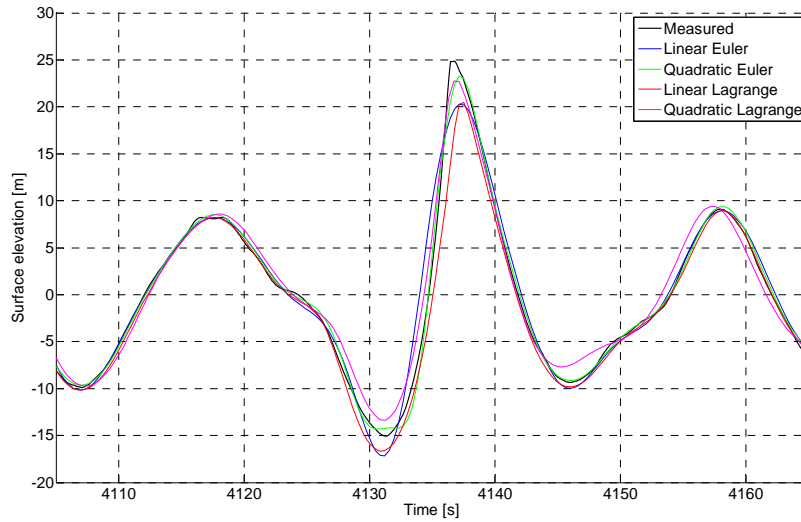


Figure 7: Measured and reconstructed time series of the surface elevation using first- and second-order Eulerian and Lagrangian models.

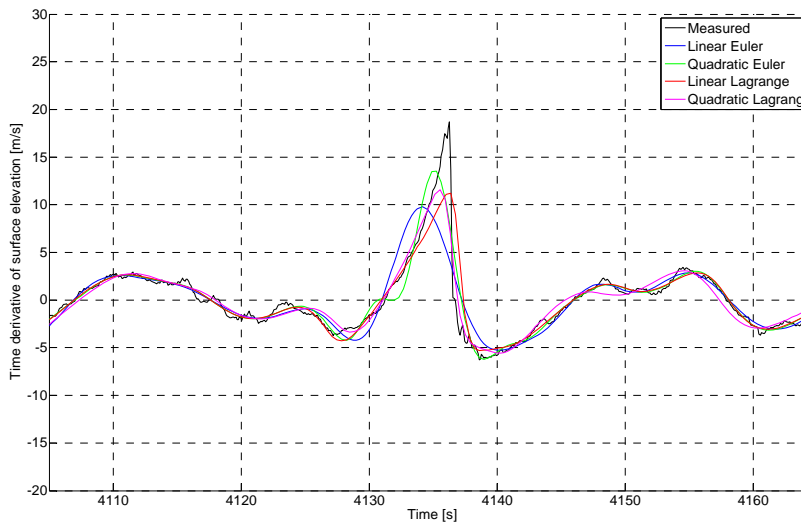


Figure 8: Time derivative of the surface elevation time series from the previous figure.

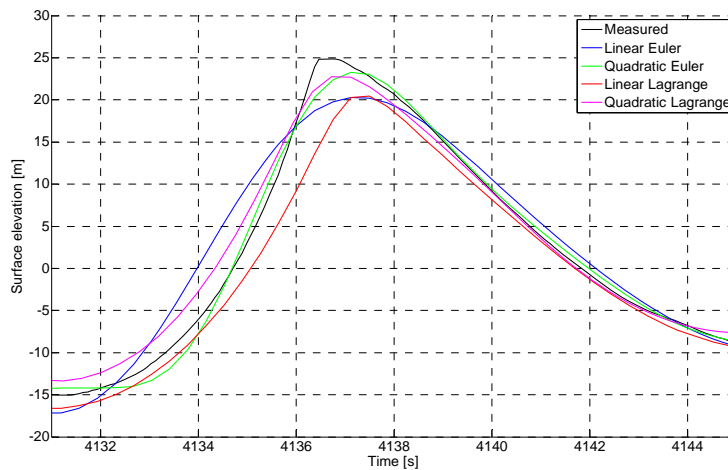


Figure 9: Close-up of Figure 7.

CONCLUSIONS

This paper has reported from an ongoing comparative study of the Eulerian and Lagrangian approaches to ocean wave modelling. Both first- and second-order solutions have been investigated. It was shown that properties such as the wave height are quite similar in both approaches. The general shape of the wave is much better captured by the Lagrangian linear model, but the failure of the mass conservation which makes some water “disappear” in the vicinity of the crest is a critical issue. The reproduction of irregular waves using a second-order Lagrangian model appears to be more challenging than when using its Eulerian counterpart because of the large second-order displacements generated by wave components with close frequencies. In order to make use of the advantages of the Lagrangian solution concerning the wave shape, an alternative solution for further investigation may be to use the modified linear Lagrangian model proposed by Fouques (2005) in which the mass conservation is exact. Kinematics in irregular waves is also an issue for further research.

REFERENCES

- Fouques, S. 2005. *Lagrangian Modelling of Ocean Surface Waves and Synthetic Aperture Radar Wave Measurements*. Doctoral Thesis, Norwegian University of Science and Technology, 2005:226, Article IV.
- Fouques, S., Krogstad, H. E., Myrhaug, D., 2005. A second order Lagrangian model for irrotational irregular waves. *Proc. Of the 5th International Symposium on Ocean Wave Measurements and Analysis, WAVES 2005*. Madrid, Spain.
- Fouques, S., Krogstad, H. E., Myrhaug, D., 2006. A second order Lagrangian model for irregular ocean waves. *ASME Journal of Offshore Mechanics and Arctic Engineering*. Vol. 128. pp. 177-183.
- Kinsman, B. 1965. *Wind Waves. Their generation and propagation on the ocean surface*. Prentice-Hall Inc., Englewood Cliffs, New Jersey.
- Lamb, H., 1932. *Hydrodynamics*. Cambridge University Press, 6th edition, pp 12, 147, 421.
- Longuet-Higgins, M. S., and Stewart, R. W. 1960. Changes in the form of short gravity waves on long waves and tidal currents. *Journal of Fluid Mechanics*. Vol 8. pp 565-583.
- Pierson, W. J., 1961. Models of random seas based on the Lagrangian equations of motion. *Tech. Rept. Contr. Nonr-285(03)*, College of Engineering, Research Division, New York University.
- Sharma, J. N., and Dean, R. G. 1981. Second-Order Directional Seas and Associated Wave Forces. *Society of Petroleum Engineers Journal*. Vol 4. pp 129-140.
- Stansberg, C. T., Gudmestad, O. T., and Haver, S. K. 2008. Kinematics under extreme waves. *ASME Journal of Offshore Mechanics and Arctic Engineering*. Vol. 130.

LABORATORY EXPERIMENTS AND SPH MODELLING OF REGULAR BREAKING WAVES

Diana De Padova^a, Robert A. Dalrymple^b, Michele Mossa^a, Antonio F. Petrillo^c

^a DIASS, Technical University of Bari, Bari, Italy

^b Department of Civil Engineering, Johns Hopkins University, Baltimore, USA

^c DIAC, Technical University of Bari, Bari, Italy

ABSTRACT

The Smoothed Particle Hydrodynamics (SPH) is a relatively new method for examining the propagation of linear and breaking waves. The development of the SPH model is still ongoing and the numerical model results require further analysis and detailed comparison with other numerical models and experimental data. Comparisons with physical model runs demonstrate the potential uses of SPH as an engineering tool. The implemented numerical code was first tested using physical experiments on wave motion fields by De Serio and Mossa (2006).

The simulations in the present paper used an artificial viscosity, following Monaghan (1992). However, there were some difficulties in establishing the correct value of the fluid viscosity.

The empirical coefficient α , used in artificial viscosity (Monaghan, 1992), is needed for numerical stability in free-surface flows, but in practice it could be too dissipative. The artificial viscosity term becomes particularly strong and is characterised by large number of particles which results in too much damping. Several improvements that we have made in the same fluid viscosity with different numbers of particles are presented here.

The study made particular reference to the velocity and free surface elevation distributions with the aim of analysing the fluid viscosity and the number of particles in terms of stability and dissipation in the fluid. The final model is shown to be able to reproduce the experimental propagation of regular and breaking waves.

INTRODUCTION

The Smoothed Particle Hydrodynamics (SPH) is a lagrangian mesh-free particle model which was introduced by Gingold and Monaghan (1977) in the field of astrophysics. For thirty years SPH has been a major numerical tool in studies on the evolution of galaxies, galactic collisions, and bolid impact. Since its introduction, it has been modified for use in solid mechanics (such as impact problems), and fluid mechanics. Monaghan (1994) showed that SPH could be used for free surface flows and it has the advantage that no special treatment is needed at the free surface and thus there are no imposed boundary conditions.

The present paper presents the modelling of the propagation of regular and breaking waves using the SPH approach. It is applied to the modelling of water waves generated in the wave flume of the Water Engineering and Chemistry Department laboratory of Bari Technical University (Italy). The comparison with physical model tests shows satisfactory agreements between the simulated and the experimental observed wave motions. Some background in SPH is assumed in this paper. Readers are referred to an overview by Monaghan (1992). For recent applications of SPH see Dalrymple and Rogers (2006).

NUMERICAL TESTS AND EXPERIMENTAL SET-UP

The implemented numerical code was first tested using physical experiments on wave motion fields by De Serio and Mossa (2006).

The experiments were performed in a wave channel 45 m long and 1 m wide located in the Water Engineering and Chemistry Department laboratory of Bari Technical University (Italy). The iron frames supporting its crystal walls are numbered from the shoreline up to the wavemaker (section 100), thus locating measurement sections which have a center to center distance equal to 0.44 m. From the wave paddle to section 73 the flume has a flat bottom, while from section 73 up to the shoreline it has a 1/20 sloped wooden bottom. A sketch of the wave flume is shown in Fig. 1.

Further details about the experimental tests carried out can be found in De Serio and Mossa (2006).

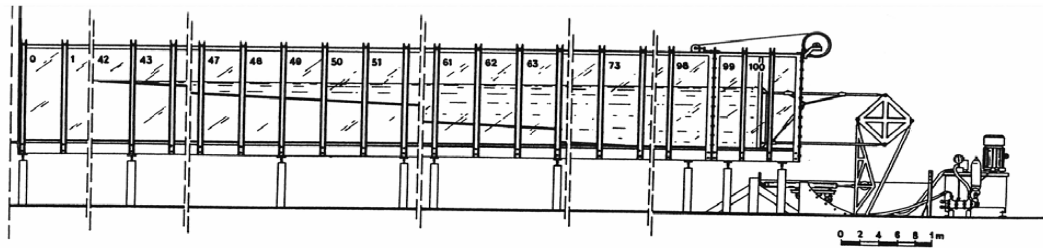


Figure 1. Sketch of the wave flume

The simulations in the present paper used an artificial viscosity, following Monaghan (1992). However, there were some difficulties in establishing the correct value of the fluid viscosity.

The empirical coefficient α , used in artificial viscosity (Monaghan, 1992), is needed for numerical stability in free-surface flows, but in practice it could be too dissipative.

The artificial viscosity term becomes particularly strong and is characterised by large number of particles which results in too much damping. Several improvements that we have made in the same fluid viscosity with different numbers of particles are presented here.

Particles were initially placed on a staggered grid with zero initial velocity. Each wall in the tank was built with two parallel layers of fixed boundary particles placed in a staggered manner described by Dalrymple and Knio (2000). In this approach the boundary particles share some of the properties of the fluid particles, but their velocities are zero and their positions remain unchanged.

The initial particle spacing is taken as $\Delta x = \Delta z = 0.022$ m and thus approximately 30,000 particles are used. A smoothing length of $h = 0.0286$ m was considered in these simulations. The choice of initial particles spacing $\Delta x = \Delta z$ depends on the physical process of the problem and the desired computational accuracy and efficiency. For a comparison between computational accuracies, we used other particle spacing $\Delta x = \Delta z = 0.019$ m and $\Delta x = \Delta z = 0.024$ m and, thus, approximately 40,000 particles with a smoothing length of $h = 0.024$ m and 20,000 particles with a smoothing length of $h = 0.031$ m were used (Table 1).

Table 1 - Characteristics of SPH simulations

Test	Time simulation [s]	Coefficient in the artificial viscosity (α)	Particle number
1	20	0.055	20,000
2	20	0.055	30,000
3	20	0.055	40,000

In all three simulations, the water depth, the wave height and the period were equal to 0.70 m, 0.11 m and 2 s, respectively, in section 0.5 m offshore the section 76 (Fig. 2).

The study made particular reference to the velocity and free surface elevation distributions with the aim of analysing the fluid viscosity and the number of particles in terms of stability and dissipation in the fluid. The final model is shown to be able to reproduce the experimental propagation of regular and breaking waves.

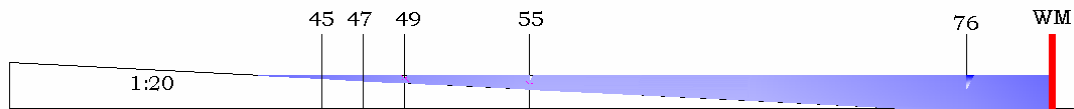


Figure 2. Measurement sections.

RESULTS

The experimental and numerical wave profiles at the location of measurement points are shown for all cases. For a defined section, we can study the distribution along the channel of the wave elevation and the horizontal and vertical velocity components for both tests.

Figures 3a ÷ 3c, 4a ÷ 4c, 5a ÷ 5c, 6a ÷ 6c, 7a ÷ 7c show the agreement of numerical data obtained by means of the three SPH models with experimental data. The artificial viscosity term, which depends on the α -parameter, becomes extremely strong with very large numbers of particles. To understand if the configuration with 30,000 particles is the best fit to the data, other two simulations with 40,000 and 20,000 particles were carried out.

The cases with the higher (40,000) and lower (20,000) number of particles revealed that the numerical wave height and the numerical velocity were not in perfect agreement with the experimental measurements.

With a number of particles equal to 30,000, the numerical elevations and the numerical velocities are shown to be in better agreement with the experimental measurements. These results show how the choice of the number of particles is needed for numerical stability for free-surface flows and the agreement with the experimental measurements.

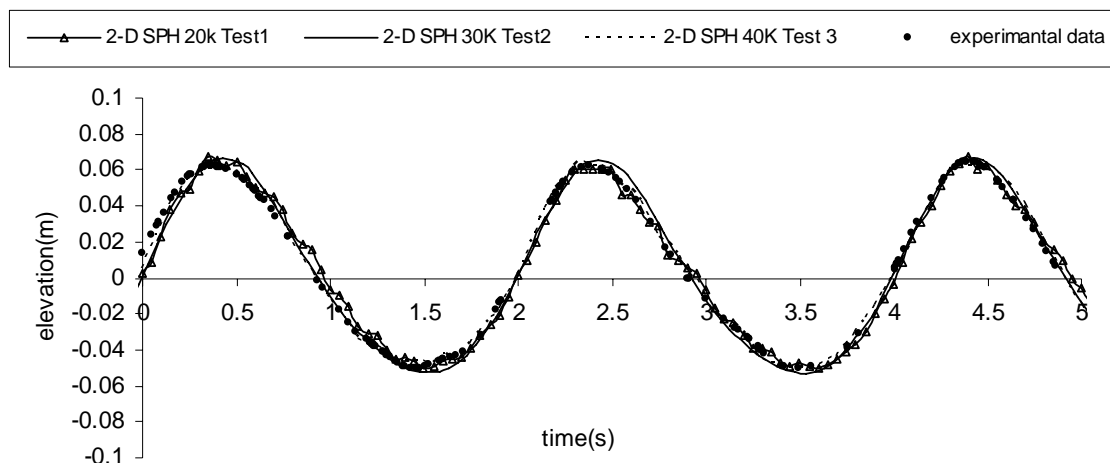


Figure 3a. - Comparison of 2-D SPH with experimental data (section 76)

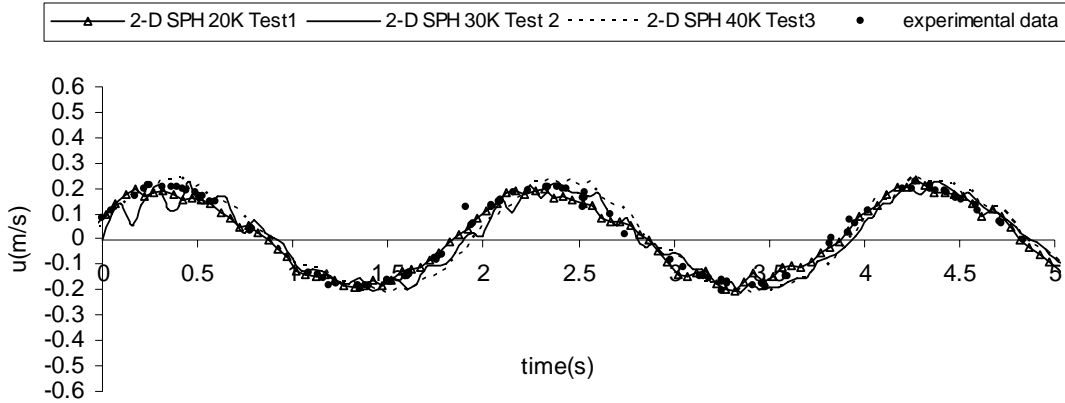


Figure 3b. - Comparison of experimental and numerical vertical horizontal components (section 76, 0.33 m from the bottom)

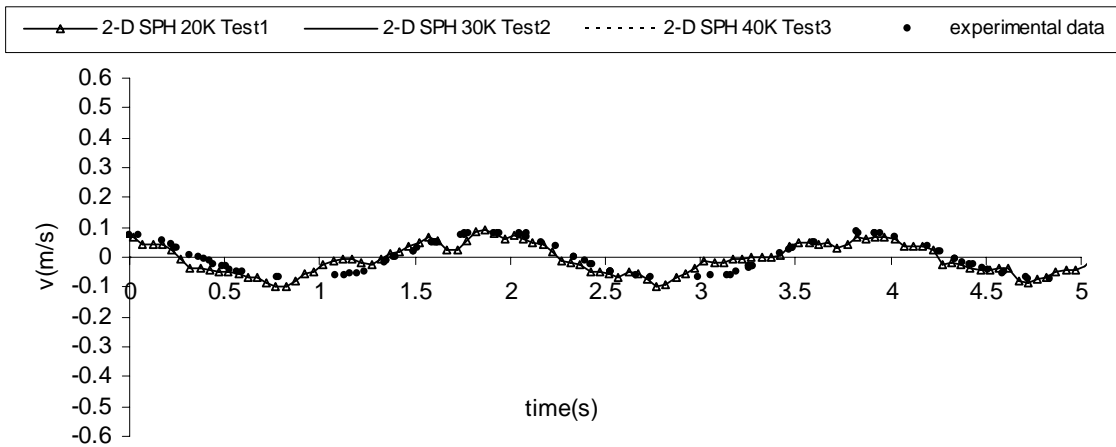


Figure 3c. - Comparison of experimental and numerical vertical velocity components (section 76, 0.33 m from the bottom)

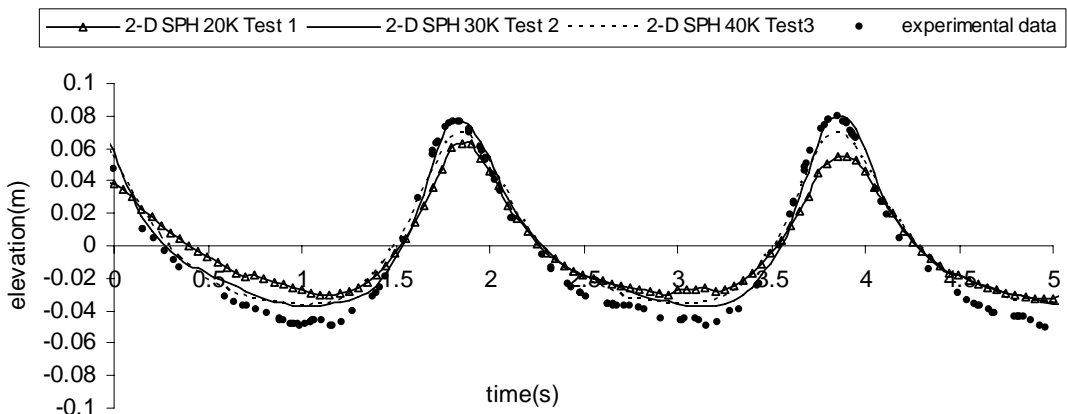


Figure 4a. - Comparison of 2-D SPH with experimental data (section 55)

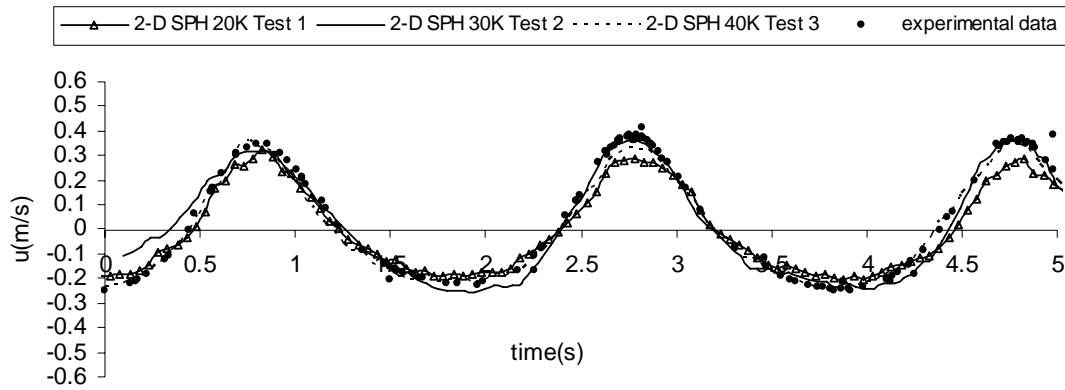


Figure 4b. - Comparison of experimental and numerical horizontal velocity components (section 55, 0.1 m from the bottom)

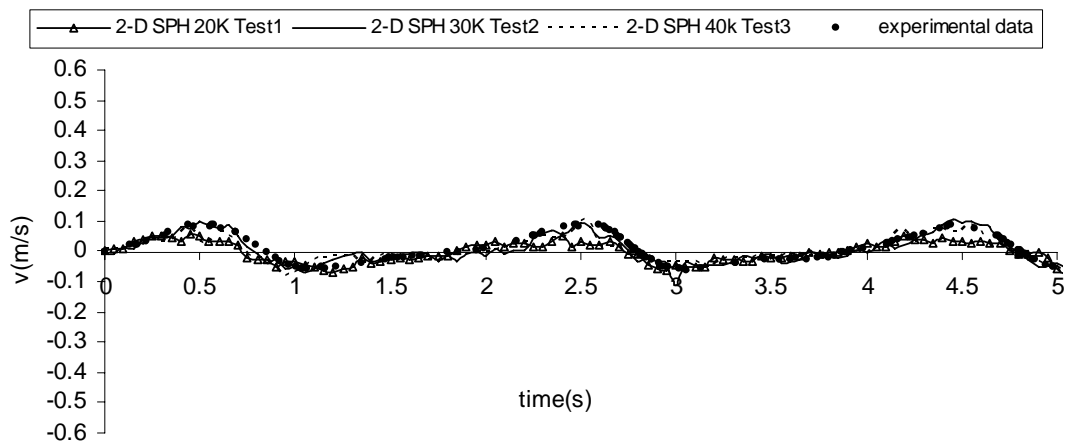


Figure 4c. - Comparison of experimental and numerical vertical velocity components (section 55, 0.1 m from the bottom)

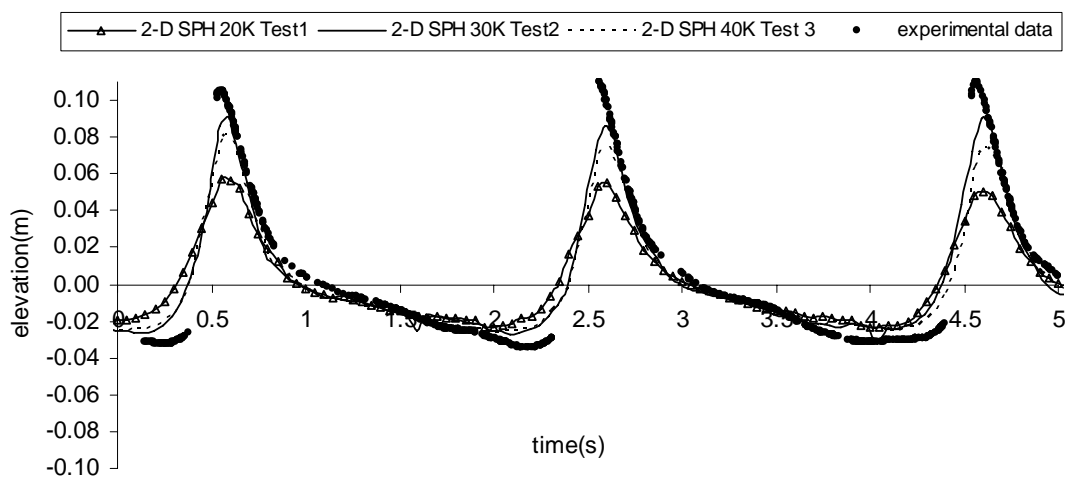


Figure 5a. - Comparison of 2-D SPH with experimental data (section 49)

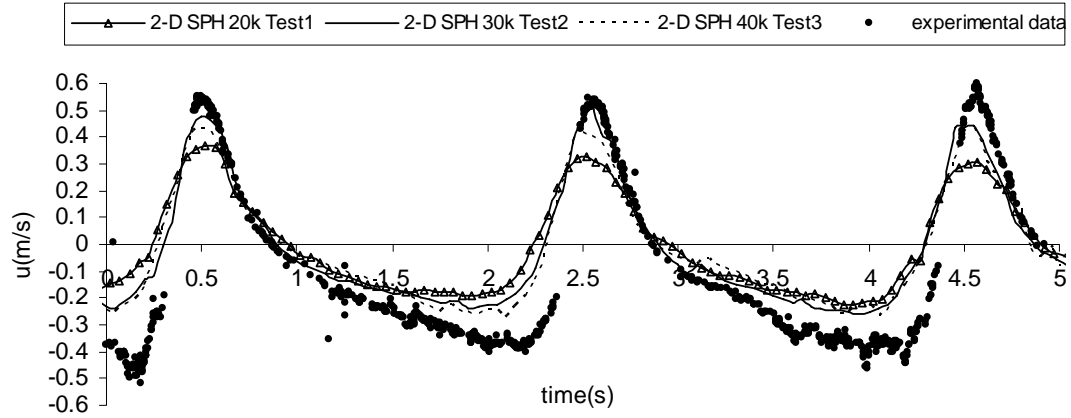


Figure 5b. - Comparison of experimental and numerical horizontal velocity components (section 49, 0.1 m from the bottom)

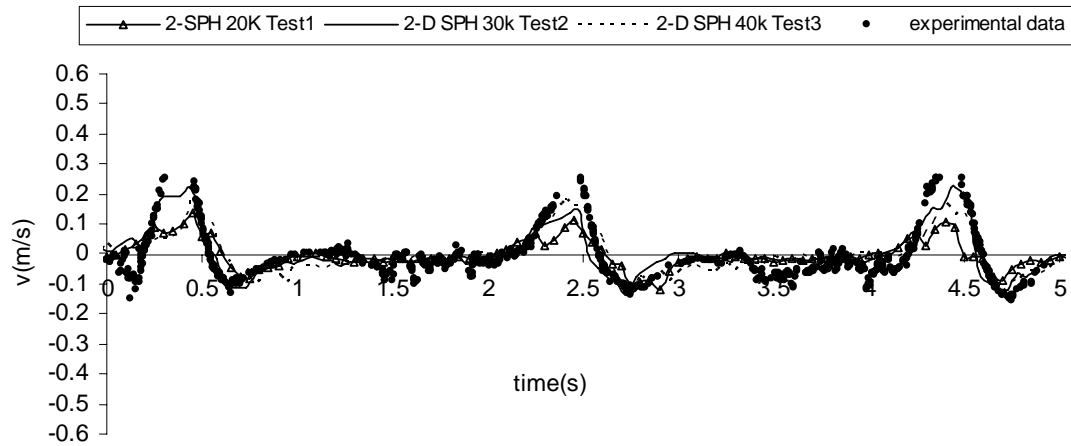


Figure 5c. - Comparison of experimental and numerical vertical velocity components (section 49, 0.1 m from the bottom)

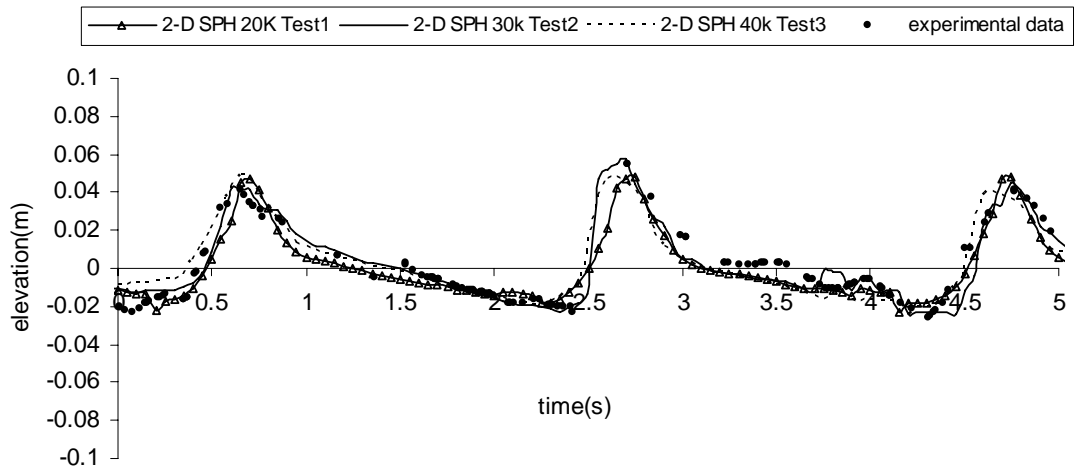


Figure 6a. - Comparison of 2-D SPH with experimental data (section 47)

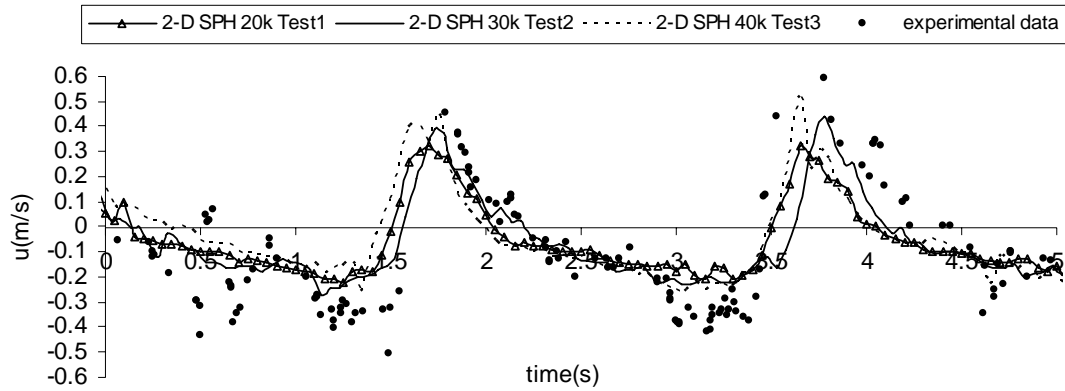


Figure 6b. - Comparison of experimental and numerical horizontal velocity components (section 47, 0.063 m from the bottom)

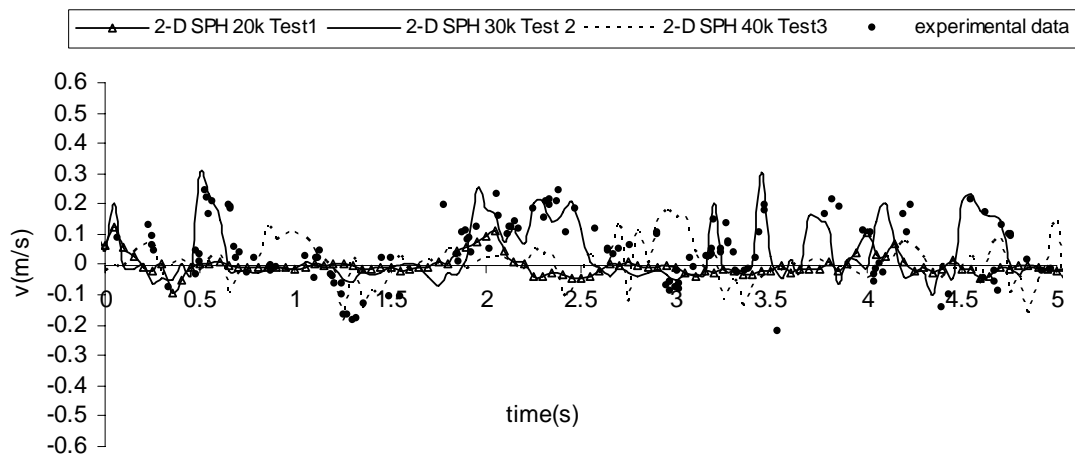


Figure 6c. - Comparison of experimental and numerical vertical velocity components (section 47, 0.063 m from the bottom)

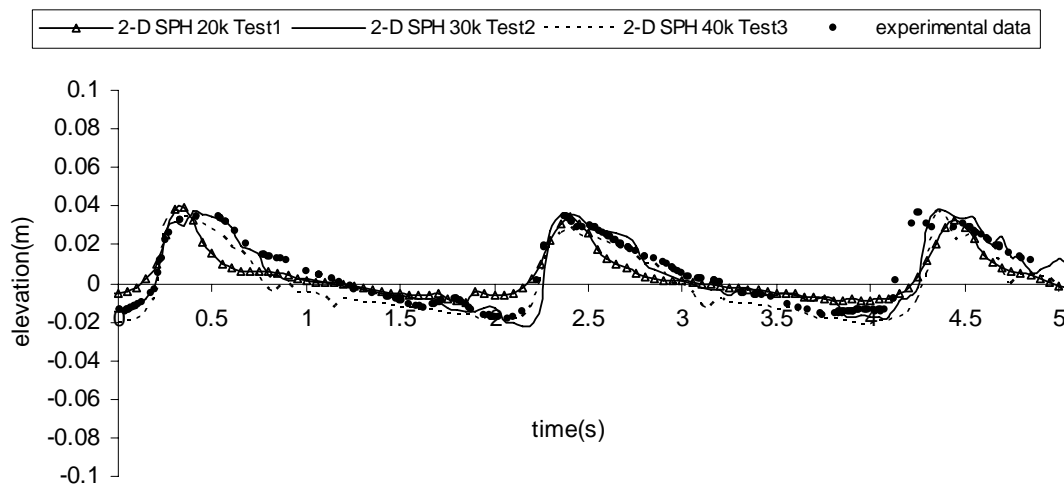


Figure 7a. - Comparison of 2-D SPH with experimental data (section 45)

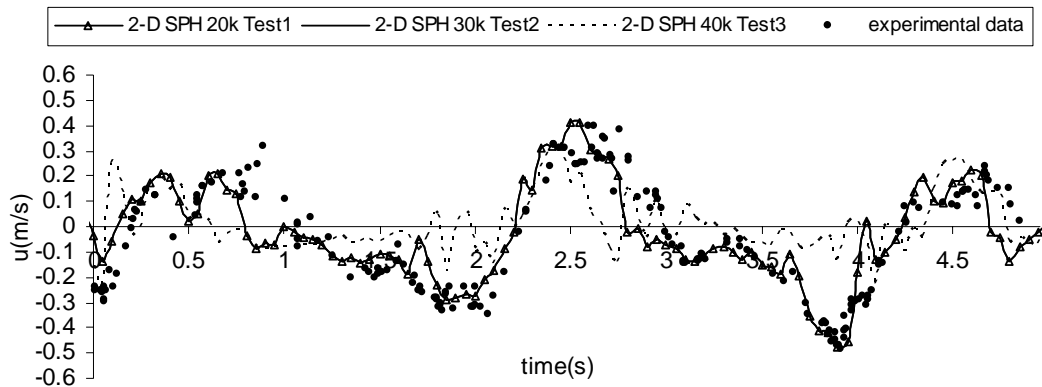


Figure 7b. - Comparison of experimental and numerical horizontal velocity components (section 45, 0.045 m from the bottom)

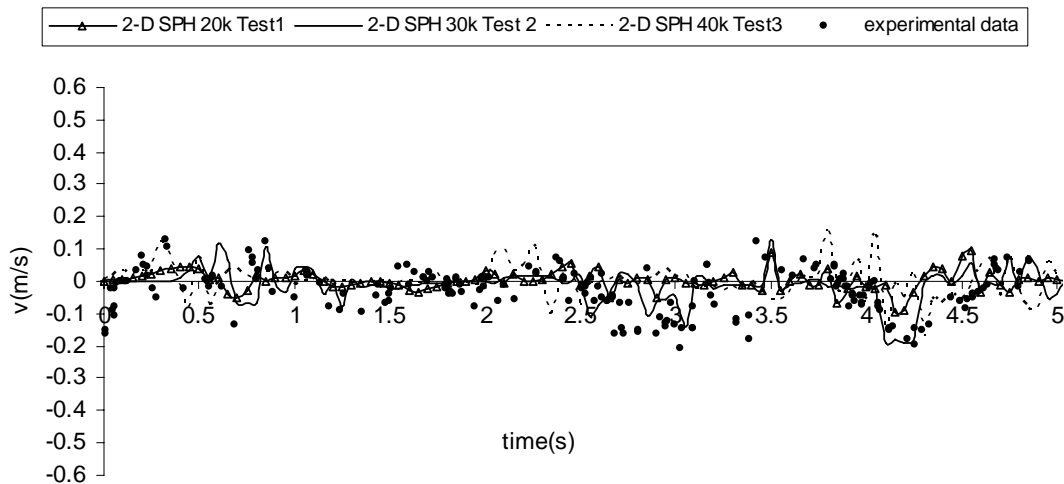


Figure 7c. - Comparison of experimental and numerical vertical velocity components (section 45, 0.045 m from the bottom)

Although Figs. 3a ÷ 3c, 4a ÷ 4c, 5a ÷ 5c, 6a ÷ 6c and 7a ÷ 7c, provide good qualitative results, it is desirable to obtain quantitative results as well. Overall statistical parameters can provide a more detailed picture of the breaking model performance. Figure 8 shows standard deviations of measured and computed surface elevations of sections 76, 55, 49, 47 and 45 (Fig. 2).

Skewness (Kennedy et al., 2000), a measure of crest-trough shape, is computed and shown in Fig. 9. Test 2 predicts this parameter very well; in fact the trend of wave skewness increases as the wave shoals and breaks, and decreases near the shoreline (section 49). Instead, in the cases with the higher (40,000) and lower (20,000) number of particles (Table 2), results change for the worse and the trend of wave skewness is not well predicted, in particular in sections 47 and 45, where the wave surface profiles are characterized by a rapid change in shape.

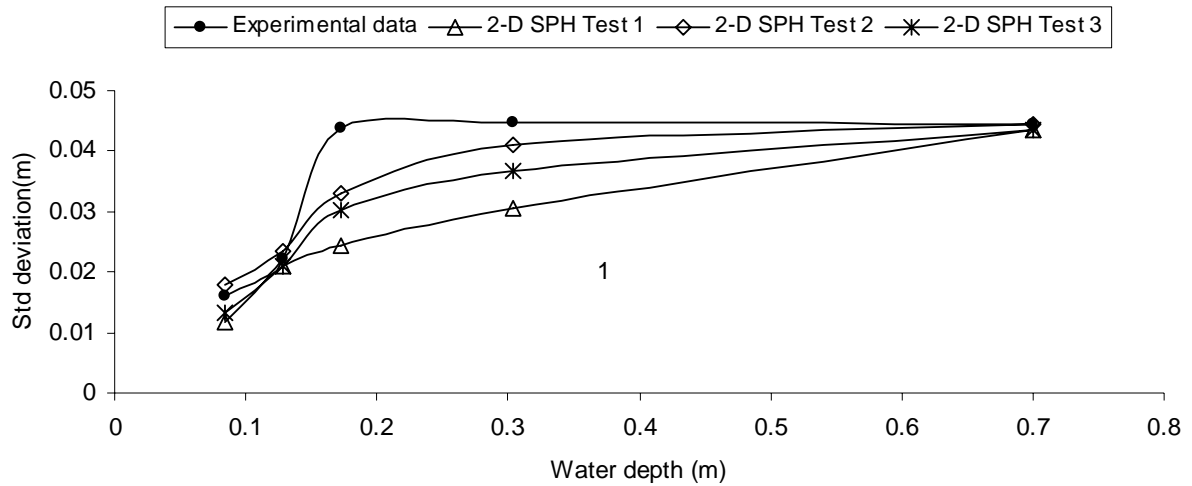


Figure 8 Comparison of experimental and numerical standard deviation of surface wave elevations

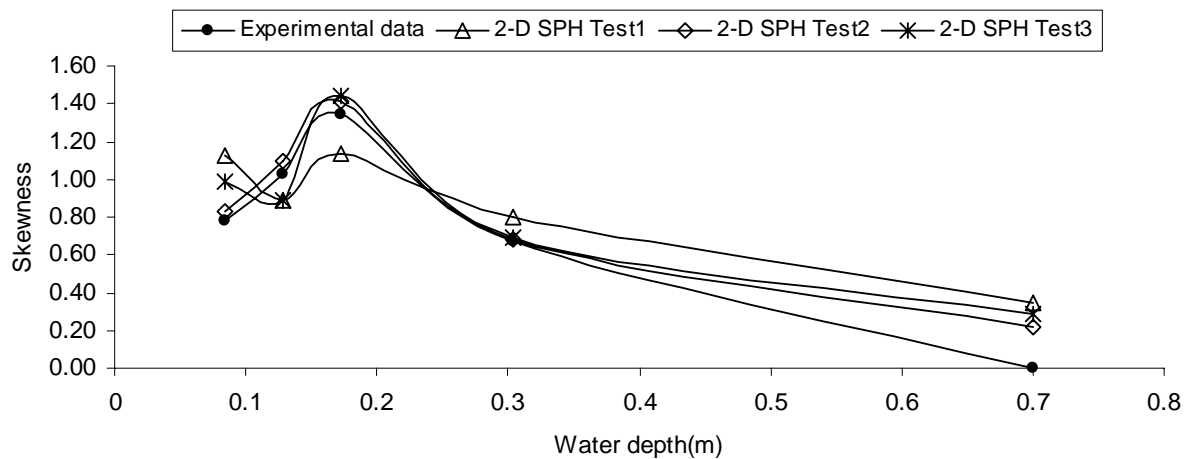


Figure 9 Comparison of experimental and numerical skewness of surface wave elevations

CONCLUSION

The importance of experimental measurements is highlighted in order to calibrate and quantitatively validate the SPH numerical model. The choice of initial particle spacing $\Delta x = \Delta z$ and the empirical coefficient α depends on the physical process of the problem and the desired computational accuracy and efficiency. The artificial viscosity term, which depends on the α -parameter, becomes extremely strong with very large numbers of particles.

Therefore, no matter what artificial viscosity term is selected, the model results depend strongly on the values of $\Delta x = \Delta z$ and, as a consequence, on the particle numbers. In the runs of the present paper (Table 1), we observed that the cases with the higher (40,000) and lower (20,000) number of particles revealed that the numerical wave height was not in good agreement with the experimental ones (Figs. 3a ÷ 3c, 4a ÷ 4c, 5a ÷ 5c, 6a ÷ 6c and 7a ÷ 7c).

The same figures indicate that the results with 30,000 particles show a better reproduction of the experimental values.

These results highlight the fact that, for a certain value of artificial viscosity, it is important to define and use a correct number of particles in the model.

Therefore, generally speaking, an appropriate number of particles should be used for a settled value of α and consequently that of the artificial viscosity.

REFERENCES

- De Serio F. and Mossa M., 2006. *Experimental study on the hydrodynamics of regular breaking waves*. Coastal Engineering 53, 99-113.
- Dalrymple, R.A., and Knio, O., 2000. *SPH modelling of water waves*. Proc., Coastal Dynamics, pages 779-787.
- Dalrymple, R. A., and Rogers, B.D., Numerical modelling of waves with the SPH Method. Proc., Coastal Engineering, 2006, pp. 53, 131-147.
- Gingold, R.A., and Monaghan, J.J., 1977. *Smoothed particle hydrodynamics: Theory and application tononspherical stars*. Mon. Not. R. Astron. Soc., 181, 375–389.
- Monaghan, J.J., 1992. *Smoothed particle hydrodynamics*. Annual Review of Astronomy and Astrophysics 30, 543–574.
- Monaghan, J.J., 1994. *Simulating free surface flows with SPH*. Journal of Computational Physics 110, 399–406.

KEYWORDS

Regular waves, physical modelling, numerical methods, SPH, fluid viscosity, particle number.

**Session B:
SPECIAL TOPICS**

COASTAL ENGINEERING IN NORWAY – A BRIEF HISTORICAL REVIEW

Alf Tørum

Norwegian University of Science and Technology, Trondheim, Norway

“OLD TIMES”

Norway has a long coastline as shown in Figure 1. The coastline is characterised by islands, shoals and skerries, deep fjords and bays. The length of the coastline envelope is some 2800 km, while the real coastline length, including fjords and bays, is some 20,000 km long. The fjords were carved out by the ice sheet that has covered the area through different ice ages after the Caledonian faulting. Figure 2 shows the maximum extent of the ice sheet covering the Scandinavian Peninsula and Northern Europe about 20 000 years ago during the latest ice age. About 10 000 years ago the coastline emerged from the ice, and the first man settled on the coastal land strip, Figure 3.



Figure 1. The Norwegian coast with fjords, bays, shoals and skerries.
From “Verdensatlas, Teknisk forlag (1997)”

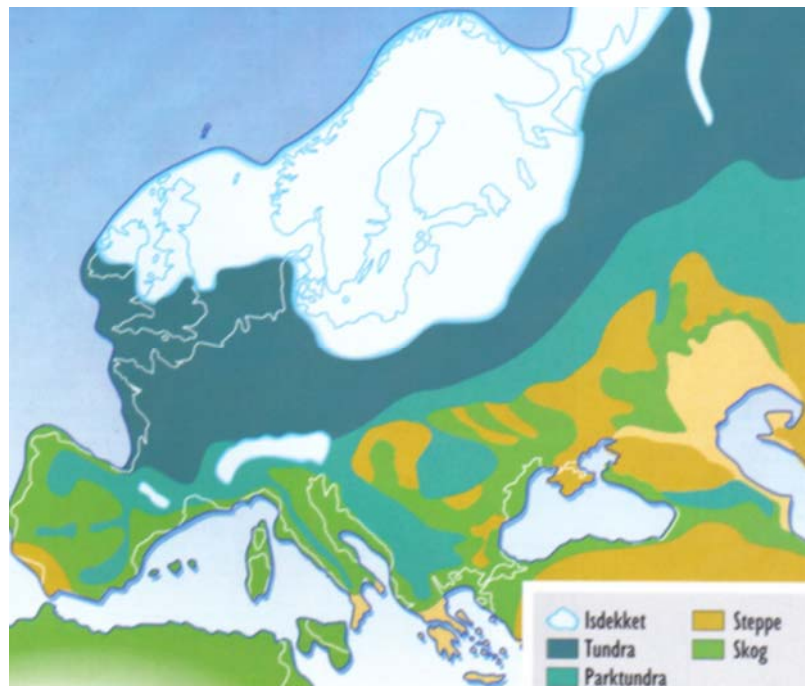


Figure 2. Maximum ice sheet coverage about 20 000 years ago. Norges historie, bind 1. (Norwegian History, Vol. 1). Aschehoug & Co. (W.Nygaard). 1994.

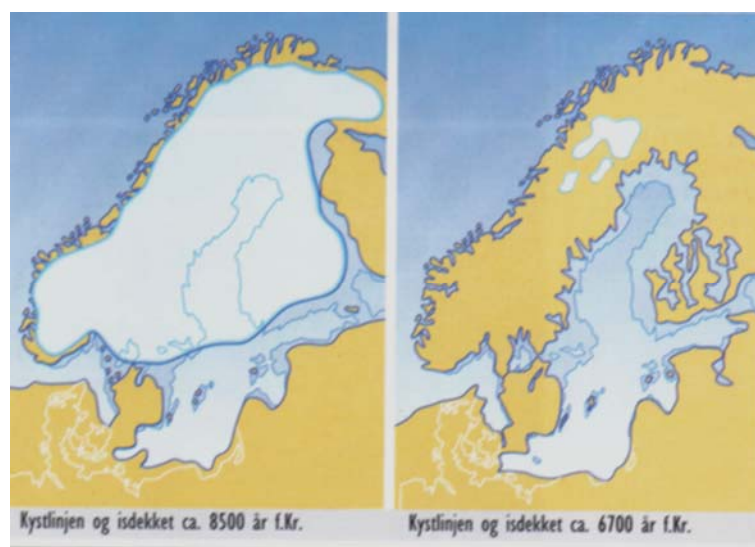


Figure 3. Ice sheet coverage about 8,500 years and 6,500 years B.C. Norges historie, bind 1. (Norwegian History, Vol. 1). Aschehoug & Co. (W. Nygaard). 1994.

The ice was some 3 km thick in the central part of the ice sheet, Figure 2. Hence the weight of this ice sheet pressed the land down such that the sea level was, as an example, about 160 m higher in the Trondheim area than it is today. On the other hand the land south of the ice sheet was elevated, as in Denmark and the Netherlands. There is still some land rising in Scandinavia, some 8 mm per year in the Gulf of Bothnia, while almost zero along the Norwegian coast, Figure 4. On the other hand the Netherlands and Denmark are sinking.

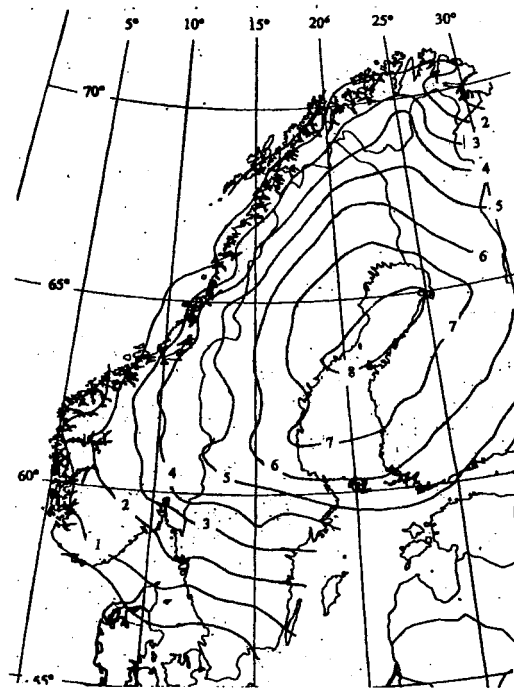


Figure 4. Present day land uplift, mm/year. (Danielsen, 2001).

The wave climate in open waters is relatively harsh. Historically the harbours that were needed were mainly natural harbours in bays or river mouths. Figure 5 shows the conditions at Trondheim around the time of the settlement of the town in 997 A.D. The water level was then approximately 4 m higher than it is today. Figure 6 shows an artist's perception of the first river harbour, Skipakrok, in Trondheim around 1100 A.D.

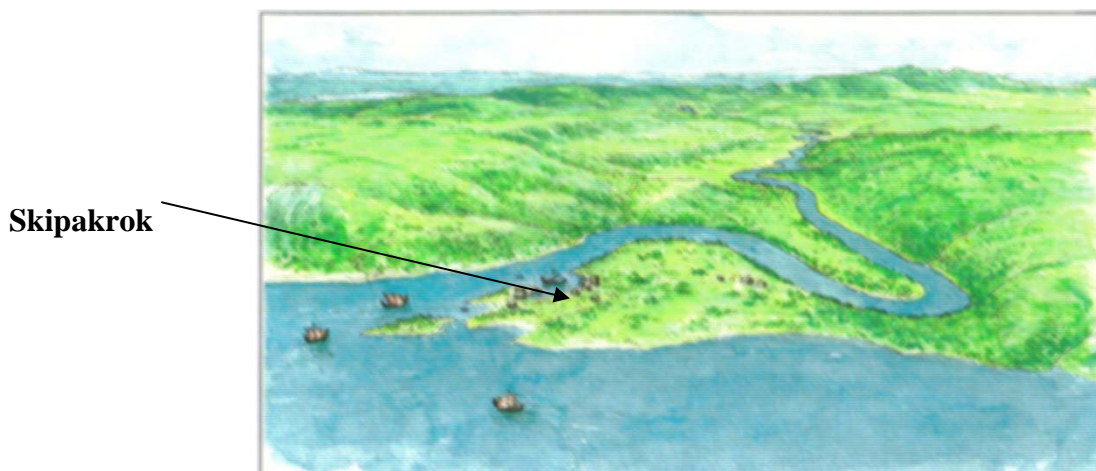


Figure 5. The conditions at Trondheim around year 1000 A.D with the harbour "Skipakrok". Norwegian Geological Survey.

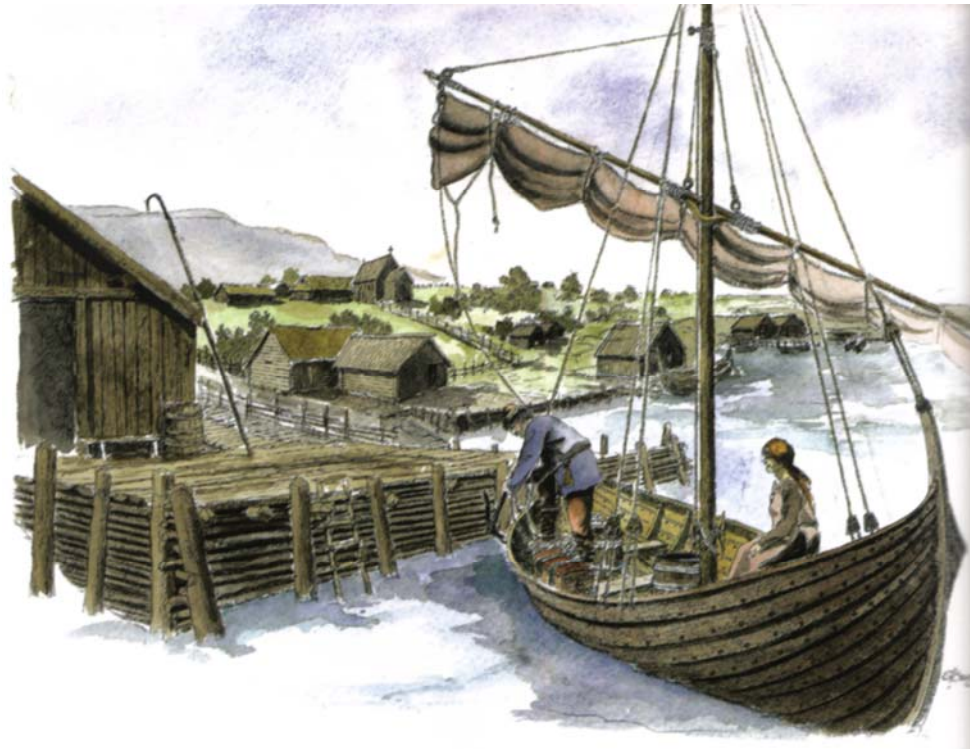


Figure 6. Trondheim's harbour, Skipakrok, around 1100 A.D. *Trøndelags historie* (The history of Trøndelag), Vol. 1, Tapir Akademiske forlag, 2005.

The first breakwater in Norway that is known from written sources is the ancient breakwater at Agdenes at the entrance to the Trondheim fjord. According to “Snorre kongesagaer” King Øystein stated around 1100 in his trial of strength with his brother, King Sigurd Jorsalfar, that “I built a harbour at Agdenes where there was previously no harbour and where everybody must travel if they are going north or south”. Figure 7 shows a photograph of the area with the location of the breakwater that apparently was built by King Øystein. The breakwater was built as a wooden crib (fir), filled with stones. Figure 8 shows the remains of this cribwork as it appeared in 1869, Meier (1869). The timber in the cribwork has been C¹⁴ dated and is from 800 to 940 A.D, indicating that the timber was cut before King Øystein's time. Other C¹⁴ dating indicates other time intervals. There are uncertainties on these datings, which is discussed by Rokoengen and Jasinski (1996), and it is believed that the timber in the crib is from the building time of King Øystein.



Agdenes.
Location of
King Øystein's
breakwater

Figure 7. King Øystein harbour at Agdenes.

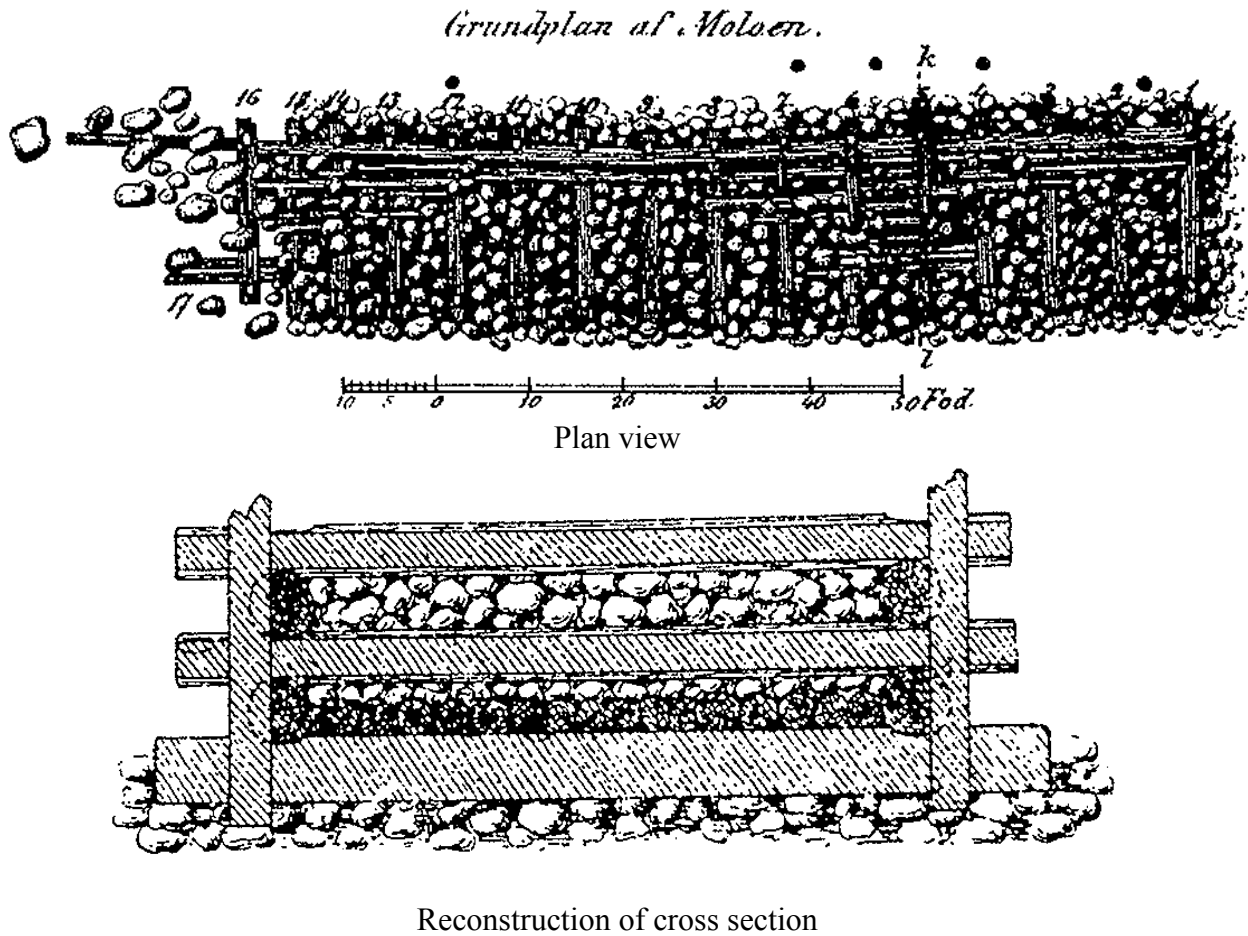


Figure 8. The cribwork breakwater at Agdenes. Plan view as seen by J. Meyer in 1869 and his reconstruction of the cross section. Meier (1869).

There has apparently been land uplift at the location of the harbour of approximately 2.5 m since King Øystein lived (Kjemperud 1986). Since the remaining timber today is located in the tidal range (from low water to high water, approximately 2.5 m difference) it is uncertain whether the crib is located at its original location or if it has been moved from a more onshore location. The Viking ships had a draft of about 1 m and did not require a water depth that had been present if the crib had been built at its present location.

MODERN TIMES

There are some fairly old maps of the Norwegian coastline. Figure 9 shows one of them from the area south of Stavanger. This map and others were prepared by the Norwegian-Danish Navy. The actual soundings were kept secret by the Navy. We see that Sirevåg is already marked as a port or anchoring place.

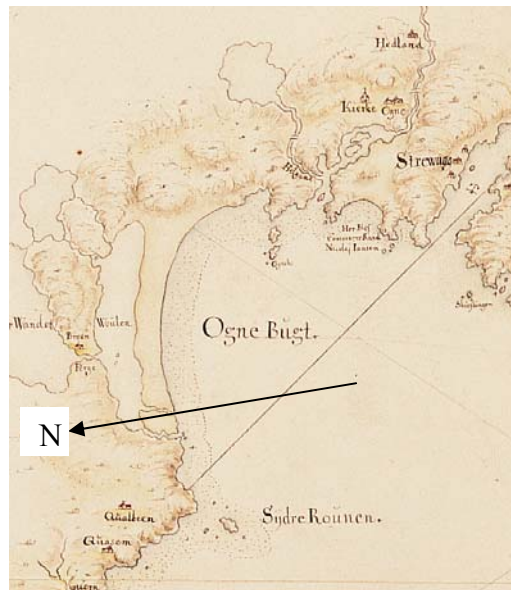


Figure 9. Ogne Bugt (with the harbour of Sirevåg).
 Taken from the antique draft of R. Juel 1708.
 Reproduced with permission no. 596/08 from
 the Norwegian Mapping and Cadastre Authority.

Most of the major Norwegian commercial harbours, including harbours associated with the shipment of oil and gas, are located in rather well sheltered fjord areas without the need of large breakwaters. The coast is mostly a rocky coast and there are few problems with littoral drift and coastal erosion.

Coastal engineering is the field of engineering related to coastal waves and their influence on the coast itself and on coastal structures. Coastal engineering in Norway has therefore been mainly associated with the development of fishing ports on or close to open coastlines. Historically fishermen settled with their row boats and sailing boats as close to the fishing grounds as possible during the fishing season. Figure 10 shows the fishing fleet in 1915 heading for the fishing grounds outside the fishing village of Sør-Gjæslingan on the Trøndelag coast. Figure 11 shows the Sula fishing village on the Trøndelag coast. This is a fishing village far out from the main coast where fishing has been conducted since the middle ages with rowboats as shown in Figure 10. The Sula harbour is relatively well protected from waves by the archipelago outside the harbour, but in “modern” times there has been built a small breakwater at the entrance to the harbour. Årviksand fishing harbour in the Troms County, Figure 12, faces the open ocean. At this location the fishermen would operate their boats by hauling them upon the beach. Later on, when the motorised fishing vessels entered the scene there was a requirement to build breakwaters. Note that there is farmland in the area. The conditions were often such that the fishermen were not only fishermen, but also had their small farms. Hence a fisherman was frequently also a farmer. While he was away during the fishing season the farming was taken care of by his family.



Figure 10. The fishing fleet heading toward the open sea fishing grounds outside Sør-Gjæslingen, Sør-Trøndelag County. SPOR, No. 1, 1995. Faculty of Archaeology and Cultural History, NTNU, Trondheim.



Figure 11. Sula fishing village, Sør-Trøndelag County. From “Den norske los”.



Figure 12. Årviksand fishing harbour, Troms County.

The following is a brow through some pictures of different fishing harbours to give an indication of the variety of lay-outs for fishing harbours.



Figure 13. Henningsvær. From “Den norske los”.



Figure 14. Værøy. From “Den norske los”.



Figure 15. Andenes. From “Den norske los”.



Figure 16. Røst. From “Den norske los”

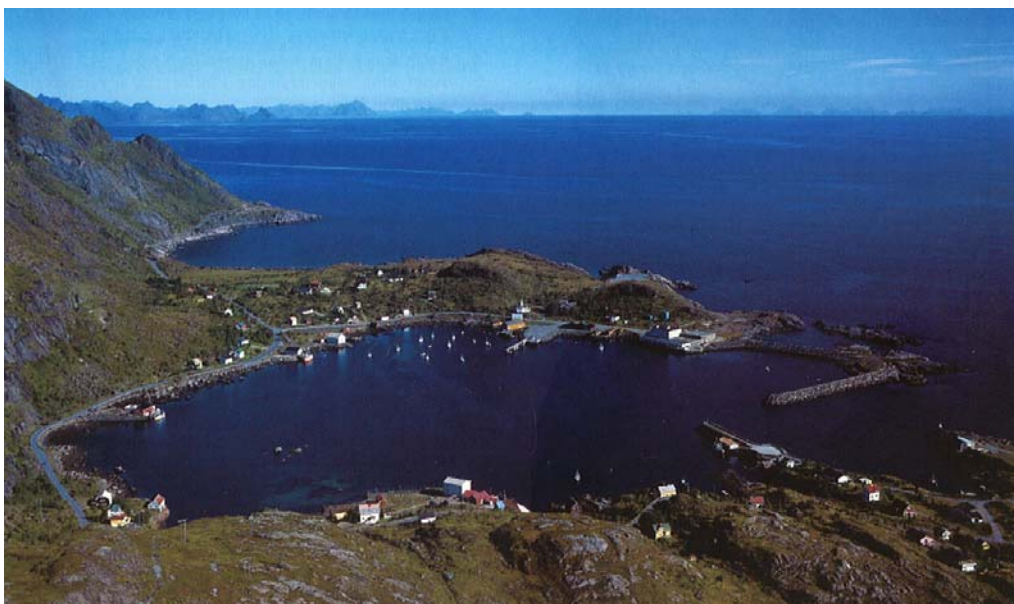


Figure 17. Moskenes. From “Den norske los”.



Figure 18. Hovsund. From “Den norske los“

Altogether some 778 breakwaters at 507 locations have been built by the Norwegian Coastal Administration, with a present value of approximately 10 billion NOK.

But coastal engineering in Norway is not only associated with breakwaters. There have also been problems with light towers on shoals in areas with large waves, pipelines on coasts, kelp vs. beach erosion etc. We will return to details on these different items later.

THE NORWEGIAN COASTAL ADMINISTRATION

The first legal provision on harbours in Norway is from 1735. This legal provision was mainly related to the responsibility of the police to obtain order in the harbours and to maintain natural harbours intact, including mooring rings and mooring hooks. Later taxes were levied on goods to fund maintenance and possibly deepening of harbours.

The forerunner to the Norwegian Coastal Administration was established in 1847, when “Kanal og Havnevæsenet” (the Canal- and Harbour Authority) was split into “Kanalvesenet” and “Statens havnevesen” (State Canal Authority and State Harbour Authority). The lighthouse administration and the piloting administration were separately organised. But in 1974 “Statens havnevesen, “Fyr og merkevesenet” (Lighthouse Administration) and “Losvesenet” (Piloting Administration) were all organised under the Norwegian Coastal Administration (NCA).

The history of the Norwegian Coastal Administration up to 1914 is well documented in “Havnevesenets historie” (1914) (The History of the State Harbour Authority).

The government provided very limited funding for harbour development. But the harbour law of 1842 stated the principle that the users of the harbours should fund the repair work and the development of the harbour through fees. This principle was strengthened in the new harbour law of 1894 and has been a governing factor up to now for partly funding of the harbours.

In the beginning the principle of financing fishing harbour development was that the government paid. However, the funding by the government was limited and it was established through the “Harbour fund” from 1873 that the users, e.g. fisheries, should pay a fee to the “Harbour fund” to use for the fishing harbour development. But this fund has not provided all the necessary funding for fishing harbour development. The government contribution has been substantial.

Mr. Roll was appointed as the director of the State Harbour Authority in 1861 and served as such until 1896. His efforts for developing the Norwegian harbours were outstanding.

A Harbour Commission was established in 1877 on the basis of decisions made by the Norwegian Parliament. Through the summers of 1877, 1878 and 1879 this commission visited the coastline from Kristiansand to the Russian border. The commission received inputs from local communities on their plans/wishes for developing their fishing harbours. Based on the commission’s work a long term, 35-years plan, was developed. This plan, with necessary adjustments, was the basis for budgeting of the development of fishing harbours for many years. Gradually the fishing harbours were developed.

As mentioned, coastal engineering is a relatively limited field of engineering in Norway. However, the development of the Norwegian fishing harbours, by the NCA, has meant a great deal to the country’s economy. Fish is one of the largest export commodities from Norway.

The development of sailing routes and the establishment of sailing beacons has also been a main activity of NCA. Their work has made the coast inhabitable. Thus NCA has served as an important infrastructure developer along the coast and their work has been and still is important for the development of the harbours, sailing routes, safe navigation and settlements along the coast.

BREAKWATERS

In the beginning, from 1847, most of the work by the Norwegian Coastal Administration was related to deepening harbours and canals. This was not considered to be difficult work, but there were many places to develop. The technical development, especially the rock blasting technique development, in the latter part of the 20th century, made it possible to build breakwaters for the exposed fishing villages. Several of these requested to have breakwaters built to save lives, boats and fishing gear. So little by little breakwater building started in Norway. The beginning can be dated to the 1860’s. The work of the harbour engineer was empirical when it came to the layout and construction of breakwaters. At that time there was no national experience, so it was necessary to obtain information from abroad. It was especially from the fishing harbours in England and Scotland that useful information and knowledge were obtained. Many of these fishing harbours were somewhat similar to Norwegian fishing harbour locations. But the knowledge acquired from England and Scotland had to be adjusted to local conditions and to the costs involved.

The first projects were small, e.g. Figure 19, but there were many of them. Everybody wanted to be the first to have a breakwater, and everybody wanted to have something as soon as possible.

The NCA had the responsibility of planning and building typical fishing ports. Social and political necessity got priority over a rational building process: the work had to be carried out at many places simultaneously.

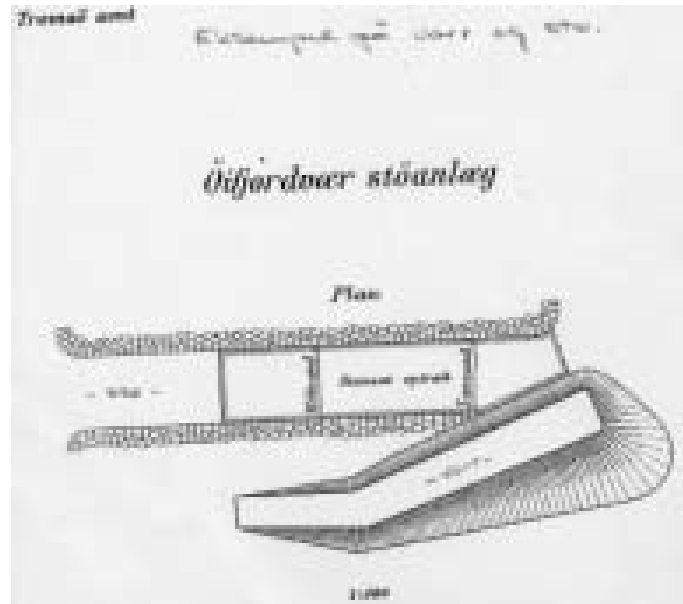


Figure 19. A small landing place protected by a breakwater. Johnsen (2003).

The breakwaters that were built up to 1900 were mainly built as blockwork with natural stones. Figure 20 shows such a breakwater at Hamningberg, Finnmark County. The forming of the stones was a respected craft and these craftsmen had a high social status and were relatively well paid.



Figure 20. Blockwork breakwater at Hamningberg, Finnmark. Johnsen (2003).

Figure 21 shows a cross section of a blockwork breakwater for shallow water. To give some extra protection large stones were placed in front of the blockwork. For deeper water an underwater mound was built to support the blockwork, Figure 22. Figure 23 is a photograph from the construction of a blockwork breakwater.

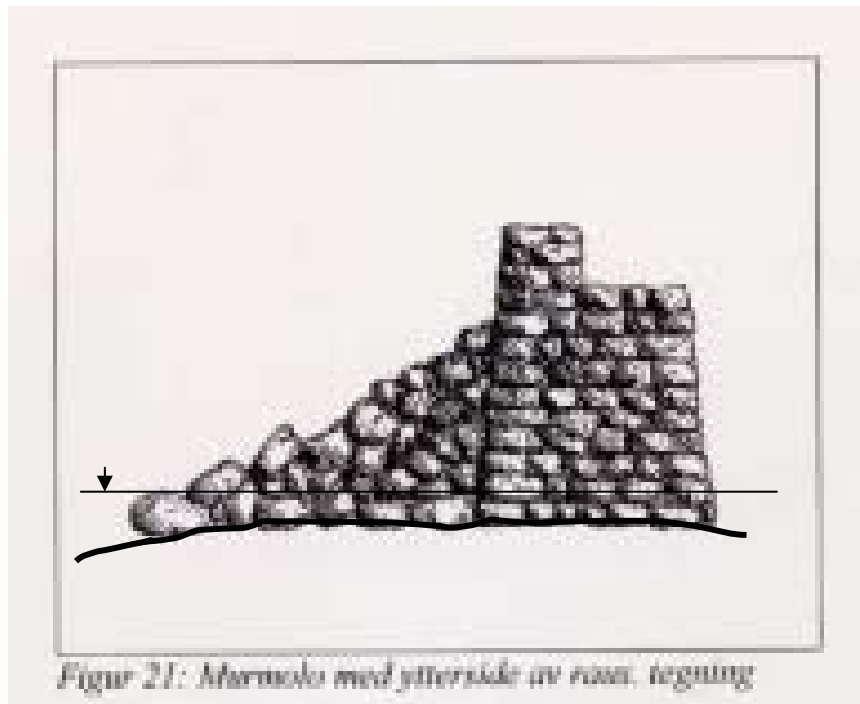


Figure 21. Blockwork breakwater – shallow water. Johnsen (2003)

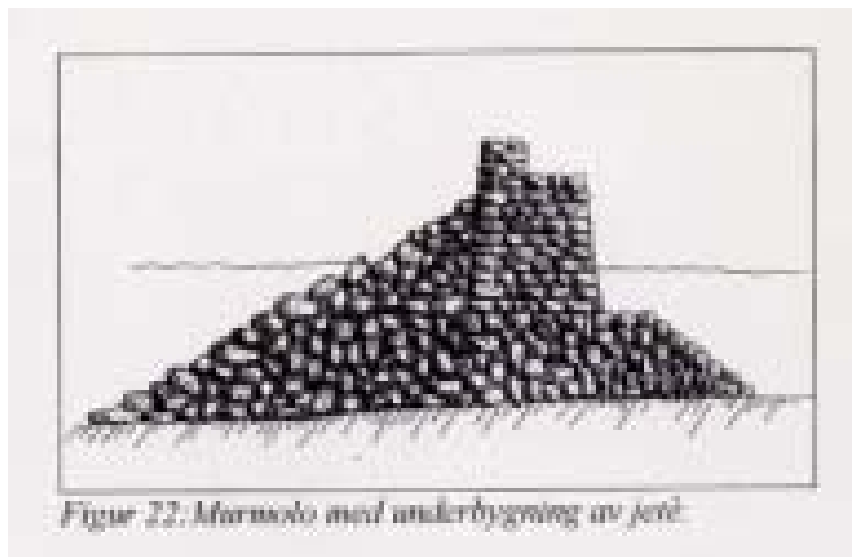


Figure 22. Blockwork breakwater – deep water. Johnsen (2003).

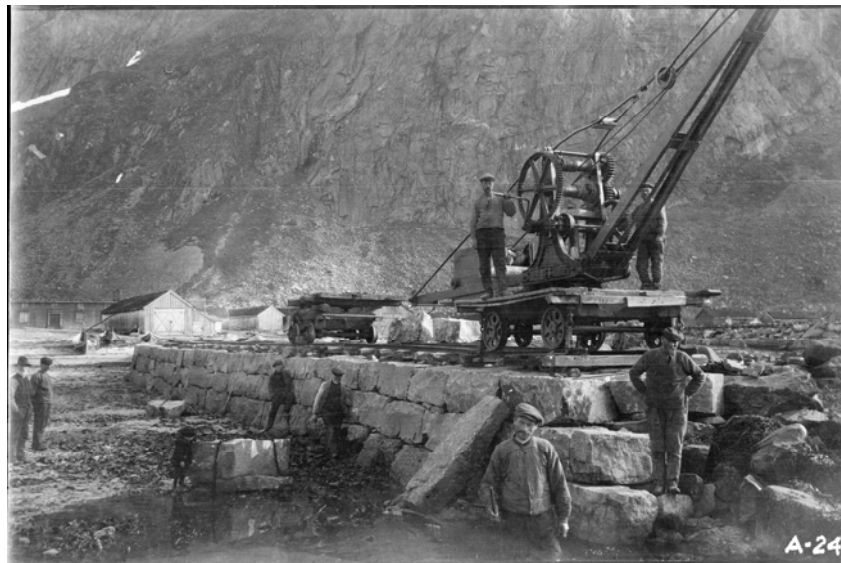


Figure 23. Construction of a blockwork breakwater. NCA

The breakwater at Vardø, built in the years 1875 – 1895, had a cross section similar to Figure 22. Around 1880 concrete was used to some extent, also for the Vardø breakwater, especially for the parts of the breakwater above low water. One of the engineers of the State Harbour Authority, H.B. Olsen, had been acquainted with the use of concrete in this manner when working on breakwater projects in Scotland. Figure 24 shows the Vardø breakwater. Note that an old canon from the Vardø Fortress has been used as bollard.



Figure 24. Vardø breakwater. Johnsen (2003).

It was a step forward when the rubble mound breakwater was introduced. In 1888 chief engineer W.A. Arentz had been on a study tour to USA and acquired knowledge about this type of breakwater. He proposed to build the planned breakwater at Bodø as a rubble mound breakwater. His calculations showed that there would be a saving in construction costs of NOK 200.000,- compared to the accepted plan. However, the Engineering Commission did not approve a rubble mound breakwater, until further studies of the necessary equipment and construction methods had

The large cover blocks, up to 10 - 30 tons, were loaded in the quarry by derrick cranes, Figure 27, on rail wagons and hauled to the crest of the breakwater by a locomotive, Figure 30. A system was developed to roll/slide the large cover blocks from the rail wagon to the breakwater slope, Figures 28 and 29. This technique depended to a large extent on the skill of the foreman. He judged the individual stones in the quarry and how he would like to place the block on the rail wagon in order for it to fit to the position he wanted the block to roll or slide. In case the block did not roll/slide to the position he wanted, the block was blasted away. This system allowed only one block armour layer. The system may look simple and primitive, but the repair records on these breakwaters show that they stand reasonably well.

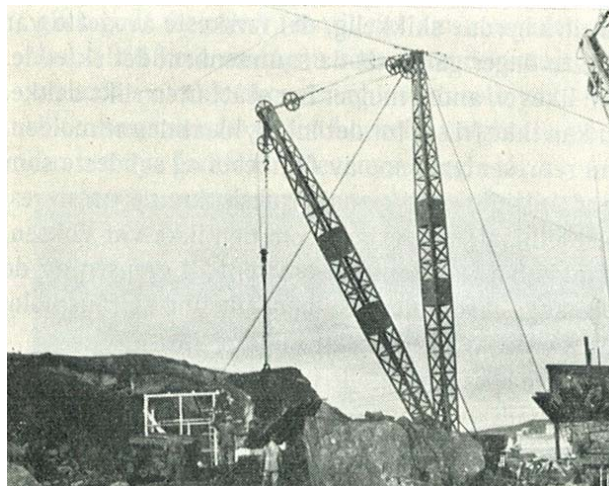


Figure 27. Derrick cranes used in Hasvik in 1953. Brandtzæg (1960).



Figure 28. A some 20 tons block on a rail wagon. NCA

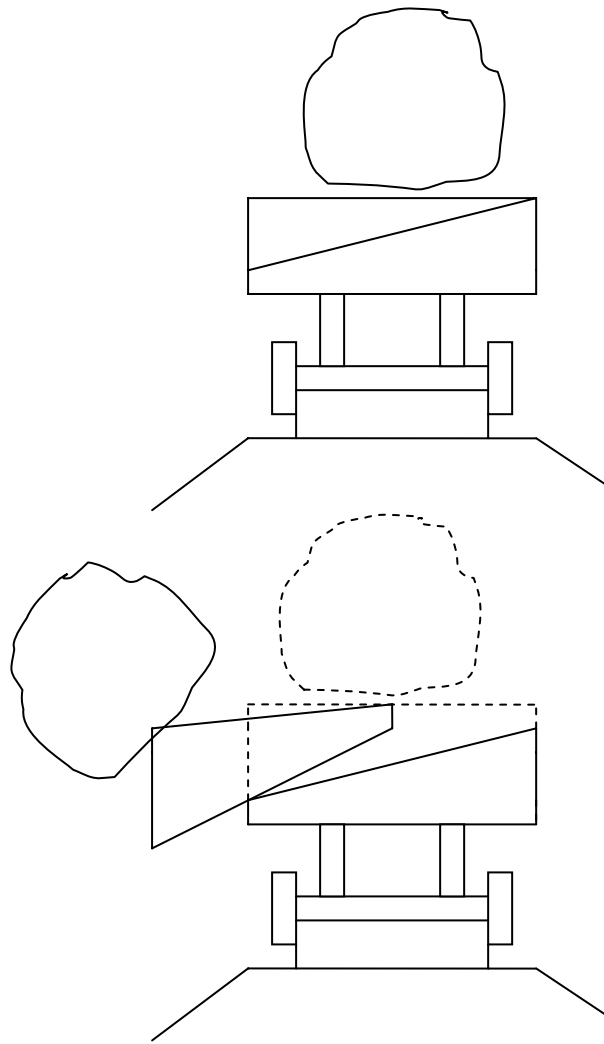


Figure 29. System to transport and slide the stones off the rail wagon.



Figure 30. A train with breakwater blocks. NCA.



Figure 31. A block being dumped from the rail wagon. NCA.

Figure 32 shows crown wall blocks placed on the crest of the Henningsvær breakwater with the system of rail transport and sliding the stones off the wagon like that shown in Figure 29.



Figure 32. Crown stones placed on the Henningsvær breakwater.

After about 1960 there was a shift towards the use of trucks for stone transportation, but still the single layer breakwater prevailed. Only some few breakwaters have been build using cranes e.g. Berlevåg, Svartnes. Natural rock has been used mainly for cover blocks. However, in Berlevåg the quarries are poor and in the 1930's cubic concrete blocks were used as cover blocks. But these failed, and in the 1960's concrete Tetrapods were used, both to repair damaged parts and as armour for an additional breakwater in Berlevåg.

BERLEVÅG

As an example of the development of a fairly heavy wave exposed fishing harbour we now look at some details of the harbour at Berlevåg. We follow to a large extent Kjelstrup (1977) and Kystverket (1981).

Berlevåg is located on the open coast in Finnmark County, Figure 33, close to fishing grounds. Figure 34 shows a photograph of the Berlevåg fishing village, while Figure 35 shows a map of the harbour area. The Coastal Express (Hurtigruten) calls at this harbour. But until 1974 the ships had to anchor in the outer bay and people and goods had to be transferred to land by barges.

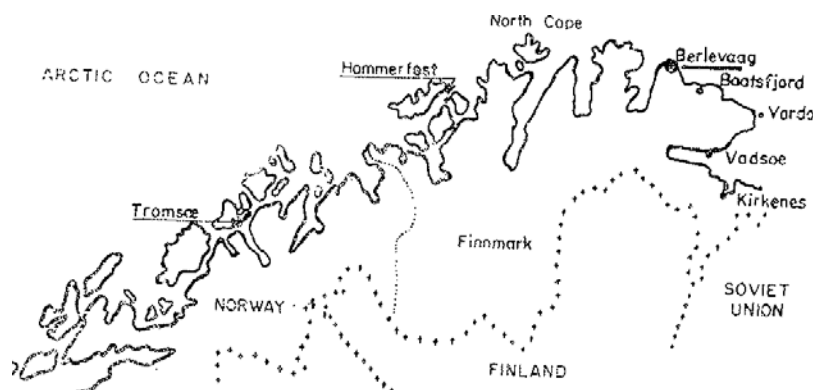


Figure 33. Location of Berlevåg.

The tidal range in the area is 3.6 m for spring tide. The storm surge level is approximately 0.5 m at its maximum. The 100-year design significant wave height for the outer breakwaters is approximately $H_s = 7$ m with peak period approximately $T_p = 15$ s. The summer time is short, but occasionally the air temperatures may be as high as 30°C . Winter temperatures may be as low as -20°C , and even -25°C , generally accompanied by strong winds. This means that the breakwaters are covered with thick layers of ice during the winter. On the other hand the sea never freezes over in Berlevåg and the breakwaters are free from damage caused by ice gouging.



BERLEVÅG sett fra SW

FOTO: Eiliv Leren

Figure 34. Berlevåg . From "Den norske los".

The inner bay, Vågen, gave some wave protection without any breakwaters and was a natural harbour.

Harbour improvements at Berlevåg started at the beginning of the 20th century with dredging of the natural harbour basin of Vågen. In 1909, however, a large number of fishing vessels in this harbour were destroyed by a NNE storm. As a result, the Varnes breakwater was built, and was completed in 1926 (see Figure 35).

A scheme to construct two new breakwaters was proposed, the Svartoksen breakwater and the Revnes breakwater, to give better protection and for the construction of a quay, primarily for the Coastal Express. The construction of the Svartoksen breakwater started in 1920. The structure was a conventional rubble mound breakwater. The quarry was located about 5 km east of the harbour and the rock was transported by a railway line. Unfortunately, the rock was of poor quality for

breakwater construction. Therefore a large quantity of rock, and much more than required for core and filter material, had to be quarried before blocks of required size could be obtained. Nevertheless, the work proceeded at a steady pace until 1932. Then a violent north-easterly gale damaged the structure considerably. It was then decided to rebuild and reinforce the breakwater with as heavy rock armour layer as 15 – 20 tons, although there were some doubts if the breakwater should be rebuilt at all because of the severe conditions and the difficulty with providing local rock of large dimensions. By the start of the Second World War the Svartoksen breakwater was still not fully repaired. The construction work was much delayed during the war. In 1944 the whole village was bombed and set on fire as the German troops withdrew from the Finnmark county. The whole Berlevåg area was totally destroyed, including the port facilities.

After the war, priority was given to rebuild houses and putting the fishing harbour into working order. It was not until approximately 1950 that work on the Svartoksen breakwater was resumed. On the outer end of the breakwater, concrete cubes of 15 tons was placed orderly (smoothly) as an armour layer. For this purpose a crane was used, acquired from the city of Haifa. Figure 36 shows a similar crane used later when placing Tetrapods on the breakwater.

By 1958 the Svartoksen breakwater was within 50 meters of completion. However, on the 6 January 1959 a heavy gale from ENE destroyed 90 meter of the seaward end of the breakwater. All the concrete blocks were washed onto the harbour side. In addition the Varnes breakwater was also heavily damaged. So what do we do now?

Hindcast analysis of the waves during the 6 January 1959 storm indicated that the significant wave height had been 7.0 - 8.0 m.

It was decided to explore the possibility of using Tetrapods to repair and rebuild the breakwater. The Director General of the Norwegian State Harbour Authority, O. Storm, and the director of the 5th District of the Norwegian Coastal Administration, B. Borhaug, visited a breakwater in the Mediterranean that was build with Tetrapods as armour layer. Chief engineer S. Kjelstrup travelled to Italy and France to study both theoretical and practical issues related to the use of Tetrapodes. The French company SOTRAMER had a patent from 1951 and for 15 years on the use of Tetrapods.

Model tests on the stability of the Tetrapods on the breakwater trunk and head were carried out by SOTRAMER/SOGREAH, by that time with regular waves. The model tests showed that 15 ton Tetrapods were sufficiently stable on the trunk and 25 tons on the head with a profile as shown in Figure 37. The old cubic concrete blocks were used at the breakwater crest.

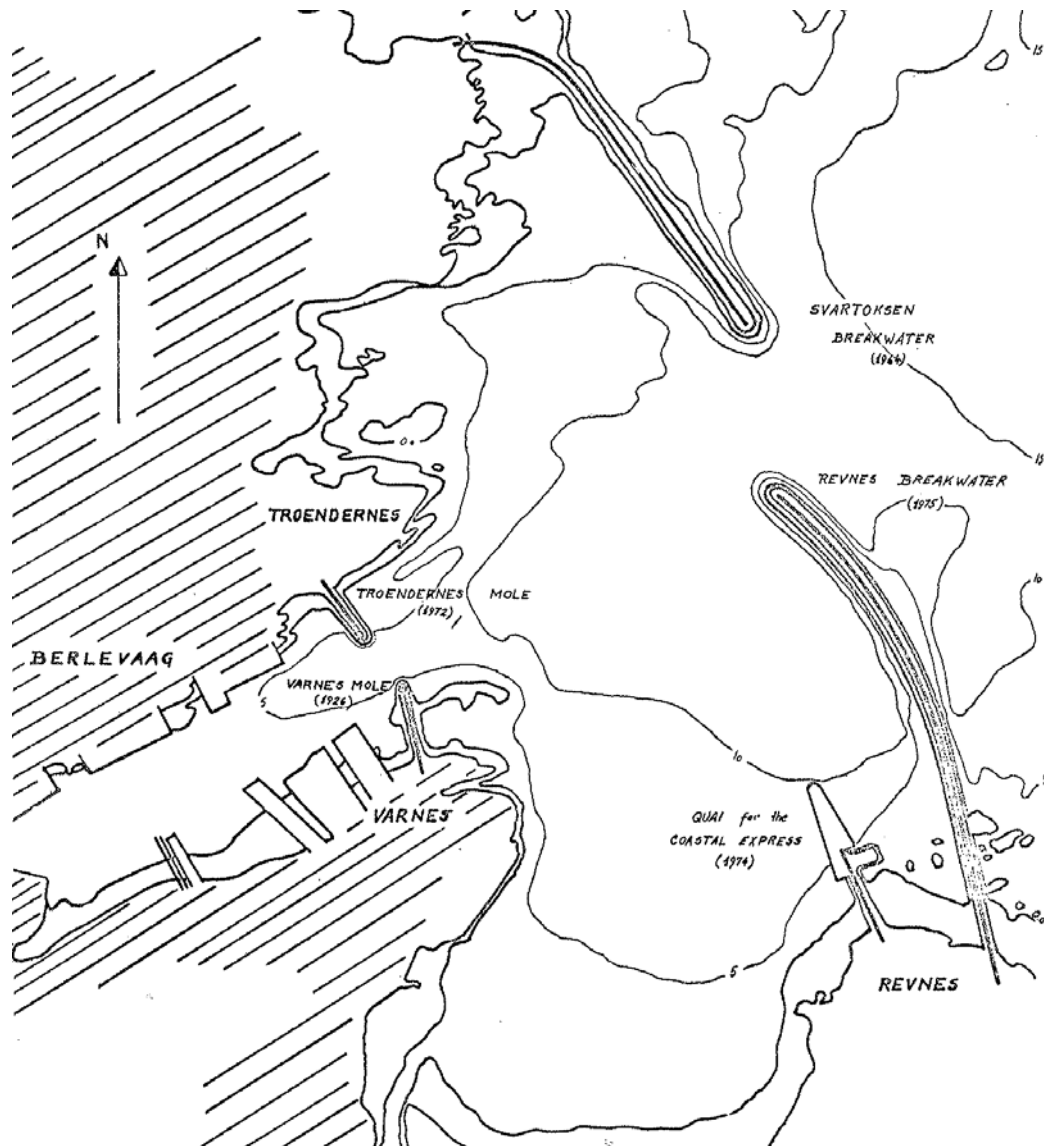


Figure 35. Berlevåg. Map of the harbour area. Kjelstrup (1977).



Figure 36. The "Haifa" crane used in Berlevåg. Kjelstrup (1977).

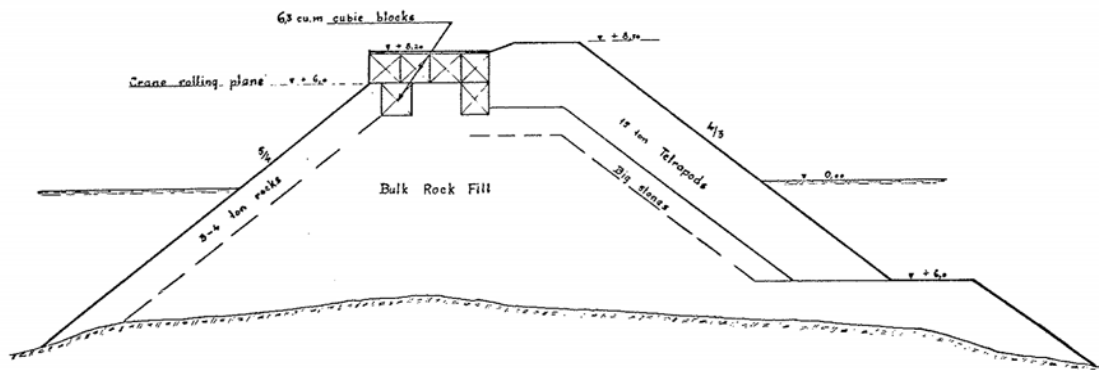


Figure 37. Profile of the Svartoksen breakwater with Tetrapods.

The royalty for the use of the Tetrapods was 15% of the production costs. The management of the Norwegian Coastal Administration, the Department of Fisheries and the Norwegian Parliament's Committee for Shipping and Fisheries reacted quickly. A Contract with SOTRAMER on the use of Tetrapods was established during the summer of 1959. The casting of Tetrapods for the Svartoksen breakwater started already the same summer.

Special attention had to be paid to the concrete quality. Up to that time Tetrapods had been used in tropical and subtropical areas where the Tetrapods never had been subjected to freezing. In Berlevåg the temperatures, as already mentioned, could be much below freezing. During a tidal cycle the concrete was then subjected to thawing and freezing. However, the Norwegian Coastal Administration had already carried out tests with different types of cement and sand for the use in their harbour and breakwater work. 400 kg of cement per cubic meter of concrete was used. An air-entraining agent in the form of resinous oil was added and the mix, which was as dry as possible (water/cement ratio below 0.45) was carefully vibrated. Samples were taken for compression tests and the mean compression strength after 28 days always exceeded 300 kg/cm². The experience is now that the concrete in the Tetrapods is very durable.

The construction of the breakwater head with 25 tons Tetrapods could not be carried out with the crane on the breakwater crest. A floating crane was used for this purpose. But the floating crane required rather calm water to be operated. The floating crane arrived at Berlevåg early in the summer of 1963. But the weather conditions were not suitable until mid-summer to operate the crane. Then a period of 3 weeks with good weather occurred. The floating crane worked day and night, so by the end of the period with good weather, the breakwater head was completed. However, due to the difficulties with the cranes, 25 tons Tetrapods were placed only under water, while 15 tons tetrapods was used above water on the head. During the winter 1963/64 some settlements occurred on the breakwater head. This was repaired during 1964, when also the concrete cover of the breakwater crest was poured. The 410 m long Svartoksen breakwater was then completed, 45 years after the work started in 1920.

The exact location of the Revnes breakwater and the Coastal Express quay was established through model tests at the River and Harbour Laboratory in Trondheim. The Revnes breakwater

was constructed in essentially the same way as the Svartoksen breakwater. One major difference was that while the stone material to the Svartoksen breakwater was transported on rail, the stone material to the Revnes breakwater was transported by trucks.

The construction time for the 650 m long Revnes breakwater was 15 years and it was completed in 1979. The period for construction work on the breakwater started in late May/beginning of June, depending on the snow conditions in the quarries. The construction work on the breakwater ended normally in late September. While the construction work was carried out, the breakwater head was vulnerable to damage if a storm occurred. Therefore a stockpile of Tetrapods were kept in reserve to quickly cover the head temporarily with Tetrapods if the weather forecast were storm from the “wrong direction”.

The Trøndernes breakwater was carried out as winter construction work during one winter. The volume of the Trøndernes breakwater and the Varnes breakwater is about the same. It took 13 years to build the Varnes breakwater, while it took only one winter to build the Trøndernes breakwater. This was partly due to the higher efficiency, especially by using trucks to transport the stone material.

After 76 years of harbour construction work in Berlevåg the harbour construction work came to an end in 1980. The breakwaters have been subjected to severe storms, but they have been reasonably stable. There have been some broken Tetrapods, but they have been replaced. The latest repair work has been to strengthen the inner part of Svartoksen breakwater, which is a part with the old rock armour.

So why such a long construction period?

As we have seen, the efficiency of breakwater construction was far lower than it is today. But the harbour development was also governed by politics and by the government budgets. As stated previously there were many harbours that requested improvement of the wave conditions by construction of breakwaters at the same time. Hence the money was to some extent “smeared” evenly over several projects, making rational planning difficult. In 1900 Norway was probably the poorest country in Europe. This explains to some extent the limited budgets that were allocated to fishing harbour development. But the climate had also a big effect on the construction time. The construction period was from late May until late September. During the rest of the year darkness and snow drifts prohibited any breakwater construction work.

BERM BREAKWATERS

Concrete armour units have only been used in Berlevåg in Norway, except some few Tetrapods at the breakwater at Ferkingstad, Hordaland County. Until 1989 the conventional one layer rubble mound breakwater prevailed in Norway. But following the development of the “modern” berm breakwater, this type of breakwater is now the prevailing breakwater in very high wave exposed areas in Norway. Prof. Bruun pointed to the S-slope as the natural “slope” of a breakwater. But the practical “reinventor” of the berm breakwater in modern times was Robert Bird of the consulting company Bird and Associates in USA. He designed a breakwater in 1982 for the US Navy at Keflavik on Iceland as a berm breakwater. The Icelanders adopted this design for many of their later breakwaters and has thus pioneered the development of this type of breakwater. Berm breakwaters in Norway have been constructed at Årviksand (in 1989), Mortavika (in 1995), Sirevåg (in 2002), Skjervøy (in 2000), Melkøya (in 2005) and Mandal (in 2006). Berm

breakwaters have not only been used by NCA, but also by the Norwegian Road Administration (ferry boat harbour Mortavika), by the city of Mandal (to protect an industrial area) and by StatoilHydro (at the LNG harbour at Melkøya).

Figure 38 shows the difference between a conventional and a berm breakwater, while Figure 39 shows the cross section of the Sirevåg berm breakwater. Figure 40 shows a photograph of the Sirevåg berm breakwater. Sirevåg is located approximately 50 km south of the city of Stavanger. The design 100-year significant wave height for the Sirevåg berm breakwater is $H_s = 7.0$ m. The idea with the berm breakwater is to build a berm in front of the breakwater and allow the waves to reshape the berm into an S-shape with a recession of the berm as shown in Figure 38. The reason for not constructing the berm with an S-shape from the very beginning is that it costs less to construct the berm with a natural slope than to construct the S-shape. The required armour unit mass for berm breakwaters is significantly lower than for a conventional rubble mound breakwater.

The berm breakwater can be built without cranes and with ordinary equipment of a contractor (showels, excavators). Figure 41 shows the placement of cover blocks on the Sirevåg berm breakwater.

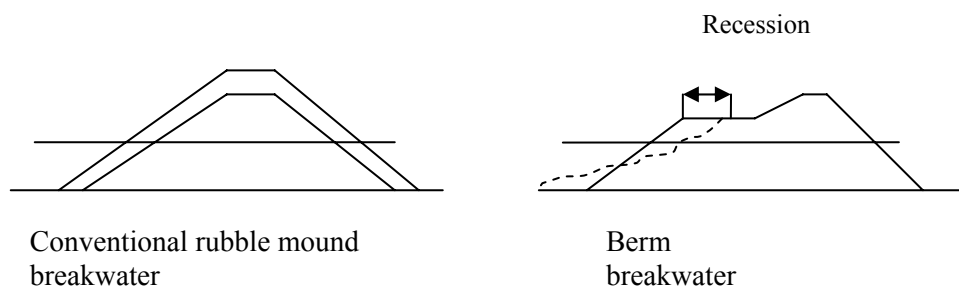


Figure 38. Conventional and berm breakwater.

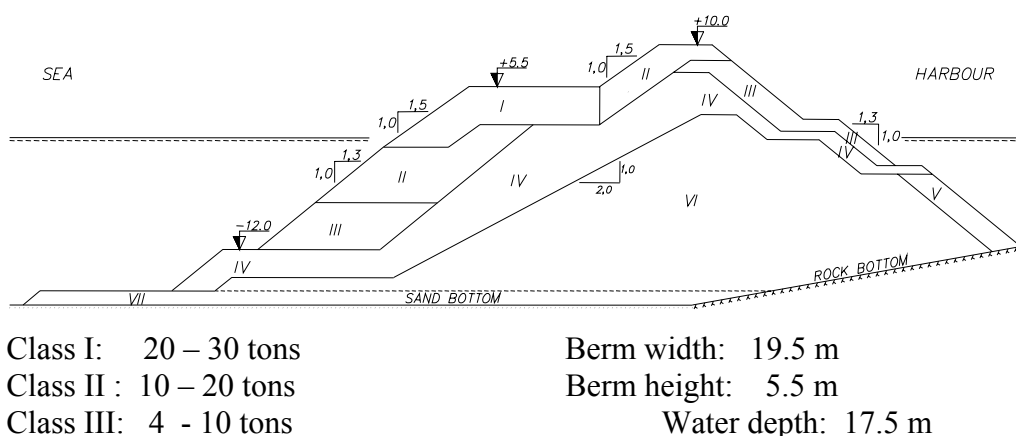


Figure 39. Cross section of the Sirevåg berm breakwater with the main stone classes.

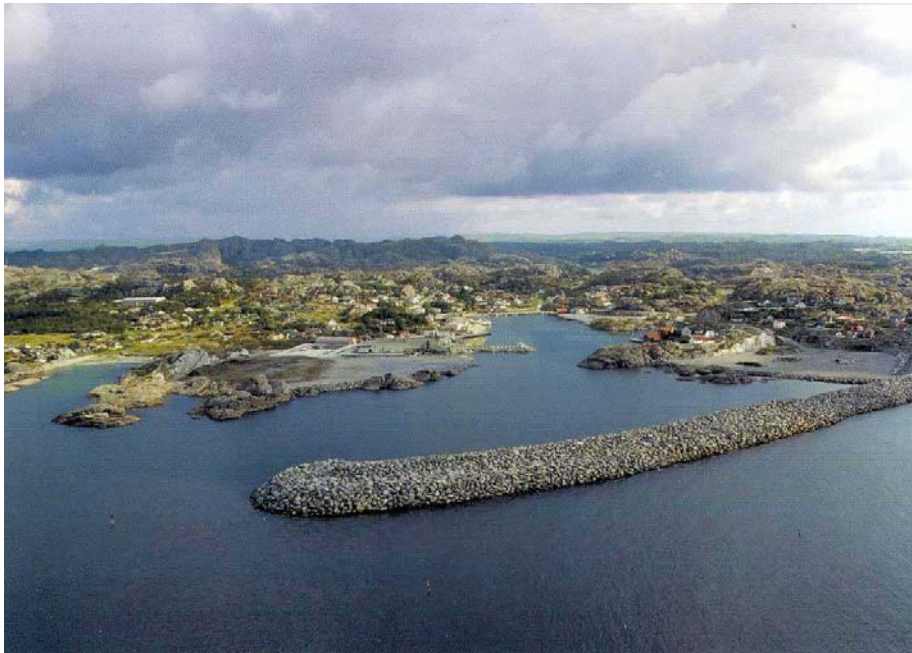


Figure 40. The Sirevåg berm breakwater. NCA.



Figure 41. Placement of cover blocks on the Sirevåg berm breakwater. NCA.

The Sirevåg berm breakwater is approximately 650 m long. It was built within 2 years without the use of cranes. This reflects the increased efficiency compared with the Berlevåg breakwaters.

Figure 42 shows the Melkøya LNG plant with the berm breakwater sea wall and berm breakwater. The design wave height on these structures varies along the structures, but maximum is approximately 7.0 m.



Figure 42. Melkøya LNG plant with the berm sea wall and berm breakwater. Photo: Eiliv Leren.

The latest planned berm breakwater is at Laukvik. Laukvik is located on the west side of the Lofoten Archipelago and faces the Norwegian Sea. The 100-year significant wave height at Laukvik is $H_s \approx 9.0$ m and is thus so far the breakwater in Norway with the largest design wave heights. The planned berm breakwater work at Laukvik is actually repair work of the outer end of a breakwater that has suffered damage several times since its construction started in 1934 on a small scale. It was further extended in the time period 1962 – 1967, but has suffered damage several times later. Figure 43 shows a satellite photograph of the harbour and Figure 44 shows the layout of the outer end of the breakwater with a planned berm breakwater. However, since the “full” berm breakwater shown in Figure 44 became expensive, a cheaper version has been adopted as shown in Figure 45



Figure 43. Satellite photograph of Laukvik.

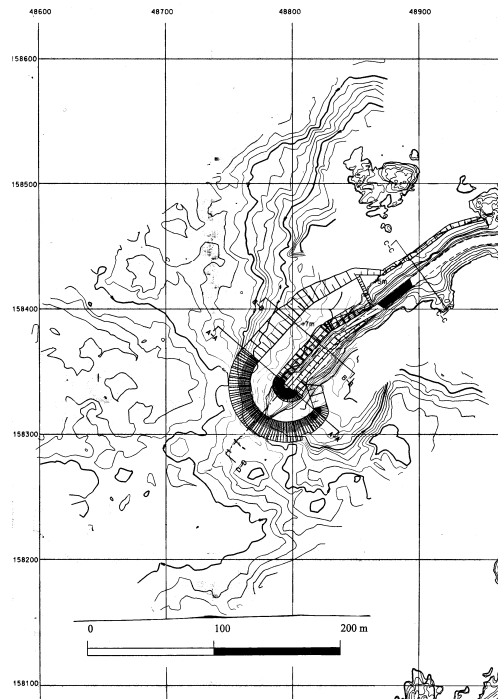


Figure 44. Layout of the outer end of the Laukvik breakwater with a planned berm breakwater.
SINTEF/NCA

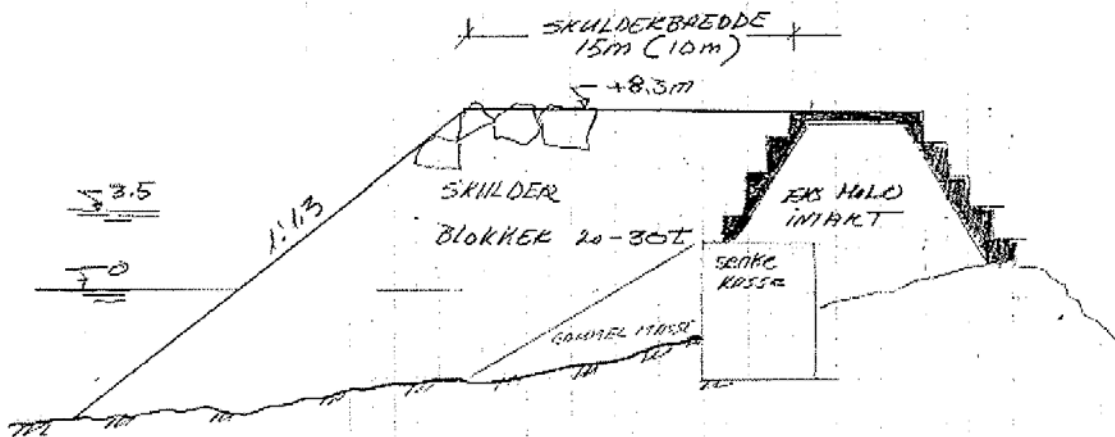


Figure 45. Tested cross section of the repair work at Laukvik. The water depth at the breakwater is 15 m. The shown cross section rests on the remains of the damaged breakwater. SINTEF/NCA.

The tested section shown in Figure 45 was sufficiently stable for wave heights up to $H_s = 10$ m. The breakwater crest height is the same as before. Thus considerable overtopping is accepted.

WAVES

In “old” days the building of breakwaters was a trial-and-error procedure. There was no detailed knowledge of design waves and no knowledge of breakwater hydraulics. It should be mentioned that during the Second World War the Norwegian scientist H.U. Svedrup, then working at the University of California, La Jolla, later at the University of Bergen, together with the Dane W. Munk, developed a method, the Sverdrup-Munk method, to forecast waves, especially for the US Marine landing sites in the Pacific Ocean. This was the forerunner for modern wave forecast and hindcast methods.

The NCA established wave measurements at several locations, mainly on open coast sites, (Berlevåg, Årviksand, Ferkingstad and Vadsø) around 1960. The longest wave measurement time series was in Berlevåg from 1959 to 1973. These wave measurements were carried out with pressure type gauges. The waves were recorded on paper charts and did not lend themselves to detailed analysis as is done today (wave height distributions, wave power spectra etc.) although some wave spectral analyses were made in 1964 of the Berlevåg recordings. However, the measurements were useful in the sense that the wave estimates now could be hinged on measurements and not only on “guesswork”.

When the oil industry came to Norway around 1970, wave measurement programs were started. The Norwegian Meteorological Institute (DNMI) developed, partly in international cooperation, wave hindcast models. DNMI has now wave hindcast data for several gridpoints in deep water in the North Sea, the Norwegian Sea and part of the Barents Sea from 1955 to 2006. The data have to some extent been verified through wave measurement programs, although it must be realised that there are always some uncertainties related to wave estimates. The wave hindcast data are also very frequently used for coastal projects. Then the waves are transformed from deep to shallow water through use of refraction/diffraction computer programs. But most of the programs are developed for mild sloping bottoms. The Norwegian coast is typically very uneven with rapidly decreasing water depths until the bottom flattens out at a depth of only some few meters, almost like steep sea mounts. There are also many shoals and skerries where the water depth is such that the waves break before they again propagate into deeper water. How waves enter fjord areas is still somewhat unknown. This makes it sometimes difficult to predict waves at shore sites.

RIVER AND HARBOUR LABORATORY (RHL).

The River Laboratory was established in 1955 as a SINTEF associate laboratory. Prior to 1955 there was a small hydraulics laboratory at the Norwegian Institute of Technology (NTH, today NTNU), established by professor O.Hegstad in 1928. This small laboratory was used for teaching purposes and for investigation of site-specific projects, especially river and hydro power projects. The new and larger hydraulics laboratory was primarily established to serve the hydropower development community as there was increased need for hydraulics laboratory services in this field. By 1960 a harbour section was added to the laboratory and “harbour” was added to its name. The key persons who established the harbour section were professor A. Brandtzæg, O. Storm, Director General of the Norwegian Coastal Administration and Håvard Berge, General Manager of RHL. The Chairman of the board of RHL, Christian Lindbo, who never accepted a “no” answer as “no” when it came to giving financial support to build RHL, should also be mentioned.

The two NTH institutes, the Institute for hydropower development and the Institute of harbour engineering, established their own laboratory facilities (basins, flumes etc.) for teaching and research purposes in the new laboratory building.



Figure 46. The River and Harbour Laboratory. 1960.

The River and Harbour Laboratory, RHL, (through times its name has changed several times but I will keep RHL), which gave a boost to coastal engineering in Norway, has been used primarily by the Norwegian Coastal Administration in the field of coastal and harbour engineering, but also by others. Approximately 40 Norwegian harbours have been model-tested in the laboratory with respect to breakwater layouts (e.g. Vardø, Hamningberg, Båtsfjord, Mehamn, Hammerfest, Sørvær, Breivikbotn, Hasvik, Kjøllefjord, Skarsvåg, Gryllefjord, Mefjordvær, Skjervøy, Vannvåg,

Årviksand, Laukvik, Andenes, Nordmela, Stø, Bleik, Svolvær, Stamsund, Værøy, Nykvåg, Steinesjøen, Melbu, Trondheim, Verdal, Rørvik, Ytre Harøy, Honningsvåg på Stad, Mekjarvik, Ferkingstad, Sandved, Mandal, Sirevåg, Åna-Sira, Moss and Fredrikstad). Several of the breakwaters have also been tested for stability. Some 10 foreign harbour projects have been model-tested at RHL, among those stability testing of the large breakwaters at Europort, The Netherlands, and Bilbao, Spain.

When the harbour activities at RHL started, only regular waves were generated in the laboratory. This was because the knowledge of irregular waves was poor and, not least, the technology for generating irregular waves in a laboratory was not readily available. However, it was realised that to have more realistic tests it was necessary to generate irregular waves. In 1964-65 RHL built a wave flume with irregular wave generation, 78 m long, 3.8 m wide and a maximum water depth of approximately 1.0 m. This flume was a big investment for the laboratory and was only realised by the financial support of, among others, the NCA. By the time it was built it was the largest flume in the world with irregular waves. The men who decided to build this flume had foresight!

To support the offshore oil industry in the beginning of the 1970's, RHL carried out tests on many of the concrete platforms built in the North/Norwegian Sea. Figure 47 shows a picture of the Ekofisk oil storage tank under model testing at RHL in 1972. Through the experience with laboratory irregular waves, RHL was also essential in the planning of the ocean wave basin at MARINTEK, Tyholt. But this is ocean engineering and will not be further dealt with.

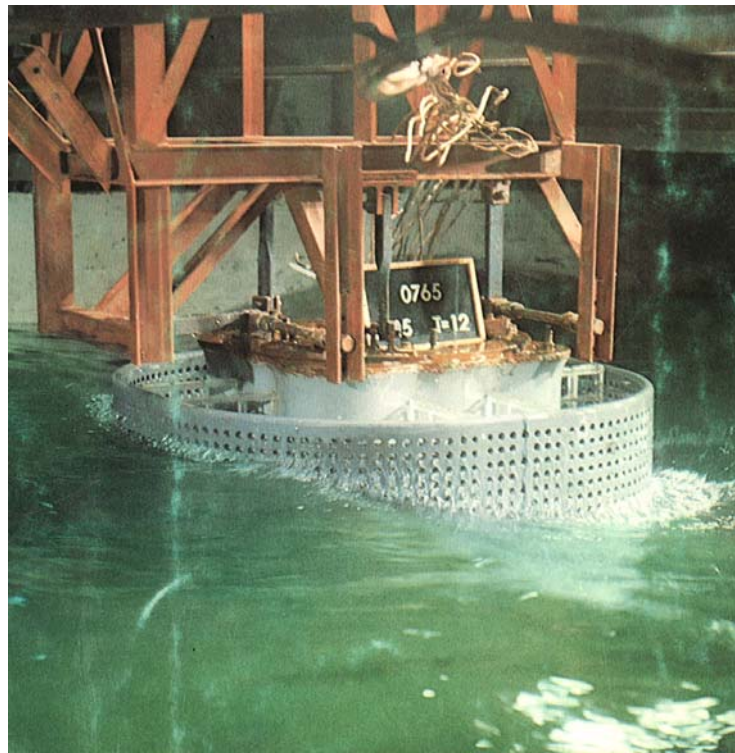


Figure 47. The Ekofisk oil storage tank under testing at RHL.

The hydropower development and river projects in Norway has almost vanished and so they have at RHL. This activity is taken over by the Department of Hydraulic and Environmental Engineering at NTNU, while the coastal and harbour activities are continued under SINTEF

Coastal and Harbour Laboratory. The Department of Civil and Transport Engineering, Marine Group, at NTNU has still their laboratory facilities in the same building.

RESEARCH

Coastal engineering has been and is a small field of engineering in Norway. Research in this field has obtained limited support from the Norwegian Research Council. Most of the research has been supported by the NCA, either through research projects at RHL or through student thesis support at NTNU/RHL. NCA has also supported the participation of RHL/NTNU personnel in three EC programs on breakwaters and local scour. However, NCA has also a limited budget. Hence, the research has also been limited.

Breakwaters

Since rubble mound breakwaters have been a key coastal engineering structure in Norway, much research has been carried out on this type of structure. At NTH professor A. Brandtzæg was active in breakwater research until he retired in 1967, actively cooperating with RHL personnel. Then professor Per Bruun was appointed professor in harbour and coastal engineering. Together with students he continued research on rubble mound breakwaters.

Numerous papers have been presented by NTNU/RHL personnel either as journal papers or as conference papers on rubble mound breakwaters. The very first international paper on the stability of rubble mound breakwaters in irregular waves was presented by RHL personnel at ICCE'66 in 1966.

It was mentioned that the Icelandic Maritime Administration has pioneered the development of the berm breakwater. However, SINTEF/NTNU personnel have participated in the forefront of the international community on the research of berm breakwaters, particularly with respect to stability and stone quality (strength and abrasion).

Probabilistic design methods have been developed for conventional rubble mound breakwaters. Only limited work on this issue has been carried out for berm breakwaters. In fact the new ISO standard, ISO 21650 "Action from waves and currents on coastal structures", requires that a probabilistic analysis of the performance of structures exposed to waves and currents be carried out. Probabilistic or performance design for berm breakwaters should be further studied.

Local scour at breakwaters has not been a big concern in Norway. However, there has been some research on this item, particularly through EU-projects. The bottom bearing capacity for Norwegian breakwaters has also generally been good. Only in a couple of cases has there been bottom failure.

Preliminary tests of pneumatic breakwaters were also run in Trondheim in 1957. It was seen that pneumatic breakwaters were not a solution for Norwegian fishing harbours. The technology, however, was applied to quite a different problem: to combat freezing of Norwegian fjords due to winter discharges of fresh water from hydropower plants, Figure 48, or to solve an estuarine problem. The first of these was at Mo i Rana. Here, the induced surface flow was designed to match the outflow of the discharge from the power plant. This has been in successful operation since 1969.

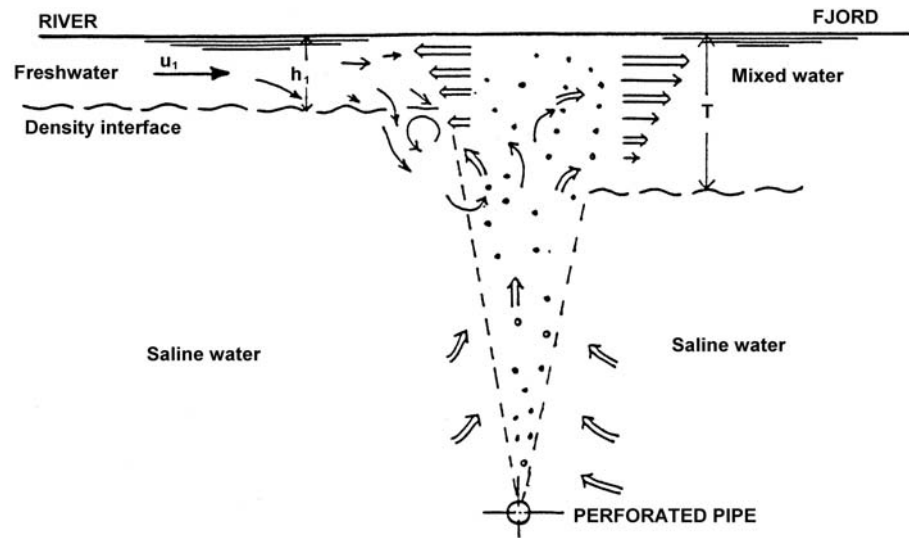


Figure 48. Principle of air curtain mixture of salt and fresh water.

Other applications of this technology internationally include the protection of coastal facilities and vulnerable sites from acute oil spills, among other things. Research is still being carried out in Trondheim on various uses of bubble curtains.

Floating breakwaters are a breakwater solution for limited fetches and for large depths. Such breakwaters are to some extent used in Norway, especially for marinas. For box type floating breakwaters tests, sponsored by the Norwegian Coastal Administration, have been conducted in short-crested waves in the ocean basin at Marintek, Figure 49.

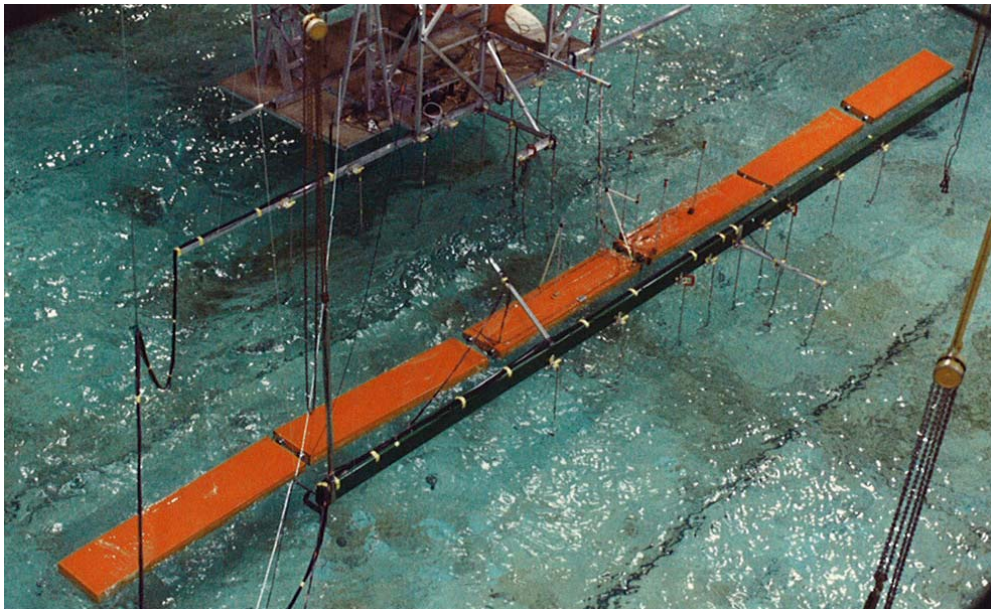


Figure 49. Floating breakwater tests at Marintek/SINTEF.

Waves

The limited resources of research funding have limited the development of large computer programs to calculate waves toward the coast and within harbours. However, by adjusting available programs to Norwegian conditions RHL/NTNU personnel have developed computer programs for more specific Norwegian conditions. It has also turned out that many of the small Norwegian fishing harbours have a complex geometry such that physical model tests have been necessary for a final design. It is not a question of either/or only, but both computer programs and physical model tests are used in synergy.

In the beginning of the 1970's when the oil industry came to Norway, RHL/NTNU personnel participated in large wave measurement and wave analysis programs for waves in deep water. The results of this and others efforts have served the coastal engineering community, as mentioned before. The deep water waves are transformed to shallow water through refraction computer programs. However, the computer programs are based on slowly varying depths. Many places along the Norwegian coast the bathymetry is complex, with shoals where the waves break before they travel further into deeper water towards the coast. In such cases it is difficult to precisely determine the wave transmission. We have a coast with few problems related to sand transport, but we have a hydrodynamically difficult coast! Thus there is a need for a Norwegian coastal wave research program.

Most breakwaters are designed with a conservative estimate of simultaneous design wave height and water level, including storm surge. Further investigations of the probability of joint occurrence of waves and water levels should be undertaken.

Light towers.

As mentioned, most of the Norwegian coast is rocky with shoals and skerries. Many of these shoals are suitable for the location of light towers. Figure 50 shows the sea floor contour of Arsgrunnen at the entrance to Boknafjorden outside Stavanger. The depth on the shoal is approximately 5 m, but the depth nearby increases rapidly to more than 70 m. The shoal is thus like an underwater mountain. A light tower was erected on this shoal, but it failed due to the high waves that enter this area almost directly from the North Sea. A new light tower was built as shown in Figure 51. This has survived many violent storms in the area.

To establish the wave forces on a structure on shoals as the Arsgrunnen is not easy. Not much was found in the literature on wave forces on such structures in such locations. Large waves increase in height and break heavily as they approach the shoal. Wave heights of three times the water depth have been measured in model tests over such shoals. Through several student theses work, supported by NCA, both the wave conditions at, and breaking wave forces on single column and tripod light towers on such shoals have been investigated.

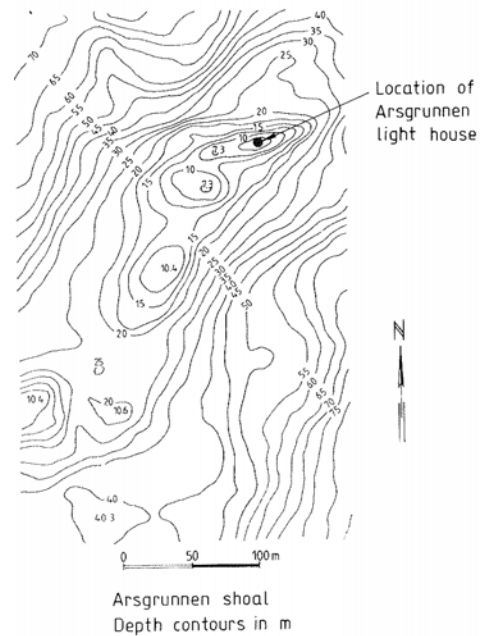


Figure 50. Arsgrunnen, Boknafjorden.

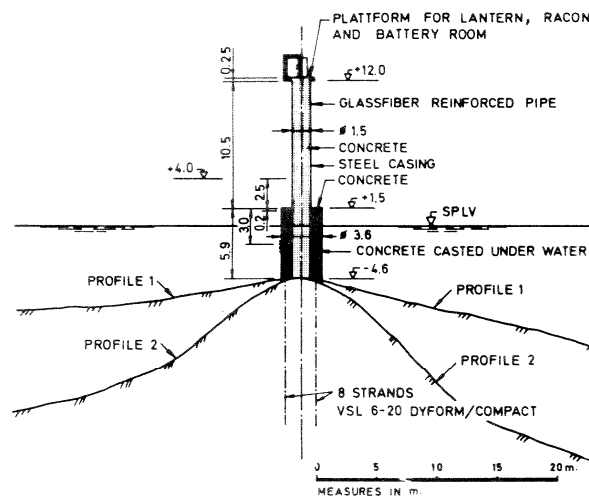


Figure 51. Light house on Arsgrunnen.

Sea vegetation and coastal erosion

It was mentioned that Norway has a rocky coast with few sandy beaches. However, there is a coastal region south of the city of Stavanger, the Jæren coast, which has many beaches of sand and gravel of glacial origin, Figure 52.



Figure 52. Sand and gravel beach at Revtingen, Jæren.

Long term beach erosion along these beaches has apparently not been a problem. However, there are large kelp fields outside some of these beaches, Figure 53.

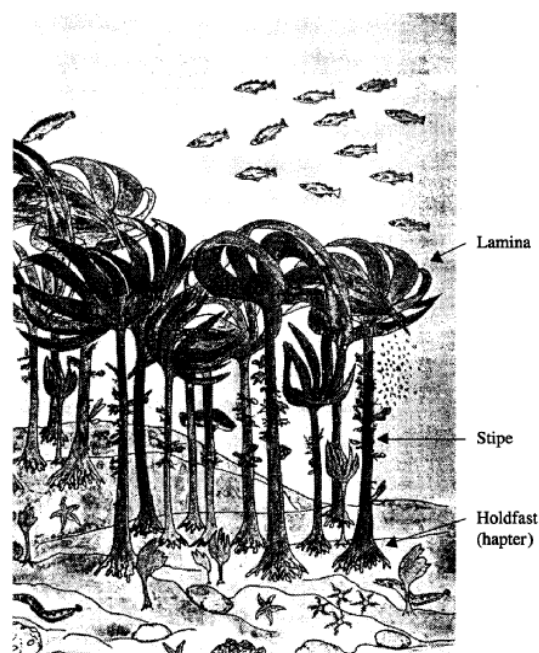


Figure 53. Kelp, *Laminaria hyperborea*. Growing density: ≈ 10 per m^2 , stipe length ≈ 1.5 m.

The kelp is being harvested and used as raw material for the production of chemicals, particularly alginates. This harvesting of kelp has caused conflicts of different kinds. One of them is the belief that the kelp dampens the waves and thus protects the beaches. It is true that kelp damps waves. But in the surf zone, the loss of wave energy is much larger by wave breaking than by the presence of kelp. Kelp dampens waves, but research has shown that the harvesting of kelp does not influence beach erosion significantly.

The farmers on the Jæren coast have previously suffered much from wind driven sand from the shores. The wind driven sand covered frequently their farmland and some farms had to be abandoned. Plans were made by the Danish/Norwegian government in 1806 to plant marram grass. However, in 1814 Norway became independent from Denmark. But the Norwegian government did not pay attention to the sand drift problems on Jæren. It was not until 1870 that Torger Nærland took the initiative to organise the farmers to plant marram grass and other plants. They succeeded to stop the sand wind drift almost completely. The sand dunes are still growing. Figure 54 shows a map from 1806 from the Reve area on Jæren. Figure 55 shows a photograph of the same area today. Where the sand drift prevailed some 200 years ago it is good farmland today, Tørum and Gudmestad (2008).

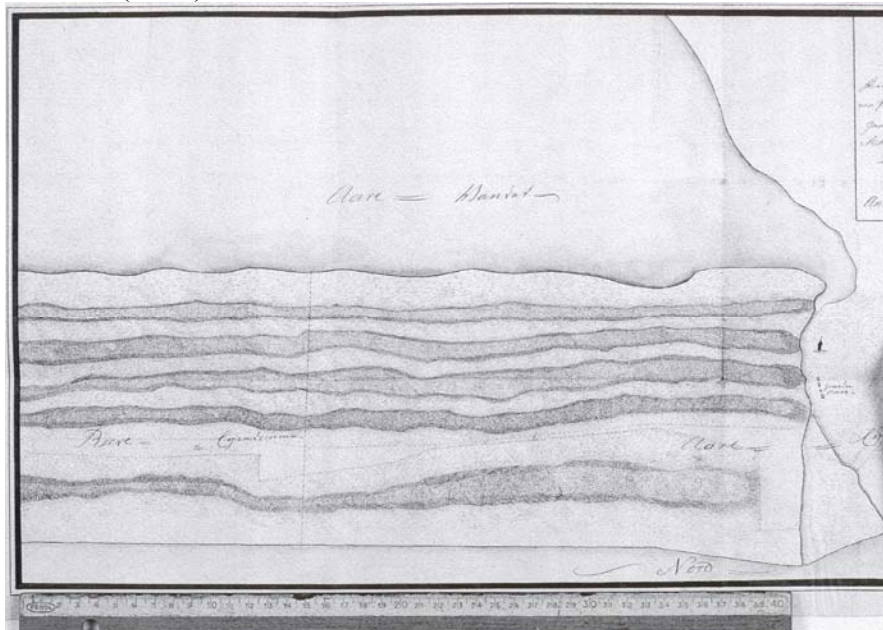


Figure 54. Orre Lake, Jæren, 1806.
Original: The National Archives (Riksarkivet) in Oslo (NRA RK 498).



Figure 55. Orre, Klepp, Jæren. Photo: Norsk Fly og Flyfoto.

Pipelines

Strictly speaking, only the shore approach and landing sites of pipelines are coastal structures. But since this item is on the agenda for this workshop, pipelines on the seabed are included in this review.

One of the conflict areas when the oil industry came to Norway was the interaction between trawl boards and pipelines. Either the fishing gear, the pipeline or both could be damaged.

Through a series of model and field tests in the 1970's it was shown that the fishing gear could be modified and the pipeline concrete coating strengthened such that the passing of trawl board across an oil or gas pipeline could be safe. Figure 56 shows the set-up for a field test in the Trondheim fjord around 1976.

More recent SINTEF research on pipelines on the sea bottom has been the investigation of the interaction between gravel mounds over pipelines and trawl boards and the interaction between gravel mounds over pipelines and falling objects, e.g. drill strings. At NTNU the stability of gravel mounds over pipelines in waves has recently been investigated.

One of the largest research projects for SINTEF is the pipeline project PIPESTAB carried out in the mid 1980's. Through this project the stability of pipelines on the sea bottom subjected to waves and currents was investigated. It involved large scale hydrodynamic tests as well as large scale tests on the interaction between a pipeline and soils.

The vortex induced vibrations (VIV) of pipelines in free spans have also been investigated. A particularly interesting project was investigation of the VIV for different turbulence intensities.

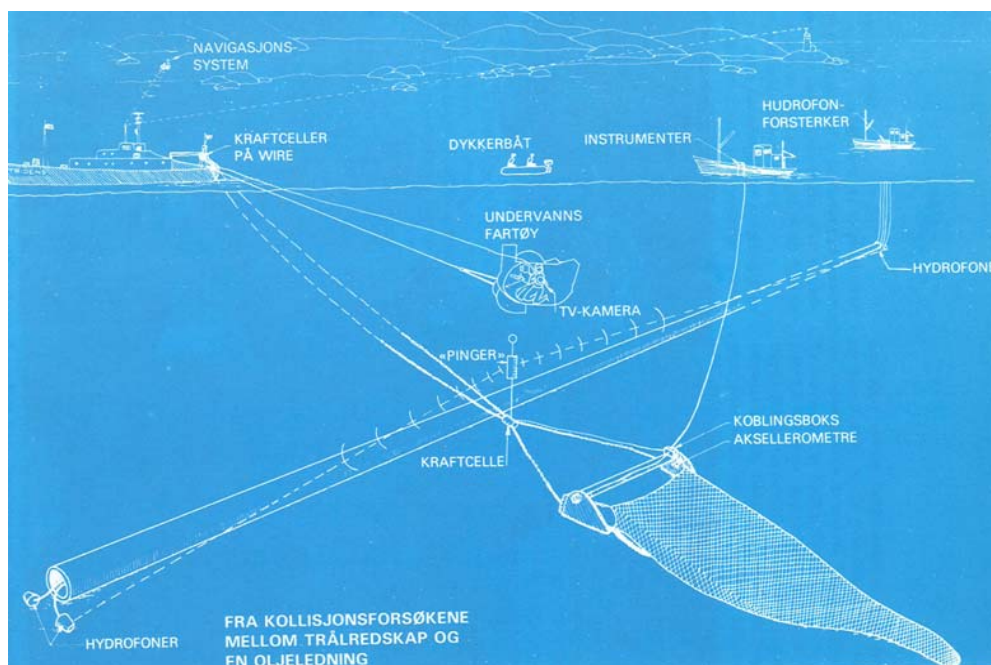


Figure 56. Set-up for a field test for pipeline-fishing gear interaction in the Trondheim fjord around 1976.

Arctic coastal engineering

There are really no significant arctic related problems in coastal engineering in Norway, except on Svalbard. There might be shipping problems in some of our fjords in some years, but not every year, particularly in the Oslo fjord area. However, as the oil industry moves into arctic or ice-infested areas, there is also a need for more knowledge on the interaction between the ice and “coastal” structures. Figure 57 shows a concept for protecting oil installations in shallow water against ice, the Shoulder Ice Barrier (SIB), while Figure 58 shows the behaviour of the ice as it presses against the structure. Ice tests have shown that the interaction with the ice is approximately as depicted in Figure 58. The concept may be developed to be an efficient breakwater in ice infested areas. Model tests on the ice and wave forces for a SIB as a breakwater have been carried out. A PhD student is presently numerically modelling, numerically and apparently successfully, the ice behaviour as the ice climb upon the structure.

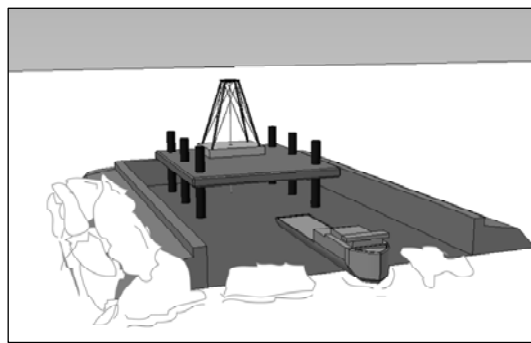


Figure 57. Shoulder ice barrier – concept.

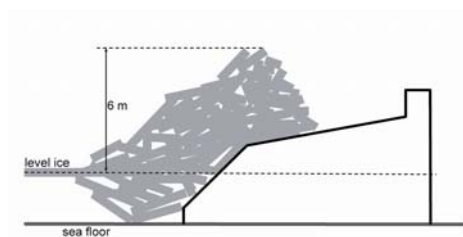


Figure 58. Shoulder ice barrier, SIB.
Behaviour of ice – tested in ice tank.

The rock on Svalbard is to a large extent sandstone. This rock is not very suitable for armour blocks on breakwaters. Research on the use of stone filled geobags as breakwater armour is in progress. This armour has to withstand waves as well as ice gouging. Figure 59 shows the study area for this project, while Figure 60 shows the geobags placed on the rubble mound structure.



Figure 59. Geobag study area on Svalbard



Figure 60. Geobag study embankment on Svalbard.

Climate change: Consequences for coastal engineering in Norway

The Intergovernmental Panel on Climate Change (IPPC) is of the opinion that there is a climate change of partly anthropogenic (manmade) origin. This change might have an effect on coastal engineering also. It appears that the change of wave climate will be almost insignificant in the southern part of Norway. In the northern part there may be an increase of 10-15%. Storm surge levels are not expected to increase significantly along the Norwegian coast.

Sea level rise seems to be the largest threat from climate change to the coastal zone in Norway. There are big uncertainties on how much the increase will be. But a “guess” is that the sea level rise will be approximately 0.6 m in the 21st century. As mentioned earlier, some parts of Norway, e.g. Oslo area, have significant land rise that counteracts to some extent the sea level rise in the 21st century.

FUTURE OF COASTAL ENGINEERING IN NORWAY

The development of fishing harbours has slowed down and we see a restructuring of the activities in the fishing industry. This will also have an influence on coastal engineering in Norway. There is a great need for knowledge of coastal engineering along the coast. However, most of the projects in smaller communities are small and the actors may not even know they have a problem. There is thus a need for a national competence center in coastal engineering in Norway. The SINTEF Coastal and Harbour laboratory (RHL) and NTNU serves to some extent this purpose. But since the authorities are not willing to give financial support to SINTEF Coastal and Harbour laboratory (RHL) and there might not be a big actor like NCA to support RHL to a similar extent as today, the economical situation of SINTEF Coastal and Harbour laboratory (RHL) is difficult. Norwegian consulting and contracting companies are not strong in coastal engineering on the international market, so there is no “pull” or “push” from them to have a national competence center.

Presently there is cooperation on the European level between the Delft University of Technology, Universitat Politècnica de Catalunya (Barcelona), University of Southampton, City University London and NTNU on the teaching of “Coastal and Marine Engineering and Management”. To quote from a brochure on this cooperation: “The need for sustainable development continues to grow and is becoming more urgent all the time, especially considering that the majority of the world’s population lives and works in coastal zones or goes there for enjoyment and relaxation”.

Arctic engineering is a big issue at NTNU with several PhD students studying ice mechanics and ice forces on structures. Sometimes, Arctic engineering involves all the classical coastal engineering problems. In addition Arctic engineering involves the problems with the ice, problems that to some extent are far more complex than the problems in coastal engineering.

So I see a new area at NTNU for coastal engineering associated with coastal zone management and with arctic engineering.

ACKNOWLEDGEMENTS

The author acknowledges the help from the following persons to provide information to this paper: Eivind Johnsen, Jann Eliassen, Håvard Berge, Sverre Bjørdal and Arnstein Watn.

The author also acknowledges comments to early version of the paper from Øivind Arntsen, Eivind Bratteland, Thomas McClimans, Ove T. Gudmestad, Sveinung Løset and Geir Moe.

REFERENCES

I have described several items for which there could be several Norwegian papers. However, I have only included typical historical references.

Berge, H., 1960. *Havnelaboratoriet ved Norges teknisk høgskole. (The Harbour Laboratory at the Norwegian Institute of Technology)*, Teknisk Ukeblad nr. 27, 1960. (in Norwegian).

Brandtzæg, A., 1960. *Rausmoloer. Norsk praksis og erfaring sammenholdt med teori og praksis. (Rubble mound breakwaters. Norwegian experience and practice compared to theory and experimental data)*. Teknisk Ukeblad nr. 27, 1960. (in Norwegian).

Danielsen, J.S., 2001. *A land uplift map of Fennoscandia*. Survey Review, 36, 282-296, 2001.

Den norske los. (The Norwegian Pilot). The Norwegian Mapping and Cadastre Authority.

Havndirektoratet, 1914. *Havnevæsenets historie. (The history of the State Harbour Authority)*.

Johnsen, E., 2003. *Om fiskerihavneutbyggingen i Norge. (The development of fishing harbours in Norway)*. Kort presentasjon i Kystverket

Kjelstrup, S., 1977. *Berlevåg harbour on the Norwegian arctic coast*. Proceedings of the conference Port and Ocean Engineering (POAC'77), St. Johns, New Foundland, Canada, 26 – 30 September 1977.

Kystverket, 1981. *Stedsomtale, Berlevåg. (Norwegian Coastal Administration (1981): Description of work at Berlevåg harbour)* (in Norwegian).

Kjemperud, A. 1986. *Late Weichselian and Holocene shoreline displacement in the Trondheimsfjord area, central Norway*. Boreas 15, pp 61 – 82.

Meyer, J. 1869. *Civilingeniør J. Meyers Inberetning om den gamle Havn og Molo ved Agdenes. (Civilingeniør J. Meyer's account on the old harbour and breakwater at Agdenes)*. Aarsberetning for Foreningen til Norske Fortidsmindemerkens Bevaring, 1869. Kriterion (Oslo).

Rokoengen, K. and Jasiski, M.J. 1996. *Sagakongenes byggeaktivitet på Agdenes. Spor etter Kong Øysteins havn i ord, jord og fjord. (The historical kings construction activities at Agdenes. Footprints of King Øysteins harbour in words, earth and fjord)*. Årbok for Fosen 1996.

Storm, O.H., 1960. *Havnelaboratoriet. (Harbour Laboratory)*. Teknisk Ukeblad, nr. 27, 1960. (in Norwegian).

Tørum, A. and Gudmestad, O.T. 2008. *On the wind driven sand on the Jæren coast*. Year book 2008 “Ætt og soger”, Rogaland Historical Society. (In Norwegian) (in press).

WAVE INTERACTION WITH MARINE VEGETATION

Inigo J.Losada
Environmental Hydraulics Institute “IH Cantabria”
Universidad de Cantabria-Santander-Spain
losadai@unican.es

Water motion due to wave dynamics and currents is a key determinant of marine vegetation physiology, production, community distribution and mortality. The understanding of vegetation mechanics requires a detailed analysis of the different processes involved in the wave/vegetation interaction process. Moreover, the presence of marine vegetation may play an important role in damping wave propagation as well as in promoting sediment stability and accretion.

During the last decades our understanding of how marine vegetation interacts with their hydrodynamic environment has increased substantially thanks to the work carried out by different researchers worldwide. Theoretical models, flume and field studies have contributed to investigate the flow structure above the vegetation, wave damping, wave forces imposed by wave action, sediment retention capacity or spatial patterns of flow and their modification within and around large vegetation fields or the potential applicability of marine vegetation to protect the coast against erosion.

During this presentation a review of the current state of the art will be given including the pioneering work of Prof. Torum and his collaborators. The review will discuss the different processes to be considered in the wave and vegetation interaction, differences between seagrass and kelp mechanics, existing theoretical and numerical models as well as available field and laboratory data. Gaps in our current knowledge will also be presented.

See Coast 2008 homepage for extras. <http://www.ivt.ntnu.no/bat/english/coast2008/>

WAVE – CURRENT – SEABED INTERACTION OVER GENERAL BOTTOM TOPOGRAPHY

K.A. Belibassakis¹, Th.P. Gerostathis¹ & G.A. Athanassoulis²

⁽¹⁾ *School of Technological Applications, Technological Educational
Institute of Athens, Ag. Spyridonos, Athens 12210, Greece.*

⁽²⁾ *School of Naval Architecture & Marine Engineering,
National Technical University of Athens,
Heron Polytechniou 9, Athens 15773, Greece.*

ABSTRACT

A new coupled-mode model is presented for wave-current-seabed interaction, with application to wave scattering by steady currents over general bottom topography. The vertical structure of the scattering wave potential is represented by a series of local vertical modes containing the propagating mode and all evanescent modes, plus an additional term accounting for the bottom boundary condition when the bottom slope is not negligible. Using the above representation, in conjunction with Luke's (1967) variational principle, the wave-current-seabed interaction problem is reduced to a coupled system of differential equations on the horizontal plane. If only the propagating mode is retained in the vertical expansion of the wave potential, and after simplifications, the present system is reduced to an one-equation model compatible with Kirby's (1984) mild-slope model (see also Liu 1990) with application to the problem of wave-current interaction over slowly varying topography.

INTRODUCTION

The evolution of water-waves in nearshore and coastal areas, and especially, in regions where ambient, tidal and other type of currents co-exist, is important for a variety of engineering applications including interaction of waves with structures, coastal management, harbour maintenance, exploitation of renewable energy sources etc. Sometimes the effects of currents on wave transformation can be substantial, since they are responsible for Doppler shifting and for causing wave refraction, reflection, and breaking. Also, currents could completely change the wave energy pattern. In particular, the characteristics of surface waves present significant variation as they propagate through non-homogeneous ambient currents, in the presence of depth inhomogeneities in variable bathymetry regions. Thus, large amplitude waves can be produced when obliquely propagating waves interact with opposing currents, see, e.g., Mei (1983). This situation could be further enhanced by inshore effects due to sloping seabeds, and has been reported to be connected with the appearance of "giant waves", Lavrenov & Porubov (2006). Extensive reviews on the subject of wave-current interaction in the nearshore region have been presented by Peregrine (1976), Jonsson (1990) and Thomas & Klopman (1997).

The study of spatial evolution of water waves and the investigation of scattering of realistic wave spectra over irregular currents, with characteristic length of variation comparable to the dominant wavelength, and including the effects of bottom irregularities, can be supported by theoretical models treating the simpler problem of monochromatic waves interacting with steady inhomogeneous currents. Wave-current interaction models over slowly varying bottom topography have been developed and studied by various authors. Under the assumption of irrotational wave motion, Kirby (1984) derived a phase-resolving one-equation model, generalizing the Berkhoff's mild-slope equation in regions with slowly varying depth and

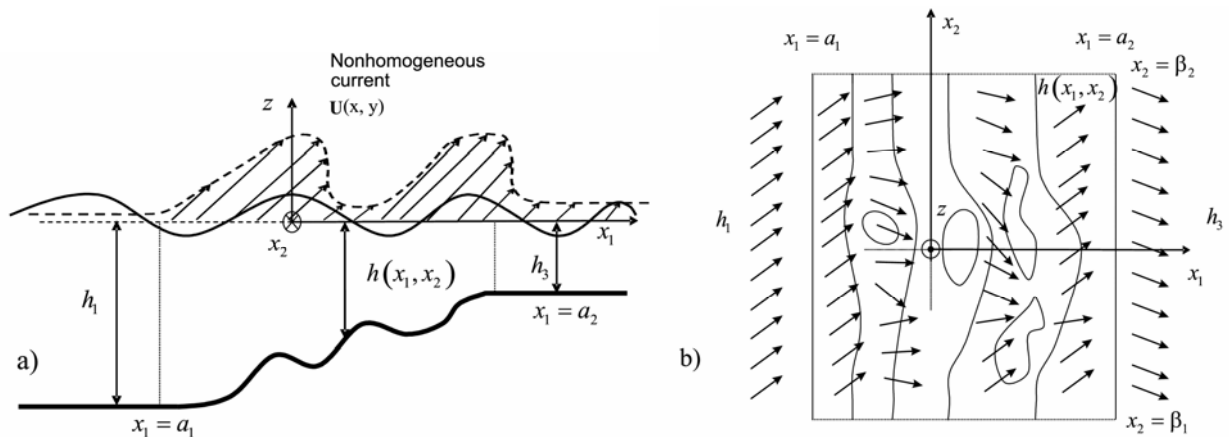


Figure 1 - Interaction of waves with currents over variable seabed topography:
(a) Vertical section, (b) Horizontal plane

ambient currents; see also Liu (1990). In the present work, a new, weakly nonlinear, coupled-mode model is developed for the wave-current-seabed interaction problem, with application to wave scattering by steady ambient currents over general bottom topography. Based on previous work by the authors (Athanasoulis & Belibassakis 1999, Belibassakis *et al* 2001, Gerostathis *et al* 2008), the vertical distribution of the scattered wave potential is represented by a series of local vertical modes containing the propagating mode and all evanescent modes, plus an additional term accounting for the bottom boundary condition when the bottom slope is not negligible (the sloping-bottom mode). Using the above representation, in conjunction with Luke's (1967) variational principle, the wave-current-seabed interaction problem is reduced to a coupled system of differential equations on the horizontal plane. If only the propagating mode is retained in the vertical expansion of the wave potential, and after simplifications and linearisation, the present system is reduced to an one-equation model (the wave-current modified mild-slope model), which after additional simplifications is shown to be compatible with Kirby's (1984) mild-slope model. The present coupled-mode system is discretized on the horizontal plane by using a second-order finite difference scheme and numerically solved by iterations. Results are presented for representative test cases corresponding to a rip current over a sloping beach in shallow water, and to a ring current in constant depth. In these cases comparisons are presented of the results obtained by the one-equation model (i.e. keeping only the propagating mode in the expansion of the wave potential) and the multi-mode system (also including the rest of the vertical modes), demonstrating the importance of the first evanescent modes and the sloping-bottom mode. The analytical structure of the present model facilitates its extension to treat fully non-linear waves, and it can be further elaborated to study wave propagation over random bottom topography and scattering by currents with general 3D structure.

THE BACKGROUND CURRENT FLOW

We consider wave propagation, in the presence of ambient, non-homogeneous current, in a variable bathymetry region; see Fig. 1. The liquid is assumed inviscid and homogeneous, and the background current flow is assumed to be steady and self-existent. Moreover, the wave flow perturbing the background current flow, which is generated by an incident wave system coming from the far up-wave region (see Fig.1), is assumed to be irrotational. A Cartesian coordinate system is used, having its origin at some point on the unperturbed free-surface ($z = 0$). The z -axis is pointing upwards and one of the horizontal axes is taken to be (approximately) aligned

with the mean direction of the transmitted wave field; see Fig. 1. The current $\mathbf{q} = (U_1, U_2, W)$ has been assumed to be steady and self-existent and the kinematics of this flow require that,

$$\nabla_3 \mathbf{q} = 0, \quad (1a)$$

$$\mathbf{q} \cdot \mathbf{n} = 0, \quad z = H(x_1, x_2), \quad \mathbf{q} \cdot \mathbf{n} = 0, \quad z = -h(x_1, x_2), \quad (2b,c)$$

where ∇_3 denotes the gradient operator in 3D, and H denotes the mean set-down associated with the background current flow. Eq. (2.c) is equivalently written in the form,

$$W + U_1 \frac{\partial h}{\partial x_1} + U_2 \frac{\partial h}{\partial x_2} = 0, \quad z = -h(x_1, x_2), \quad (2c')$$

Assuming the current to be nearly horizontal and its velocity components to be small, the mean set-down can be neglected ($H \approx 0$), and the kinematical free-surface boundary condition (2b) can be linearised as follows:

$$W = 0, \quad z = 0. \quad (2b')$$

The dynamics of the steady background current are described through the corresponding Bernoulli equation, stating that total energy is conserved along the streamlines (Batchelor 1967),

$$Q = \frac{1}{2} |\mathbf{q}|^2 + \frac{P}{\rho} + gz = \text{const} = \frac{1}{2} |\mathbf{q}_\infty|^2 + \frac{P_\infty}{\rho} + gz_\infty, \quad (3)$$

where ρ is the liquid density, g is the gravitational acceleration and z_∞ denotes the vertical position of each streamline at infinity. Taking P_∞ to be the static pressure of the fluid at rest, obtained by the superposition of the atmospheric and the hydrostatic pressure at infinity,

$$P_\infty = p_a - \rho g z_\infty, \quad (4)$$

we finally obtain the following equation

$$\frac{P}{\rho} = \frac{1}{2} (|\mathbf{q}_\infty|^2 - |\mathbf{q}|^2) + \frac{p_a}{\rho} - gz. \quad (5)$$

The total (current and wave) flow velocity \mathbf{u} , as well as the background current flow velocity \mathbf{q} , both satisfy Euler equations. Subtracting these equations by parts and omitting approximately the terms associated with the vorticity of the background flow ($\nabla_3 \times \mathbf{q}$), which is assumed to be weak, we finally obtain the following approximate Bernoulli equation,

$$\frac{p}{\rho} + \frac{\partial \varphi}{\partial t} + \mathbf{q} \cdot \nabla_3 \varphi + \frac{1}{2} |\nabla_3 \varphi|^2 = 0, \quad (6)$$

where $\varphi(x_1, x_2, z; t)$ denotes the (disturbance) wave potential, $\nabla_3 \varphi = \mathbf{u} - \mathbf{q}$, and p is the wave-induced pressure, defined as the difference between the total (P_u) and the background (P) pressure, $p = P_u - P$. Using the above equations, we finally obtain the following Bernoulli equation expressing the conservation of energy of the studied wave-current problem:

$$P_u - p_a = -\rho \left[gz + \frac{\partial \varphi}{\partial t} + \frac{1}{2} (|\mathbf{u}|^2 - |\mathbf{q}_\infty|^2) \right]. \quad (7)$$

VARIATIONAL FORMULATION

The variational principle governing the total fluid motion is formulated using Luke's (1967) functional, that is based on integration of pressure in the domain (see also Massel 1989),

$$\mathcal{L} = \iiint_t \int_{x_1, x_2} \int_{z=-h(x_1, x_2)}^{z=\eta(x_1, x_2; t)} (P_u - p_a) dz dx_2 dx_1 dt, \quad (8)$$

where $\eta(x_1, x_2; t)$ denotes the free-surface elevation associated with the total wave and current flow. Using (7), the above equation is written as follows

$$\mathcal{L} = -\rho \iiint_t \int_{x_1, x_2} \int_{z=-h(x_1, x_2)}^{z=\eta(x_1, x_2; t)} \left[gz + \frac{\partial \varphi}{\partial t} + \frac{1}{2} (|\mathbf{u}|^2 - |\mathbf{q}_\infty|^2) \right] dz dx_2 dx_1 dt. \quad (9)$$

Using the fact that the current has been assumed essentially horizontal ($W \ll U_1, U_2$) and slowly varying ($|\mathbf{q}|^2 \approx |\mathbf{q}_\infty|^2$), the quantity $|\mathbf{u}|^2 - |\mathbf{q}_\infty|^2$ in the right-hand side of Eq.(9) can be approximated as follows: $|\mathbf{u}|^2 - |\mathbf{q}_\infty|^2 \approx U_1 \frac{\partial \varphi}{\partial x_1} + U_2 \frac{\partial \varphi}{\partial x_2} + (\nabla_3 \varphi)^2$. Using the latter and requiring the above functional to be stationary, $\delta \mathcal{L} = 0$, and after carrying out the algebra, we finally obtain the following variational equation (see also Massel 1989, Eq.1-35)

$$\begin{aligned} & -\rho \iiint_t \int_{x_1, x_2} \left\{ \left[\frac{1}{2} \left(U_1 \frac{\partial \varphi}{\partial x_1} + U_2 \frac{\partial \varphi}{\partial x_2} + (\nabla_3 \varphi)^2 \right) + \frac{\partial \varphi}{\partial t} + g\eta \right]_{z=\eta(x_1, x_2, t)} \delta \eta \right. \\ & \left. - \left[\frac{\partial \eta}{\partial t} + \left(U_1 + \frac{\partial \varphi}{\partial x_1} \right) \frac{\partial \eta}{\partial x_1} + \left(U_2 + \frac{\partial \varphi}{\partial x_2} \right) \frac{\partial \eta}{\partial x_2} - \left(W + \frac{\partial \varphi}{\partial z} \right) \right]_{z=\eta(x_1, x_2, t)} \delta \varphi + \right. \\ & \left. - \left[\frac{\partial \varphi}{\partial z} + \frac{\partial \varphi}{\partial x_1} \frac{\partial h}{\partial x_1} + \frac{\partial \varphi}{\partial x_2} \frac{\partial h}{\partial x_2} \right]_{z=-h(x_1, x_2)} \delta \varphi - \left[\int_{z=-h(x_1, x_2)}^{z=\eta(x_1, x_2; t)} \left(\frac{\partial^2 \varphi}{\partial x_1^2} + \frac{\partial^2 \varphi}{\partial x_2^2} + \frac{\partial^2 \varphi}{\partial z^2} \right) dz \right] \delta \varphi \right\} dx_2 dx_1 dt = 0, \quad (10) \end{aligned}$$

where also the continuity equation concerning the background current, Eq.(1), and the bottom boundary condition, Eq. (2c), have been used. The equations governing the fully non-linear wave-current problem are derived from the above principle, Eq. (10).

THE NONLINEAR COUPLED-MODE SYSTEM

Following previous works (se.g., Athanassoulis & Belibassakis 2002, Belibassakis & Athanassoulis 2006), we use the following local-mode series expansion of the wave potential

$$\begin{aligned} \varphi(\mathbf{x}, z, t) = & \varphi_{-2}(\mathbf{x}, t) Z_{-2}(z; h, \eta) + \varphi_{-1}(\mathbf{x}, t) Z_{-1}(z; h, \eta) +, \\ & + \varphi_0(\mathbf{x}, t) Z_0(z; h, \eta) + \sum_{n=1}^{\infty} \varphi_n(\mathbf{x}, t) Z_n(z; h, \eta) \end{aligned} \quad (11)$$

in the variable bathymetry region, where $\mathbf{x} = (x_1, x_2)$. In the above expansion, the mode $n=0$ (i.e., $\varphi_0(\mathbf{x}) Z_0(z; h, \eta)$) denotes the *propagating mode* and the remaining terms, $n = 1, 2, \dots$, are the *evanescent modes*. The term $\varphi_{-1}(\mathbf{x}, t) Z_{-1}(z; h, \eta)$ is a correction term, called the *sloping-bottom mode*, properly accounting for the satisfaction of the Neumann bottom boundary condition on the non-horizontal parts of the bottom. The term $\varphi_{-2}(\mathbf{x}, t) Z_{-1}(z; h, \eta)$ is a corresponding term introduced to ensure the satisfaction of the free-surface boundary condition. The rest of functions $Z_n(z; \mathbf{x})$, $n = 0, 1, 2, \dots$, appearing in Eq. (11), are obtained as the eigenfunctions of the following local vertical Sturm-Liouville problems formulated with respect to the local depth and the intrinsic frequency $\sigma = \omega - \mathbf{U} \cdot \mathbf{k}$:

$$Z_n'' + k_n^2 Z_n = 0, \quad -h(\mathbf{x}) < z < \eta(\mathbf{x}; t), \quad (12)$$

$$Z_n'(-h(\mathbf{x})) = 0, \quad z = -h(\mathbf{x}), \quad Z_n' - \mu Z_n(0) = 0, \quad z = \eta(\mathbf{x}; t), \quad (13)$$

where the prime denotes differentiation with respect to z . The parameter μ is taken to be the intrinsic frequency parameter $\mu = \sigma^2/g$, where ω denotes the characteristic absolute wave frequency. The definition of the intrinsic frequency depends also on the vector wavenumber \mathbf{k} , a quantity which is associated with the wave kinematics (see e.g. Jonsson 1990), and thus, it is clearly dependent on the solution $\varphi(x_1, x_2; z)$. This fact introduces intrinsic nonlinearity to the wave-current scattering problem, and iterations are necessary for its solution. The local vertical eigenfunctions are obtained from Eqs. (12, 13) as follows:

$$Z_0 = \frac{\cosh[k_0(z+h)]}{\cosh[k_0(\eta+h)]}, \quad Z_n = \frac{\cos[k_n(z+h)]}{\cos[k_n(\eta+h)]}, \quad n=1, 2, \dots, \quad (14)$$

where the wavenumbers $k_n = k_n(h, \eta)$ are obtained as a solution to the local dispersion relation,

$$\sigma^2 = k_0 g \tanh[k_0(h+\eta)] = -k_n g \tan[k_n(h+\eta)], \quad n \geq 1. \quad (15)$$

As concerns the sloping-bottom mode $\varphi_{-1} Z_{-1}$, a specific convenient form of the function $Z_{-1}(z; \mathbf{x})$ is given by

$$Z_{-1} = \frac{\mu_0 h_0 - 1}{2h_0(\eta+h)}(z+h)^2 + \frac{1}{h_0}(z+h) + \frac{2h_0 - (\eta+h)(\mu_0 h_0 + 1)}{2h_0}, \quad (16)$$

where the parameters $\mu_0, h_0 > 0$ are positive constants, having the following properties: $Z_{-1}'(z=\eta) - \mu_0 Z_{-1}(z=\eta) = 0$, $Z_{-1}'(z=-h) = 1/\mu_0$. However, other forms are also valid. Finally, as concerns the free surface mode $\varphi_{-2} Z_{-2}$, a specific convenient form of the function $Z_{-2}(z; \mathbf{x})$ is given by,

$$Z_{-2}(z; h, \eta) = \frac{\mu h_0 - 1}{2(\eta+h)h_0}(z+h)^2 - \frac{\mu h_0 + 1}{2h_0}(\eta+h) + 1, \quad (17)$$

having the properties: $Z_{-2}'(z=\eta) - \mu_0 Z_{-2}(z=\eta) = 1/\mu_0$, $Z_{-2}'(z=-h) = 0$, however other forms are also possible; see also Belibassakis & Athanassoulis (2006) for more details. Using the representation (11) in the variational equation (10), and after the algebra, we obtain an equivalent reformulation of the wave-current scattering problem in the form of the following *nonlinear Coupled Mode System* (CMS) of equations,

$$\sum_{n=-2}^{\infty} \left(A_{mn}(\eta) \nabla^2 \varphi_n + \mathbf{B}_{mn}(\eta) \cdot \nabla \varphi_n + C_{mn}(\eta) \varphi_n \right) + \frac{\partial \eta}{\partial t} + \mathbf{U} \cdot \nabla \eta - W = 0, \quad (18a)$$

$$\sum_{n=-2}^{\infty} \left(\frac{\partial \varphi_n}{\partial t} + [Q_n]_{z=\eta} \varphi_n \frac{\partial \eta}{\partial t} + \mathbf{U} \nabla \varphi_n + W \varphi_n \frac{\partial Z_n}{\partial z} \right) + g\eta + \frac{1}{2}(U_1^2 + U_2^2 + W^2) + \sum_{\ell=-2}^{\infty} \sum_{n=-2}^{\infty} \left(a_{\ell n}^{(0,2)}(\eta) \varphi_{\ell} \frac{\partial^2 \varphi_n}{\partial x^2} + a_{\ell n}^{(1,1)}(\eta) \frac{\partial \varphi_{\ell}}{\partial x} \frac{\partial \varphi_n}{\partial x} + \mathbf{b}_{\ell n}(\eta) \varphi_{\ell} \frac{\partial \varphi_n}{\partial x} + c_{\ell n}(\eta) \varphi_{\ell} \varphi_n \right) = 0, \quad (18b)$$

where $\nabla = (\partial/\partial x_1, \partial/\partial x_2)$ is the horizontal gradient operator. The matrix coefficients $A_{mn}(\eta)$, $\mathbf{B}_{mn}(\eta)$, $C_{mn}(\eta)$ are all dependent on the free-surface elevation (η) and are defined by

$$A_{mn}(\eta) = \langle Z_n, Z_m \rangle = \int_{z=-h(x_1, x_2)}^{z=\eta(x_1, x_2, t)} Z_n(z; h, \eta) Z_m(z; h, \eta) dz, \quad (19a)$$

$$\mathbf{B}_{mn}(\eta) = 2 \langle \nabla Z_n, Z_m \rangle + \left[\left(\nabla Z_n \cdot \nabla h + \frac{\partial Z_n}{\partial z} \right) Z_m \right]_{z=-h(\mathbf{x})} + \nabla \eta [Z_n Z_m]_{z=\eta(\mathbf{x}, t)}, \quad (19b)$$

$$C_{mn}(\eta) = \left\langle \frac{\partial^2 Z_n}{\partial z^2}, Z_m \right\rangle + \left[\left(\nabla Z_n \cdot \nabla h + \frac{\partial Z_n}{\partial z} \right) Z_m \right]_{z=-h(\mathbf{x})} + \left[\left(\nabla Z_n \cdot \nabla \eta - \frac{\partial Z_n}{\partial z} \right) Z_m \right]_{z=\eta(\mathbf{x}, t)}, \quad (19c)$$

where the brackets denote the inner product in the vertical interval:

$$\langle f(z), g(z) \rangle = \int_{z=-h(\mathbf{x})}^{z=\eta} f(z) g(z) dz. \text{ Moreover, the matrix coefficients } a_{\ell n}^{(0,2)}, a_{\ell n}^{(1,1)}, \mathbf{b}_{\ell n} \text{ and } c_{\ell n}$$

are similarly defined; see also Athanassoulis & Belibassakis (2007).

The weakly nonlinear CMS

By assuming small wave amplitudes and considering the wave velocity field to be time harmonic with angular frequency ω , we introduce the complex velocity potential

$$\varphi(x_1, x_2, z; t) = \text{Re} \{ \varphi(x_1, x_2, z) \exp(-i\omega t) \}. \quad (20)$$

In this case, the variational principle (10) simplifies as follows

$$\begin{aligned} & \rho \iint_{x_1 x_2} \left\{ -\frac{1}{g} \left[(-i\omega + \mathbf{U} \cdot \nabla)^2 \varphi + \frac{\partial \varphi}{\partial z} + (\nabla \mathbf{U}) \cdot (-i\omega + \mathbf{U} \cdot \nabla) \varphi \right]_{z=0} \delta \varphi + \right. \\ & \left. + \left[\frac{\partial \varphi}{\partial z} + \nabla \varphi \nabla h \right]_{z=-h(\mathbf{x})} \delta \varphi + \int_{z=-h(\mathbf{x})}^0 \left(\nabla^2 \varphi + \frac{\partial^2 \varphi}{\partial z^2} \right) dz \delta \varphi \right\} dx_2 dx_1 = 0, \quad (21) \end{aligned}$$

where, from now on, $\varphi = \varphi(x_1, x_2, z)$ denotes the complex wave potential. Furthermore, noting that the term $(-i\omega + \mathbf{U} \cdot \nabla)^2 \varphi + (\nabla \mathbf{U}) \cdot (-i\omega + \mathbf{U} \cdot \nabla) \varphi$, appearing in the integral on the mean free-surface ($z=0$) can also be written as follows:

$$A = -\omega^2 \varphi - 2i\omega(\mathbf{U} \cdot \nabla) \varphi - i\omega(\mathbf{U} \cdot \nabla) \varphi + \nabla \cdot (\mathbf{U} [(\mathbf{U} \cdot \nabla) \varphi]),$$

the variational principle for small-amplitude time-harmonic wave motion, Eq. (21), is finally put in the form:

$$\iint_{x_1 x_2} dt dx_1 dx_2 \left\{ \int_{z=-h(\mathbf{x})}^{z=0} \left(\nabla^2 \varphi + \frac{\partial^2 \varphi}{\partial z^2} \right) dz + \left[\frac{\partial \varphi}{\partial z} + \nabla \varphi \nabla h \right]_{z=-h(\mathbf{x})} - \left[\frac{A}{g} + \frac{\partial \varphi}{\partial z} \right]_{z=0} \delta \varphi \right\} = 0. \quad (22)$$

Also, in this case, the local-mode series expansion of the wave potential is simplified as follows

$$\varphi(\mathbf{x}; z) = \sum_{n=-1} \varphi_n(\mathbf{x}) \cdot Z_n(z; \mathbf{x}), \quad (23)$$

where the functions $Z_n(z; \mathbf{x})$, $n=0,1,2,\dots$, appearing in Eq. (23), are obtained as the eigenfunctions of local vertical Sturm-Liouville problems (12, 13), formulated with respect to the local depth and the local intrinsic frequency ($\sigma = \omega - \mathbf{U} \cdot \mathbf{k}$) in the vertical interval $-h(\mathbf{x}) < z < 0$. Thus, in the examined case the local vertical eigenfunctions are given by

$$Z_0 = \frac{\cosh[k_0(z+h)]}{\cosh(k_0h)}, \quad Z_n = \frac{\cos[k_n(z+h)]}{\cos(k_nh)}, \quad n=1,2,\dots, \quad (24)$$

where the wavenumbers k_n are obtained as a solution to the (simplified) local dispersion relation associated with the intrinsic frequency:

$$\sigma^2 = k_0 g \tanh(kh) = -k_n g \tan(k_nh). \quad (25)$$

As concerns the sloping-bottom mode $\varphi_{-1}Z_{-1}$, a specific alternative form of the function $Z_{-1}(z; \mathbf{x})$ used in this case is defined by

$$Z_{-1} = h \left[(z/h)^3 + (z/h)^2 \right], \quad (26)$$

having the following properties: $Z'_{-1}(z=-h)=1$, $Z_{-1}(z=-h)=0$, and $Z'_{-1}(z=0)=Z_{-1}(z=0)=0$ (see also the discussion by Athanassoulis & Belibassakis 1999).

Using the representation (23), in conjunction with the properties of Z_n , we obtain

$$\left. \frac{\partial \varphi}{\partial z} \right|_{z=0} = \mu \varphi = \frac{\sigma^2}{g} \varphi, \quad \text{on } z=0. \quad (27)$$

Introducing the above result in the last form of the variational principle, Eq. (22), we obtain

$$\iint_{x_1 x_2} dt dx_1 dx_2 \left\{ \int_{z=-h(x_1, x_2)}^{z=0} \left(\nabla^2 \varphi + \frac{\partial^2 \varphi}{\partial z^2} \right) dz + \left[\frac{\partial \varphi}{\partial z} + \nabla \varphi \nabla h \right]_{z=-h(x)} - \left[\frac{A}{g} + \frac{\sigma^2 \varphi}{g} \right]_{z=0} \delta \varphi \right\} = 0. \quad (28)$$

Using the local-mode representation (23) in the variational equation (28), we finally obtain the weakly nonlinear *coupled-mode system* (CMS) of equations, in the form

$$\sum_n \left\{ a_{mn} \nabla^2 \varphi_n + \left[\mathbf{b}_{mn} + \frac{2i\omega}{g} \mathbf{U} \right] \nabla \varphi_n + \left[c_{mn} + \frac{\omega^2 - \sigma^2}{g} + \frac{i\omega}{g} (\nabla \cdot \mathbf{U}) \right] \varphi_n - \frac{1}{g} \nabla \cdot (\mathbf{U} [(\mathbf{U} \cdot \nabla) \varphi_n]) \right\} = 0, \quad m = -1, 0, 1, \dots, \quad (29)$$

In Eqs. (29) the coefficients $a_{mn}, \mathbf{b}_{mn}, c_{mn}$ are defined by:

$$a_{mn} = \langle Z_m, Z_n \rangle, \quad \mathbf{b}_{mn} = 2 \langle \nabla Z_n, Z_n \rangle + Z_n(-h) Z_m(-h) \nabla h, \quad (30a,b)$$

$$c_{mn} = \left\langle \nabla^2 Z_n + \frac{\partial^2 Z_n}{\partial z^2}, Z_n \right\rangle + \left(\left. \frac{\partial Z_n}{\partial z} \right|_{z=-h} + \nabla Z_n \nabla h \right) Z_n(-h). \quad (30c)$$

The one-equation model

In the case of slowly varying bottom and current(s), a significant simplification of the above CMS (29) can be obtained by keeping only the propagating mode ($n=0$) in the local-mode series expansion of the wave potential (23), which essentially describes the propagation features. In this case, the above coupled-mode system is reduced to the following *one-equation model* on the horizontal plane,

$$a_{00} \nabla^2 \varphi_0 + \left[\mathbf{b}_{00} + \frac{2i\omega}{g} \mathbf{U} \right] \nabla \varphi_0 - \frac{1}{g} \nabla \cdot (\mathbf{U} [(\mathbf{U} \cdot \nabla) \varphi_0]) + \left[c_{00} + \frac{\omega^2 - \sigma^2}{g} + \frac{i\omega}{g} (\nabla \cdot \mathbf{U}) \right] \varphi_0 = 0. \quad (31)$$

The coefficients $a_{00}, \mathbf{b}_{00}, c_{00}$ are given by Eqs. (30) for $m=n=0$, and are calculated to be:

$$a_{00} = \int_{z=-h}^0 Z_0^2 dz = \frac{1}{2k_0} \tanh(k_0 h) \left(1 + \frac{2k_0 h}{\sinh(2k_0 h)} \right) = \frac{1}{g} CC_g, \quad (32a)$$

$$\mathbf{b}_{00} = \nabla a_{00} = \frac{1}{g} \nabla CC_g = 2 \langle \nabla Z_0, Z_0 \rangle + Z_0^2 (-h) \nabla h, \quad (32b)$$

$$c_{00} = k_0^2 a_{00} + \langle \nabla^2 Z_0, Z_0 \rangle + \nabla Z_0 \nabla h Z (-h) = k_0^2 a_{00} + c_{00}^{(2)}. \quad (32c)$$

We note here that the coefficient $c_{00}^{(2)} = \langle \nabla^2 Z_0, Z_0 \rangle + \nabla Z_0 \nabla h Z (-h)$ contains extra terms proportional to first and second horizontal derivatives of the depth function (proportional to bottom slope and curvature), as well as first and second horizontal derivatives of the horizontal current velocity components U_1 and U_2 . Using the above expressions of the coefficients in the one-equation model (31) and multiplying by g , it is easily seen that the latter takes the form

$$\nabla (CC_g \nabla \phi_0) - \nabla \cdot \{ \mathbf{U} [(\mathbf{U} \cdot \nabla) \phi_0] \} + 2i\omega \mathbf{U} \cdot \nabla \phi_0 + [k_0^2 CC_g + g c_{00}^{(2)} + \omega^2 - \sigma^2 + i\omega (\nabla \cdot \mathbf{U})] \phi_0 = 0, \quad (33)$$

which will be called the *modified mild-slope equation* for wave scattering by ambient current in general bottom topography. We note here that the model (33), in the case of no current ($U=0$), exactly reduces to the *modified mild slope equation* derived by Massel (1993) and Chamberlain & Porter (1995). Furthermore, it is worth noticing here that if the term $c_{00}^{(2)}$ is omitted, then Eq. (33) reduces exactly to the mild slope equation derived by Kirby (1984), in its time-harmonic form; see, e.g., Chen *et al* (2005).

NUMERICAL RESULTS AND DISCUSSION

In this section, numerical results are presented for two representative test cases corresponding to a rip current over a sloping beach in shallow water, and to a ring current in constant depth.

The case of rip current

Wave-induced rip currents, created by longshore currents converging into periodic rips and forming independent coastal circulation cells, play an important role in coastal morphodynamics. Also, rip currents, in conjunction with local amplification of wave energy, are responsible for many accidents in beaches. In order to illustrate the effects of a rip current, in conjunction with slow changes of the bathymetry, on the wave scattering, we examine a sloping beach of uniform slope 1/50. Using the similar expressions introduced by Chen *et al* (2005), the structure of the rip current $\mathbf{U} = (U_1, U_2)$ considered in this example is modelled as follows:

$$U_1 = -0.0681 x_1 F(x_1 / 76.2) F(x_2 / 7.62), \quad (34a)$$

$$U_2 = -0.256 \left[2 - (x_1 / 76.2)^2 \right] F(x_1 / 76.2) \int_{\tau=0}^{\tau=x_2/7.62} F(\tau) d\tau, \quad (34b)$$

where $F(\tau) = (2\pi)^{-1/2} \exp(-\tau^2 / 2)$.

The structure of the current is shown in Figs. 2 and 3, and, its maximum value is selected to be 0.5m/s. We consider unit-amplitude harmonic waves of period $T=14$ s (corresponding to a swell) propagating along the x_1 -axis (normally to the bottom contours). In this case, the phase velocity of the incident wave is $C=5.5$ m/s. The scattered wave field by the above configuration as calculated by means of the solution of the present modified mild-slope equation (using only one mode) is plotted in Fig.2a (phase) and Fig.3a (amplitude). The same result calculated using three

modes ($n = -1, 0, 1$) is comparatively plotted in Fig.2b (phase) and Fig.3b (amplitude). In the examined case, a 350m by 200m horizontal domain is considered, discretised by using 151 equidistant points along each horizontal direction. In this case, a significant focusing of wave energy as the shallow-end of the variable bathymetry region is approached is observed, taking place immediately shorewards the formation of the rip current. Also, in this area (where energy is maximized) the greatest differences between the one and three mode solution are observed. To illustrate the role and the relative significance of the various modes, the amplitudes of the propagating mode $\varphi_0(x, y)$, the first evanescent mode $\varphi_1(x, y)$ and the sloping-bottom mode $\varphi_{-1}(x, y)$, are plotted in Fig.4 a), b) and c), respectively. We observe in these figures that the main effects of wave refraction and diffraction are carried out by the propagating mode. This fact justifies the use of the simplified, one-equation MMS model to obtain approximate results. However, as shown by Athanassoulis *et al* (2003), the applicability of the latter model is restricted to slowly varying bottom topographies. Moreover, in Fig.4 we observe that the first evanescent mode $\varphi_1(x, y)$ is one order of magnitude less than the propagating mode. This mode is clearly connected with the non-horizontal part of the bottom. Furthermore, the sloping-bottom mode $\varphi_{-1}(x, y)$ is of the same order of magnitude, in the swallow area of the bottom.

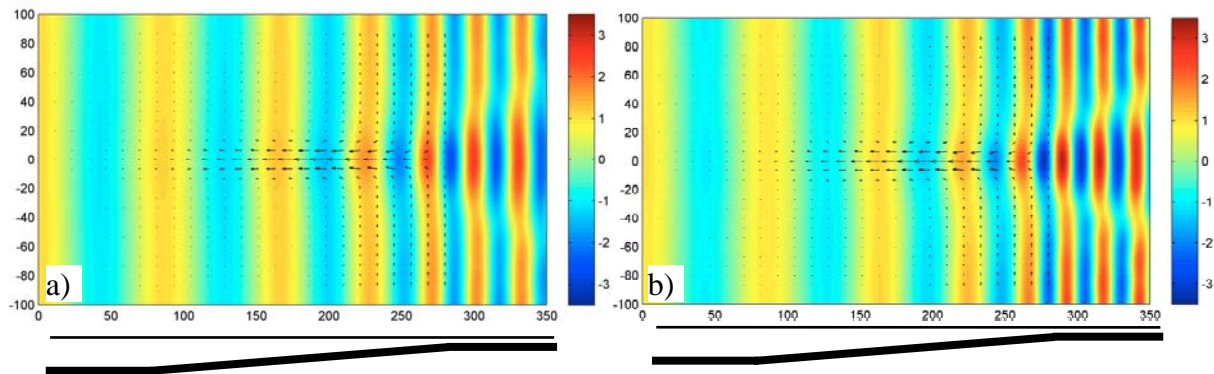


Figure 2 - Real part of the scattered wave field on the free surface by a rip current in a sloping (1:50) beach region: (a) 1 mode solution, (b) 3 mode solution.

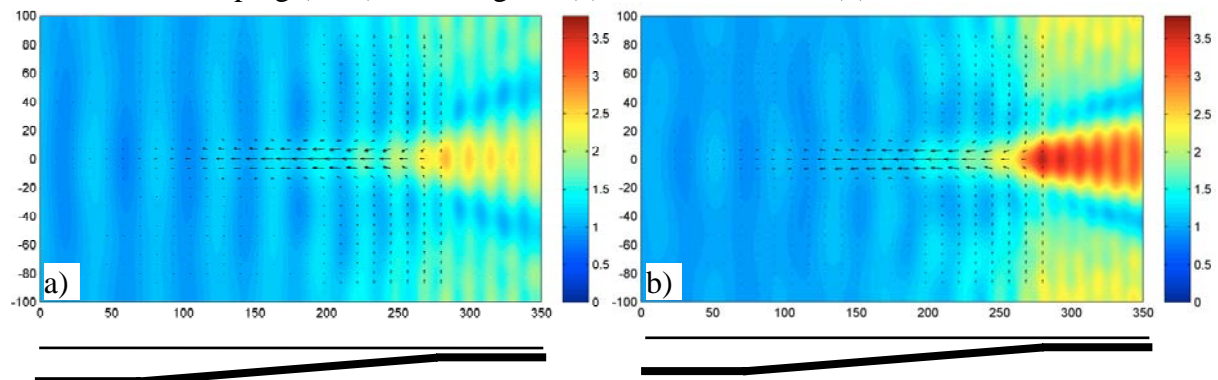


Figure 3 - Amplitude of the scattered wave field by a rip current in a sloping (1:50) beach region, with depths ranging from 4m to 0.5m: (a) 1 mode solution, (b) 3 mode solution.

The case of a ring current

In this example we consider wave scattering by a ring current in constant depth $h=10\text{m}$, examined also by Chen *et al* (2005). Such current structure is commonly seen in open sea and coastal areas, and has important impact on physical and biological processes; see Mapp *et al* (1989). Following Yoon & Liu (1989), the background current flow associated with the vortex

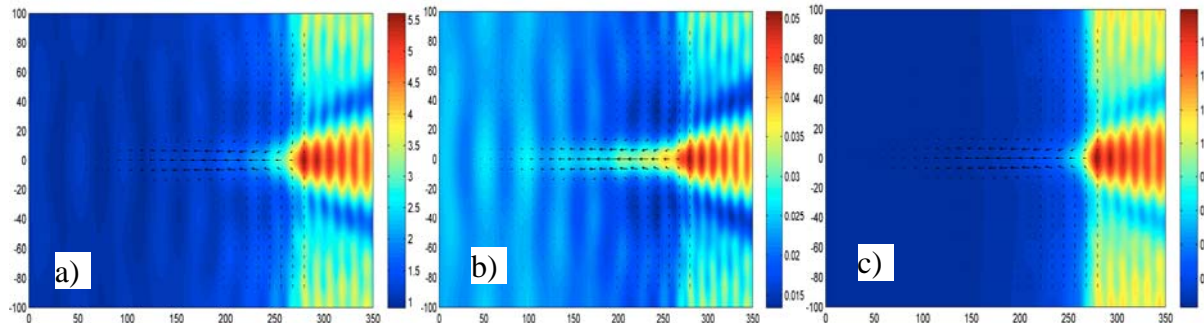


Figure 4 - Modal amplitudes of the scattered wave field by a rip current in a sloping beach region: (a) the propagating mode ($n=0$), (b) the first evanescent mode ($n=1$) and (c) the slopping bottom mode ($n=-1$).

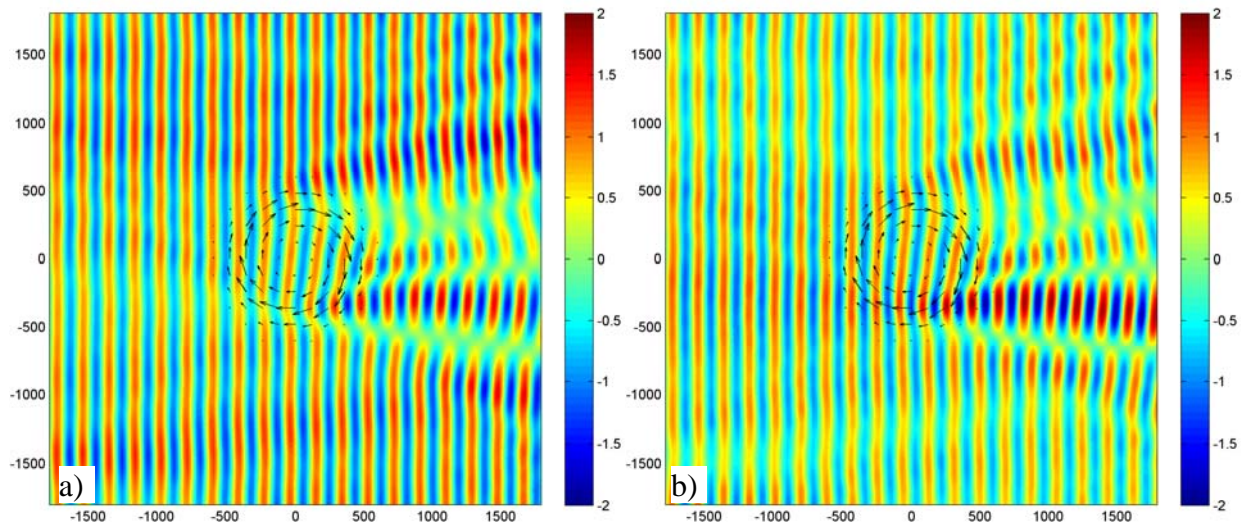


Figure 5 - Real part of the scattered wave field on the free surface: (a) 1 mode solution and (b) 3 modes solution.

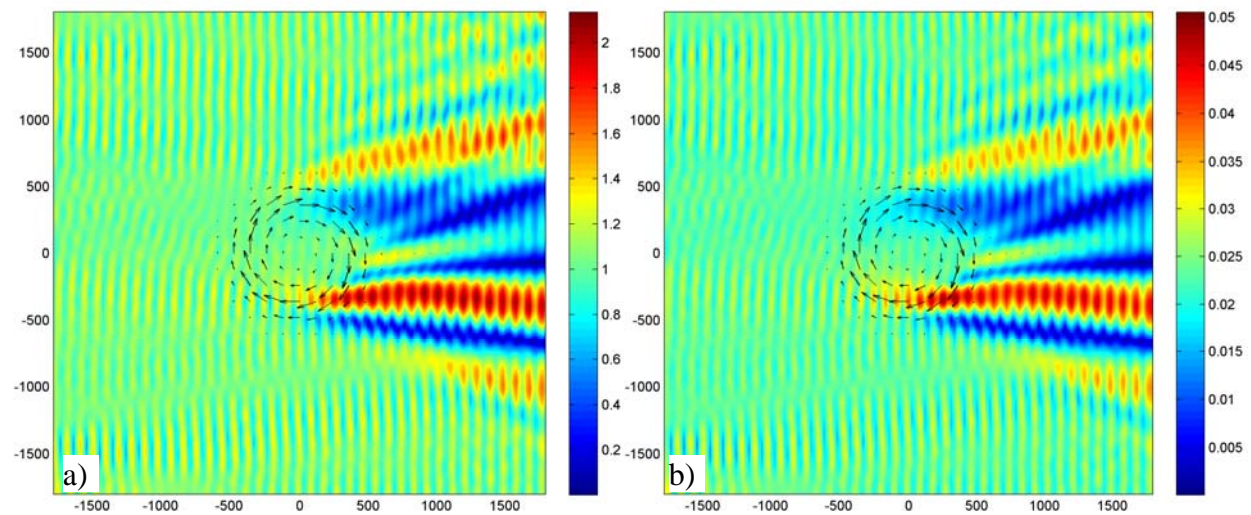


Figure 6 - Comparison of modal amplitudes: (a) the propagating mode ($n=0$), and (b) the first evanescent mode ($n=1$).

ring is defined by,

$$U_r = 0, \quad U_\theta = \begin{cases} C_5 (r/R_1)^N, & r \leq R_1 \\ C_6 \exp[-(R_2 - r)^2/R_3^2], & r \geq R_1 \end{cases} \quad (35)$$

where U_r and U_θ denote the radial and tangential components of the horizontal flow \mathbf{U} , in a cylindrical-polar coordinate system ($R = |\mathbf{x}|$, $\theta = \tan^{-1}(x_2/x_1)$) with origin at the center of the vortex ring. The following values of the parameters (see Mapp *et al* 1985) have been selected to describe the vortex-ring: $C_5 = 0.9$ m/sec, $C_6 = 1.0$ m/sec, $N = 2$,

$$R_1 = 343.706 \text{ m}, \quad R_2 = 384.881 \text{ m}, \quad R_3 = 126.830 \text{ m}.$$

The vortex ring creates a shearing current with maximum tangential velocity 1m/s, see Fig.5. We consider unit-amplitude harmonic waves of period $T=20$ s, propagating along the x_1 - axis, with phase velocity $C=9.74$ m/s, and scattered by the above vortex-ring current. In the examined case, a 2km by 2km horizontal domain is considered, which is discretised by using 201 equidistant points along each horizontal direction.

Numerical results obtained by the present model using one and three modes are shown in Fig.5 as concerns the real part of the wave field on the free surface. The focusing and defocusing of wave energy in the area downwave the vortex ring are well reproduced. In this case, the differences between the two solutions are very small, due to the fact that the bottom is flat, and thus, the slopping bottom mode is zero (by definition). This fact is clearly illustrated in Fig.6, where the amplitude of the propagating (Fig.6a) and the first evanescent mode (Fig.6b) are comparatively plotted. It is seen in this example that the first evanescent mode is one order of magnitude less than the propagating mode and thus, the one-mode solution obtained using the one-equation model Eq. (31) is an excellent approximation.

CONCLUDING REMARKS

A coupled-mode model for the wave-current-seabed interaction problem is presented, with application to wave scattering by ambient currents in variable bathymetry regions. Based on an appropriate variational principle, in conjunction with a rapidly-convergent local-mode series expansion of the wave potential in a finite subregion containing the current variation and the bottom irregularity, the present system can be considered as a generalization of the one derived by Athanassoulis & Belibassakis 2002 for the propagation of waves in variable bathymetry regions. The key feature of the present method is the introduction of an additional mode, describing the influence of the bottom slope, and accelerating the convergence of the local-mode series. If only the propagating mode is retained in the vertical expansion of the wave potential, the above coupled-mode system is reduced to the one-equation enhanced model called the *modified mild-slope equation for wave-current flow*, generalizing the corresponding mild-slope equation derived by Kirby (1984). Finally, the analytical structure of the present system facilitates its extension to various directions as, e.g., to non-linear wave-current scattering problems and more general current profiles.

ACKNOWLEDGMENTS

The present work has been supported by the Operational Program for Educational and Vocational Training II (EPEAEK II) and particularly the PYTHAGORAS II project. The project is co-funded by the European Social Fund (75%) and National Resources (25%).

REFERENCES

Athanassoulis, GA and Belibassakis, KA, 1999, A Consistent Coupled-Mode Theory for the Propagation of Small-Amplitude Water Waves over Variable Bathymetry Regions, *J. Fluid. Mech.*, 389, pp. 275-301.

- Athanassoulis G.A. and Belibassakis K.A., 2002, A Nonlinear Coupled-Mode Model for Water Waves over a General Bathymetry, *Proc. 21st Int. Conf. on Offshore Mechanics and Arctic Engineering, OMAE2002*, Oslo, Norway.
- Athanassoulis, G.A., Belibassakis, K.A., 2007, A coupled-mode method for non-linear water waves in general bathymetry with application to steady travelling solutions in constant but arbitrary depth, *Journal Discrete and Continuous Dynamical Systems DCDS-B*, pp. 75-84 (devoted to 6th Int. Conference on Dynamical Systems and Differential Equations, Poitiers, June 25-28, 2006).
- Athanassoulis, G.A., Belibassakis K.A. and Georgiou Y., 2003, Transformation of the Point Spectrum over Variable Bathymetry Regions, *13th Intern. Offshore and Polar Conference and Exhibition, ISOPE2002*, Honolulu, Hawaii, USA.
- Batchelor, G.K., 1967, *An Introduction to Fluid Dynamics*, Cambridge University Press.
- Belibassakis K.A. & Athanassoulis G.A., 2006, A Coupled-Mode Technique for Weakly Nonlinear Wave Interaction with Large Floating Structures Lying over Variable Bathymetry Regions, *Applied Ocean Research*, 28, pp. 59-76.
- Belibassakis, K.A., Athanassoulis, G.A. and Gerostathis Th.P., 2001, A Coupled-Mode Model for the Refraction-Diffraction of Linear Waves over Steep Three-Dimensional Bathymetry, *Applied Ocean Research*, 23 (6), pp. 319-336.
- Chamberlain, P.G. and Porter, D., 1995, The modified mild-slope equation, *J. Fluid Mech.*, 291, 393-407.
- Chen, W, Panchang, V and Demirbilek, Z., 2005, On the Modelling of Wave-Current Interaction Using the Elliptic Mild-Slope Equation, *Ocean Engin.*, 32, pp 2135-2164.
- Gerostathis, T., Belibassakis, K.A., Athanassoulis, G.A., 2008, A Coupled-Mode Model for the Transformation of Wave Spectrum over Steep 3d Topography. A Parallel-Architecture Implementation, *Journal of Offshore Mechanics and Arctic Engineering (JOMAE)*, 130.
- Jonsson, I.G., 1990, *Wave-Current Interactions*, In B. LeMehaute & D.M. Hanes (eds.) *The Sea*, 9(a), Ocean Eng. Sc., pp. 65-120, John Wiley, New York.
- Kirby, J.T., 1984, A note on linear surface wave - current interaction over slowly varying topography, *J. Geophysical Res*, 89, pp. 745-747.
- Lavrenov I.V. and Porubov A.V., 2006, Three Reasons for Freak Wave Generation in the Non-Uniform Current, *European Journal of Mechanics - B/Fluids*, 25, pp. 574-585.
- Liu, P.L.-F., 1990, Wave Transformation. In B. LeMehaute & D.M. Hanes (eds.) *The Sea*, 9(a), Ocean Eng. Sc., John Wiley, New York.
- Luke J.C., 1967, A Variational Principle for a Fluid with a Free Surface, *J. Fluid Mech.*, 27, pp. 395-397.
- Mapp, G.R., Welch, C.S., Munday, J.C., 1985, Wave Reflection by Warm Core Rings. *J. Geoph. Res.*, 90, 7153-7162.
- Massel, S.R., 1989, *Hydrodynamics of Coastal Zones*, Elsevier.
- Massel S. R., 1993, Extended refraction-diffraction equation for surface waves, *Coastal Eng.*, 19, 97-126.
- Mei, C.C., 1983, *The Applied Dynamics of Ocean Surface Waves*, John Wiley & Sons
- Peregrine, D.H., 1976, Interaction of Waves and Currents. *Adv. Appl. Mech.* 16, pp. 9-17.
- Thomas, G.P. and Klopman, G., 1997, Wave-Current Interaction in the Nearshore Region. In J.N. Hunt (ed.) *Gravity Waves in Water of Finite Depth*, Computational Mech. Publications.
- Yoon, S., Liu, P.L.-F., 1989, Interactions of Currents and Weakly Nonlinear Water Waves in Shallow Water. *J. Fluid. Mech.*, 205, 397-419.

KEYWORDS

Water waves in variable bathymetry, wave-current-seabed interaction.

KINETIC ENERGY APPROACH TO DISSOLVING MULTIPHASE PLUMES

Kristian Etienne Einarsrud¹ and Iver Brevik²

¹Department of Physics, NTNU, Trondheim, Norway

²Department of Energy and Process Engineering, NTNU, Trondheim, Norway

ABSTRACT

In the present work an alternative to the entrainment hypothesis description of buoyant plumes is given. The model is presented is an integral plume model based on conservation of mass, momentum and kinetic energy and is thus denoted as a “kinetic energy approach”.

The kinetic energy approach introduces an unknown variable I , being dependent on turbulent correlations and is thus denoted as the “turbulent correlation parameter”. In the present work a simple correlation between the turbulent correlation parameter I , initial mass-fluxes Q_0 and depth of release D is given as a closure model.

The kinetic energy approach is compared to experiments, yielding satisfactory results, both in the case of I determined from experimental data and in the case when I is determined from the correlation between mass-flux and release depth.

INTRODUCTION

The motivation for studying bubble plumes is evident, from the fact that these plumes are encountered in a variety of engineering problems. To mention a few, plumes have been used to damp sea waves in harbours (pneumatic breakwaters), to prevent surface ice formation in harbours, to mix stratified fluid layers, to re-aerate lakes, and finally to protect installations from shock waves produced by underwater explosions (cf., for instance, Bhaumik, 2005).

With increasing sub-sea activities plumes have acquired increased importance from a risk assessment point of view. It becomes imperative to obtain knowledge about the implications of a rupture, or even a breakage, of a sub-sea pipeline. Thus in case of an underwater blowout of inflammable gas, one wishes answers to the following questions:

- What is the concentration of gas at the free surface?
- What is the extension of the area covered by gas at the surface?
- What is the rising time of the gas?

The aim of the present work is to provide a theoretical framework from which answers to these questions can be given, in a quick and reasonably accurate way.

MODEL FORMULATION

The model used to describe the dissolving plume is based on Brevik and Killie's (1996) model of axisymmetric air-bubble plumes and uses a sub-model based on the semi-empirical Ranz-Marshall equation to predict the dissolution of the gaseous phase, similar to the approach used by Wüest et al. (1992) to describe dissolving plumes with the entrainment hypothesis.

The model is based on a mixed-fluid formalism and is used to describe a simple bubble plume in the zone of established flow.

The goal of the model is to predict the width and rise time of the air-bubble plume, as well as the quantity of gas at the surface when it is released from a depth D below the still water surface. The origin is taken to be at the source, with the z -axis pointing towards the surface.

Main assumptions

- The ambient fluid is unstratified and stagnant, meaning that all ambient properties (temperature, density etc) are taken to be constant and that cross-flows are not present.
- The Boussinesq assumption is used, meaning that the gas density is negligible when compared to the ambient density in all terms except for buoyancy. This implies that the void fraction is negligible when compared to hold-up.
- Mass transfer is assumed to be described by the mean bubble size.
- On average, the number of bubbles is assumed constant, implying that coalescence and break-up of bubbles is in equilibrium.
- Bubble expansion is assumed to be isothermal and the gas is assumed to be ideal.
- The solubility of the gas is assumed to be determined by Henry's law.
- The plume is assumed to be fully turbulent and viscous stresses are assumed to be negligible when compared to turbulent stresses.
- Lateral variations of the Reynolds-stresses are assumed to be dominating.
- Turbulent correlations are assumed to be self-preserving (as described by Tennekes and Lumely (2001)).
- The plume is assumed to be self-similar within the zone of established flow and relevant properties are assumed to be described by Gaussian distributions.

Mass transfer

The rate of mass transferred from the dispersed phase to the ambient fluid can be described by the semi-empirical Ranz-Marshall equation, relating the change in the mass of one bubble to its size and the solubility of the gas in question. Combining the Ranz-Marshall equation with the assumption of isothermal expansion yields a differential equation for the bubble radius of the form:

$$\frac{dr_b}{dz} = -\frac{Kp'_{atm}(c_s - c_i)}{u_{zb}\rho_{gs}(D' - z)} + \frac{r_b}{3(D' - z)} \quad (1)$$

where r_b is the mean bubble radius, K is the mass transfer coefficient, p'_{atm} is the atmospheric pressure expressed as the head of a water column, c_s is the solubility of the gas in ambient, c_i is the in situ concentration of gas (i.e. the concentration of dissolved gas in the ambient), u_{zb} is the vertical bubble velocity, ρ_{gs} is the density of gas at the surface, $D' = D + p'_{atm}$ and D is the depth of release. Dissolution thus acts against the expansion, reducing the bubble radius and thus reducing the buoyancy of the flow.

Momentum equation

As the plume is assumed to be fully turbulent, a RANS approach is chosen to describe the flow of the plume. In the RANS (Random Averaged Navier-Stokes) approach the velocity field u of the Navier-Stokes equation is decomposed into an average and fluctuating part, e.g.:

$$u = \bar{u} + u' \quad (2)$$

before averaging the equation, as described in for instance in Davidson (2006). The averaging process yields an unknown term dependent on the velocity fluctuations and is denoted as a Reynolds-stress tensor.

The momentum equation obtained by using the assumptions sketched earlier is given as:

$$\frac{\partial}{\partial z} \bar{u}_z^2 + \frac{1}{r} \frac{\partial}{\partial r} (r \bar{u}_r \bar{u}_z) = \alpha_g g + \frac{1}{\rho_w r} \frac{\partial}{\partial r} (r \tau_{rz}) \quad (3)$$

where overlined quantities represent mean values, α_g is the void fraction and τ_{rz} is the Reynolds-stress tensor. The RANS equation is integrated over a cylindrical control volume with radial boundaries taken at infinity in order to obtain an integral plume model.

In order to advance further, assumptions must be made on the distribution of velocity and void fraction over the cross section of the plume. Using the self-similarity assumption the plume velocity and void fraction (represented by a number-density) are modelled by Gaussian distributions of the form:

$$\bar{u}_z(r, z) = u_c(z) e^{-\frac{r^2}{2\sigma^2}} \quad (4)$$

and

$$\rho_n(r, z) = \rho_{nc}(z) e^{-\frac{r^2}{2\lambda^2\sigma^2}} \quad (5)$$

where u_c and ρ_{nc} represent centreline values of the vertical velocity and number density of bubbles, respectively. $\sigma = \sigma(z)$ represents the typical width of the plume and λ is a number smaller than unity representing the relative width between the inner bubble core and upward water flow.

Insertion of the Gaussian distributions and integration of the RANS equation finally yields the momentum flux equation, stated as:

$$\frac{d}{dz} u_c^2 \sigma^2 = \frac{g V_b N (1 + \lambda^2)}{\pi [u_c + u_s (1 + \lambda^2)]} \quad (6)$$

where V_b is the volume of a single bubble, N is the number flux of bubbles and u_s is the slip velocity of the bubbles (assumed to be a function of the bubble radius r_b)

Kinetic energy equation

Multiplication of RANS equation with the vertical velocity component u_z , insertion of Gaussian distributions and integration over the mentioned control volume yields the following equation for the flux of kinetic energy:

$$\frac{d}{dz} u_c^3 \sigma^2 = \frac{3}{\pi} \frac{g V_b N u_c}{u_c + u_s (1 + \lambda^2)} - u_c^3 \sigma I \quad (7)$$

where

$$I = 6 \int_0^\infty f \eta^2 e^{-\frac{1}{2} \eta^2} d\eta \quad (8)$$

is an unspecified constant to be determined from experiment. The turbulent correlation parameter I arises from the assumption of that the Reynolds-stresses are self-preserved, as discussed in Tennekes and Lumley (2001).

METHOD OF SOLUTION

The three given differential equations form a closed set given that u_s , λ and I can be determined from experiment and that initial conditions for u_c , σ and r_b are provided.

In the present formalism the slip velocity u_s is determined from curve fittings to experimental data of Haberman and Morton (1954), allowing for variable slip velocities as the radii of bubbles change.

Various values for the relative distribution width λ exist in the literature. However, a value of 0.8 is used in the comparative study of existing models conducted by Bhaumik (2005), yielding good results. The value of 0.8 is also used by Milgram (1983) when comparing his experiments to theory. As the experiments of Milgram (1983) form the basis for comparison between the present model and experiment, $\lambda = 0.8$ is used in the kinetic energy approach as well.

The turbulent correlation parameter can either be determined from a turbulence model or from experiments. The latter approach is used in the present formulation, where the optimal value of I is determined from experiments of Milgram (1983) and Fanneløp & Sjøen (1980) (data reproduced in Milgram (1983) is used). Four different initial flow rates Q_0 were used, varying from 0.0312 kg/s to 0.767 kg/s.

The model equations are solved with I as a free parameter, and I is varied until good accordance with the experimental data for the centerline velocity u_c and plume width b is obtained. The plume width b is defined as:

$$b = \sqrt{2} \sigma \quad (9)$$

Samples of the analysis of the data of Milgram (1983) are given in the following figures:

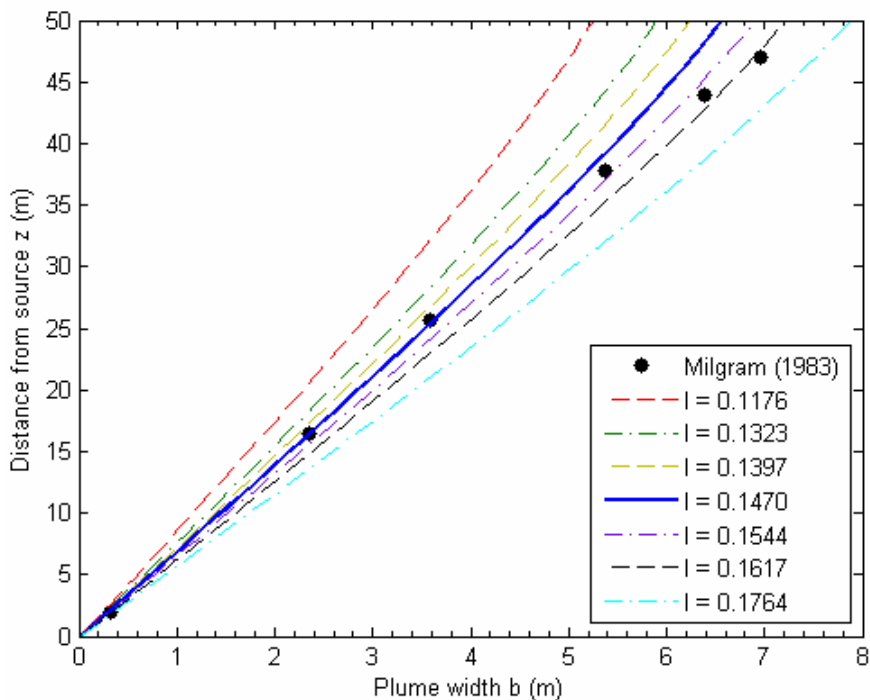


Figure 1: Determination of optimal I from plume width b , $Q_0 = 0.3679\text{kg/s}$. Solid line shows optimal fit for the given mass rate (based on optimum for b and $u=u_c$), while dashed lines show results when I is chosen up to 20% from optimum.

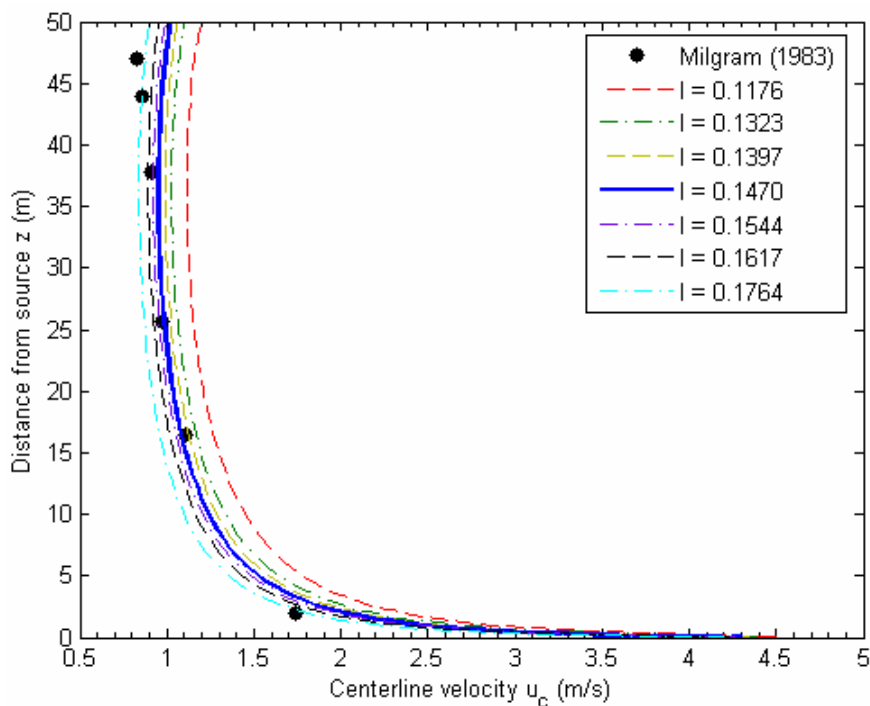


Figure 2: Determination of optimal I from centreline velocity u_c , $Q_0 = 0.3679\text{kg/s}$. Solid line shows optimal fit for the given mass rate (based on optimum for b and $u=u_c$), while dashed lines show results when I is chosen up to 20% from optimum.

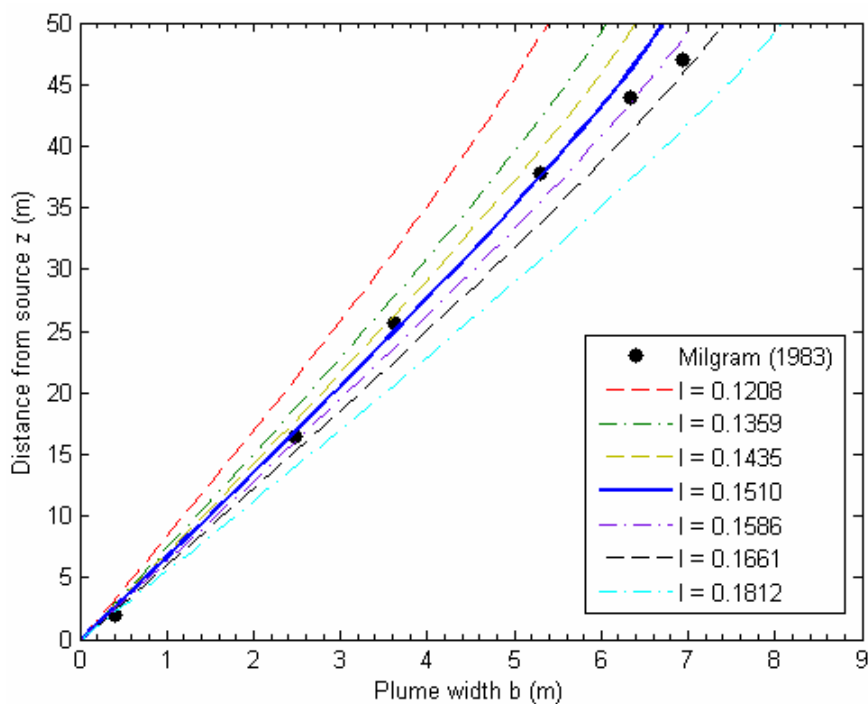


Figure 3: Determination of optimal I from plume width b , $Q_0 = 0.7670$ kg/s. Solid line shows optimal fit for the given mass rate (based on optimum for b and $u=u_c$), while dashed lines show results when I is chosen up to 20% from optimum.

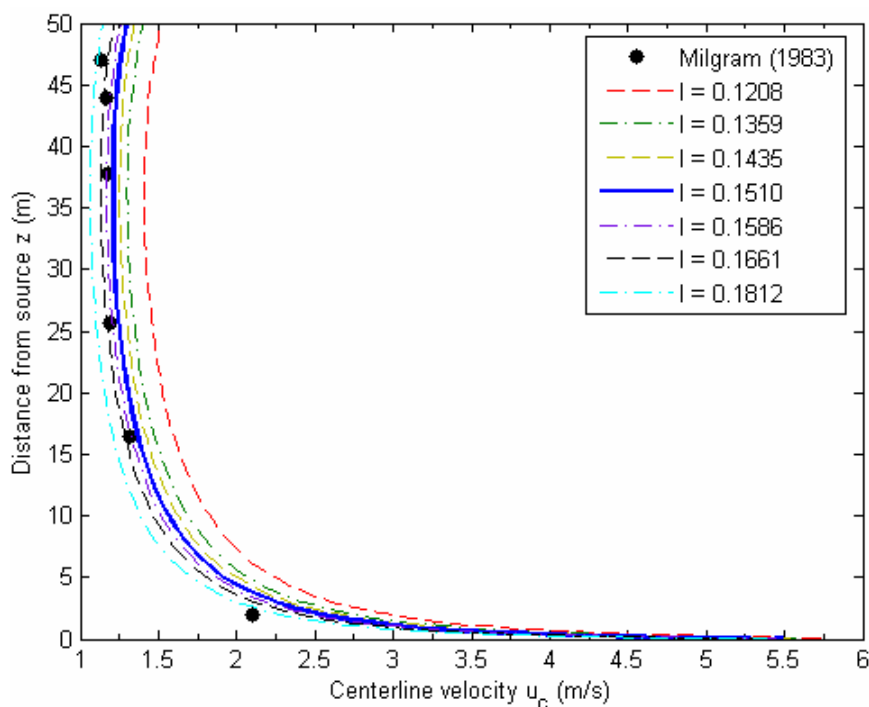


Figure 4: Determination of optimal I from centreline velocity u_c , $Q_0 = 0.7670$ kg/s. Solid line shows optimal fit for the given mass rate (based on optimum for b and $u=u_c$), while dashed lines show results when I is chosen up to 20% from optimum.

As figures 1 to 4 show, a good fit between theory and experiment is obtained if I is given an optimal value. The same analysis is conducted with the experiments of Fanneløp & Sjøen (1980) yielding a good fit for the plume width, but systematically over-predicting centreline velocities. This apparent discrepancy is believed to be due that the initial conditions for the centreline velocities are based on the assumption that the plume is not constrained by walls, as in the experiments of Milgram (1983). Overall results from the determination of I are given in tables 1 and 2.

Table 1: Key results from calibration from Milgram (1983). Four initial release rates Q_0 are investigated from a release depth D of 50 m. The table gives relevant quantities for simulations done with optimal values for I (I_{opti}) chosen. The mean centerline velocity \bar{u}_c is calculated from the depth of release ($D=50$ m) divided by the total rise time t_{rise} .

Q_0 (kg/s)	Q_{surf} (kg/s)	b_{surf} (m)	t_{rise} (s)	\bar{u}_c (m/s)	I_{opti} (-)
0.031	0.027	3.37	67.50	0.74	0.075
0.153	0.137	4.60	47.90	1.04	0.102
0.368	0.331	6.60	45.50	1.10	0.147
0.767	0.703	6.73	35.00	1.39	0.151

Table 2: Key results from calibration from Fanneløp and Sjøen (1980). Four initial release rates Q_0 are investigated from a release depth D of 10 m. The table gives relevant quantities for simulations done with optimal values for I (I_{opti}) chosen. The mean centerline velocity \bar{u}_c is calculated from the depth of release ($D=10$ m) divided by the total rise time t_{rise} .

Q_0 (kg/s)	Q_{surf} (kg/s)	b_{surf} (m)	t_{rise} (s)	\bar{u}_c (m/s)	I_{opti} (-)
0.007	0.006	1.00	12.80	0.78	0.100
0.013	0.013	1.19	11.30	0.89	0.120
0.019	0.019	1.24	10.10	0.99	0.125
0.029	0.028	1.39	9.50	1.05	0.140

Brevik and Killie (1996) point out that the turbulent correlation parameter I in general could be a function of the initial mass flux Q_0 and depth of release D . Tables 1 and 2 show that the value of I increases with increasing Q_0 . However, even though the values of Q_0 in table 2 are significantly lower than in table 1, the optimal values of I are similar. This suggests that decreasing values of D yield increasing values of I .

I is a dimensionless quantity, however it is not possible to combine D and Q_0 into a dimensionless group. This suggests the presence of some other parameter also influencing the turbulent correlations. A natural choice is the viscosity coefficient μ . Even though viscosity is neglected in the governing equations, it is still important for damping out turbulence at small scales. The following dimensionless group can be constructed based on the three mentioned parameters:

$$\text{Re}_E = \frac{Q_0}{D\mu} \quad (10)$$

In order to make predictions for an arbitrary value of Re_E , the values of I presented in tables 1 and 2 are fitted to a function of the form

$$I = a \cdot \ln(Re_E) + b \quad (11)$$

where a and b are model constants. The function is chosen because of its relatively simple form and its ability to qualitatively reproduce the behaviour observed. A least square scheme is adopted for determining the constants, yielding

$$I = 0.0219 \ln(Re_E) + 0.1010. \quad (12)$$

A plot of the least square fit and optimal values determined from experiment is shown in figure 5.

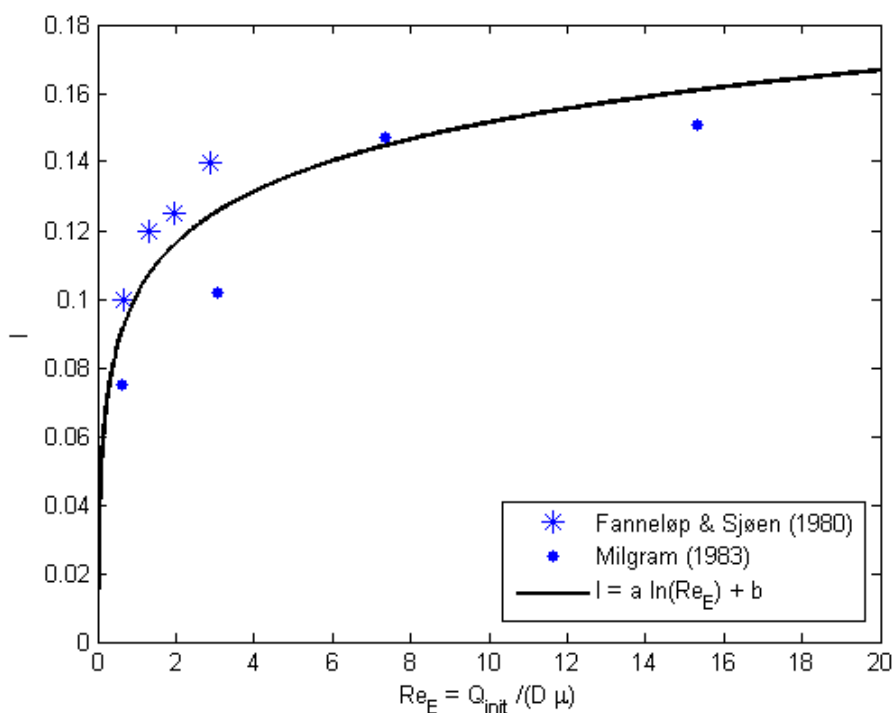


Figure 5: Least square fit for relation between I and Re_E . Solid circles show values for I obtained from the experimental data of Milgram (1983) and stars values for I obtained from experimental data of Fanneløp and Sjøen (1980). Solid line shows the least square fit to a function of the form $I = a \ln Re_E + b$.

RESULTS

The model presented together with the least square fit for I , forms a closed set of equations suitable for predicting plume parameters. In the following figures, the kinetic energy approach is compared to a simple model for the plume width b , based on the entrainment hypothesis:

$$b(z) = \alpha z + r_0 \quad (13)$$

where α is the entrainment coefficient and r_0 is the diffuser radius. The experiments of Milgram and Van Houten (1982) (data reproduced in Milgram (1983)) are used as a basis for comparison. The entrainment coefficient α is chosen as a mean of the optimal values determined from experiments in Milgram (1983). Results from the entrainment model are expected to yield a better fit, as the entrainment coefficient is chosen from optimal values, whereas the turbulent correlation parameter I is determined from equation 10.

Results are presented in figures 6 and 7.

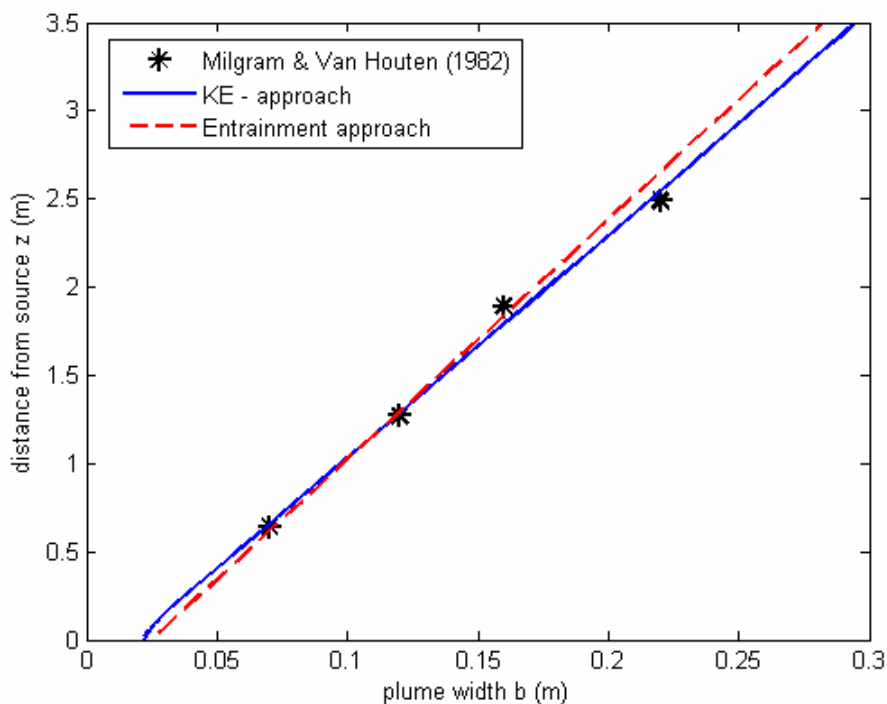


Figure 6: Comparison of models, $Q_0 = 0.00153$ kg/s. Points show experimental data of the plume width b (Milgram and Van Houten (1982)). The blue solid line shows predictions of plume width based on the kinetic energy approach whereas the red dashed line shows the same predictions based on the entrainment hypothesis.

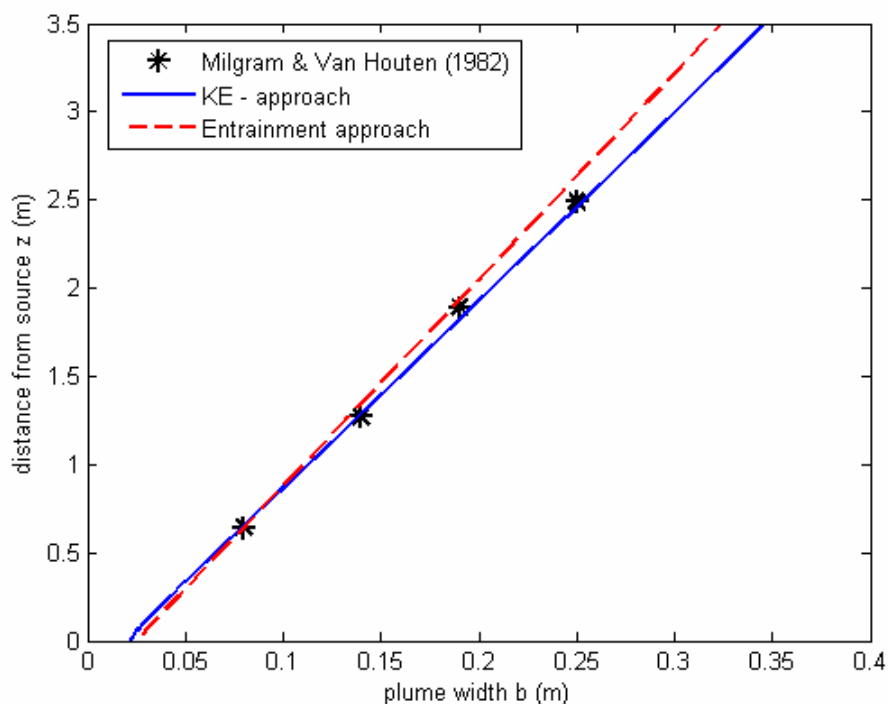


Figure 7: Comparison of models, $Q_0 = 0.00304$ kg/s. Points show experimental data of the plume width b (Milgram and Van Houten (1982)). The blue solid line shows predictions of plume width based on the kinetic energy approach whereas the red dashed line shows the same predictions based on the entrainment hypothesis

IMPORTANCE OF DISSOLUTION

In order to investigate the robustness of the model, a sensitivity analysis of critical parameters is conducted. In the sensitivity analysis the effects of parameter variation on the plume width b , mass-flux at the surface Q_{surf} and the mean centerline velocity \bar{u}_c are investigated.

The prediction of the mass-flux of the dispersed phase is found to be relatively robust. Some variation (1%) is found when varying the bubble radius, (smaller bubbles yielding more dissolution) and when varying the molecular diffusivity (larger diffusivities yielding more dissolution). These findings are in accordance to those found by Wüest (1992). The width of the plume b and mean centerline velocity \bar{u}_c show little sensitivity to these parameters, suggesting that the dissolution itself has little influence on the other plume properties, as long as the dissolution is moderate.

Dissolution becomes important in the three following cases:

- Small bubble sizes
- Small release rates
- Large depths of release

CONCLUDING REMARKS

The kinetic energy approach to buoyant plumes of Brevik and Killie (1996) is compared to experiments carried out by Milgram (1983) and is found to reproduce experimental data with satisfactory accuracy. The suggest that the model presented yields a good starting point for the description of the dynamics and dissolution of gas in the zone of established flow for an air-bubble plume, given that the turbulent correlation parameter I is chosen correctly.

With the comparison between model and experiment, a simple relation between the turbulent correlation parameter I , the initial rate of release Q_0 , depth of release D and the viscosity μ is identified.

Comparison with experiments and models based on the entrainment coefficient show that a value of I determined from the simple relation

$$I = 0.0219 \ln(\text{Re}_E) + 0.1010 \quad (14)$$

yields satisfactory predictions.

The benefit of models based on the entrainment hypothesis is that the concept is relatively well understood and implemented for various uses, yielding satisfactory results. The major drawback of the approach is the difficulty of determining the value of the entrainment coefficient from parameters which are simple to measure.

Besides being relatively simple to implement, having fast convergence and promising accuracy when compared to experiments, the idea of using a conservation equation for the kinetic energy is especially interesting from a physical point of view, as it provides insight into the physics driving the plume. The mathematical framework needed is somewhat more complicated, but more physics are contained in the model. Another positive aspect of the kinetic energy approach is that the unknown turbulent correlation parameter I can be determined from parameters which are easily accessible.

A combination of the simplicity of the entrainment hypothesis and the solid physical grounds of the kinetic energy approach should be sought in order to develop state of the art tools for future risk management of sub-sea gas releases, exploiting the benefits of both approaches.

REFERENCES

- Bhaumik T. 2005. *Numerical Modeling of Multiphase Plumes: A Comparative Study Between Two-Fluid and Mixed-Fluid Integral Models*, MSc Thesis, Texas A&M University, 148p.
- Brevik I. and Killie R. 1996. Phenomenological Description of Axisymmetric Air-Bubble Plume. *International Journal of Multiphase Flow*, vol. 22, No. 3, pp 535 - 549.
- Davidson P. A. 2006. *Turbulence: An Introduction for Scientists and Engineers*. Oxford University Press, 657p.
- Fanneløp T. K. and Sjøen K. 1980. Hydrodynamics of Underwater Blowouts, *Prox. AIAA 18th Aerospace Sci. Meeting*.
- Haberman W. L. and Morton R. K. 1954. An Experimental Study of Bubbles Moving in Liquids, *Proceedings of American Society of Civil Engineering*, vol. 80, pp 379 – 427.
- Milgram J.D. 1983. Mean Flow in Round Bubble Plumes, *Journal of Fluid Mechanics*, vol. 133, pp 345 – 346.
- Milgram J. H. and Van Houten R. J. 1982. Plumes from Sub-Sea Well Blowouts. *Proceedings of the 3rd International Conference BOSS*, vol. 1, pp 650 – 684.
- Ranz W. E. and Marshall W. R. Jr. 1952. Evaporation from Droplets, Parts I & II. *Chemical Engineering Progress*. vol. 48, pp 173 – 180.
- Tennekes H. and Lumley J. L. 2001. *A first course in turbulence, Eighteenth printing*. The MIT press, 300p.
- Wüest A., Brooks N. H. and Imboden D. M. 1992, Bubble Plume Modeling for Lake Restoration, *Water Resources Research*, vol. 28, no. 12, pp 3235 – 3250.

KEYWORDS

Multiphase Plumes, Plumes, Turbulence

SENSITIVITY OF SHIP MOTIONS TO SEA BOTTOM MODELLING

Frøydis Solaas¹ and Ivar Fylling¹
¹Marintek AS, Trondheim, Norway

ABSTRACT

The effect of different bottom models on the motions of tankers moored at a jetty is studied by use of the potential theory panel program WAMIT5.3. The bottom is represented by a separate fixed panel body in the analysis in addition to the panel model of the free floating ship. To the authors' knowledge no validation of such modelling has been published. Therefore a parameter study was carried out, in order to provide basis for a partial validation. Seven different representations of the bottom topography were studied for two tankers in ballast and loaded conditions. Emphasis was on the sway motion of the tankers, since this was the most important response for dynamic mooring line and fender loads for the studied case. The study shows that the choice of model representing the sea bottom in front of the jetty has a considerable influence on the calculated response characteristics for the ship. When modelling the bottom with a fairly realistic topography the horizontal motion responses are larger than in a flat bottom finite water depth case, but smaller than if the bottom topography were assumed to be represented by a plane slope.

INTRODUCTION

Ormen Lange is the second largest gas field on the Norwegian Continental Shelf and currently ranks as the largest development in the European offshore arena. Norsk Hydro has been responsible for developing the gas field, while Shell is taking over as operator.

The gas from the field is processed onshore at the Nyhamna Process Plant, and one of the export products is condensate which is loaded on 30.000 to 100.000 DWT tankers at a jetty. The jetty area is exposed to ocean waves from northwestern sector, with up to 1 m significant wave height, and peak periods in the range of 10 - 15 sec. These deep water waves, coming towards the steep beach, are a challenge for berthed tankers, and may influence the availability of the jetty.

The bottom topography in the jetty area is typical for the Norwegian coast, with relatively "uneven" and steep slopes that make wave propagation and wave response predictions relatively complicated. Simplified representation of the sea bottom in hydrodynamic simulations with the potential theory panel program WAMIT5.3, Fylling (2005) gave large responses, compared to a finite water depth case. The results from the study were used to estimate availability of the berth, and calculations showed that it could be expected that during winter the availability of the product jetty would be low and the mooring system specification was revised to allow larger ship motions. This was studied further in Fylling (2006) where different and more refined panel models representing the sea bottom in front of the jetty were developed and the response characteristics for a tanker calculated for the different bottom models.

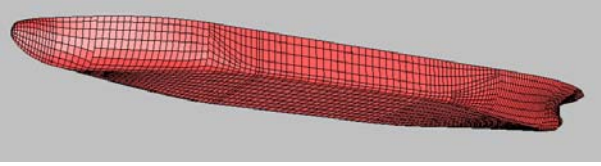
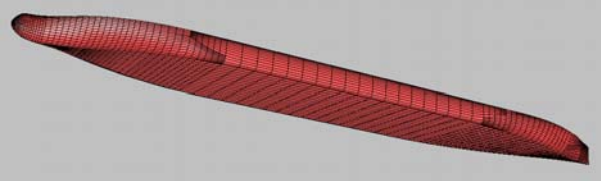
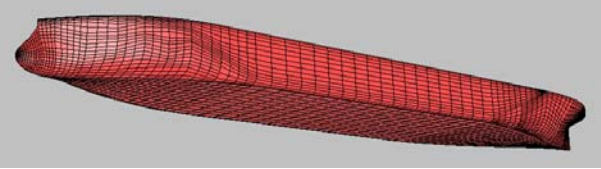
HYDRODYNAMIC MODEL DESCRIPTIONS AND CALCULATIONS

The radiation-diffraction program WAMIT5.3 (1995) is used to calculate the hydrodynamic properties of two tankers located above different representations of the Nyhamna bottom topography. Linear potential theory is used in WAMIT, which means that small amplitudes and

motions are assumed. The multi-body option in WAMIT is used, where the ship and the bottom is represented as two bodies in the analysis. The ship is modelled as a free floating body and the bottom as a fixed body. In the present case, with nearly beam sea waves and long wave periods, the slow drift second order force is of minor importance compared with the first order forces. Therefore the second order potential solution is not considered in these analyse.

Calculations were performed for a condensate tanker with length 172 m, breadth 32 m and a fully loaded displacement of 49.000 m³, and for a lager tanker with length 232 m and breadth 42 m in full-load and ballast conditions, with displacement 120.000 m³ and 60.000 m³, respectively. The different panel models of the ships are described and shown in Table 1

Table 1 – Description of ship models.

Ship model	Description	
cond_fulload.gdf 	Lpp = 172 m B = 32 m D = 11 m KG = 10.14 m R _{ROLL} = 11.6 m R _{PITCH} = 41.3 m R _{YAW} = 41.3 m	Condensate tanker Loaded condition Volume = 49310 m ³ C _B = 0.81 Total number of elements: 3198
tanker_ballast.gdf 	Lpp = 232 m B = 42 m D = 7.5 m KG = 8.4 m R _{ROLL} = 16.6 m R _{PITCH} = 66.8 m R _{YAW} = 67.7 m	Tanker Ballast condition Volume = 59900 m ³ C _B = 0.82 Total number of elements: 4438
tank_loaded.gdf 	Lpp = 232 m B = 42 m D = 14.3 m KG = 12.3 m R _{ROLL} = 13.2 m R _{PITCH} = 54.3 m R _{YAW} = 55.0 m	Tanker Loaded condition Volume = 118850 m ³ C _B = 0.85 Total number of elements: 4466

The Nyhamna bottom topography is shown in Figure 1. The different bottom models are described in Table 2. In addition to analysis with panel models of the bottom, analyses were run for deep water and for finite water with constant depth 35 m. The depth of 35 m is chosen as representing the water depth at the location of the ship centre when moored at the berth.

The wedge shaped bottom model no. 1 and the bottom model of the Nyhamna bottom topography, bottom model no. 5, are shown together with the loaded tanker in Figures 2, 3 and 4. All of the bottom panel models have a length equal to 400 m, 2.3 times the shortest ship and 1.7 times the longest.

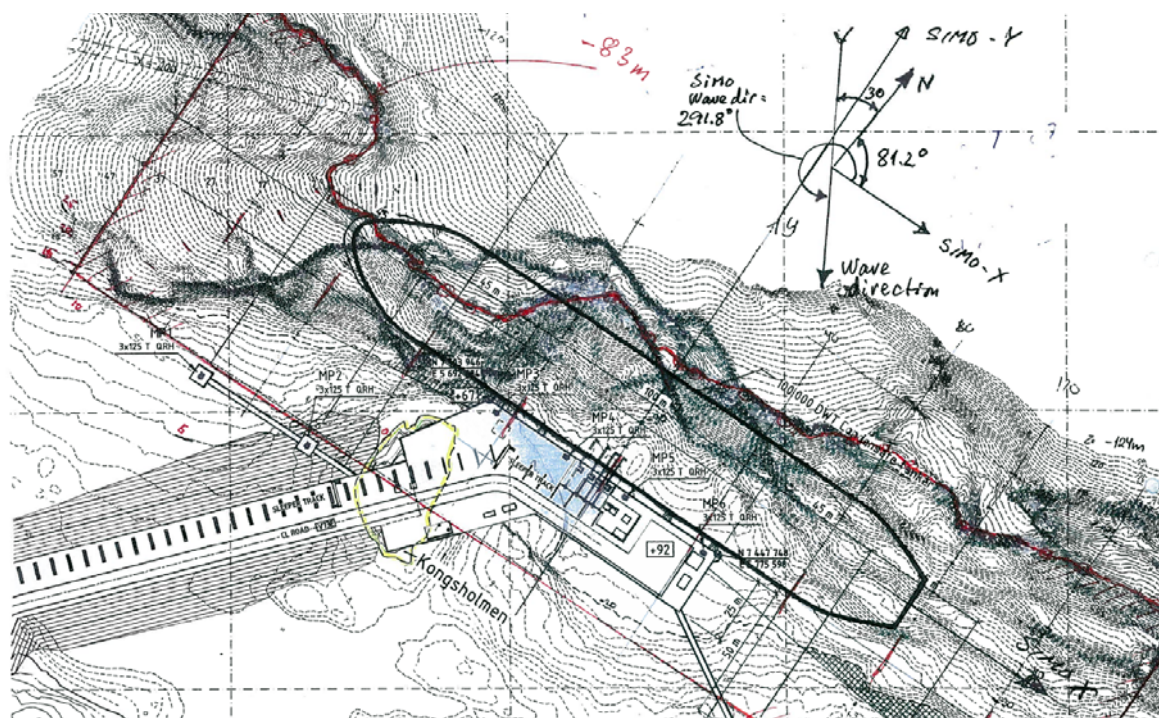


Figure 1 –Location map with bottom topography with 1 m equidistance.
The 83 m depth contour is marked in red the ship in black.

Table 2 – Description of bottom models.

Name	Description
Deep water	No bottom effect included.
Finite water depth	Finite water analysis option with constant water depth 35 m. No panel model to represent the bottom effect.
Bottom 1: Wedge 	Triangular profile with plane slope from -5 to -50 m depth. Profile breadth 95 m. Water depth 50 m.
Bottom 2: Flat top box 	Rectangular profile modeled as a flat box from -35 to -50 m depth. Profile breadth 95 m. Water depth 50 m.
Bottom 3: Wedge 	Triangular profile with plane slope from -2 to -50 m depth. Profile breadth 101.33 m. Water depth 50 m.
Bottom 4: Composite wedge 	Bottom represented by 3 profiles from -2 to -70 m depth and -18 to -70 m depth. Profile breadth 60 to 120 m. Water depth 70 m.
Bottom 5: Nyhamna 	Fairly realistic bottom topography. 11 profiles with 40 m spacing. Water depth 83 m.

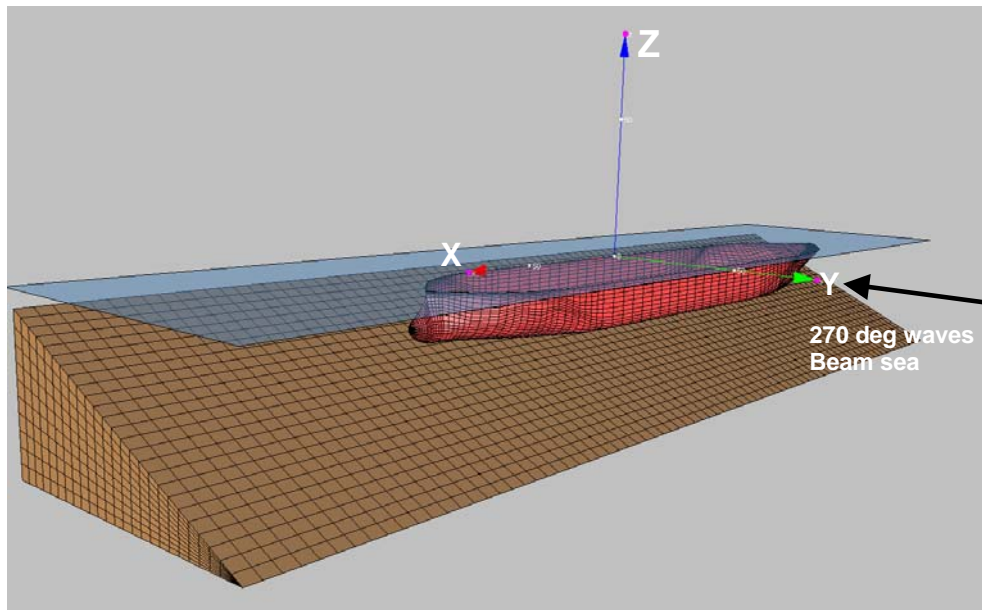


Figure 2 – Loaded tanker and bottom modelled as a triangular profile (Bottom1).

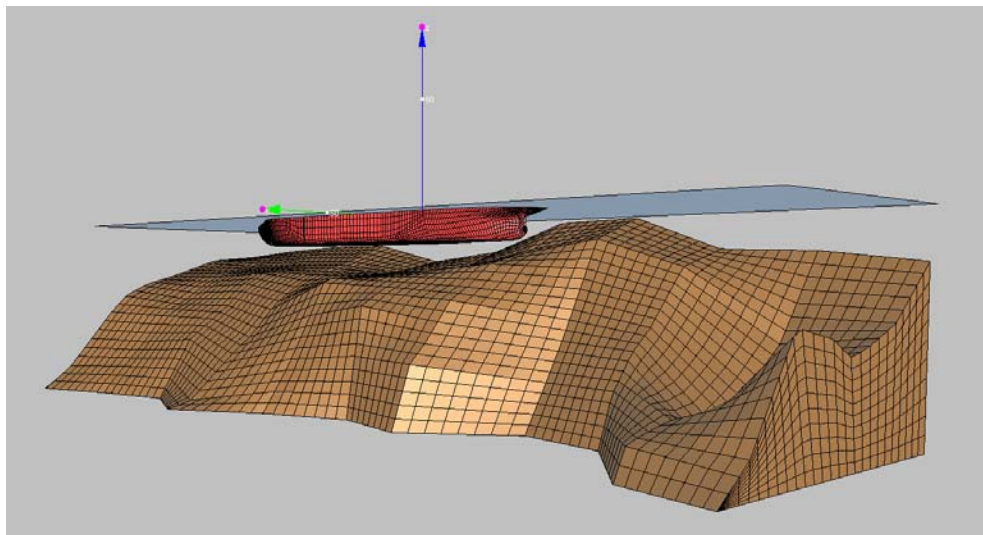


Figure 3 – Loaded tanker and model of Nyhamna bottom topography to 83 m depth (Bottom5), fish view, seen from NW.

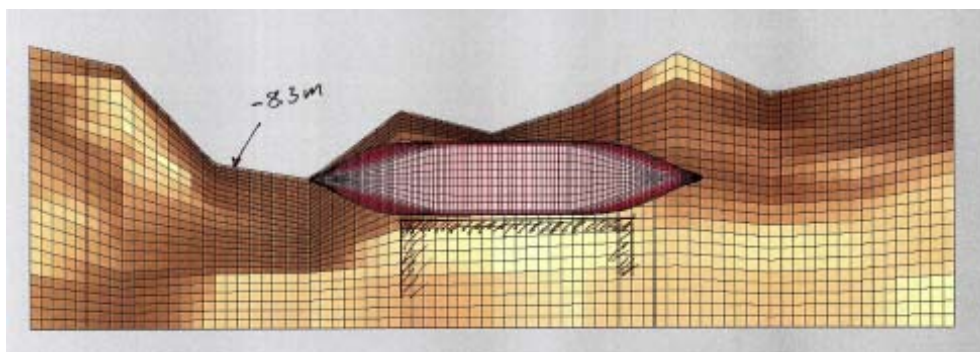


Figure 4 – Bird's view of the model of Nyhamna bottom topography to 83 m depth (Bottom 5). Observe that the panel model does not follow the contour lines, with exception of the 83 m contour.

RESPONSE ANALYSIS

The frequency domain description of the hydrodynamic properties calculated by WAMIT was converted to time domain description (retardation functions) and included in a time domain simulation model in SIMO (2007). This model also comprises mooring line and fender models, and takes into account non-linear wave, wind- and current forces. The simulation program generates time series of irregular excitation forces, mooring forces and ship motions. The time series of motion and forces are processed to provide characteristic extreme loads. A parameter study with variation of wave heights and spectral peak periods, gave basis for estimation of operational limits and availability evaluation of the jetty. It turned out that the lateral motions caused un-acceptable loads in the initially specified hawsers and fenders too frequently, and the mooring system was modified to accept larger wave induced motions.

In view of the lack of validation of this approach to the steep shore influence, a parameter study of alternative bottom models was carried out. This was done as a frequency domain analysis dealing with linearized wave frequency sway motions and vertical and horizontal wave orbital motions, wave kinematics. Some results from this study are presented in this paper.

The sway motion of the ship is the most important response for dynamic mooring line and fender loads in this case, and is therefore selected for comparison. Only motions in the wave frequency domain are compared here.

RESULTS AND DISCUSSION

Motion transfer functions for sway motion for different wave directions are shown in Figure 5 for the loaded condensate tanker for water depth 35 m and for the Nyhamna bottom profile. When comparing motions for wave direction 270 degrees, it is seen that for periods below 8 s, the motion is quite similar. Between 8 and 12 s the Nyhamna bottom profiles gives smaller motions than the 35 m constant depth case. Above 12 s periods the motions for Nyhamna are getting larger than for the 35 m depth case.

Note the wave input in WAMIT is the far-field, deep water wave. The local wave specification at the berth site is 'disturbed', both by the bottom and by the shore reflection. When using the transfer functions from WAMIT, one must ensure that the input wave height reflects the far-field, undisturbed wave height for the 2-body case. For the finite depth, flat bottom case, WAMIT uses the finite depth potential as input wave field, and the local wave height must be used as a basis for response analyses.

To compare the sway motions in irregular sea, a JONSWAP wave spectrum coming from 90 deg. towards the berth (wave direction 270 deg in WAMIT) with peak periods in the range 6 to 16 s is used. The resulting sway motion is presented as 3 hour extremes. Results for the condensate tanker are shown in Figure 6 and for the large tanker in Figure 7.

It is seen that for peak periods shorter than 10 s all of the bottom models give responses fairly close to the deep water case. The flat-bottom 35 m depth case gives increasing sway motions with increasing wave period, up to 40% above the deep water case for 16 s peak period.

The flat-top panel model (Bottom2) gives a response equivalent to that of the un-limited 35 m depth model. This indicates that the extension of the bottom 'body' is sufficient for the ship sizes, and that the method of representing the bottom by a fixed body represents the limited water depth effects on ship motions.

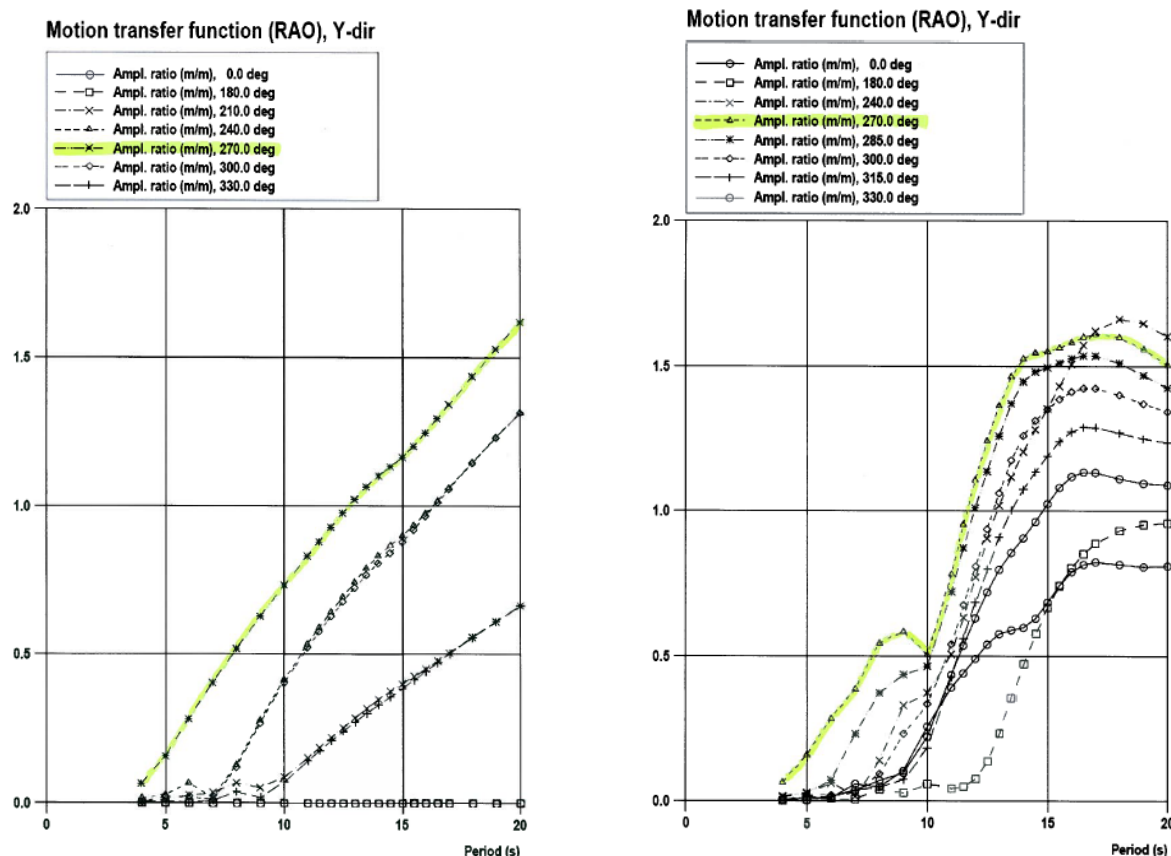


Figure 5 –Motion transfer function in sway for loaded condensate tanker in water with constant depth 35 m (left) and above the Nyhamna bottom model (right).

The plane sloping seabed model, Bottom1 and Bottom3, gives results that are sensitive to the truncation below the water line. Extending the bottom towards the shore and upwards, from 5 to 2 m below the sea level gives smaller sway motion for peak periods shorter than 13 s, and larger motion for longer wave periods. This is related to different reflection properties.

Modifying the plane model, Bottom1, by deflecting it to different, and curved profiles at the middle and at the two ends, Bottom4, gives a considerable reduction of sway motions for wave periods longer than 10 s. The non-flat bottom models are expected to reduce the sensitivity to inaccuracies in the shore modelling. The ‘irregular’ bottom topography, simulating the actual site, still in a fairly rough manner, gives sway motions in between the ‘original’ model, Bottom1, and the deflected version, Bottom4.

Although some uncertainty still remains, particularly related to the shore-side truncation of the seabottom body model, the results of these variations indicate that the Nyhamna bottom model is representative and fairly robust.

A more thorough validation of the approach should, however, be carried out. This will require model tests of ships or ship sections close to steep beaches.

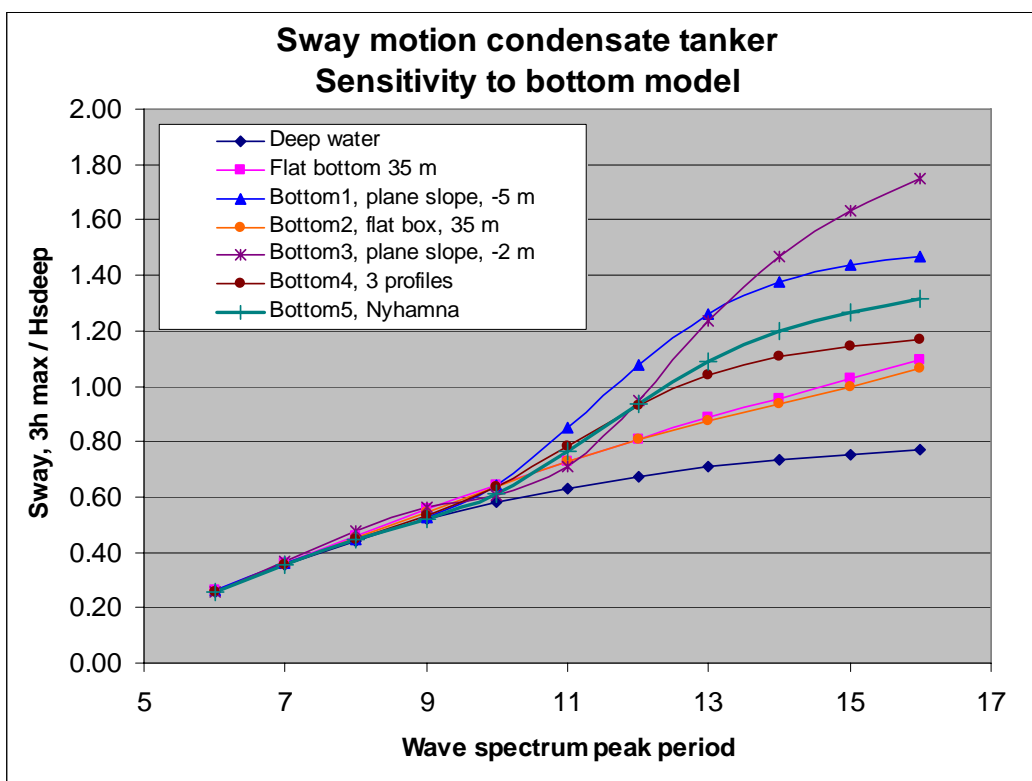


Figure 6 – Sway response of loaded condensate tanker on different bottom models.

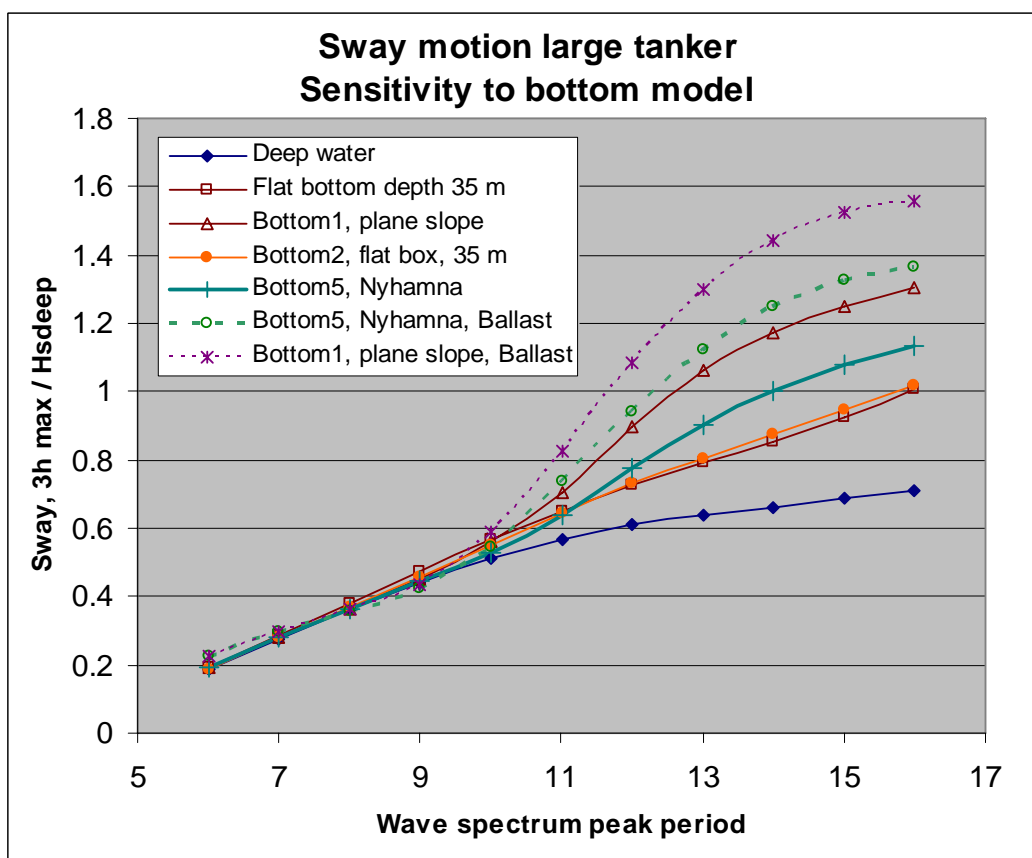


Figure 7 – Sway response of ballasted and loaded tanker on different bottom models.

WAVE KINEMATICS

To study the bottom model influence on the wave kinematics, WAMIT calculations are performed for bottom model Bottom1 (wedge) and Bottom5 (Nyhamna) without the ship present. In addition an analytical calculation of finite water depth kinematics was carried out. The results are presented in Figure 9 and Figure 10, where the vertical and horizontal wave amplitudes are shown at the point where the ship centre would be located. The difference between wave orbital motions in infinite and finite water depths is shown in principle in Figure 8. For deep water the vertical wave amplitude Z_D is equal to the horizontal amplitude Y_D and equal to half the wave height H . At finite water depth the horizontal amplitude Y_S is larger than the vertical Z_S , and the horizontal amplitude for finite water is larger than for deep water. The wave length on the other hand is shorter at finite than at deep water. The wave period remains unchanged.

The ratio of horizontal to vertical motion amplitudes is:

$$\frac{Y}{Z} = \frac{\cosh(kh)}{\sinh(kh)} \quad (1)$$

Where k is the wave number and h the water depth. See for example Faltinsen (1990) for further details on the wave theory.

The analytical result indicates a small reduction of wave height, within 10%, and most in the range 10 to 14 s. The WAMIT results show a strong period sensitivity, both for the plane inclined bottom (Bottom1, wedge) and for the irregular topography (Bottom5, Nyhamna), with from 40% increase to 40% reduction of vertical wave amplitude, in the 10 to 14 s period range.

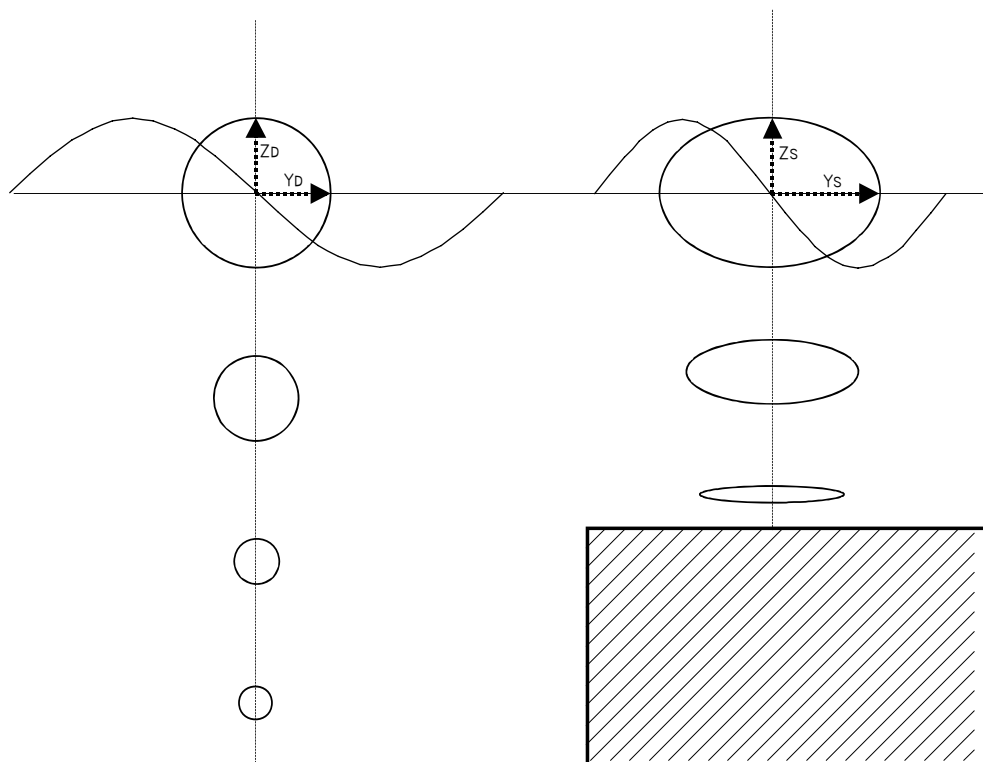


Figure 8 –Wave kinematics at deep (left) and finite (right) water. At deep water $Z_D=Y_D=H/2$. At finite depth $Y_S>Z_S$ and $Y_S>Y_D$.

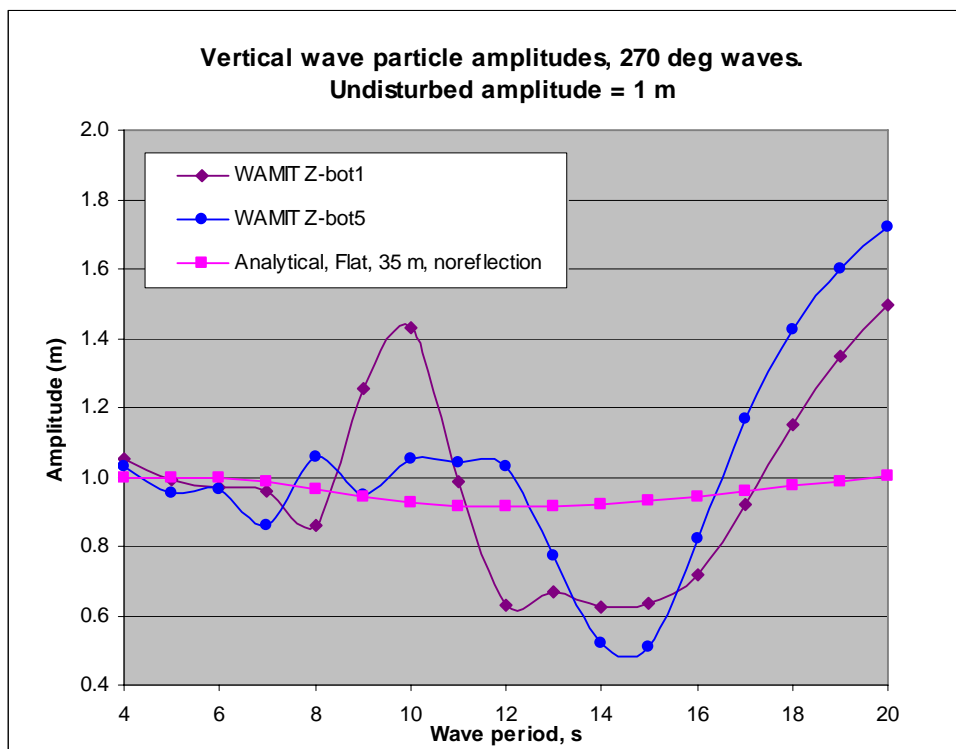


Figure 9 – Regular wave height (vertical amplitude) at the ship centre location, relative to deepwater height for analytical 35 m depth case and WAMIT bottom models Bottom1 (wedge) and Bottom5 (Nyhamna).

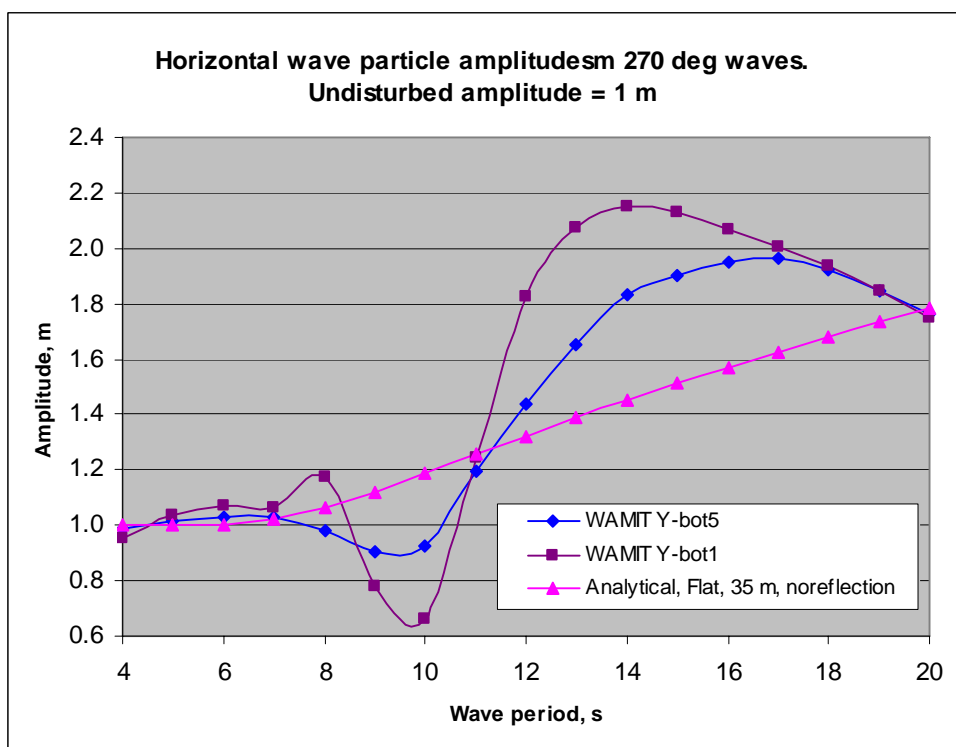


Figure 10 – Regular horizontal amplitude at the ship centre location, relative to deepwater amplitude for analytical 35 m depth case and WAMIT bottom models Bottom1 (wedge) and Bottom5 (Nyhamna).

A combination of these characteristics with wave spectra give, however only moderate variations of significant wave height within $\pm 5\%$ of the deep water value, as shown in Figure 11.

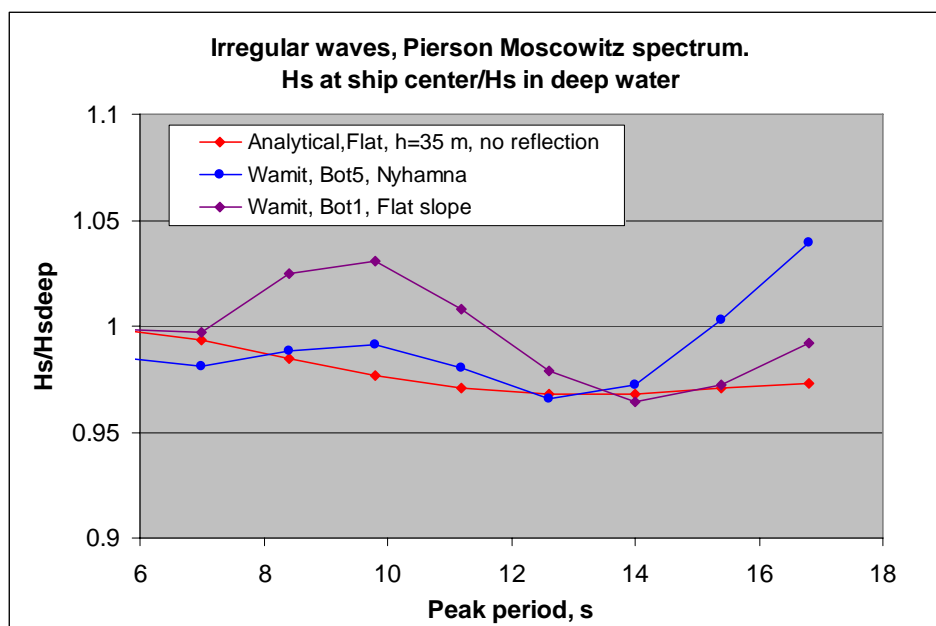


Figure 11 – Ratio of significant wave height at the ship centre location, relative to deepwater height for analytical 35 m depth case and WAMIT bottom models Bottom1 (wedge) and Bottom5 (Nyhamna).

CONCLUSIONS

The study shows that the choice of model representing the sea bottom in front of the jetty has a considerable influence on the calculated response characteristics for a moored tanker. When modelling the bottom with a realistic topography the horizontal motion responses are larger than in a flat bottom finite depth case, but smaller than if the bottom topography were assumed to be represented by a plane slope. Further research, also including experimental investigations, should be encouraged in order to obtain more knowledge about mooring loads at exposed coastal locations.

ACKNOWLEDGEMENT

The presented work was carried out as a part of the Ormen Lange project ‘Mooring of Tankers at Nyhamna’ performed at Marintek during 2006. We wish to thank the Ormen Lange Project for permission to present the results.

REFERENCES

- Faltinsen, O.M. 1990 *Sea Loads on Ship and Offshore Structures*. Cambridge University press.
- Fylling, I. 2005. *Mooring of Tankers at Nyhamna Vol 1, 3 and 4*. Marintek Report 511428.00. Trondheim, Norway. Unpublished.
- Fylling, I. 2006 *Mooring of Tankers at Nyhamna Phase2*. Marintek Report 550071.00.01. Trondheim, Norway. Unpublished.
- SIMO users manual*, 2007. Marintek Report 516412.00.04, Trondheim, Norway.
- Wamit Version 5.3 A radiation-diffraction panel program for wave-body interaction*. 1995. Department of Ocean Engineering Massachusetts Institute of Technology.

KEYWORDS

Tankers, Ship motions, Jetty, Bottom model, Water depth, Panel program.

FUTURE WIND, WAVE AND STORM SURGE CLIMATE IN THE NORTHERN SEAS: A REVISIT

L.P. Røed^{1,2} and J.B. Debernard¹

¹Norwegian Meteorological Institute, Oslo, Norway

²Dep. of Geosciences, University of Oslo, Oslo, Norway

ABSTRACT

We consider possible changes in the future climate of wind, wave and storm surge for a region covering the Northern Seas by comparing results from downscaled models for the two time periods 1961–1990 and 2071–2100. Available for the study were four atmospheric downscalings of the Hadley Centre's A2 and B2 scenarios, the Max-Planck Institute's B2 scenario and the Bjerknes Centre's A1B scenario. We find 1) a decrease in wind speed south of Iceland accompanied by a decrease of about 4–6% in the significant wave height, 2) that there is an increase in the eastern North Sea that continues into the Skagerrak, and 3) along the North Sea east coast and in the Skagerrak the annual 99-percentiles of the significant wave height and the storm surge residual increase 6–8% and 8–10%, respectively. These results are robust across the various choices in global models and emission scenarios.

INTRODUCTION

The study is motivated by the concern raised in reports by the Intergovernmental Panel on Climate Change (IPCC, 2007) that there is a possibility for a rougher wave climate and increased storm surges in the Northern Seas in the future. The concern is raised based on global simulations that project possible future increases in the intensity of storms. Although different global models predict a relatively consistent rise in the global mean temperature, the regional changes are highly variable, and at the present stage, the regional effects of global climate change must be regarded as far from being conclusive. The question has become particularly relevant after the release of the Arctic Climate Impact Assessment report (ACIA, 2004) stating that the Arctic has warmed at a rate twice that of the rest of the world over the past few decades.

Another concern raised by the IPCC is the possibility of a rise in the water level due to 1) thermal expansion of sea water, and 2) melting of the Greenland and Antarctic ice sheets. Notice that the Greenland ice sheet alone has the potential of raising the water level about 6-7 meters. Thus without any change in the wave and storm surge climate the combined effect is potentially harmful, e.g., to harbours and coastal infrastructures. A rise in sea level due to these factors is, however, outside the scope of the present study. Here we focus on possible changes in the wave and storm surge climate due to the expected changes in wind climate projected by various global climate change scenarios.

In an earlier study, Debernard et al. (2002) (hereafter DSR) made projections of the future regional wind, wave and storm surge climate in the Northern Seas based on an atmospheric downscaling of one of the earlier IPCC scenarios (the Max-Planck Institute's global GSDIO scenario). Their method was to first make a dynamic downscale of the global climate scenario using a regional atmosphere model, and then use these downscaled wind and sea surface pressure scenarios as forcing for stand alone wave and storm surge models. They found that the changes in the Northern Seas wind, wave and storm surge climate, with a few exceptions, were mostly small and insignificant. However, other studies using regional storm surge models (Lowe

In a series of studies utilizing empirical downscaling methods relating seasonal mean sea level pressure from AOGCMs to wave height, Wang et al. (2004), Wang and Swail (2006) and Cairesa et al. (2006) find large variations in the predicted changes in the Northern Seas due to differences in emission scenarios and to the choice of global models.

In view of these findings and those reported in the recent Arctic Climate Impact Assessment report (ACIA, 2004), we think it would be useful to investigate whether the results reported earlier carry over when dynamically downscaling more recent IPCC scenarios, in particular those used by ACIA (2004). Since we use the same method and computational domain as DSR, this study is a straightforward extension of their work to include new climate change scenarios.

SCENARIOS AND PERIODS SIMULATED

The new scenarios used here are the global SRES A2 and B2 simulations from the Hadley Centre's (HC) atmospheric global climate model (AGCM) HADAM3H (hereafter referred to as HADA2 and HADB2, respectively), one SRES B2 simulation from the Max-Planck Institute's (MPI) AGCM ECHAM4 (hereafter referred to as MPIB2), and one SRES A1B simulation from the Bjerknes Centre for Climate Research's (BCCR) global coupled climate model BCM (hereafter referred to as BCA1B). The A2 scenario has a rapid increase in the emission of greenhouse gases while the B2 scenario is among the more moderate scenarios used in the IPCC TAR (IPCC, 2001). The A1B is intermediate between the others but closest to the B2 scenario. For comparison the earlier GSDIOsimulation from MPI used byDSR is based on the IS92a scenario with a slightly higher increase in the emissions than the B2 scenario.

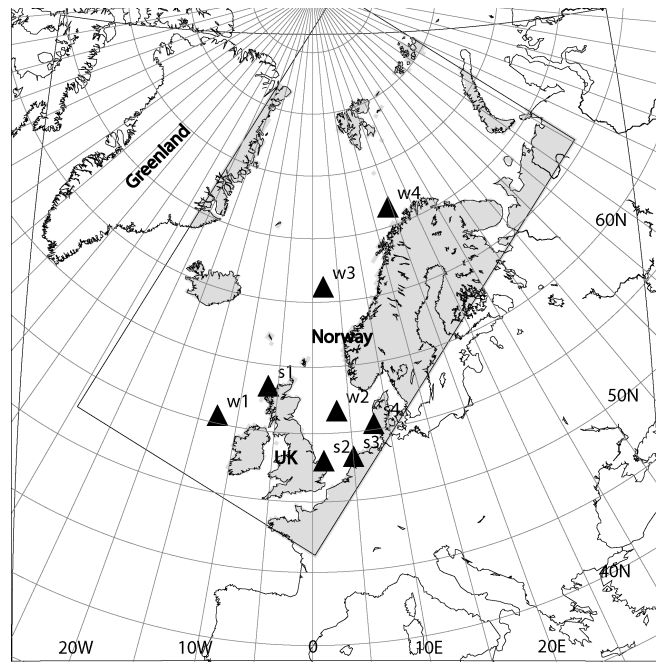


Figure 1. Geographical area covered by the regional atmosphere model used in the downscaling and the wave model. Also shown is the domain used by the storm surge model (inner frame) in addition to coastal stations and offshore positions used for analysis of the change in the largest storms. The coastal stations are s1: Stornoway, s2: Lowestoft, s3: Texel Noordzee, and s4: Esbjerg, while the offshore stations are w1: Buoy K4 near Rockall, w2: Ekofisk, w3: Weather ship MIKE and s4: Tromsøflaket.

As in DSR we base our calculations on dynamic downscaling of these global scenarios. A detailed description of the downscaling procedure and of the atmospheric results is found in Haugen and Iversen (2008). The downscaled results consist of two time-slice periods of 30-yr each, one from 1961 - 1990 and a second from 2071 - 2100. We refer to these periods henceforth as the control and the future climate, respectively. The difference between the two time-slices thus yields one possible regionalized climate change scenario over a 110 yr period.

METHOD

As in DSR we derive the projected wave and storm surge climate by using state of the art wave (WAM) and storm surge models (MIPOM). For details and references see Debernard and Røed (2008). The areas covered by the models are shown in Figure 1, which also shows the location of the coastal stations.

The production by use of the above model systems results in seven 30-yr-long time-series at the respective model grid points for each of the variables, namely wind speed (WS), significant wave height (SWH), and what we here refer to as storm surge residual (SSR). The latter is defined as the water level minus the astronomical tide. Of these seven series, three represents the downscaling of the various global models' rendition of today's climate (control), while the remaining four are simulations of the future climate.

We analyse the time-series by comparing different statistical measures from the control with the same statistics from the scenario. The statistics are defined over a year or a season. Thus, from one control period we get 30 values of the statistics which constitutes a population with a spread defined by the interannual variability. We then compare this population with the population from its respective scenario to check if there is a significant difference between the two. Because the populations are generally not normal distributed, we apply the Wilcoxon rank-sum test rather than the more common Student's t-test (Bhattacharyya and Johnson, 1977). However, alternative tests with the Student's t-test show that the results are robust with respect to the choice of method. A probability less than 5% thus means that the chance that the two 30-yr time-series comes from the same population is less than 5%. If this is the case we consider the difference to be statistical significant on the 95% confidence level. In the figures presented in Section 4 we have shaded the areas were this level is less than 95% in light grey (e.g. Fig. 2). In addition to comparing the changes for each individual scenario, we also define a multi-model population by collecting the same statistical measures from different simulations into one population for the control and one for the scenario before the statistical tests are evaluated. To avoid a bias in the populations towards the climate and response of the HC model, the combined analysis utilizes only the HADB2, MPIB2 and BCA1B scenarios. We prefer the HADB2 scenario over the HADA2 since this gives us a more homogeneous group of emission scenarios.

We present the results from these statistical analyses by showing fields of the relative change in the population mean between the scenario and control periods. The relative change in a quantity V is defined as

$$C_V = \frac{V_{Sc} - V_{Ctr}}{V_{Ctr}} \times 100, \quad (1)$$

where C_V denotes the change experienced in V , while the subscripts Sc and Ctr denote, respectively, the future climate value (scenario) and control value of V .

As relatively robust measures of the extreme events we use the annual and seasonal 99-percentiles. These quantities are based on all of the data in the time-series, that is, 6-hourly values for WS and SWH and 1-hourly values for the SSR.

To investigate the extreme events more closely, we have also extracted the 100 highest events of SWH and SSR from each time-slice at selected locations. In each series, the events are sorted in ascending order. To prevent one storm from biasing the extremes the events are selected such that there is a time span of at least 48 h between any two events. In this way, we assume that each event represents an individual, independent storm. A qq-plot of the events from the scenario against the events from the control, is then indicative of a change in the wave or storm surge climate if there is a significant deviation from the 1:1 line..

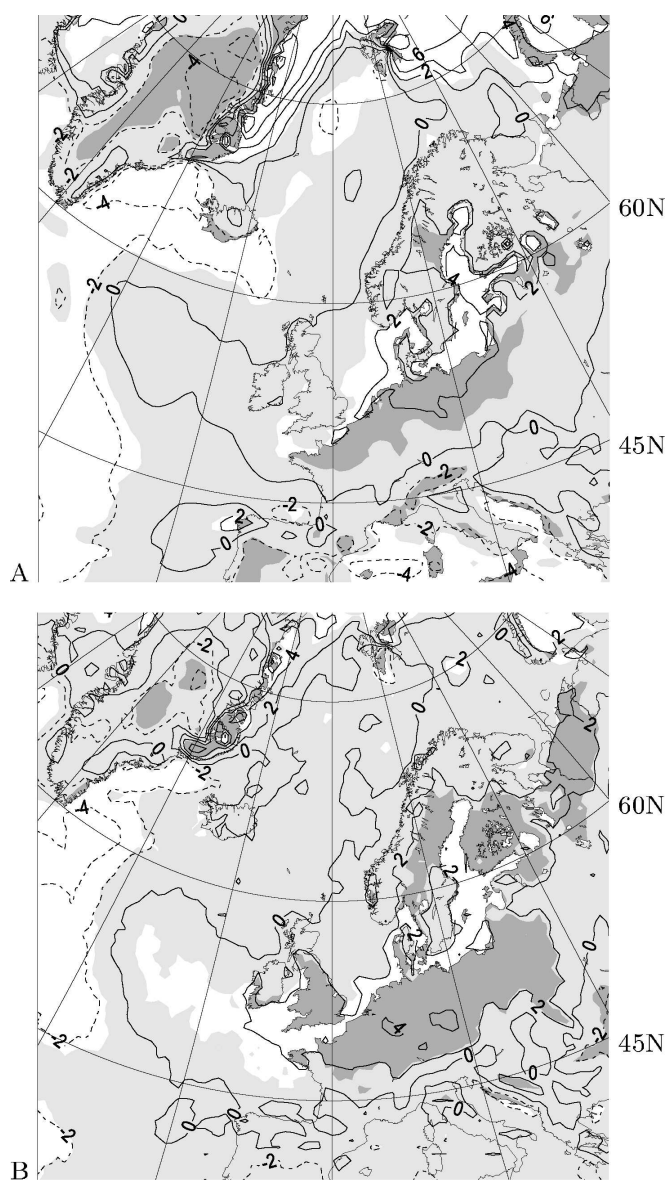


Figure 2. Relative changes (in percent) in wind from the combined analysis of the HADB2, MPIB2 and BCA1B scenarios. Upper panel (A) displays the annual mean while the lower panel (B) shows the annual 99-percentile. Solid lines are positive values, dashed lines indicate negative values. The light grey-shaded region indicates areas where the changes are insignificant from the statistical test, while white and dark grey shaded areas denotes areas where the changes are statistically significant over ocean and land areas, respectively.

RESULTS

We start by showing results from the combined multimodel analysis. As revealed by Fig. 2, the horizontal patterns of the relative differences in annual mean, annual 99-percentile and annual maximum of WS are very similar. Generally, they show a reduction in WS near the western boundary of the domain, and an increase (2–4%) from west of the British Isles and eastward over the North Sea, European continent north of the Alps, and also northward into the Baltic Sea. This is a robust feature in the results and, as discussed shortly, it is accompanied by significant changes in the wave and surge climates (Figs. 3 and 4, respectively). The increase in the eastern part of the domain is consistent with an decreased return period of high wind events, as found by Haugen and Iversen (2008) when analysing the same wind data.

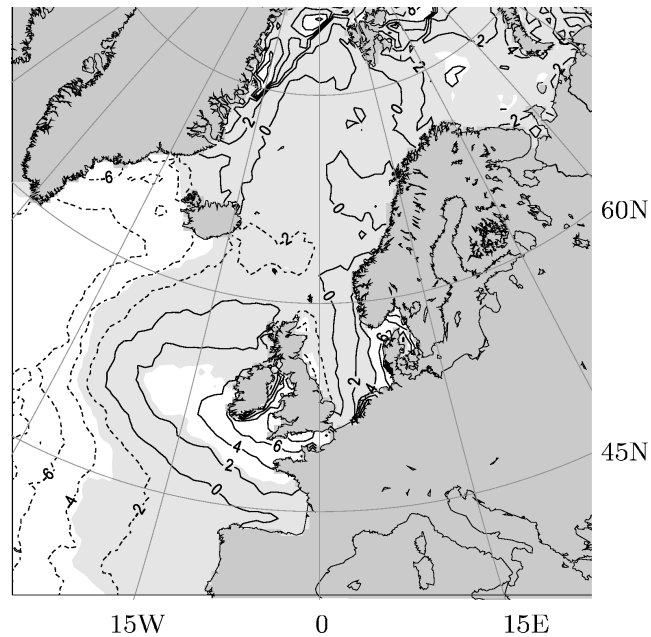


Figure 3. Same as Fig. 2, but displaying relative changes in annual 99-percentile of SWH from the combined analysis of the HADB2, MPIB2 and BCA1B scenarios.

Somewhat surprisingly we observe that the area of statistical significance in SWH is actually expanded compared to that for WS. We should keep in mind though that SWH depends not only on WS, but also on the wind fetch and the frequency and periods by which the wind changes its directions. For instance a change in the wind direction may cause a change in the SWH, in particular in coastal areas and seasonally ice covered areas, without any change in the WS. For example we see this along the east coast of United Kingdom (UK) where the SWH is decreasing while there is a small increase in WS. This response is due to a more westerly wind-field (not shown), which causes the SWH close to the coast to be fetch limited. The same sort of reduction is also found in the annual mean SWH (significant change of -2 to -4%) at this location (not shown). Accordingly we interpret the observed differences in relative change and the size of the area of statistical significance between WS and SWH as indicating changes in other conditions as well.

As evident from Fig. 4, the annual 99-percentile of SSR, shows some of the same response as the SWH, but with local differences. In this regard we note that the dependency of the storm surge response on wind is even more compound than for waves. The response not only depends on the WS and wind direction, but also depends on the movement of the storm centre as for instance shown by Gjevik and Røed (1976) and Martinsen et al. (1979). In addition, a storm surge usually propagates along the coast as a trapped planetary wave. Therefore, a single storm

surge event has the potential of affecting a large area, but its local impact depends on the local coastline geometry and topography as well. Accordingly, how a specific location is affected by a storm surge is highly dependent on the movement of the storm that generates it and on the local topology. Even small changes in wind direction are crucial to whether a specific site experiences a high surge or not. We should also keep in mind that large storm surges are mainly experienced in shallow waters or at sites close to the shore. Inherently, the impact of storm surges therefore has a very local character and is highly influenced by local coastline geometry and bottom topography.

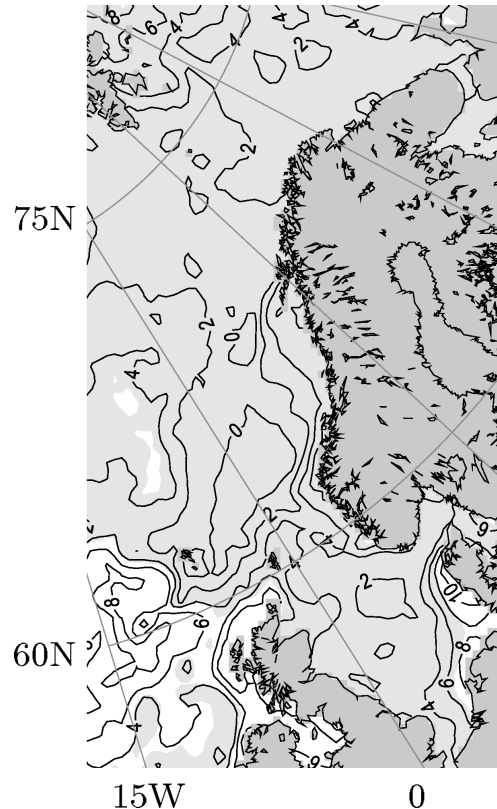


Figure 4. Same as Fig. 2, but displaying relative changes in annual 99-percentile of SSR from the combined analysis of the HADB2, MPIB2 and BCA1B scenarios. The domain is truncated compared to the whole computational area depicted in Fig. 1 to exclude the direct effect of the open boundary FRS zones. In addition, most areas normally covered with sea ice, are omitted to reduce the amount of data stored for the analysis.

With this in mind and with reference to Fig. 4 we note that in areas along the coast of the Netherlands, in the German Bay, and along the west coast of Denmark, there are significant increases in the 99-percentile of SSR (6–10%). In the Skagerrak and Kattegat the increase in SSR is 4–6%, but only spotwise significant along the Swedish coast (not visible from the figure). This contrasts the significant increase in SWH of 6–8% (Fig. 3) and in WS of 3% (Fig. 2B) found in this area. There is also a significant increase in SSR of the order of 6% at the northwest coast of British Isles that coincides with the increases in WS and SWH.

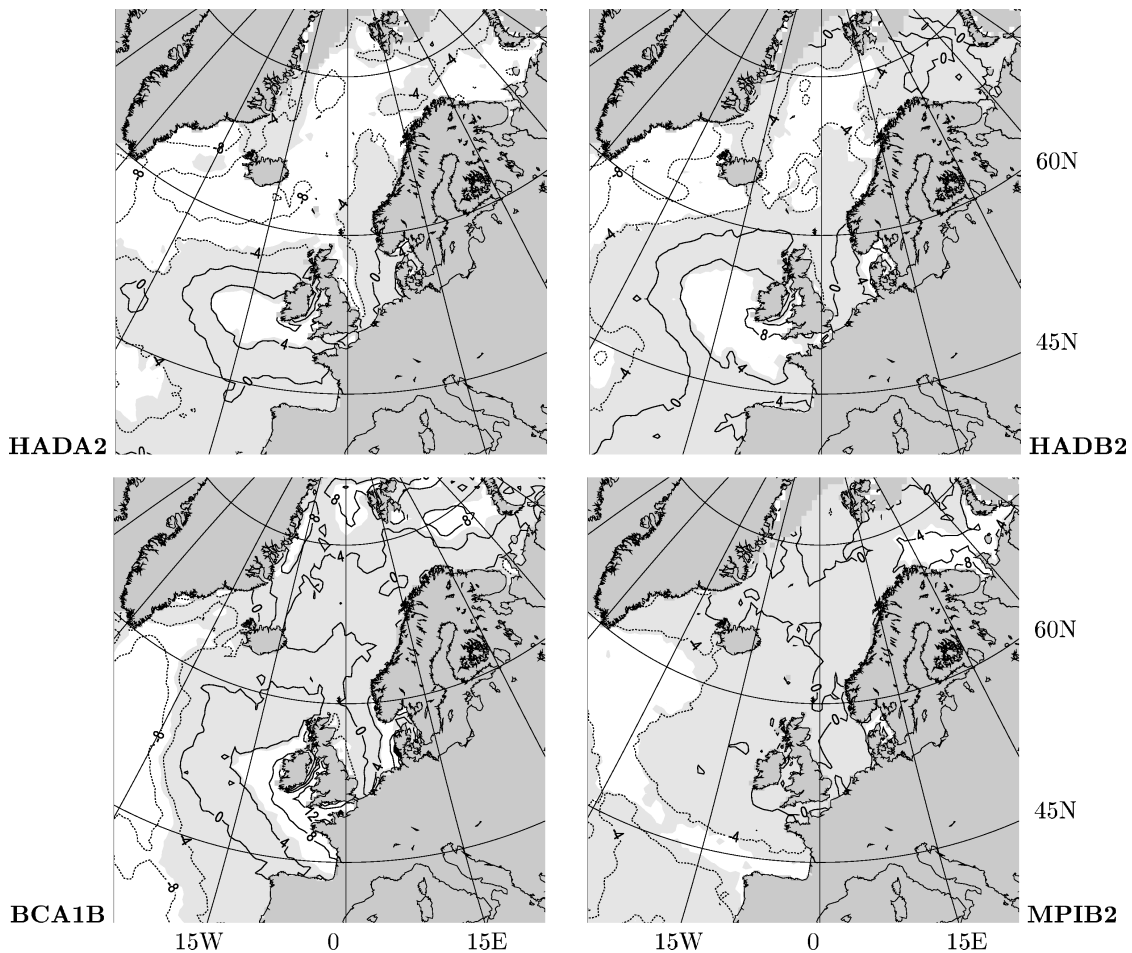


Figure 5. Same as Fig. 2, but displays the relative changes in the annual 99 percentile of SWH from the HADA2, HADB2, BCA1B and MPIB2 scenarios.

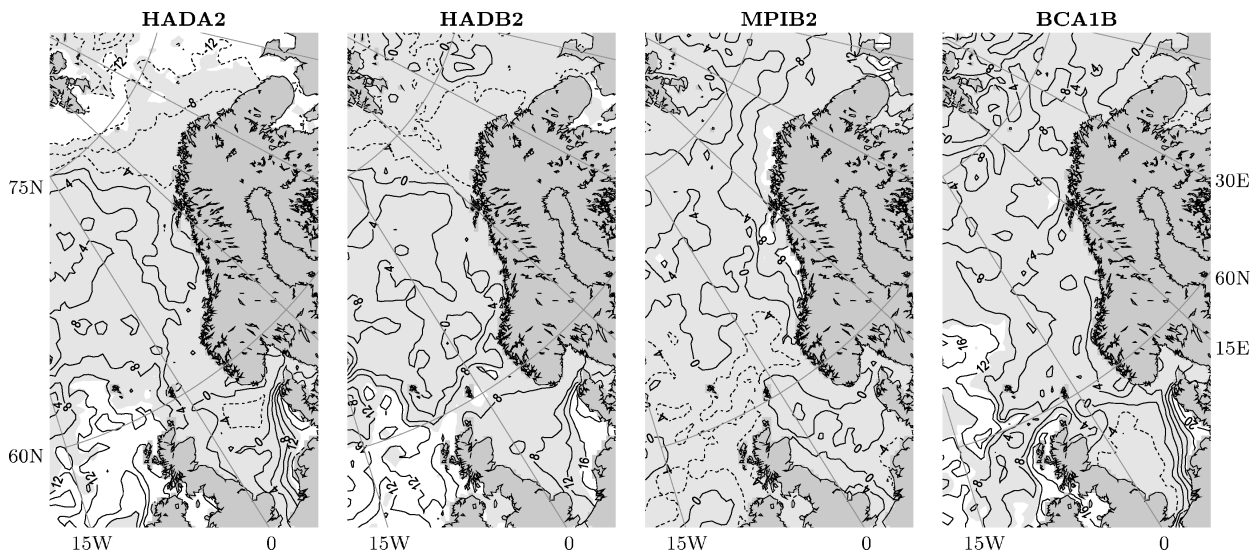


Figure 6. Same as Fig. 2, but displaying relative changes in 99-percentile of SSR for the winter season from the HADA2, HADB2, MPIB2 and BCA1B. The depicted domain is truncated as in Fig. 4.

We now turn our attention to the four individual scenarios and differences between them. As revealed by Fig. 5 the largest changes from the control in annual 99-percentiles of SWH are experienced in BCA1B followed by HADA2 and HADB2. In contrast the changes in MPIB2 are

mostly small and the areas of statistically insignificant changes larger. Another striking feature of interest is the similarity between the two very different emission scenarios of HADA2 and HADB2 and the dissimilarity between the two equal emission scenarios of HADB2 and MPIB2. Nevertheless, all the scenarios show a decrease in SWH in the western part of North Atlantic, an increase in the eastern North Sea, and an increase in the Skagerrak. The increase west of the British Isles found in the 99-percentile of SWH in the combined analysis (Fig. 3) is found in all scenarios except MPIB2, but is only evident in BCA1B for the annual mean SWH (not shown). This supports the conclusion that the increase in annual 99-percentile of SWH west of British Isles (Fig. 3) is mainly due to changes in the winter storms.

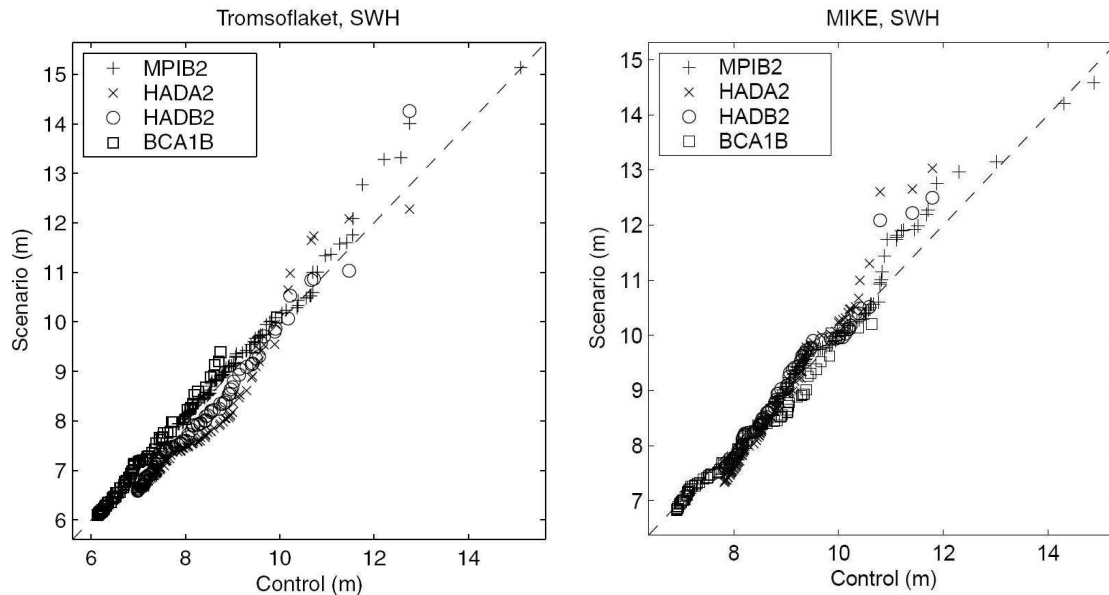


Figure 7. qq-plots of SWH for the 100 largest events from the scenario plotted against the 100 largest events from the control period.

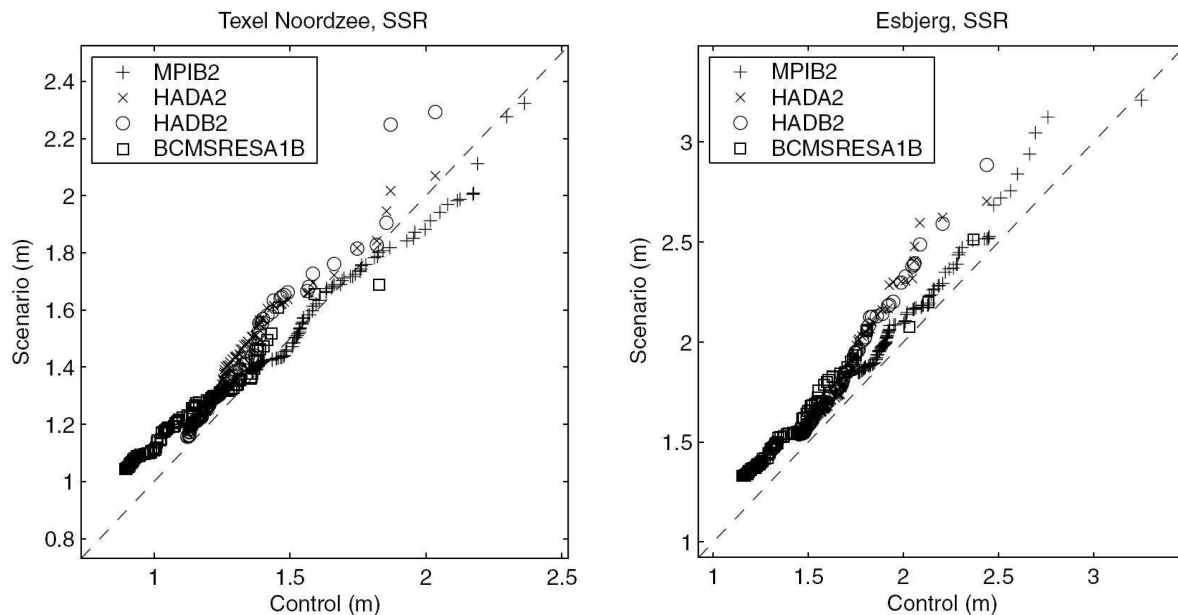


Figure 8. Same as Fig. 7, but showing the results for the storm surge residual.

An important issue to address is what happens to the extreme high wave and high surge events in a warmer climate, we find it worthwhile to have a closer look at the extremes via a storm

analysis. To this end Figs. 7 and 8 show results related to the change in isolated extreme events for wave and storm surge, respectively, at some of the stations shown in Fig. 1.

We note from the qq-plots that both SWH and SSR show large differences between the individual scenarios. Apparently, the MPI scenario is much more energetic than the others giving higher waves and surge events, while those based on the BCCR simulations are the least energetic. This might in part be a consequence of the differences in the global model scenario used for the downscaling. Differences in global model resolution and physics give boundary conditions for the regional atmosphere model that influence the interior storm climate in the regional model. The relative difference plot (Figs. 9 and 10) is a convenient way of comparing the actual change in extreme events between the scenarios despite the large differences in model climates.

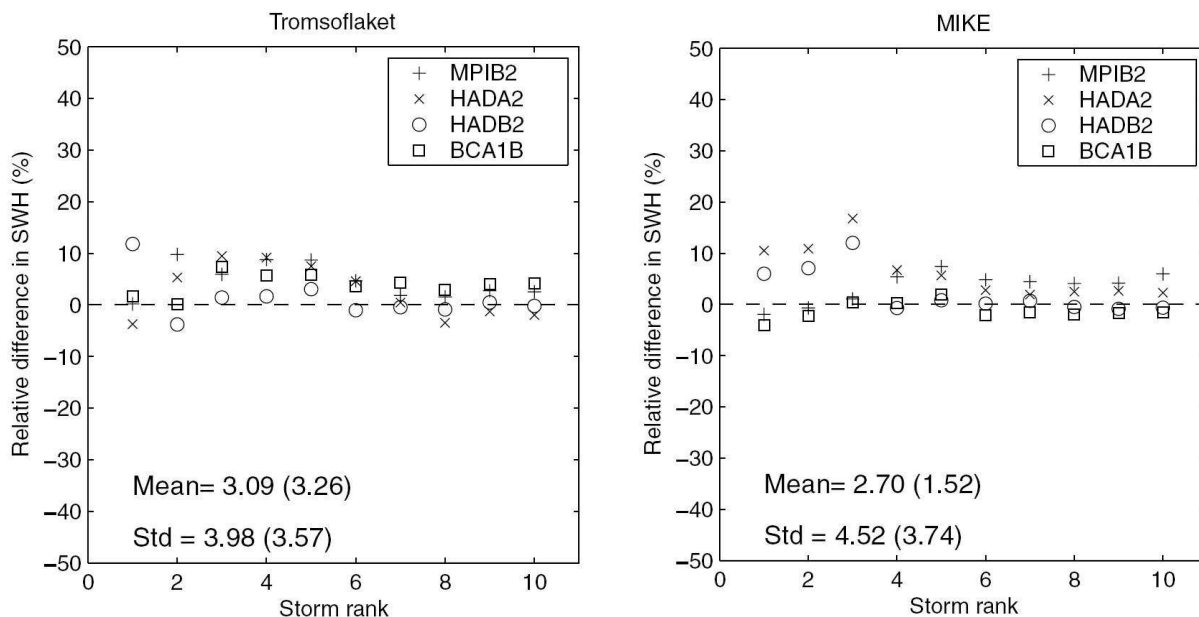


Figure 9. Displayed is the relative difference in percent of SWH (from eq. 1) at Tromsøflaket (left panel) and MIKE (right panel) for the 10 largest events, numbered after event rank such that the leftmost point show the relative difference between the largest event in the scenario, versus the largest event in the control. The numbers gives the mean and standard deviation (SD) of all the data points in the figure. The numbers in parentheses gives the same numbers excluding data points from the HADA2 scenario.

Generally, we note that the results from these analyses confirm the results for the annual 99-percentiles in Figs. 3 and 4 quite nicely. Examining the relative difference for SWH at Tromsøflaket as displayed in Fig. 9 (left panel), we find a tendency for the largest events to be higher in the future climate. The figures for the mean relative difference indicate an increase in the highest wave events of 3–4%, but we observe that the standard deviation is as large as or larger than the mean difference. We also observe that the two HC scenarios have a tendency to give the same sign of the response at a selected site for a selected rank. Due to their common control period they use the same event to represent the control climate, and therefore, the calculated relative differences are not independent between the two scenarios. This gives a bias in the pictures towards the response of the HC model. However, excluding the HADA2 scenario, the figures in parentheses still show a small increase in the largest 10 events.

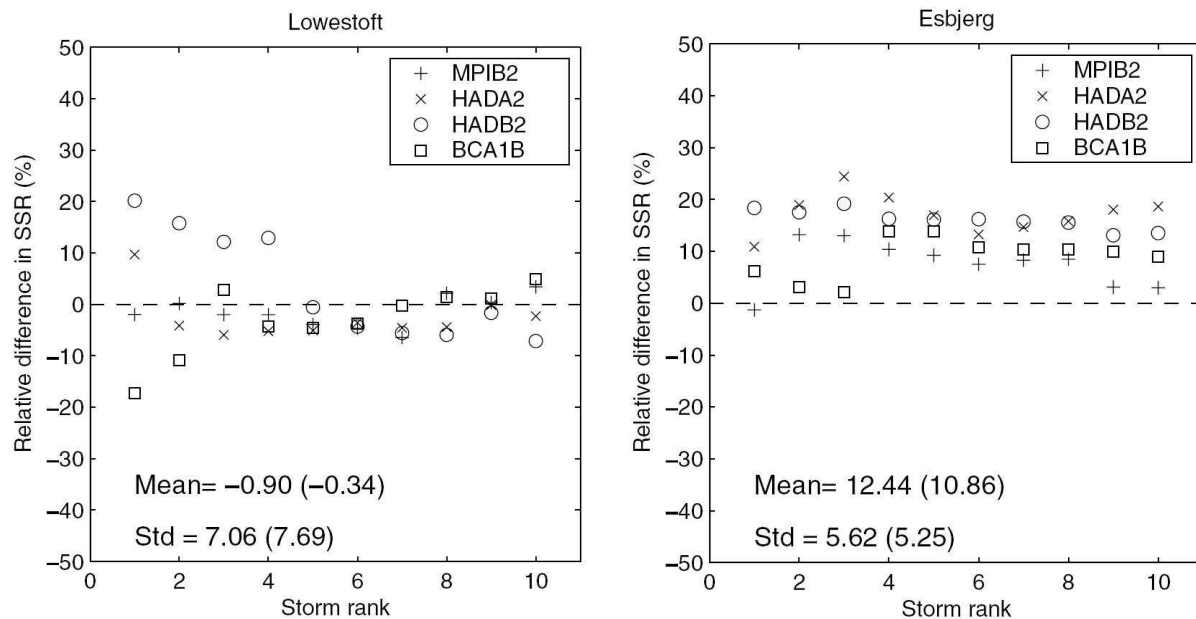


Figure 10. Same as Fig. 9, but for SSR at Lowestoft (left panel) and Esbjerg (right panel), respectively.

The same comments as for the SWH are valid for the extreme SSR events (Fig. 10). We find, however, a larger spread in the relative changes of the high SSR events than for the high SWH events. This is also reflected in a higher standard deviation in the relative differences. For instance Lowestoft situated at the west coast of the North Sea shows no relative change in the mean, but a high variability among the estimates. On the other hand, the increase we find in the extreme SSR at Esbjerg in the 99-percentile plots is also evident when the individual events are investigated. This is the only site where the mean relative change in the 10 largest events is considerably greater than the standard deviation among the estimates. Despite the short distance between the stations Texel Nordzee (not shown) and Esbjerg, there are large differences in the change. This underlines the findings of Debernard et al. (2002) that the storm surge experienced at a specific location depends on the movement of the storm, the wind direction and local conditions in coastline geometry and topography.

CONCLUSIONS

The most robust result we find is a decrease in WS and SWH in the open ocean areas southwest of Iceland. This decrease is statistically significant and is approximately 6% for the annual 99-percentile of SWH from the combined analysis. The decrease is most pronounced in HADA2 and HADB2, but it is significant in all simulations.

Another important, robust result is that there are considerable increases in the SWH and SSR along the North Sea east coast and in the Skagerrak. The changes in the annual 99-percentile of SWH and SSR are 6–8% and 8–10%, respectively, from the combined analysis. For SWH, the changes are evident in all simulations and for all seasons, and constitute the most robust signal in these simulations. In addition, this roughening of the SSR climate is in accordance with the results from STOWASUS-2001 (2001), Lowe et al. (2001), Lowe and Gregory (2005), Woth (2005) and Woth et al. (2006). It is, however, somewhat contrary to the results from Debernard et al. (2002) who found a minor, insignificant change in this area only. Interestingly, the ECHAM4 global model used in Debernard et al. (2002) is the same as used in the MPIB2 scenario, but with a different emission scenario. The changes in SSR in the North Sea from the MPIB2 scenario are smaller and less significant than from the other models.

Based on the analysis we also note that, as expected, the changes in the future wave and storm surge climate are in accord with the change in the wind climate. The largest changes are detected in BCA1B, but there is a substantial dissimilarity between the two B2 scenarios (HADB2 and MPIB2, respectively). In contrast, there is a strong similarity between the two scenarios based on input from the HC's global scenario simulations (HADB2 and HADA2). Therefore, the uncertainty associated with projecting the future wind, wave, and storm surge climate appears to be more linked to which global climate model system is used, rather than which emission scenario is selected.

We find that there is a considerable difference between the climates of the simulations from different centres. The MPIB2 control wind climate appears to be much more energetic than the others, giving higher wave and surge events, while the BCCR control is the least energetic. Of the three global models, the BCCR model has the coarsest resolution on the boundary fields for the atmospheric downscaling (T42), while the resolution in the data from the HC and MPI is better (near T106).

We emphasise that the results near the ice edge are severely hampered by the treatment of sea ice in the global scenarios. This has a decisive influence on the atmospheric downscaling. As is well known, the different global models give very different seasonal ice covers. Hence downscaling of scenarios from them are expected to produce large discrepancies in the downscaled WS climate in these areas, which in turn impacts the projections of future wave and storm surge climates. One way to avoid this problem is to replace the atmosphere alone model by a fully coupled atmosphere-ice-ocean model to let the ocean and sea ice be a coupled and interactive part of the downscale. With a regional coupled atmosphere-ice-ocean model, as for instance described in Debernard and Køltzow (2005), the model is able to produce its own ice cover, consistent with, and in response to the local atmosphere-ocean interactions.

Finally, based on the possibility of more frequent strong wind events, society should prepare for higher extreme surge and wave events in the future. However, it is difficult to give uncertainty estimates for the changes, and this is especially true if we concentrate on specific locations. As shown in this study, large differences in the estimated future change are found over small horizontal distances even within the North Sea.

ACKNOWLEDGEMENTS

The authors thank Jan Erik Haugen for making the downscaled results available to us, and to Jon Albretsen for running the WAM wave model. This research was supported in part by the Research Council of Norway through the national climate project RegClim (Grant No. 120656/720). Support for computations was provided by NOTUR (Norwegian High Performance Computing Consortium).

REFERENCES

- ACIA 2004. Impacts of a Warming Climate, Arctic Climate Impact Assessment. Cambridge University Press, Inc.
- Bhattacharyya, G. K. and Johnson, R. A. 1977. *Statistical Concepts and Methods*. John Wiley & Sons, Inc.
- Cairesa, S., Swailb, V. R. and Wang, X. L. 2006. Projection and analysis of extreme wave climate. *J. Climate* **19**, pp. 5581–5605, doi:10.1175/JCLI3918.1.
- Debernard, J., Sætra, Ø. and Røed, L. P. 2002. Future wind, wave and storm surge climate in the northern North Atlantic. *Clim. Res.* **23**, pp. 39–49.

- Debernard, J. and Køltzow, M. Ø. 2005. *Technical documentation of the Oslo Regional Climate Model, version 1.0*. Technical Report 8, RegClim General Technical Report. Norwegian Meteorological Institute, Oslo, Norway.
- Debernard, J. B., and Røed, L. P. 2008. Future wind, wave and storm surge climate in the Northern Seas: a revisit. *Tellus*, **60A**, pp. 427–438. doi:10.1111/j.1600-0870.2008.00312.x
- Gjevik, B. and Røed, L. P. 1976. Storm surges along the western coast of Norway. *Tellus* **28**, pp. 166–182.
- Haugen, J. E, and T. Iversen. 2008: Response in extremes of daily precipitation and wind from a downscaled multi-model ensemble of anthropogenic global change scenarios. *Tellus*, **60A**, pp. doi:10.1111/j.1600-0870.2008.00315.x.
- IPCC, 2007: Climate Change 2007: The Physical Science Basis. Contribution of Working Group I to the Fourth Assessment Report of the Intergovernmental Panel on Climate Change. Eds.: Solomon, S., D. Qin, M. Manning, Z. Chen, M. Marquis, K. B. Averyt, M. Tignor and H. L. Miller. Cambridge University Press, United Kingdom and New York, USA..
- Lowe, J. A. and Gregory, J. M. 2005. The effects of climate change on storm surges around the United Kingdom. *Phil. Trans. R. Soc. A* **363**, pp. 1313–1328, doi:10.1098/rsta.2005.1570.
- Lowe, J. A., Gregory, J. M. and Flather, R. A. 2001. Changes in the occurrence of storm surges around the United Kingdom under a future climate scenario using a dynamic storm surge model driven by the Hadley Centre climate model. *Clim. Dyn.* **18**, pp.179–188.
- Martinsen, E. A., Gjevik, B. and Røed, L. P. 1979. A numerical model for long barotropic waves and storm surges along the western coast of Norway. *J. Phys. Oceanogr.* **9**, pp. 1126–1138.
- STOWASUS-2100 2001. *Synthesis of the STOWASUS-2100 project: regional storm, wave and surge scenarios for the 2100 century*. Technical Report 01-3, Danish Climate Centre.
- Wang, X. L. L. and Swail, V. R. 2006. Climate change signal and uncertainty in projections of ocean wave heights. *Clim. Dyn.* **26**, pp. 109–126, doi:10.1007/s00382–005–0080–x.
- Wang, X. L. L., Zwiers, F. W. and Swail, V. R. 2004. North Atlantic Ocean wave climate change scenarios for the twenty-first century. *J. Climate* **17**, pp. 2368–2383, doi:10.1175/1520–0442(2004)017.
- Woth, K. 2005. Future North Sea storm surge extremes. *Geophys. Res. Lett.* **32**, L22708, doi:10.1029/2005GL023762.
- Woth, K., Weisse, R. and von Storch, H. 2006. Climate change and North Sea storm surge extremes: an ensemble study of storm surge extremes expected in a changed climate projected by four different regional climate models. *Ocean Dyn.* **56**, pp. 3–15, doi:10.1007/s10236–005–0024–3.

KEYWORDS

Climate change, numerical models, waves, storm surges

DRAG FORCES ON AND FLOW AROUND AND THROUGH POROUS CYLINDERS

Lars Gansel¹, Thomas A. McClimans² and Dag Myrhaug¹
¹NTNU, Trondheim, Norway
²SINTEF Fisheries and Aquaculture, Trondheim, Norway

ABSTRACT

Experiments were carried out to investigate the flow around and through porous cylinders and to measure the forces on and the wake characteristics downstream from fish cages. Dye experiments were conducted on cylinders with porosities of 0%, 33%, 66% and 77%. Force and PIV measurements were carried out on cylinders with porosities of 0%, 30%, 60%, 75%, 82% and 90%. The Reynolds numbers, based on the diameter of the models, ranged from 2600 to 8700 (dye experiments) and from 1000 to 20000 (force and PIV measurements), respectively. The data indicate, that a qualitative shift in the flow patterns around and through porous cylinders occurs at a porosity of about 70%. Fouling on fish cages might lead to changes of the flow characteristics around the fish cage and thus might influence the distribution patterns of particles and dissolved matter. Fouling also leads to increased forces on fish cages and moorings.

INTRODUCTION

The aim of this study was to measure the drag forces on porous cylinders and to characterise the flow around and through cylinders with different porosities. Drag is a major mechanism by which current loads are transferred to fish cages (Swift *et al.*, 2006) and the moorings. Noymer *et al.* (1998) found that the drag force on cylinders depends on the Reynolds number and the permeability of the cylinder. Also the characteristics of the flow field around cylinders depend on the Reynolds number and the porosity of the cylinder (Bhattacharyya *et al.*, 2006). Fouling on fish cages is a serious problem in marine aquaculture (Swift *et al.*, 2006) and can lead to a rapid decrease of the net aperture (Braithwaite *et al.*, 2006). The flow around and through fish cages determines the oxygen supply into the net pens as well as the distribution patterns of dissolved nutrients and particles. Several studies evaluated the environmental impact of marine fish farms (e.g. Neori *et al.*, 2003; Sarà *et al.*, 2003) and the availability of waste from marine fish farms for the cultivation of molluscs and seaweed (e.g. Cheshuk *et al.*, 2002; Troell *et al.*, 1997). Most of these studies were based on the analysis of different parameters at certain locations in or around fish cages. The water flowing through and around net pens will not distribute particles and dissolved substances and gases evenly (Gansel *et al.*, 2008). Better knowledge of the flow through and around net pens will help to establish better models for the prediction of the distribution of dissolved nutrients, oxygen and particles in and around fish cages.

MATERIAL AND METHODS

Particle image velocimetry (PIV)

PIV is a highly accurate technique for measuring the instantaneous flow field. A Dantec PIV system was used during the experiments. The system consisted of a dual head laser (Litron Nano Range, wavelength: 532µm), two CCD high speed cameras (resolution: 1280 x 1024 pixels) and Dantec's Flow Manager software. Both lasers were fired simultaneously in single frame mode

for increased light intensity. White, neutrally buoyant plastic spheres with a diameter of $50\mu\text{m}$ were used as seeding particles.

Force measurements

The drag and lateral (lift) forces on the models were measured with strain gauges (HBM PW15A; accuracy class C3, C3MR). Strain gauges are designed so they can bend along one axis and a conductive metal strip inside the strain gauges lengthens or shortens, depending on the direction of a force. Strain gauges are insensitive to lateral forces and therefore two strain gauges were used to record drag and lateral forces simultaneously. The strain gauges were calibrated with a set of weights of known mass.

Experimental setups

Two different setups were used for the experiments. Setup 1 was designed for dye experiments in a flume, Setup 2 for PIV and force measurements in a towing tank.

Setup 1

All dye experiments were carried out in a flume. Square metal pins (about $1 \times 1\text{mm}$) were arranged in a circle with a diameter of 0.087m on the bottom of the flume. Three different porous cylinders (33%, 66% and 77% porosity) and a solid cylinder were tested. The different porosities were realized by using different clearances between individual pins. A solid cylinder was tested in addition. The water height was about 0.02m and ink was added to the water flow manually, using a syringe. There were marks with known distances on the bottom of the flume. All experiments were recorded with a Video camera (Sony Handycam), that was mounted about 2m above the setup. A scheme of Setup 1 is shown in Figure 1.

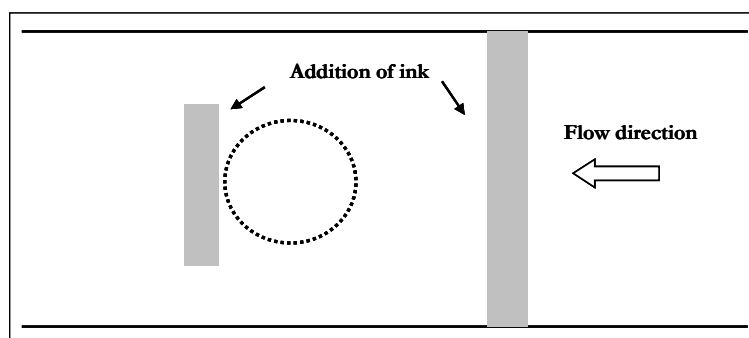


Figure 1 – Scheme of setup 1 during dye experiments. Ink was added with a syringe in the shaded areas.

Setup 2

All PIV and force measurements were conducted in a towing tank with glass walls. The tank is 13.5m long, 0.6m wide and 1.5m deep. One solid and five porous cylinders with porosities of 30%, 60%, 75%, 82% and 90% were used. All porous models were made from metal mesh. The individual strings of the mesh of the different models had the same dimensions, while the sizes of the openings were different. The cylinders had a diameter (D) of 0.1m and a length (L) of 0.3m . The dimensions of the models assured that there was no direct interaction of the wake and the walls and bottom of the towing tank within the first five diameters ($5D$) behind the models. The diameter of the individual strings of the metal mesh was 1.5mm , which is close to the diameter of single strings of fish cage netting. The towing speeds ($0.05\text{-}0.2\text{m/s}$) were within the range of typical current velocities in locations with salmon farms at the Norwegian coast. The

models were mounted on a thin round, metal plate with a diameter of 0.2m and a thickness of 2mm (Plate 2 in Figure 2), which was connected to a bigger round, metal plate (Plate 1 in Figure 2) with two strain gauges. This assembly was mounted on a heavy metal plate with three extension rods with a diameter of 0.01m and a length of 0.3m and fixed to a motor driven carriage on top of the tank. A scheme of setup 2 is shown in Figure 2.

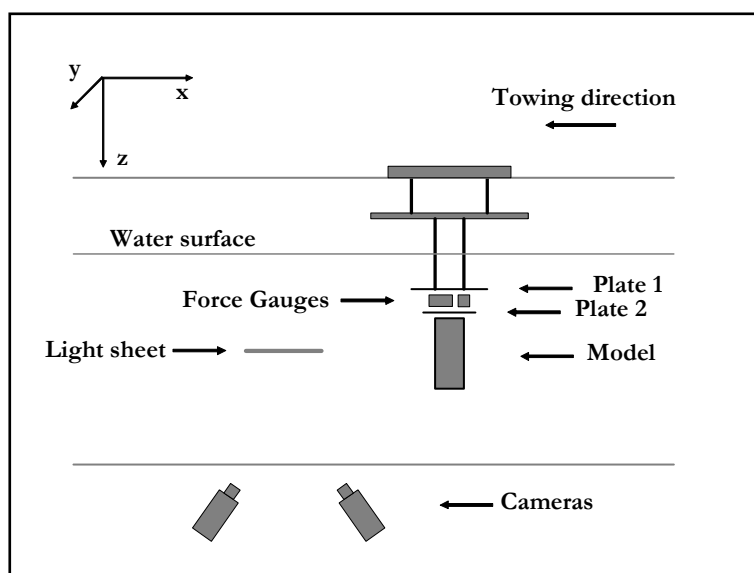


Figure 2 – Scheme of setup 2 during PIV tests and force measurements.

Dye experiments and towing tests

The dye experiments were carried out at two different flow speeds: 0.03m/s and 0.12m/s, which corresponds to Reynolds numbers ($Re = U_{\infty} \cdot D / \nu$ where U_{∞} is the flow speed, D is the diameter of the model and ν is the kinematic fluid viscosity) of about 2600 and 8700. Ink was added with a syringe either about 0.3m in front of the cylinders or directly behind the cylinders in order to visualize the flow patterns through and around the models. The flow speed was controlled digitally and cross checked by analyses of the recordings.

Towing tests were conducted at three different towing speeds: 0.01m/s, 0.05m/s and 0.2m/s. The Reynolds numbers based on the diameter of the models ranged from 1000 to 20000. A right-handed, three-dimensional Cartesian coordinate system was applied as shown in Figure 2.

Calculations

All force measurements were repeated once. The (tare) forces on the setup including all the mountings were measured and subtracted from the measurements including the models. The maximum values of the drag force within a time series were determined, and the drag force was calculated as a time average. The total force is the sum of drag force and lateral force. The expected drag force on the solid model was calculated as:

$$F_D = 0.5 \cdot C_D \cdot A \cdot \rho \cdot U_\infty^2, \quad (1)$$

where C_D is the drag coefficient (here $C_D = 1$), A is the cross sectional area perpendicular to the flow, ρ is the density of the fluid, and U_∞ is the towing speed.

PIV is an optical measurement technique. Due to the camera angles and optical effects caused by transition between different media in the optical path, the recorded images are distorted. The Flow Manager software makes use of calibration grids to convert the movement of particles in the flow to an undistorted velocity field. The 3D PIV data were converted using a multi-level grid with the dimensions 270mm x 190mm and an offset of 4mm between the two levels of the grid.

Time series of the velocity components in the x-, y- and z-directions (u , v , w) at single points in space along cross sections behind the models were constructed from PIV data. The mean (time averaged) velocity in x-direction within a time series was calculated as $\bar{u} = \sum_{i=1}^t u_i / t$, where t is the number of time steps within a time series.

Profiles of specific turbulent kinetic energy (TKE) were calculated from time series of u , v and w on three cross sections behind the models. The mean of the time series for all three velocity components (u , v and w), as well as the deviations from the mean were calculated. The TKE was calculated as:

$$TKE = 0.5 \cdot (\overline{u'^2} + \overline{v'^2} + \overline{w'^2}), \quad (2)$$

where u' , v' and w' are the deviations from the mean of the time series of u , v and w .

RESULTS

Flow patterns

Figure 3 shows a sketch of the flow patterns around and through a solid and three porous cylinders with porosities of 33%, 66% and 77%. The flow around the solid cylinder is characterized by a distinct velocity increase at the sides of the cylinder and the development and separation of vortices from both sides of the wake. This leads to an oscillating motion of the wake. Water is not only flowing around, but also through the porous models. Water enters the upstream half of the 33% open model at an angle of almost 90° to the surface of the cylinder. The water entering this model flows towards the center of the cylinder and curls outwards after passing the center of the cylinder. A recirculation along the side of the cylinder occurs. A substantial amount of water flows through the 66% and 77% open models. In both cases water is forced around the cylinder and some of the water enters the model at an angle smaller than the angle between the main flow direction and the cylinder wall. This pattern becomes weaker with increasing porosity from the 33% to the 77% open model. The water leaves the porous models at an angle to the initial flow direction. This angle decreases with increasing porosity from the 33% to the 77% open models.

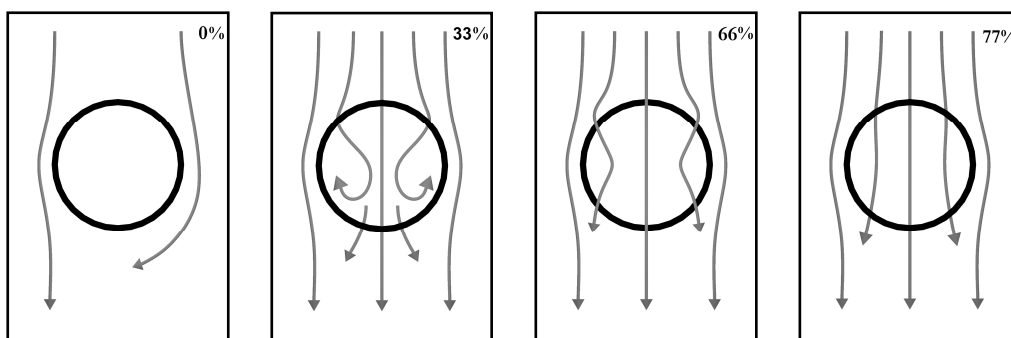


Figure 3 – Scheme of the flow patterns around and through cylinders with porosities of 0%, 33%, 66% and 77% at a flow speed of about 0.12m/s.

Observations of the flow field derived from PIV data showed that swirls at the flanks of the wake interact with the walls of the tank from about 0.5m (5D) downstream from the centerline of the solid model. That is well beyond the region where the present data were acquired. Clearly, there was no interference of the walls of the tank and the wake downstream from the porous models.

Velocity defect

An increase of the porosity of the cylinders leads to a decrease of the velocity defect behind the models and to a decrease in the width of the wake (see Figure 4). The wake, indicated by the width of the positive velocity defect, one diameter downstream from the solid cylinder is about 50% wider than the wake downstream from the porous models (see Figure 4). The velocity increase at the flanks of the solid cylinder is about 20% of the towing speed, while it is only about 5% at the flanks of the porous cylinders (see Figure 4). The 82% and the 90% open models show distinct fluctuations with six (82%) and four (90%) peaks, respectively.

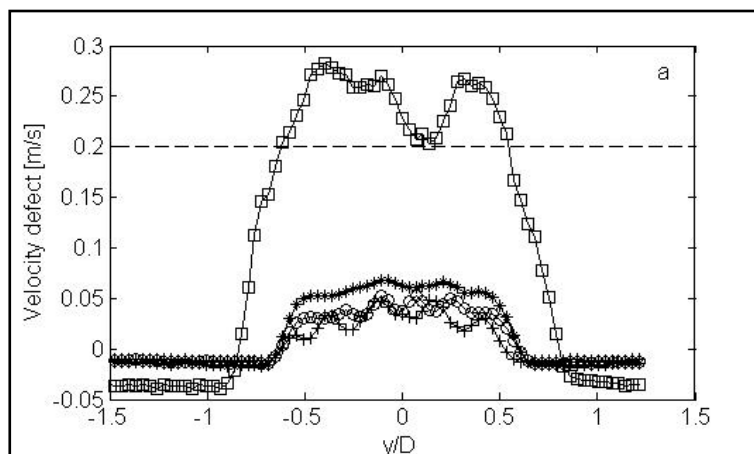


Figure 4 – Velocity defect ($u-U_\infty$) in the wake of solid and porous cylinders 1D downstream from the center line of the cylinders. \square solid cylinder, $*$, \circ and $+$ 75%, 82% and 90% open cylinders, respectively. The towing speed (U_∞) was 0.2m/s.

Half spreading angles

The half spreading angles of the wakes are the angles between the initial flow direction and the outer boundary of the wake at one side of the cylinder. The half spreading angles of the wakes downstream of the models decreased from 20° to 5° with increasing porosity from 0% to 75% porosity (see Table 1). There was no change of the spreading angle of the wake with porosity from the 75% to the 82% and 90% open model. A porosity of only 30% did lead to a reduction of the spreading angle by more than 50%.

Table 1 - Half spreading angles of the wakes at a towing speed of 0.2m/s.

Porosity	0%	30%	60%	75%	82%	90%
Half spreading angle of the wake	20°	9°	8°	5°	5°	5°

TKE

The specific turbulent kinetic energy (TKE) decreases with increasing porosity (see Figure 5). One diameter downstream from the centerline of the models, the main part of the TKE is located within the wake downstream from cylinders with porosities from 75% to 90%. The highest values of the TKE are found in the middle of the wake downstream from the 82% and 90% open models, while the TKE peaks in the middle and at the flanks of the wake downstream from the 75% open cylinder. The TKE peaks only at the flanks of the wake one diameter downstream from the solid model.

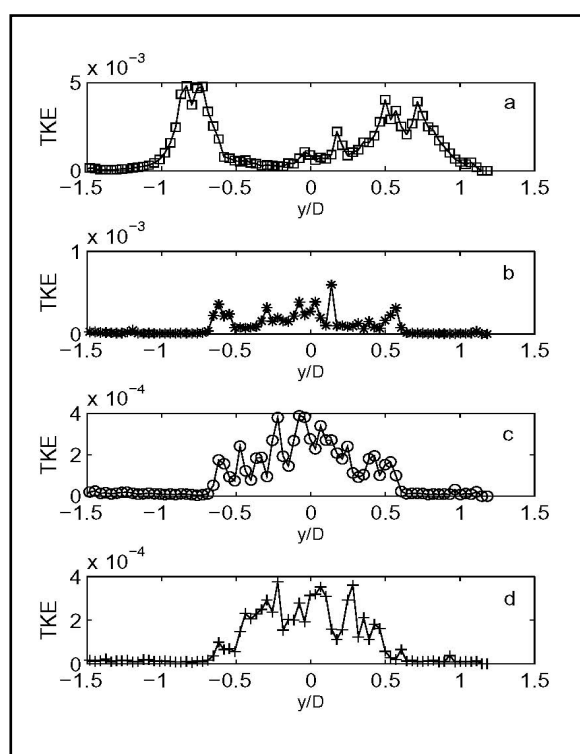


Figure 5 – TKE (m^2/s^2) in the wake of a solid (a), a 75% open (b), a 82% open (c) and a 90% open (d) cylinder 1 diameter downstream from the center-line of the cylinders. The towing speed (U_∞) was 0.2m/s. Note the different scales.

Forces

The measured drag forces on the solid cylinder at towing speeds of 0.01m/s and 0.05m/s agree well with the expected drag forces (see Table 2). The measured drag force at a towing speed of 0.2m/s is only about 75% of the expected drag force, which is mainly caused by 3D effects due to the finite length of the cylinder.

Table 2 – Expected (with $C_D = 1$) and measured drag forces on the solid cylinder at three towing speeds.

Towing speed [m/s]	0.01	0.05	0.2
Expected drag force [N]	0.0015	0.0375	0.6
Measured drag force [N]	0.0089	0.0389	4.6

The instantaneous total forces on the models and the maximum values of instantaneous drag forces within a time series decrease steadily with increasing porosity (see Figure 6). The time averaged drag forces on the models decrease steadily with increasing porosity from the 30% to the 90% open cylinder, but the solid cylinder shows a time averaged drag force below that of the 30% and 60% open cylinders. In the case of the porous models, the total forces on the cylinders were about 100% higher than the time averaged drag forces and about 50% - 70% higher than the maximum values of the drag forces within a time series. The differences are even bigger in case of the solid cylinder.

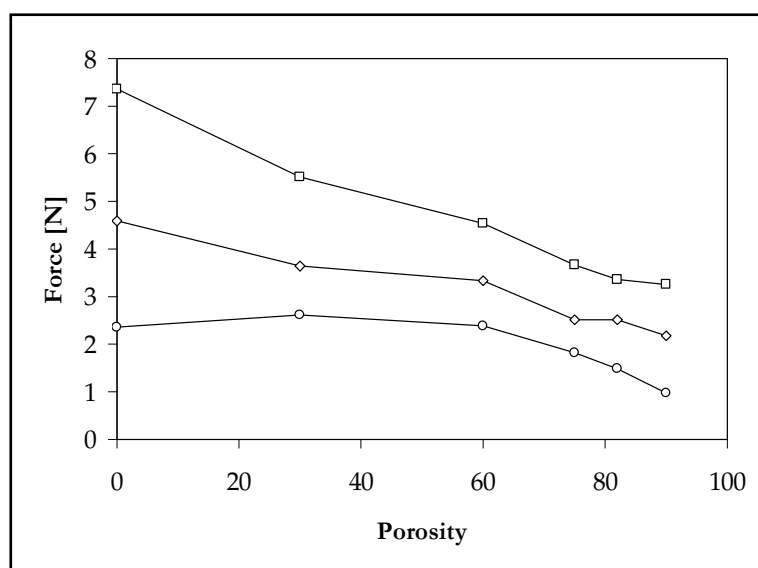


Fig. 6 – Instantaneous total forces (□), maximum values of the drag force within a time series (◇) and time averaged drag forces (○) on models with different porosities. The towing speed during the experiments was 0.2m/s).

DISCUSSION

Increasing porosity leads to a stronger water flow through the cylinders. The flow patterns around and through porous cylinders do not differ significantly with alteration of the porosity at high porosities (above 66%) but become less pronounced with increasing porosity of the models. A shift in the flow characteristics seems to occur with an alteration of the porosity between the 33% and the 66% open model. This agrees with the TKE profiles, which indicate a

shift in the flow characteristics at a porosity of around or below 75%. An increase in porosity is associated with more water flowing through the model, less increase of the flow speed at the flanks of the cylinders and to a decrease of the angle at which water leaves the cylinders in comparison to the initial flow direction on the backside of the models. Therefore, an increase in porosity leads to a narrower wake. There were 6 and 4 peaks within the fluctuations of the velocity defect in the wakes of the 82% and 90% open models. The 82% open cylinder consisted of 6 vertical strings and the 90% open model of 4 vertical strings. Presumably, the spacing between individual strings is big enough to allow single vortex streets to develop from individual strings of the mesh. The forces on porous cylinders increase rapidly with decreasing porosity. The time averaged drag forces on the models are much lower than the maximum values within a time series, which can be explained partly by fluctuations in the directions of the flow around the cylinders and in the wake. The time averaged drag forces on the solid model were below the forces on the 30% and 60% open models. This can be explained by a stronger periodic oscillation of the wake behind the solid model in comparison to the wake behind the porous cylinders. A periodic oscillation of the wake (due to eddy separation) leads to an oscillation of the drag forces in time. The lateral forces will oscillate with the same period, but a phase shift of π . The total forces should therefore be more stable in time, than the drag forces.

Biofouling is a serious problem in marine aquaculture (Hodson *et al.*, 1999; Ruokolaiti, 1988). Fouling on fish cage netting will reduce the porosity and may alter the flow around fish cages. Braithwaite *et al.* (2006) found that the net aperture occlusion can exceed 20% within a time period of only two weeks. The porosity of an Atlantic salmon fish cage (usually about 80%) could therefore decrease by 25% from about 80% to 60% within a short time. Thus, biofouling might lead to a change of the flow characteristics around and through a fish cage and to higher forces on the fish cage and cage mounts. The water flow through the cage can be weakened, the conversion of energy into turbulence can be changed, and the spreading angle of the wake can be increased. A reduced water flow through the fish cage will lead to reduced oxygen supply for the fish. Differences in the wake propagation and the turbulence characteristics will lead to different distribution patterns of particles and dissolved nutrients from the fish cage. A reduction of the porosity from 82% to 60% will lead to a substantial increase of the forces acting on fish cages. The maximum values of the drag force and instantaneous total forces on the cage will increase by over 30%. The average drag forces will increase by about 60%. These findings agree with results from a study by Swift *et al.* (2006), who found that fouling on nets might lead to a strong increase in the drag on the cages.

CONCLUSIONS

Increasing the porosity of cylinders leads to increased water flow through the cylinder. The flow around and through highly porous cylinders (porosity above 75%) might vary quantitatively with varying porosity, but the flow pattern might not change significantly. A change in the flow and wake characteristics seems to occur at a porosity of around 70%. Increasing porosity also leads to decreasing forces on porous cylinders, but it is important to distinguish between instantaneous forces and time averages of forces due to the oscillating direction of the flow. A porous cylinder will experience forces that exceed the time averaged force periodically.

Biofouling will have a substantial influence on the forces on a fish cage, the flow through and around a fish cage and the wake. Fouling therefore is an important factor for the design and operation of marine fish farms. Biofouling plays an important role for the distribution of particles and nutrients as well as for the oxygen supply for the fish inside a net pen.

ACKNOWLEDGEMENTS

The possibility to perform the work was provided through a PhD Fellowship from the Faculty of Engineering Science and Technology at the Norwegian University of Science and Technology. The work was partly financed by the Norwegian Research Council through the Programs *Integrate* and *Create* at SINTEF Fisheries and Aquaculture.

REFERENCES

- Bhattacharyya, S., Dhinakaran, S. and Khalili, A., 2006. Fluid motion around and through a porous cylinder. *Chemical Engineering Science*. Vol. 61. pp. 4451-4461.
- Braithwaite, R. A., Cadavid Carrascosa, M. C. and McEvoy, L. A., 2006. Biofouling of salmon cage netting and the efficacy of a typical copper-based antifoulant. *Aquaculture*. Vol. 262. pp. 219-226.
- Cheshuk, B. W., Purser, G. J. and Quintana, R., 2002. Integrated open-water mussel (*Mytilus planulatus*) and Atlantic salmon (*Salmo salar*) culture in Tasmania, Australia. *Aquaculture*. Vol. 218. pp. 357-378.
- Gansel, L., McClimans, T. A., Myrhaug, D., 2008. The effects of fish cages on ambient currents. *Proc. 27th International Conference on Offshore Mechanics and Arctic Engineering*. Estoril, Portugal, 15-20. June 2008. (In Press)
- Hodson, S. L., Burke, C. M. and Bisset, A. P., 1999. Biofouling of fish-cage netting: the efficacy of a silicone coating and the effect of netting colour. *Aquaculture*. Vol. 184. pp. 277-290.
- Neori, A., Chopin, T., Troell, M., Buschmann, A. H., Kraemer, G. P., Halling, C., Sphigel, M. and Yarish, C., 2003. Integrated aquaculture: rationale, evolution and state of the art emphasizing seaweed biofiltration in modern mariculture. *Aquaculture*. Vol. 231. pp. 361-391.
- Noymer, P. D., Glicksman, L. R. and Devendran, A., 1998. Drag on a permeable cylinder in steady flow at moderate Reynolds numbers. *Chemical Engineering Science*. Vol. 53. pp. 2859-2869.
- Ruokolaiti, C., 1988. Effects of fish farming on growth and chlorophyll a content of *Cladophora*. *Marine Pollution Bulletin*. Vol. 19. pp. 166-169.
- Sarà, G., Scilipoti, D., Mazzola, A. and Modica, A., 2003. Effects of fish farming waste to sedimentary and particulate organic matter in a southern Mediterranean area (Gulf of Castellammare, Sicily): a multiple stable isotope study (d13C and d15N). *Aquaculture*. Vol. 234. pp. 199-213.
- Swift, M. R., Fredriksson, D. W., Unrein, A., Fullerton, B., Patursson, O. and Baldwin, K., 2006. Drag force acting on biofouled net panels. *Aquacultural Engineering*. Vol. 35. pp. 292-299.
- Troell, M., Halling, C., Nilsson, A., Buschmann, A. H., Kautsky, N. and Kautsky, L., 1997. Integrated marine cultivation of *Gracilaria chilensis* (Gracilariales, Rhodophyta) and salmon cages for reduced environmental impact and increased economic output. *Aquaculture*. Vol. 156. pp. 45-61.

KEYWORDS

Porous cylinder, drag force, velocity defect, TKE, PIV, fish cage.

Session C: BREAKWATERS

COAST 2008, Trondheim, Norway

Presentation of Hans F. Burcharth

Aspects of breakwater design

Berm breakwaters

The performance of Sirevåg breakwater is revisited and compared to predictions by a new stability formula for berm breakwaters. Optimum design safety levels are discussed on the basis of probabilistic economical optimizations.

A large breakwater on exposed location

Design considerations related to the very large rubble mound breakwater at Punto Langosteira, La Coruña, Spain are discussed. This includes influence of construction material, safety during construction and stability of the structural parts determined by model tests. A new round head stability formula is presented.

Optimum design safety levels

The outcome of a comprehensive study of design safety levels for breakwaters, based on economic optimization, is presented.

See Coast 2008 homepage for extras. <http://www.ivt.ntnu.no/bat/english/coast2008/>

WAVE FIELD AND SCOUR CHARACTERISTICS AROUND SUBMERGED VERTICAL AND SEMICIRCULAR BREAKWATERS

*D. Morgan Young and Firat Y. Testik**

Civil Engineering Department, Clemson University, Clemson, SC 29634-0911, USA

Abstract

A laboratory study is presented herein investigating the effects of submerged vertical and semicircular breakwaters on local wave field and morphodynamics. This study aims to determine relationships for the wave reflection coefficient and the resultant two-dimensional onshore scour along the base of submerged breakwaters. The reflection coefficient is observed to rely mainly a dimensionless submergence parameter. Two semi-empirical parameterizations are proposed to predict reflection coefficients for the two breakwater types. Three important scour characteristics are investigated: maximum scour depth, scour length, and the distance of maximum scour depth location from the onshore breakwater face. The characteristics of onshore breakwater scour are found to be independent of submerged breakwater shape/type.

***Corresponding author:**

Firat Y. Testik
Civil Engineering Department
110 Lowry Hall
Clemson University
Clemson, SC 29634-0911, USA
Tel: +1 (864) 656-0484
Fax: +1 (864) 656-2670
E-mail: ftestik@clemson.edu

Keywords: submerged breakwaters, vertical breakwater, semicircular breakwater, waves, reflection coefficient, scour

INTRODUCTION

Offshore breakwaters are coastal structures that are commonly employed to provide protection to valuable coastal areas such as marinas, ports, and beaches from energetic ocean waves. The principle function of breakwaters is to cause waves to prematurely break, thereby reducing destructive wave forces often imparted on vulnerable shorelines; a task partially completed by the reflection of incident wave energy back out to sea. As more wave energy is reflected out to sea, less energy is imparted to the beach. High energy waves do not only impair the aesthetics of tourist-strewn beaches but storm-type waves can also damage sensitive ecosystems such as reefs, wetlands, and nesting areas. Traditionally, emerged breakwaters, or breakwaters whose crest pierces the mean water level, have been used to accomplish this task. Recently, submerged breakwaters, or breakwaters that lie entirely beneath the mean water level, have become more common. Submerged breakwaters are designed to offer protection by inducing partial reflection-transmission and/or breaking of large waves (Grilli et al. 1994). One advantage of submerged breakwaters is that they are often more aesthetically pleasing than emerged breakwaters, which is critical to the tourism industry in most coastal areas (Johnson, 2005). Another advantage of submerged breakwaters is their ability to maintain the landward flow of water, which may be important for water quality considerations (Kobayashi et al., 2007). On the other hand, submerged breakwaters usually dissipate less wave energy than emerged breakwaters.

Various types of submerged breakwaters exist; examples include vertical breakwaters, semicircular breakwaters, rubble mound breakwaters, and geosynthetic breakwaters. This study centers on the analysis and comparison of submerged vertical and semicircular breakwaters. Submerged vertical breakwaters typically exist as a sturdy vertical wall while submerged semicircular breakwaters are composed of a precast reinforced concrete structure built with a semicircular vault and bottom slab (Yuan and Tao, 2003). While submerged vertical breakwaters usually reflect more incident wave energy than submerged semicircular breakwaters, submerged semicircular breakwaters are oftentimes more stable under wave forcing, thusly decreasing the potential for failure.

Upon the introduction of a structure into a flow field, wave transformations occur. For breakwaters, an important wave transformation characteristic is the wave reflection and, thereby, the reflection coefficient (C_r), which is a measure of the incident wave energy that is reflected out to sea.

$$C_r = \left(\frac{H_r}{H_i} \right) \dots\dots\dots (1)$$

where H_r represents the reflected wave height and H_i represents the incident wave height. As C_r increases, less incident wave energy is available to be imparted on the shoreline. Therefore, estimation of the C_r value is crucial in determining the effectiveness of a breakwater.

Several experimental studies investigated wave reflection characteristics for submerged breakwaters. Losada et al. (1996) studied the effects of both regular and irregular waves on C_r for submerged breakwaters. It was found that submerged breakwaters under the influence of regular waves induce smaller C_r values than submerged breakwaters tested under irregular waves. However, the difference in C_r values between the two scenarios did not exceed 5%. Stamos et al. (2001), in their study of wave reflection for rigid and flexible breakwater cases, reported that the reflection coefficient increases with the increase in the stiffness of the breakwater. They also investigated the effects of kh (k – wave number, h – still water depth) on C_r and found no functional trend between the two.

When a structure is placed in a marine environment, the presence of the structure changes the flow field in its immediate environment, resulting in the formation of vortices around the structure which may induce scour (Sumer et al. 2001). Tang et al. (1998) investigated flow separation of a solitary wave passing over a submerged obstacle. Both the experimental and numerical results illustrated that as the wave passed over the structure a large vortex was first formed onshore of the structure accompanied by a secondary vortex below it (ideal conditions for potential onshore scour). With regards to oscillatory flows, Testik et al. (2005) observed that periodic horseshoe vortices form on both sides of a submerged finite length horizontal bottom-mounted cylinder that can be considered to mimic a submerged breakwater. As the flow changes direction, these vortices flip from one side of the submerged cylinder to the other.

When the vortices and the altered bed shear stress are sufficiently strong enough to induce initiation of sediment motion, sediment adjacent the coastal structure is transported away from the structure, and the process known as scouring occurs. If a structure experiences significant scour, the foundation integrity may be compromised and the structure could fail. Structural failure due to overturning/settling and structural failure due to sliding are common failure modes for submerged breakwaters (Hughes, 2002). Scour can occur along the trunk of breakwaters (two-dimensional) or at the head, or end, of a breakwater (three-dimensional). Since the majority of breakwater research has historically focused on emerged breakwaters, the majority of breakwater-induced scour studies focus on the evolution of scour offshore of the breakwater (e.g., Xie, 1981; Hughes and Fowler, 1991). Sumer et al. (2001), reviewing results from submerged breakwater studies, concluded that offshore scour at the trunk of submerged breakwaters experiences deposition and sometimes small scour due to significantly reduced wave reflection; a result mirrored by the current study. Therefore, this study centers on the analysis of two-dimensional scour that forms *onshore* of the breakwater.

This document is organized as follows. Experimental setup and methodology are briefly described in Section 2. Results for wave reflection from submerged breakwaters and breakwater-induced onshore scour are presented in Sections 3 and 4, respectively. Conclusions and discussions are given in Section 5.

EXPERIMENTAL SETUP AND METHODOLOGY

The experiments are carried out in a wave tank (12m x 0.6m x 0.6m) that mimics the oceanic coastal zone (see Fig. 1 for a schematic of the wave tank). The tank consists of a beach with adjustable sandy (quartz sand with a median diameter, $d = 0.067\text{cm}$) slope (0-1:20), a wave generator assembly, and walls composed of 1cm thick Plexiglas for visualization. A full account of the experimental setup and methodology can be found in Young and Testik (2008).

The offshore face of the breakwater is set as the x-axis origin with the positive x-direction being offshore. The bottom of the wave tank is set as the y-axis origin with the positive y-direction set towards the water surface. Six spatial locations onshore and offshore of the breakwater (see Fig. 1) are used in measuring wave elevations and water particle velocities.

Flow velocity measurements are taken using an acoustic Doppler velocimeter (ADV). Water surface elevation data are collected by three capacitance-type wave gauges. A Laser Displacement Sensor (LDS) is used to collect sand surface elevation data. The reflection coefficient (C_r) is calculated using a MATLAB code using a method introduced by Goda and Suzuki (1976).

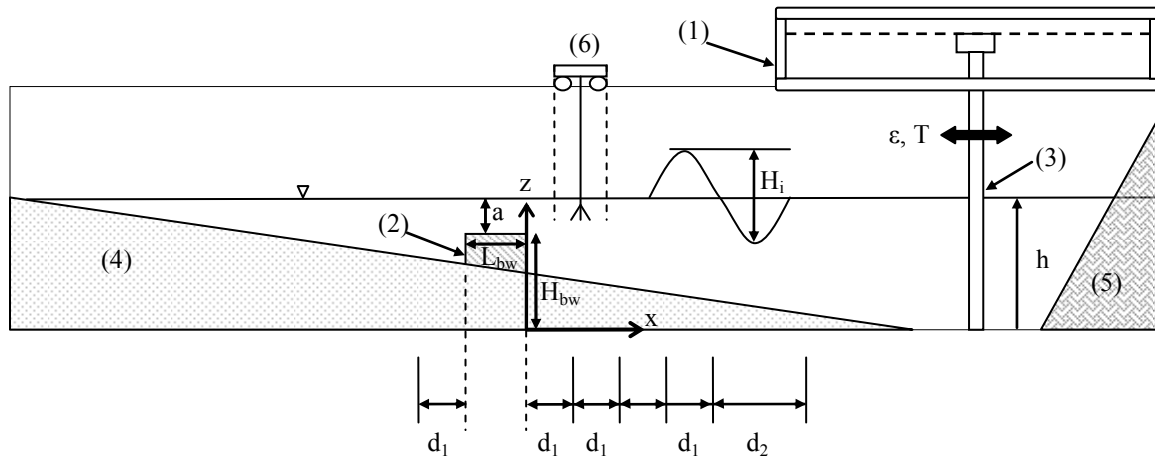


Figure 1. Wave tank schematic: (1) linear actuator and motor; (2) breakwater; (3) wave paddle; (4) sloping sandy beach; (5) wave absorber; (6) moveable cart assembly with wave gauges and Acoustic Doppler Velocimeter (ADV). Symbols: a - depth of submergence, L_{bw} - breakwater length, H_{bw} - breakwater height, H_i - incident wave height, ϵ - amplitude of wave paddle excursion, T - wave period, h - still water depth at the paddle, $d_1 = 50\text{cm}$, $d_2 = 100\text{cm}$.

Preliminary experiments were conducted to identify the primary governing dimensionless parameters. These preliminary experiments indicated the importance of only three dimensionless

parameters: the Keulegan-Carpenter number ($KC = \left(\frac{H_i \pi}{L_{bw}}\right)$), the mobility number

$$\left(\psi = \left(\frac{\left(\frac{H_i \pi}{T \sinh(kh)}\right)^2}{g * d}\right)\right),$$

g^* -reduced gravitational acceleration acting on the sediment due to

buoyancy forces), and the dimensionless breakwater submergence, $\left(\frac{a}{H_i}\right)$, (see the caption of Fig.

1 for definition of symbols).

WAVE REFLECTION

To quantify the efficacy of submerged breakwaters in reflecting wave energy out to the sea, the reflection coefficient, $C_r (=H_r/H_i)$, was investigated for both vertical and semicircular breakwaters. Experiments indicated that the only dimensionless parameter that governs the wave reflection is $\frac{a}{H_i}$, the dimensionless submergence depth. Measured wave reflection coefficients

for vertical and semicircular breakwaters were observed sharing the same exponential functional dependency on $\frac{a}{H_i}$ with different constant coefficients as follows.

$$C_{r\text{-vertical}} = 0.5e^{\left(-1.25\frac{a}{H_i}\right)} \dots\dots\dots (2)$$

$$C_{r\text{-semicircular}} = 0.5e^{\left(-2.0\frac{a}{H_i}\right)} \dots\dots\dots (3)$$

It should be noted that measured reflection coefficients are corrected by taking into account the background wave reflection that is intrinsic to wavetanks due to boundaries such as tank walls

and wave paddle. In the oceanic coastal zone, typical reflection coefficients for similar beach profiles are around 0.02. However, the wave tank in the present study consistently produces reflection coefficients around 0.06 even on horizontal and sloping beaches without breakwaters. Therefore, the background reflection coefficient is subtracted from the measured reflection coefficient for each experimental run. The corrected reflection coefficient provides an accurate account of reflection solely due to the breakwater.

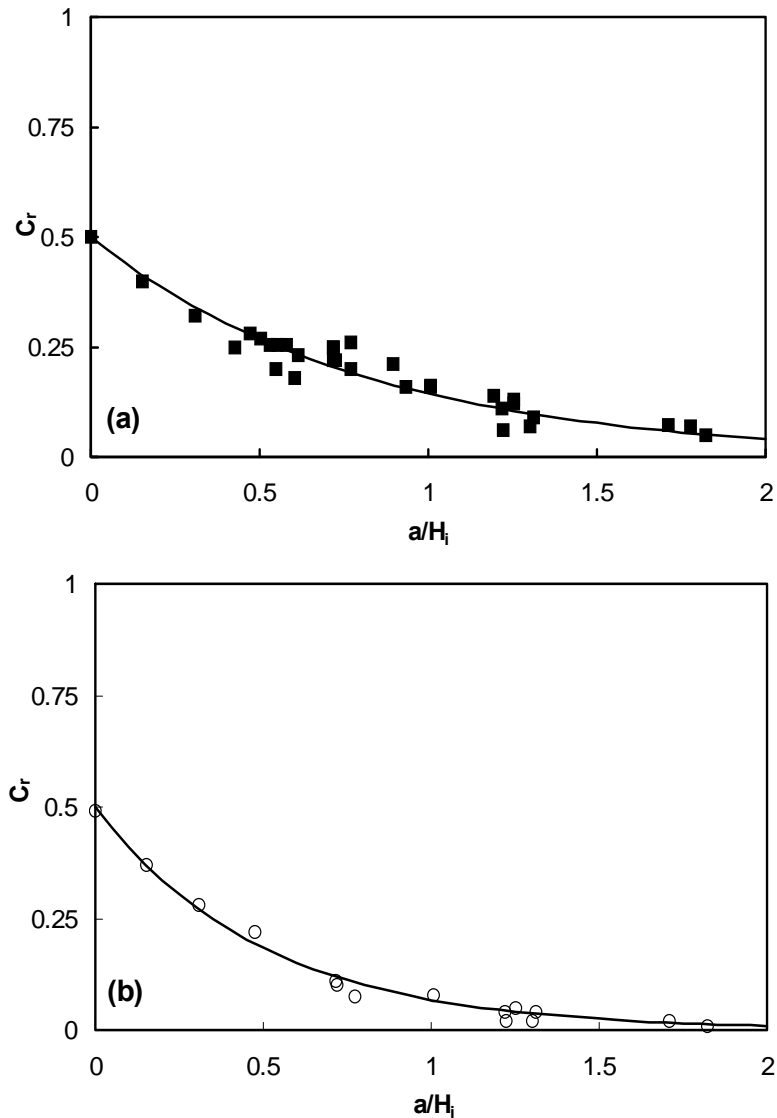


Figure 2. Relationship between $\left(\frac{a}{H_i}\right)$ and C_r for (a) vertical breakwaters and (b) semi-circular breakwaters. Solid lines – estimate by Eqn. 2 for (a) and estimate by Eqn. 3 for (b); (■) – measured for (a), (○) – measured for (b).

Dependency of measured and estimated C_r values for vertical (Fig. 2a) and semicircular (Fig. 2b) breakwaters on $\frac{a}{H_i}$ values are shown in Fig. 2. This figure illustrates that as $\frac{a}{H_i}$ decreases (for fixed H_i and decreasing a), C_r increases for both types of breakwaters. As $\frac{a}{H_i}$ becomes zero (breakwater's crest at the still water surface), C_r reaches its maximum value, 0.5. For the

asymptotic case when $\frac{a}{H_i}$ approaches infinity, C_r approaches zero. In order for $\frac{a}{H_i}$ to approach infinity, either a approaches infinity (finite breakwater height at infinite water depth) while H_i remains finite or H_i approaches zero (absence of waves) while a remains finite.

A comparison of the reflection coefficients for vertical and semicircular breakwaters under the same conditions (same $\frac{a}{H_i}$ values) is undertaken as well. The ratio between the two breakwaters' reflection coefficients goes to one as the breakwater's crest approaches the still water surface. This finding indicates that for relatively small submergence depths breakwater shape does not play a significant role in the wave reflection. However, as submergence depth increases, the difference between wave reflection by vertical and semicircular breakwaters becomes pronounced.

BREAKWATER-INDUCED ONSHORE SCOUR

This section describes the scour formations onshore of the submerged breakwaters. Note that scour formations offshore of the submerged breakwaters are observed to be insignificant for the experimental conditions considered.

Two different onshore scour patterns/regimes with different characteristics are identified in the experiments: attached scour and detached scour. Definition sketches for these two scour regimes are given in Fig. 3. Onshore scour is classified as attached scour when the scour hole is connected to the onshore face of the breakwater while detached scour occurs when the scour hole is not connected to the breakwater. For both scour regimes, the important scour characteristics of engineering importance are scour length (L_s), scour depth (S_{max}), and the distance of S_{max} location from the onshore breakwater face (D_s). Hence, in this study quantitative scour modeling efforts are focused on identifying the conditions for the occurrence of each scour regime and estimation of the values of the aforementioned scour characteristics.

The principal factor in the selection of the scour regime is concluded to be the Keulegan-Carpenter number (KC), and the following condition determines the scour type:

$$\text{attached scour: } KC = \left(\frac{H_i \pi}{L_{bw}} \right) \leq \pi \dots\dots\dots (4)$$

$$\text{detached scour: } KC = \left(\frac{H_i \pi}{L_{bw}} \right) > \pi \dots\dots\dots (5)$$

Attached scour occurs when the incident wave height at the breakwater is less than or equal to the length of the breakwater. In this case, the turbulent jet formed by the breaking wave impacts on the crest of the breakwater, thereby scouring sediment starting from the immediate vicinity of the onshore face of the breakwater. Conversely, the vortex formed by a breaking wave whose height is larger than the breakwater will scour sediment that lies farther away from the onshore face of the breakwater. As this vortex moves onshore, it pushes sediment onshore and pushes scoured sediment offshore towards the breakwater, causing sediment accumulation at the onshore face of the breakwater.

While the maximum scour depth (S_{max}) does not depend on the scour regime, scour length (L_s) and the distance of S_{max} location from the onshore breakwater face (D_s) do depend on the scour regime. A semi-empirical parameterization for S_{max} is elucidated below.

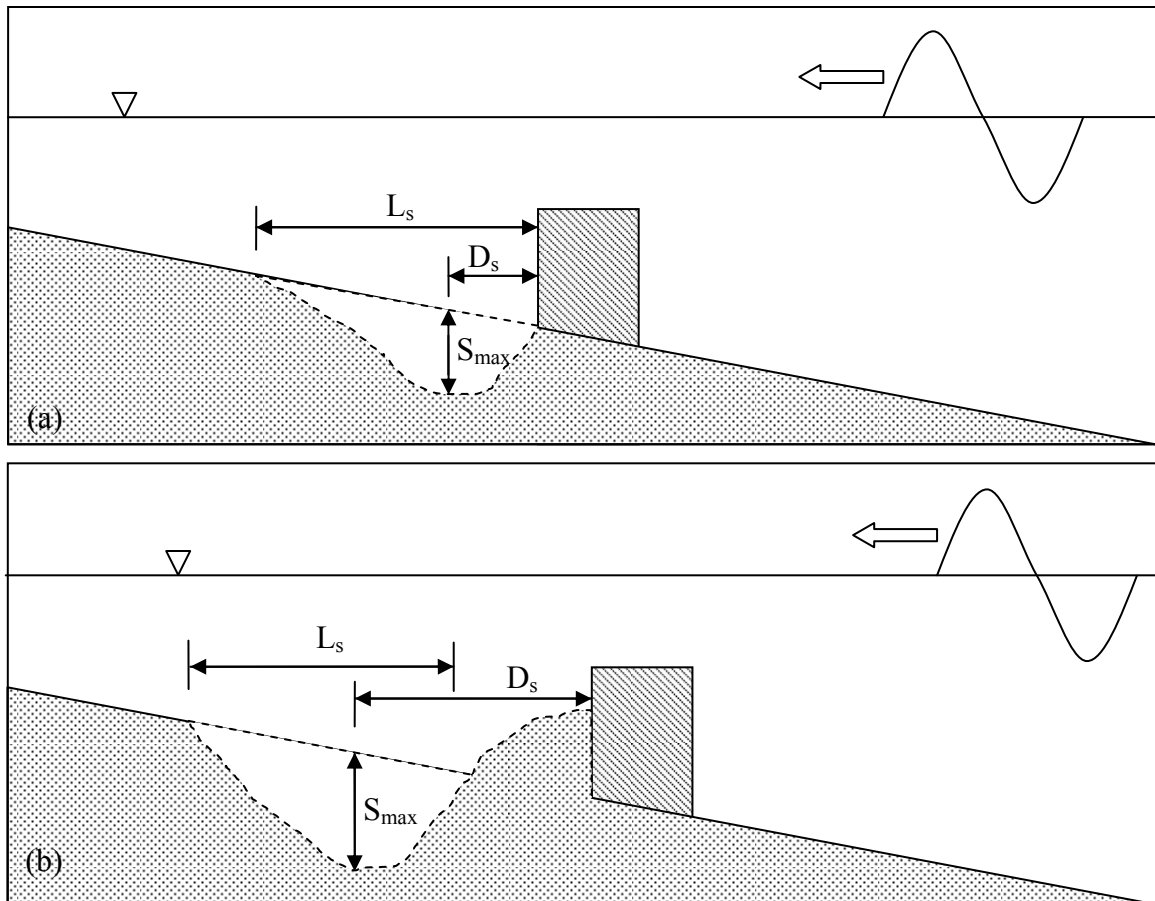


Figure 3. Definition sketch for scour patterns and parameters: (a) attached scour, (b) detached scour.

Maximum Scour Depth, S_{max} :

The maximum scour depth is defined as the maximum vertical distance between the initial sand level ($t=0\text{min}$) and the final sand level (after ~ 3000 waves) in the scour hole onshore of the breakwater. Analysis of the experimental data showed that the dimensionless maximum scour depth (S_{max}/L_{bw}) is a function primarily of the Keulegan-Carpenter number and the mobility number only. The dimensionless maximum scour depth is observed to vary linearly with the KC and to the one half power with ψ , indicating that maximum scour depth is a quadratic function of incident wave height. Since wave height and maximum flow velocity are related linearly from linear wave theory, it can be concluded that maximum scour depth is a quadratic function of maximum flow velocity; hence, a linear function of drag force. Therefore, as the incident wave height increases, the breaking waves impart a larger force on the localized onshore sediment, causing deeper scour. The proposed semi-empirical parameterization for the dimensionless maximum scour depth is given by Eqn. 6.

$$\frac{S_{max}}{L_{bw}} = 0.0125\psi^{0.5} KC \dots\dots\dots (6)$$

The dimensionless maximum scour depth data from all of the experiments are presented in Fig. 4. Since the scour regime does not factor into the maximum scour depth value, the estimate by Eqn. 6 (solid line) fits well to the S_{max}/L_{bw} observations for both attached and detached scour regimes (symbols).

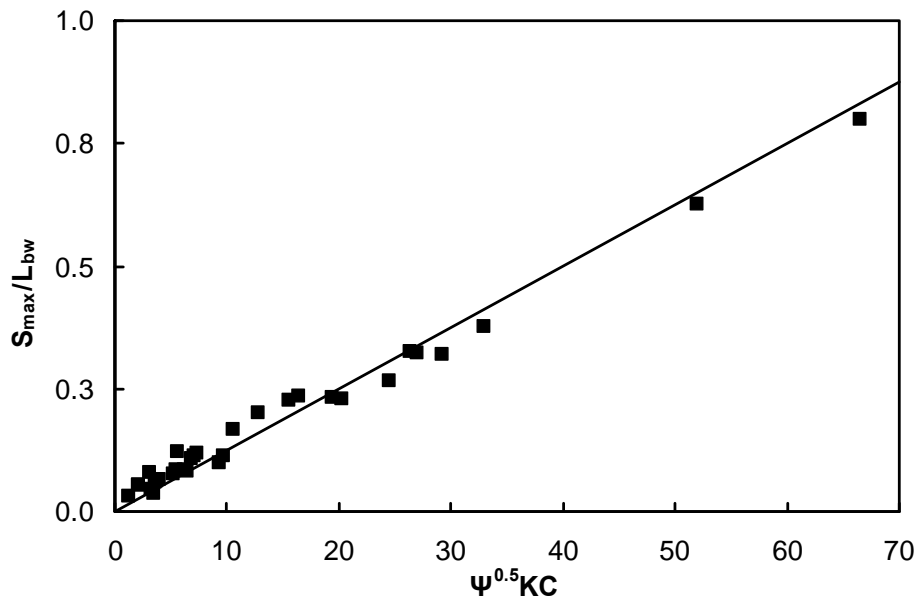


Figure 4. Relationship between $\psi^{0.5}KC$ and $\frac{S_{max}}{L_{bw}}$. Solid line – estimate by Eqn. 6; symbols – measured values.

Scour Length (L_s) and the Distance of S_{max} Location to the Onshore Breakwater Face (D_s):

Dimensionless scour length (L_s/L_{bw}) is observed to be a linear function of the Keulegan-Carpenter number with different proportionality constants for the attached and detached scour regimes. Note that dependency of scour length on KC has been documented previously for piles (Carreiras et al., 2000; Mory et al., 2000; and Larroude' and Mory, 2000) and cylinders (Voropayev et al., 2003; Testik et. al, 2007) with different functional forms. In the detached regime (small KC), L_s/L_{bw} experiences a large linear growth rate as KC increases. A transition zone exists between attached and detached scour regimes (i.e. vicinity of the regime separation point) and is characterized by a sudden change in the dimensionless scour length value from one regime to the other. As KC increases past the transition zone and the scour becomes detached, L_s/L_{bw} increases at a much smaller rate.

Even though the maximum scour depth is observed to be independent of the scour regime, the distance of S_{max} location from the onshore breakwater face (D_s) is observed to depend on the scour regime. Similar to the dimensionless scour length, D_s/L_{bw} is found to be linearly proportional to KC with different proportionality constants for each scour regime. Unlike L_s , D_s increases at a slow rate with increasing KC while the scour is attached. Once again, a transition zone occurs at $KC=\pi$ and is associated with a sudden jump in the D_s/L_{bw} values from one regime to the other. Once the scour becomes detached, D_s increases at a much higher rate.

CONCLUSIONS

This study investigates the effects of submerged vertical and semi-circular breakwaters on the wave field and scour development. The primary goals of the conducted research are to provide accurate parameterizations for estimating the wave reflection coefficient and geometrical characteristics of the two-dimensional onshore scour induced by the breakwater. Results of this study are expected to be useful in the conceptual design of submerged semi-circular and vertical breakwaters.

The experiments centered on the wave reflection coefficient led to the conclusion that dimensionless submergence depth (a/H_i) is the sole dimensionless flow parameter for determining C_r value. Semi-empirical parameterizations for the reflection coefficients for submerged breakwaters of vertical and semi-circular shape are developed (Eqn. 2 and Eqn. 3). The reflection coefficient parameterizations for both breakwater types were found to share the same functional dependency on a/H_i yet different constants are used in each. For both types of breakwaters, maximum C_r value is 0.5 for the dimensionless submergence depth value of zero. The C_r values decrease as the dimensionless submergence depth increases, with a larger decrease for semi-circular breakwaters indicating their reduced efficiency compared to their vertical counterparts.

Breakwater-induced onshore scour by bed-load sediment transport mode is studied. Two different scour regimes, attached and detached, are identified. Scour is classified as attached scour when the scour hole is connected to the onshore breakwater face and as detached scour when the scour hole is not connected to the onshore face of the breakwater. Selection of the scour regime is governed by the $KC (= \frac{H_i \pi}{L_{bw}})$ value of the flow. Attached scour occurs when KC

value is less than or equal to π while detached scour occurs when KC value is greater than π (see Eqns. 4 and 5). Therefore, detached (attached) scour occurs when the height of the incident wave is larger than (less than or equal to) the length of the breakwater. This knowledge is expected to be useful to coastal engineers designing a breakwater that induces either of these reported scour regimes under design wave conditions. For example, attached scour may be preferable for a shorter extent of the armor layer from the breakwater face while detached scour may be preferable for a reduced sliding failure threat.

Three principle onshore scour characteristics that were studied are depth of scour (S_{max}), length of scour (L_s), and distance of S_{max} location from the onshore breakwater face (D_s). These three scour geometrical characteristics are integral in analyzing a breakwater project for potential failure. An important conclusion of the study is that the breakwater shape plays *no role in determining the scour characteristics*. It is observed that S_{max} value does not depend on scour regime and is determined by KC and ψ (Eqn. 6). On the other hand, L_s and D_s values are observed to depend on the scour regime and are determined by KC solely.

The importance of breakwaters cannot be overstated. The financial advantages of establishing these structures as part of a comprehensive beach nourishment plan, together with their obvious use as environmental support systems, can positively impact vulnerable coastlines in times of need. Submerged breakwaters serve both these purposes while remaining hidden beneath the water surface and maintaining attractive aesthetics. This study, investigating the principal factors of breakwater-flow field alteration and breakwater-induced scour, presents physics-based models for the wave reflection and onshore scour characteristics. It is expected that these findings will be useful for civil engineers in their continuously difficult and admirable endeavor of protecting coastlines.

ACKNOWLEDGMENTS

This research was supported by the funds provided by College of Engineering and Science at Clemson University to the second author. This work is part of the M.Sc. thesis of the first author conducted under the guidance of the second author. We would like to thank Mr. Siamak M. Mohammadi for his help in the instrumentation.

REFERENCES

- Carreiras, J., Larroude, P., Seabra-Santos, J., Mory, M., 2000. Wave scour around piles. Abstract of paper for 27th ICCE, Sydney, ASCE .
- Goda, Y., Suzuki, Y., Estimation of incident and reflected waves in random wave experiments. Port and Harbor Research Institute, Ministry of Transport, Nagase, Yokosuka, Japan, 1976.
- Grilli, S.T., Losada, M.A., Martin, F., 1994. Characteristics of solitary wave braking induced by breakwaters. ASCE Journal of waterway, port, coastal, and ocean engineering, Vol. 120, No. 1, pp. 74-92.
- Hughes, S.A., and Fowler, J.E., 1991. Wave-induced scour prediction at vertical walls. Proceedings of Coastal Sediments' 91, Seattle, WA, ASCE, vol. 2, 1886-1900.
- Hughes, S.A., 2002. Design of maritime structures: scour and scour protection. United States Army Corps of Engineers.
- Johnson, H.K., 2005. Wave modeling in the vicinity of submerged breakwaters. Coastal Engineering (53), pp. 39-48.
- Kobayashi, N., Leslie, E.M., Takao, O., Melby, J., 2007. Irregular breaking wave transmission over submerged porous breakwater. ASCE Journal of waterway, port, coastal, and ocean engineering, Vol. 133, No.2. pp. 104-116.
- Larroude', Ph., Mory, M., 2000. Erosion autour de structures co^ tie`res. VIe`me Journe`es Nationales Ge`nie Civil—Ge`nie Co^ tier, Caen *.
- Losada, I.J., Silva, R., Losada, M.A., 1996. Interaction of non-breaking directional random waves with submerged breakwaters. Coastal Engineering (28), pp. 249-266.
- Mory, M., Larroude', Ph., Carreiras, J., Seabra Santos, F.J., 2000. Scour around pile groups. Proceedings of Coastal Structures 99, Santander, Spain, 7 – 9 June, 1999, vol. 2. Balkema, Rotterdam, Netherlands, pp. 773–781.
- Stamos, D.G., Hajj, M.R., 2001. Reflection and transmission of waves over submerged breakwaters. ASCE Journal of Engineering Mechanics, Vol 127, No. 2. pp. 99-105.
- Sumer, B.M., Whitehouse, J.S., Torum, A., 2001. Scour around coastal structures: a summary of recent research. Coastal Engineering (44), pp. 153-190.
- Tang, C.J., Chang, J.H., 1998. Flow separation during solitary wave passing over submerged obstacle. ASCE Journal of Hydraulic Engineering, Vol. 124, No. 7. pp. 742-749.
- Testik, F.Y., Voropayev, S.I., Fernando, H.J.S., 2005. Flow around a short horizontal bottom cylinder under steady and oscillatory flows. Physics of Fluids, Vol. 17, pp. 1-12.
- Testik, F.Y., Voropayev, S.I., Fernando, H.J.S., Balasubramanian, S., 2007. Mine Burial in the Shoaling Zone: Scaling of Laboratory Results to Oceanic Situations. IEEE Journal of Oceanic Engineering, Vol. 32, No. 1, pp. 204-213.

- Voropayev, S.I., Testik, F.Y., 2003. Burial and scour around short cylinder under progressive shoaling waves. *Ocean Engineering*, Vol. 30, pp. 1647-1667.
- Xie, S.L., 1981. Scouring patterns in front of vertical breakwaters and their influence on the stability of the foundations of the breakwaters. Report, Department of Civil engineering, Delft University of Technology, Delft, The Netherlands, September, 61 p.
- Young, D.M., Testik, F.Y., 2008. Wave field and scour characteristics around submerged vertical and semicircular breakwaters. *Coastal Engineering* (Under Review).
- Yuan, D., Tao, Jianhua, T., 2003. Wave forces on submerged, alternately submerged, and emerged semicircular breakwaters. *Coastal Engineering* (48), pp. 75-93.

IMPROVED EFFICIENCY OF BUBBLE CURTAINS

Thomas McClimans

SINTEF Fisheries and Aquaculture, Trondheim, Norway

ABSTRACT

Bubble curtains have been used in Norway to mix seawater to the freshwater outflow from hydropower plants to avoid freezing of fjords during the winter. These robust systems produce bubbles up to the stability limit of about 5 cm diameter. The bubbles slip through the water at a speed comparable to the rising plume speed, halving the time they can contribute to buoyancy. It is suggested that the use of small bubbles with a slip speed much less than the plume speed can improve the efficiency of the supplied air. Preliminary tests in a small flume show that there are several challenges to address including the pressure needed to produce small bubbles, bubble coalescence and possibly supersaturation of nitrogen in areas with fish farms.

INTRODUCTION

During the Second World War the Allies were looking for a method to combat waves during landing operations at Normandy. They needed a system that was portable. Although we have no documentation of the developments during the war, Taylor (1955) presented the theory of using air curtains to induce currents to combat waves. The idea then was to produce a surface flow that would act against the group velocity of the waves and trip the waves in much the same way a berm breakwater works. Engineering aspects of this scheme were tested at Wallingford (Bulson, 1961). In Norway, the technology was applied to quite a different problem: to combat freezing of Norwegian fjords due to winter discharges of fresh water from hydropower plants. The first of these was at Mo I Rana (Rye, 1978). Here, the induced surface flow was designed to match the outflow of the discharge from the power plant. Moreover, the thickness of the outflow from the bubble curtain was to match the thickness of the outflowing freshwater. This has been in successful operation since 1969.

The pneumatic curtain at the narrows in Holandsfjord, in northern Norway, is more complicated due to tidal currents. The mooring system had to be designed to maintain a long, horizontal air pipe across the channel several meters above the sea bed, but within the wave zone (Eidnes & Tørum, 2001). A photo of the surface disturbance from the bubble curtain in Holandsfjord is shown in Figure 1. The outflow from the power plant is coming from the left (Eidnes, 2004). This system has been operating for 5 winters and is being upgraded to save energy costs for air compressors (McClimans & Jenssen, 2008).



Figure 1. Surface disturbance from the bubble curtain in Holandsfjord (Eidnes, 2004). The brackish outflow is coming from the left.

These applications use large bubbles near the instability limit of a few cm in diameter. This is achieved with a simple, robust design with nozzles/holes that require little maintenance. These, however, are expensive to operate continuously, due to the inefficiency of the buoyancy flux of large bubbles and increasing energy prices. However, a more advanced technological solution faces several challenges in an environment with waves, currents and marine growth, among other factors. The objective of the present study is to improve the efficiency of bubble curtains for mixing seawater to the freshwater from hydropower plants like outflow from the Svartisen power plant to Holandsfjord (McClimans & Jenssen, 2008).

Freshwater is known to have a maximum density at 4°C at atmospheric pressure. The temperature of maximum density decreases with salinity, as does the freezing point. The two lines cross at a salinity of 25 ppt, above which further cooling causes normal convection and exchange with deeper water. Thus, a mixture of 25 ppt is a minimum requirement to avoid ice formation seaward of the bubble curtain during periods of very cold, still air and radiative cooling during the long winter nights.

INDUCED FLOWS BY A BUBBLE CURTAIN

For the design of a bubble curtain, the criteria used for the amount of water to be lifted followed the recommendation of Bulson (1961) for damping waves in harbors. The surface-induced flow had the maximum horizontal velocity V and thickness h necessary to counteract the outflow from the river. Bulson showed that $V \approx Q^{1/3}$, where Q is the air flow. A sketch of the 2 dimensional induced flow field from a bubble curtain is shown in Figure 2 (for this case, $V = u_1$). Since the volume fluxes are enormous for this task, studies were made to increase the efficiency of the artificial upwelling obtained by Bulson. Trætteberg (1967) tested the effect of supplying the air flow through two and three parallel pipes. The results of surface velocity induced by two parallel pipes at depth D and separation B , normalized to Bulson's single pipe result V_{Bulson} , are shown in Figure 3. The single pipe result for half the air flow ($Q/2$), equivalent to separate plumes, is also noted. A B/D of 0.15 was recommended. A $V/V_{Bulson} = 1.2$ gives a 70% effective increase in Q . The results using three parallel pipes were inferior to those for two.

The two-pipe arrangement is the line source equivalent of a ring diffuser used in several other applications (e.g. Wüest *et al.*, 1992). In spite of this result, most systems are designed with a single pipe to simplify the mooring system as for the one in Holandsfjord.

Sægrov (1975) challenged the application of the Bulson criterion, which applied to wave kinematics in a non-stratified sea at rest. Starting with the extensive results of Kobus (1968), which showed a *vertical volume flux* proportional to $Q^{1/2}$, also for homogeneous water, Sægrov ran tests of a curtain in the stratified waters of the Dora submarine dock, adjacent to the Nid River in Trondheim. Sægrov showed that the vertical transport must break through the surface layer to mix the water masses. For less Q , there is essentially no mixing. Above this necessary discharge, the data showed an increase similar to Kobus'. Brevik & Kristiansen (2002) criticized the results of Kobus and, indeed, within the data scatter, both Kobus' and Sægrov's results could support a $Q^{1/3}$ dependency as well.

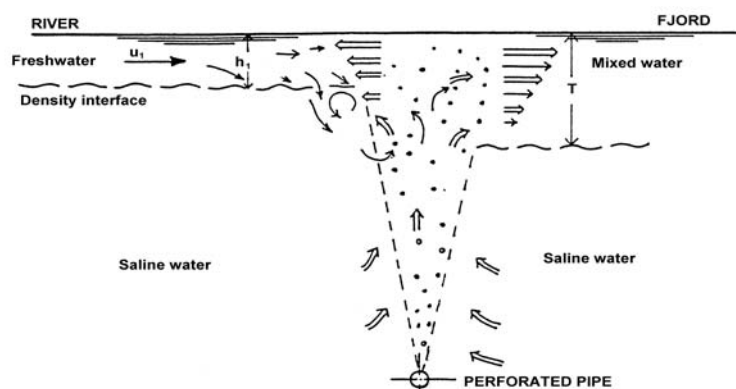


Figure 2. A sketch of the flow induced by a bubble curtain under a river outflow (Eidnes, 2004).

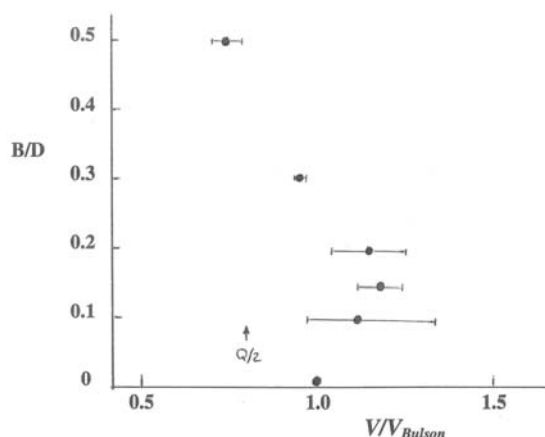


Figure 3. Laboratory results of the gain by using two parallel pipes (Trætterberg, 1967).

Aseada & Imberger (1993) considered a continuously stratified recipient, including the case of a nearly two-layer environment. The dome of upwelled water fronts against the brackish water, creating a mixing surface. Without advection of the surface layer, the mixture intrudes between layers on both sides of the bubble curtain. The criterion that the induced surface velocity and thickness match the outflowing brackish water (see Figure 2) assures an effective mixing and a seaward transport of the mixture. It turns out that this criterion also provides the necessary flux of salt water to achieve the required mixing.

Other specific criteria for the present application are that the source of buoyancy be deep enough to lift significant amounts of warm, saline water from the deeper layer to the upper, buoyant mixing layer to produce a surface salinity above 25 ppt and that the pipes and floats be deep enough to avoid interference with surface vessels. These are apparently all fulfilled using the criteria of Bulson for pneumatic breakwaters (Eidnes, 2004). To avoid freezing during the winter, some power stations submerged their outflows in the fjord to produce a mixture exceeding a salinity of 25 ppt. The one-phase plume has been shown to be more energy efficient than a bubble curtain (Hansen *et al.*, 2003), but must operate all year round, rather than only during the 5 winter months of significant sub-zero temperatures.

A CASE FOR SMALL BUBBLES

Although large bubbles produce highly turbulent wakes, they slip through the water column at speeds comparable to the transport speed in the rising plume ($1/4$ - $1/2$ m/s). Most *laboratory* plume studies are also run with slip velocities on the order of plume rise speeds (e.g. Fanneløp and Sjøen, 1980). This reduces the duration of their effective buoyancy force. If the air bubbles could be held in place longer, the efficiency of the buoyancy would be higher. A measure of the efficiency of a bubble curtain is the entrainment coefficient α , the ratio of ambient fluid engulfed by the plume to the transport in the plume. An earlier study of bubble plumes by Rowe *et al.* (1989) showed an increase in α as the source strength increased. This may explain the greater dependence on Q ($V \sim Q^{1/2}$) claimed by Kobus. This result can be interpreted as an increase of the transport speed in the plume relative to the bubble slip speed. As the ratio of plume speed to slip speed increases to infinity, with Q , the bubble plume approaches a single phase plume like a heat discharge or a submerged freshwater discharge in the sea. The plume speed for a continuum (single phase) plume is proportional to $Q^{1/3}$, similar to Bulson's results, and independent of depth (Fischer *et al.*, 1969, Ch. 9). A similar improvement in entrainment can be achieved for smaller plumes by reducing the slip speed of the rising bubbles, *i.e.* by using smaller bubbles. As the slip speed reduces to zero, the bubble plume approaches the single phase plume.

The slip velocity of bubbles is not a simple relation due to the various flow regimes (Figure 4). As the flow around the bubble goes from laminar (Stokes) flow to the turbulent regime, there is a transition from an increasing slip speed to a nearly constant speed of about 25 cm/s until the bubble diameter approaches Reynolds numbers $Re \equiv du_s/\nu = 2500$, where d is the bubble diameter, u_s is the slip speed and ν is the kinematic viscosity. Beyond this, the slip speed rises to about 70 cm/s as the bubbles approach their stability limit of a diameter around 5 cm. Note also that the slip speed is much more complicated for clean bubbles than for "dirty" bubbles, that is, bubbles with contaminated surfaces. These results are also affected by the temperature/viscosity of the water.

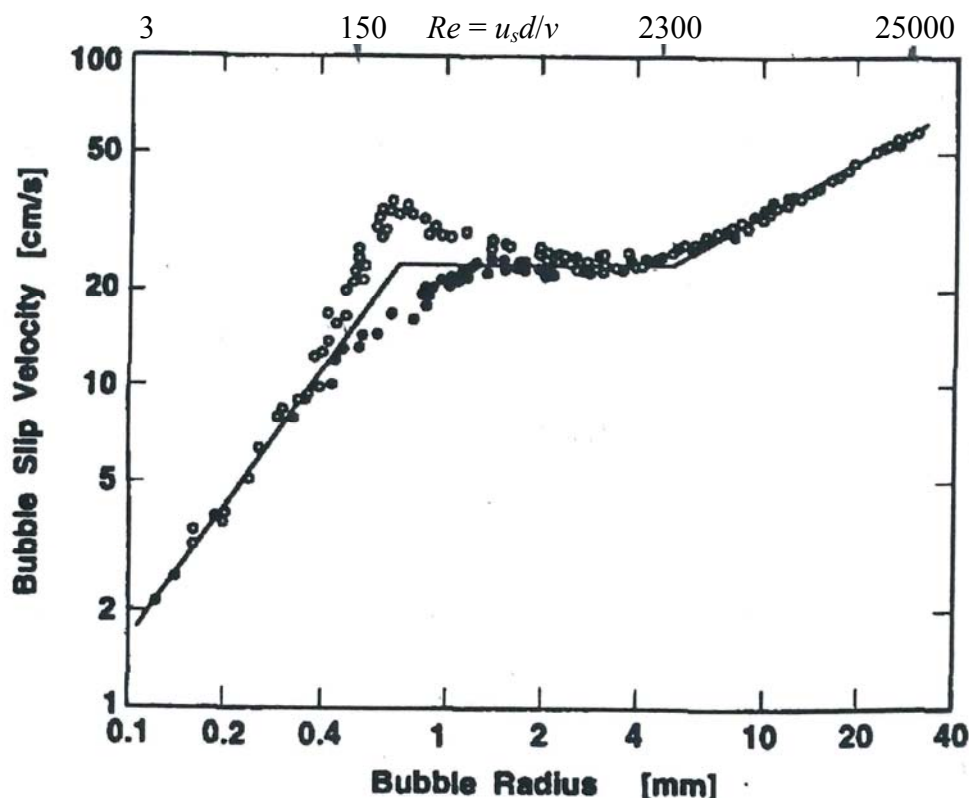


Figure 4. The slip speed of bubbles. Open circles: clean bubbles, filled circles: dirty bubbles (adapted from Wüest *et al.*, 1992).

ONE AND TWO-PHASE PLUMES

The effectiveness of the plume can be viewed as the ratio of the width of the buoyancy distribution compared with the width of the induced flow, often called λ . For single phase, 3-D plumes, this is about 1.2 (Fischer *et al.*, 1979). For bubble plumes, this is usually less than 1. Estimates of this ratio vary from 0.6 to 0.85 (Fanneløp & Sjøen, 1980; Brevik & Kristiansen, 2002). Indeed, most investigators use a value close to 0.8. This is due to the tendency for bubbles to collect near the center of the plume (Leitch and Baines, 1989). However, Rowe *et al.* (1989) showed an increase of λ approaching 1.2 for very large (high speed) plumes. A brief comparison of the results for one and two phase plumes is given in Table 1. The inverse square of λ can be interpreted as the plume Prandtl number, Pr_p , expressing the ratio of the horizontal viscosity to the diffusivity. For the continuum (single phase flow) $Pr_p = 0.7$, while a typical value for the two-phase bubble plume is 1.5.

Table 1. A comparison of various widths of one and two phase plumes.

<u>Ratio of widths</u> (λ)	<u>2-D (curtain)</u>	<u>3-D</u>
Freshwater/momentum (List*)	1.35	1.2
Bubbles/momentum (Fanneløp**)	0.85	0.8
Bubbles/dye (Leitch & Baines)	-	~ 1/3

* Fischer *et al.* Ch. 9

** Fanneløp *et al.* ; Fanneløp & Sjøen

PLUME TURBULENCE

The values for the single phase plume can be seen as a result of the turbulent eddies formed by the buoyancy flux – a series of ring vortices (Figure 5). The upper flow in the rings transports buoyant fluid to the side, where it has a negative velocity defect, thereby giving a relatively more narrow velocity profile. It is apparent that the buoyancy in this outer part is important for the vertical force and entrainment. The results of Trætteberg (1969) represent an attempt to spread the bubbles and increase the effective width for a limited range of heights above the source. Rowe *et al.* (1989) show an increase of entrainment by more than 50% as the plume strength increases by increasing Q . For large eddy speeds, more bubbles will diffuse to the outer portion of the plume. The large plumes all have bubbles at the limits of stability (2-4 cm diameter), with slip speeds on the order of $1/4$ - $1/2$ m/s.

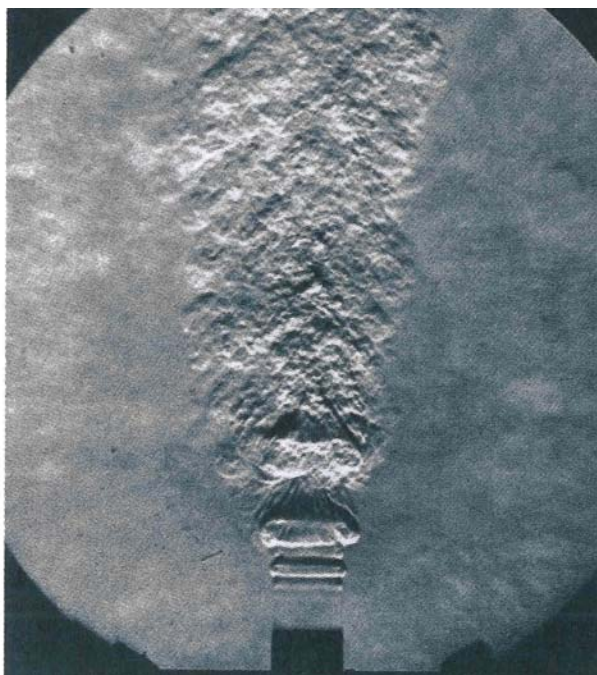


Figure 5. Toroidal eddy formation from the momentum flux at the source of a 3-D plume (Fischer *et al.*, 1969).

A COMPARISON OF A BUBBLE CURTAIN AND A SUBMERGED FRESHWATER DISCHARGE AT SEA

Table 1 shows the difference between one and two phase plumes. The study by Hansen *et al.* (2003) mentioned above compared the efficiency of the two alternatives to lift nutrient-rich seawater to the euphotic zone to enhance the growth of non-toxic algae. The efficiency of a bubble curtain in terms of the flux Richardson number (ratio of produced potential energy to energy supply (Turner, 1973)) was about 5 %. The freshwater plume from a hydropower plant, with a very simple diffusor plate gave almost twice the efficiency of energy of the bubble curtain. Figure 6 shows the surface boil of this scheme. A measure of success of the energy efficiency in lifting water to the surface is the quiescence of the surface boil. A quiet dome indicates that the flow is weakly turbulent and that the surface rise is merely a result of the accelerations from vertical to horizontal velocities. The mixture in the boil sinks below the upper layer and spreads over the fjord at 5 – 10 m depth. In spite of the efficiency of the process, relative to a bubble plume, there is still room for improvement (*e.g.* a more efficient diffusor).

Fanneløp & Sjøen (1980) and Brevik & Kristiansen (2002) have treated the boil of a bubble plume in different ways. For the case of the mixing to a river plume, the boil is advected by the surface layer (Figure 1), creating a more difficult modeling situation, like that shown in Figure 2. An important parameter is the ratio of the surface river flux to the artificial upwelling.



Figure 6. The surface boil above a submerged freshwater discharge in Sognefjord (Hansen *et al.*, 2002).

Since the size of the schemes is so large (energy consumption on the order of 1 MW) we are now looking for possible improvements. In principle, with buoyancy forcing, the upper limit to the flux Richardson number (mixing efficiency) is expected to be near 20 %. Indeed, Asaeda & Imberger (1993) computed efficiencies up to 20% for some cases. Although less efficient in general, the bubble curtain is more portable than a submerged freshwater discharge, so we are first looking for possibilities of improving these systems. Trætteberg (1969) showed one possibility (Figure 3).

IMPROVING THE EFFICIENCY OF BUBBLE CURTAINS

Wüest *et al.* (1992) presented many features and ideas of how to improve bubble plumes and possible consequences of these changes. The present application differs from theirs, in that the submergence depth here is on the order of 10 m, and we are concerned with a line source with a very large volume flux. The idea behind the improvement is to approach the efficiency of the freshwater plume by using small enough bubbles to simulate a continuum in which the bubbles have a vanishingly small slip velocity. To make a fair comparison, the buoyancy of the source mixture of bubbles should simulate that of freshwater discharge in the fjord, with an air-to-water (void) volume fraction of 2½ %. This requires an average separation of bubbles of about $3d$, which could lead to frequent collisions and coalescence to larger bubbles. The present bubble curtains force air through 2 - 4 mm diameter holes, producing the largest stable bubbles in the plume (diameter $d = 2 - 4$ cm), so coalescence is not of concern for these systems. Although these cause a large amount of small scale turbulence, their slip velocity $u_s = O(1/2 \text{ m/s})$ is of the same order of magnitude as the plume rise so they carry a reduced amount of water with them on their way to the surface.

To approach a continuum, requires that the bubbles are in the Stokes flow regime with $Re = O(1)$. This gives a u_s an order of magnitude less than the plume rise. With $u_s = O(1 \text{ cm/s})$, bubble clouds will also have a longer residence time in the (mixed) seawater at the surface, before entering the atmosphere, enhancing convective mixing with the ambient flow near the surface.

NITROGEN SUPERSATURATION

The main purpose of spargers in nature and aquaculture is to oxygenate the water. Wüest *et al.* (1992) have modeled the gas transfer to the water phase and suggest that bubbles lose their buoyancy through absorption of gas to the water (see also Motarjemi & Jameson, 1978). At large depths (pressures) the gas saturation level is very low. This raises the question of supersaturation of nitrogen, when using air, which can be lethal to fish. This can be a problem in Norwegian waters where there are several fish farms. Fish in cages cannot escape the toxic water as wild fish do. With the large bubbles of the present systems, there is less dissolution of air at depth and the turbulence of the bubbles secures equilibrium to the atmosphere. We have not yet documented supersaturation due to existing bubble curtains. On the contrary, they have been suggested as a solution to the problem of supersaturated water in hydropower systems due to the compression of air in open shafts along the tunnels in the mountains and attendant temperature increases as the outflow is heated by the sun.

WORK IN PROGRESS

There is reason to believe that artificial upwelling using bubble curtains can be made significantly more energy-effective than today's operating systems. This may also lead to newer applications. The main thrust is to determine if small bubbles have the key to a more efficient momentum transport and if they can be applied without negative side effects (like reduced turbulent mixing and supersaturation of nitrogen). To address some of the above issues associated with microbubble plumes, we have set up a series of laboratory tests. One of the first attempts to simulate a plume that resembles a single phase plume is shown in Figure 7. Here, the microbubbles are produced by pressing air through a TRAC LOCK sparger in water of 40 cm depth. The milky cloud near the bottom consists of bubbles between 100 and 500 μ . The first decimeter shows the typical plume eddy formations of the milky fluid as seen in Figure 5. Clearly, the bubbles on the outer branches of the plume are the smaller ones.

Farther up the column, there appear to be swarms of larger bubbles closer to the center of the plume. This change of character reveals another challenge for implementing microbubble plumes: coalescence of smaller bubbles into larger ones due to collisions. Here, the uniform separation of the microbubbles is an important factor to maintain. A faulty distribution of the bubbles at the source can be a problem. Indeed, the TRAC LOCK sparger is flat to avoid the coalescence of bubbles that is a problem with cylindrical spargers.

The usual technique to produce well separated microbubbles is to shear them off the sparger with a throughflow (so called dynamic sparging). This is a more complicated system than we want to test at this stage, and may not give the density of bubbles that we want. Other methods are showing modest improvements (Silvia Lucas Malé, personal communication). Unfortunately, the turbulence created by the plume dynamics, as well as ambient turbulence entrained by the plume, enhances encounters. There is therefore a question as to whether or not the buoyancies needed for this task require a bubble density that will lead to too many collisions, in the near field compared to a sparse distribution for other applications.

Another issue to consider is the energy required to produce microbubbles. The production of the increased surface (inversely proportional to the diameter) for a given Q is 1500 Pa (15 cm water height) for a diameter of 0.1 mm bubble diameter. The corresponding pressure needed to press the air through the sparger is 150,000 Pa (15 m water height)! This has to be solved using spargers with other properties, if possible.

CONCLUSION

For most applications in fjords, typical plume rise speeds in the above mentioned applications are $\frac{1}{4}$ - $\frac{1}{2}$ m/s, on the order of bubble slip speeds for large bubbles. An alternative to approaching the efficiency of buoyance of a one phase plume is to reduce the slip speed of the bubbles. This can be achieved by producing micro-bubbles (100-500 μ m) in the Stokes flow regime, with slip speeds on the order of a few cm/s. There has been, however, some concern that bubble curtains can contribute to super-saturation of nitrogen to the detriment of aquaculture. For the shallow applications at hand, bubbles of this size should not be dissolved to a significant degree in the sea, but the preliminary laboratory tests show that ambient turbulence may hold some small bubbles in suspension for a long enough time to exacerbate the problem. Micro-bubbles can be produced using sintered tubing – so-called spargers. Although these are commonly used in lake restoration (e.g., Wüest *et al.*, 1992) there are technical challenges in the sea, one of them being marine fouling. This and other challenges are being considered now. The energy required to press air through spargers may be the final curtain for the intended application.

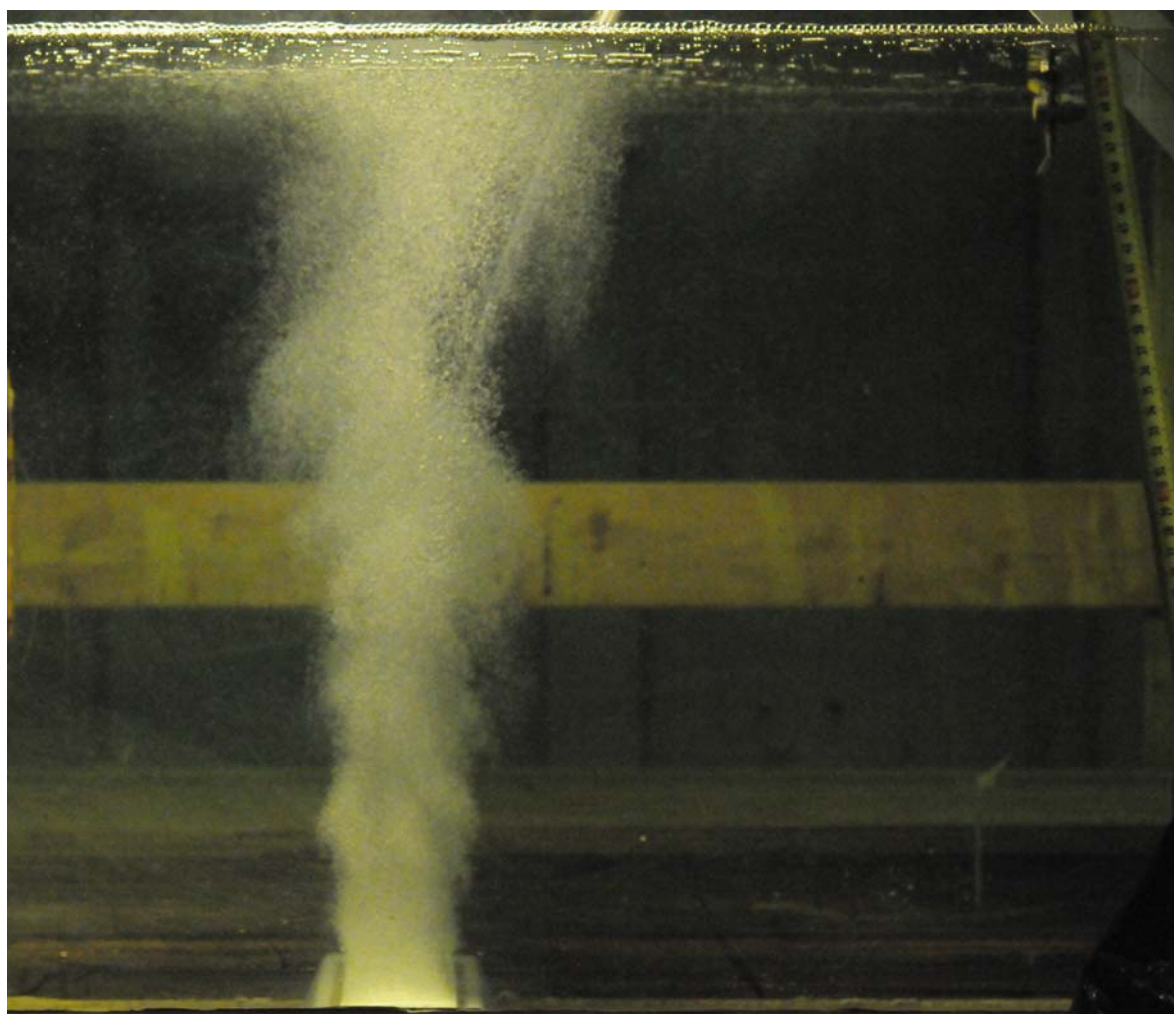


Photo: Geir Tesaker

Figure 7. An end view of a bubble curtain in 40 cm of water across a 60 cm flume.

ACKNOWLEDGMENTS

I thank Grim Eidnes for permission to reproduce Figure 1, Anton Trætteberg for permission to publish the results from his 1965 laboratory studies and Silvia Lucas Malé and Geir Tesaker for information on the work-in-progress. The work has received support from Statkraft and the Dept. of Hydraulic and Environmental Engineering, NTNU.

REFERENCES

- Asaeda, T. and Imberger, J. 1993. Structure of bubble plumes in linearly stratified environments. *J. Fluid Mech.* 249: 35-57.
- Brevik, I. and Kristiansen, Ø. 2002. The flow in and around air-bubble plumes. *Int. J. Multiphase Flow* 28:617-634.
- Bulson, P.S. 1961. Current produced by an air curtain in deep water. *The Dock and Harbour Authority* 42:15-22.
- Eidnes, G. 2004. Bubble curtain to prevent freezing. Paper No. 2004-JSC-217, *Proc. 14th Int. Offshore and Polar Engineering Conf.*, Toulon, France. 5 pp.
- Eidnes, G. and Tørum, A. 2002. Bubble curtain in Holandsfjorden. Currents, forces and engineering. *SINTEF Report STF80 F02001*. 36 pp. (In Norwegian)
- Fanneløp, T.K. and Sjøen, K. 1980. Hydrodynamics of underwater blowouts. *Norwegian Maritime Res.* 8:17-33.
- Fanneløp, T.K., Hirschberg, S. and Küffer, J. 1991. Surface current and recirculating cells generated by bubble curtains and jets. *J. Fluid Mech.* 229:629-657.
- Fischer, H.B., List, E.J., Koh, R.C.Y., Imberger, J. and Brooks, N.H. 1969. *Mixing in Inland and Coastal Waters*, Academic Press, 483 pp.
- Hansen, A.H., Fredheim, A., Lien, E., McClimans, T.A., Reitan, K.I., Tangen, K. and Olsen, Y. 2003. Use of air bubbles and submerged freshwater discharge as methods for the production of toxic-free mussels. *SINTEF Report STF80 A032090*. (59 pp) (In Norwegian)
- Kobus, H.E. 1968. Analysis of the flow induced by air-bubble systems. Ch. 65, part 3 Coastal Structures. Vol. II, *Proc. 11th Conf. on Coastal Engineering, London*.
- Leitch, A.M. and Baines, W.D. 1989. Liquid volume flux in weak bubble plume. *J. Fluid Mech.* 205:77-98.
- McClimans, T.A. and Jenssen, L. 2008. Svartisen Power Plant. Evaluation of microbubbles to increase the efficiency of the bubble curtain at Enganeset. *Dept. of Hydraulic and Environmental Engineering, NTNU Report B1-2008-1*. ISBN 82-7598-076-3. 10 pp. (In Norwegian)
- Motarjemi, M. and Jameson, G.J. 1978. Mass transfer from very small bubbles – the optimum bubble size for aeration. *Chem. Eng. Sci.* 33:1415-1423.
- Rowe, R.D., Poon, J.Y.C. and Lareshen, C.J. 1989. A simple method for predicting bubble plume properties. *Proc. 23rd Int. Assoc. Hydr. Res.*, Ottawa, D-23-30.
- Rye, H. 1978. Overview of VHL reports and technical notes concerning the bubble curtain at Mo I Rana. *SINTEF Technical Note 602522.20*, 19 pp. (In Norwegian)
- Sægrov, S. 1978. Bubble curtain in layered water. *SINTEF Report STF60 F78015*. 30 pp. (In Norwegian)
- Taylor, G.I. 1955. The action of a surface current, used as a breakwater. *Proc. R. Soc. Lond. A* 231:466-478.
- Trætteberg, A. 1967. Bubble curtain with air supply from parallel pipes. *SINTEF Report*, Project No. 600185, 13 pp. (In Norwegian)
- Turner, J.S. 1973. *Buoyancy effects in fluids*. Cambridge University Press. 367 pp.
- Wüest, A.J., Brooks, N.H. and Imboden, D.M. 1992. Bubble plume modeling for lake restoration. *Water Resources Res.* 28:3235-3250.

Session D: PIPELINES

COASTAL ENGINEERING APPLICATIONS ON PIPELINES

Hermann Moshagen
BHM Engineering Services AS
(Formerly: Statoil)

ABSTRACT

Coastal engineering comes into application on pipelines when offshore pipelines enter the onshore area or when onshore pipelines enter the sea. Offshore pipeline technology has developed from hardly anything in the 1960es into the large scale international industry it is today. Thousands of kilometres of offshore pipelines have been built over the last 3 to 4 decades transporting oil and gas from offshore fields or from onshore terminals to the market, ref. Figure 1, showing the North Sea gas pipeline network. Similar pictures may be shown from offshore oil and gas development areas in other parts of the world. In parallel to this large scale commercial development impressive advances in pipeline technology have also taken place, Ref. 1.

Application of coastal engineering may be essential for a successful realisation of such pipelines. The paper gives examples of such applications in recent pipeline projects in the North Sea area. The appearance of coastal technology in design codes is also addressed.

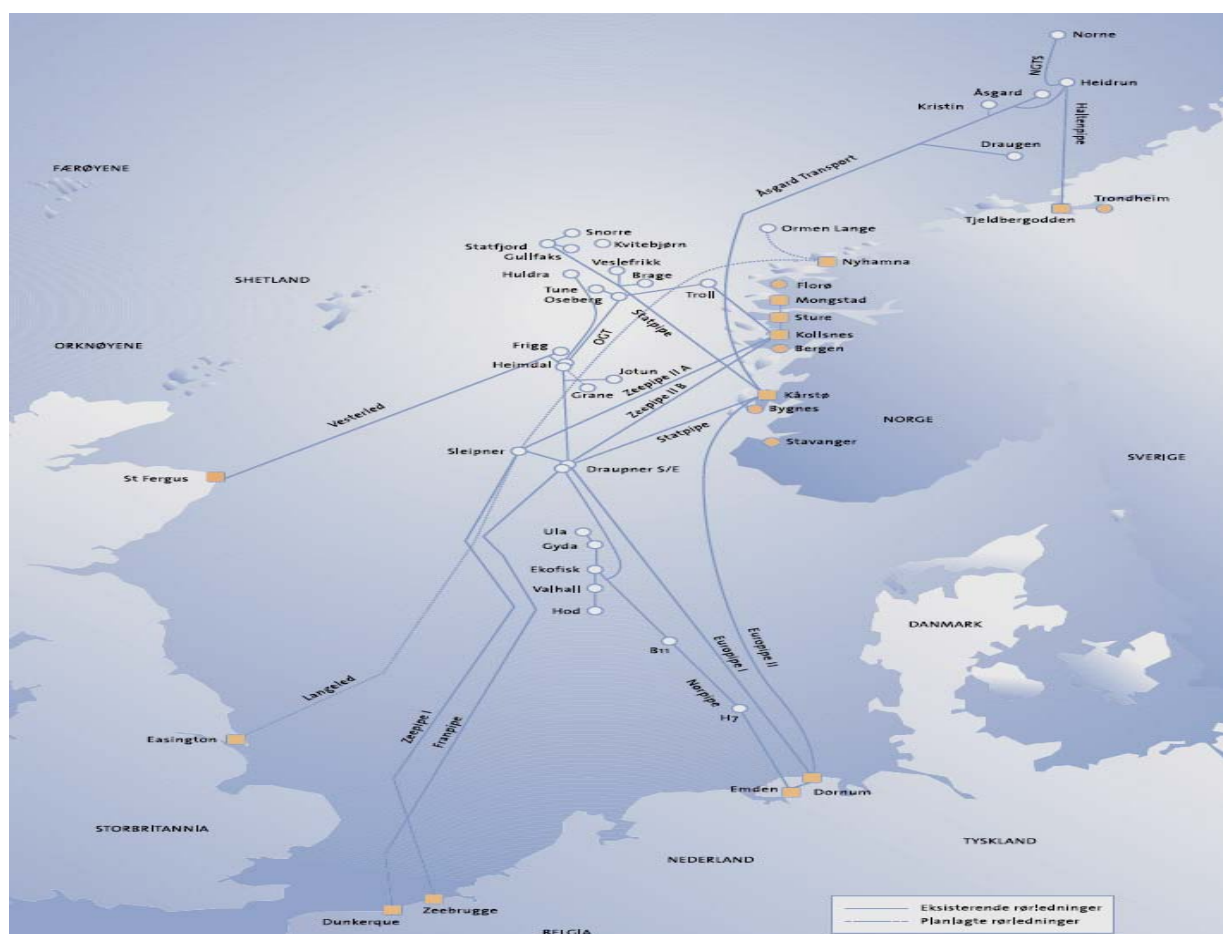


Figure 1. North Sea Gas Pipelines (Source: Gassco)

The route follows the tidal inlet Accumer Ee between the two islands of Baltrum and Langeoog. The pipeline is routed along one of the main tidal channels further inwards and is taken on land through a concrete tunnel (2 km) crossing the tidal flat, ref. Figure 2. Coastal Engineering; Coastal Modelling; Pipeline Shore Approach; Pipeline Landfal I; Nearshore Pipeline; Pipeline Codes.

The coastal area characteristics are:

- a range of sandy islands paralleling the coastline of the mainland
- tidal inlets separating the islands and dominated by strong tidal flows
- wide tidal flats or mudflats towards the mainland on the inside, flooded at high tide and dry at low tide
- tidal channels spreading and collecting the tidal flows over the entire mudflat area
- shallow sand bar area seawards and just outside of the tidal inlet
- high rate of sediment transport in the whole area
- frequent wave braking outside islands and tidal inlets

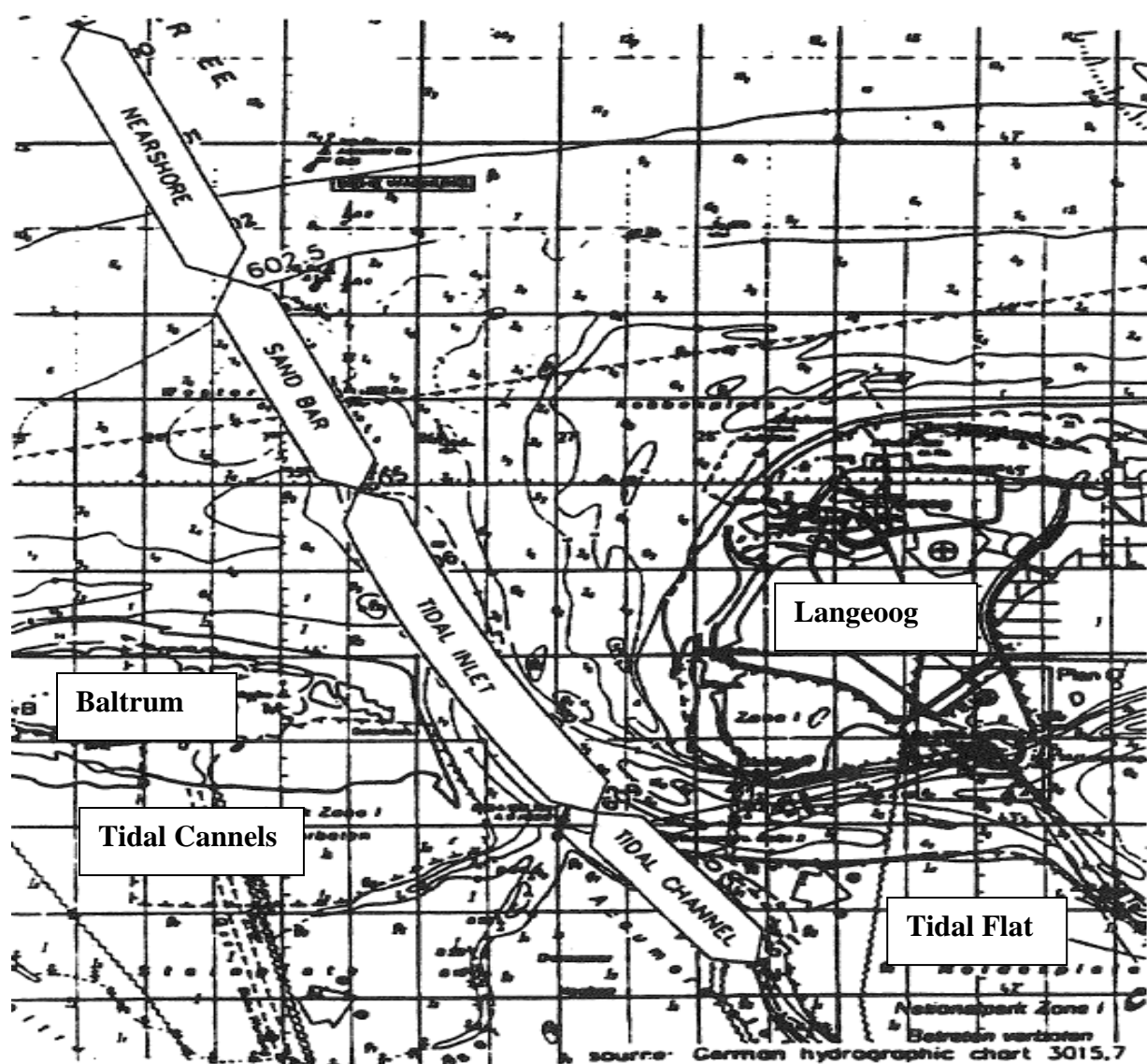


Figure 3. Europipe 1 Coastal Area Characteristics

As an over all statement one may say that the entire coastal landscape appears as a long term result of coastal hydrodynamic, sediment transport and coastal morphology processes, ref. Figure 3. The islands are habitats for local communities. The tidal channels and inlet are used for sailing for public transportation and locally based fishing boats.

Finding an acceptable *Pipeline Shore Approach Solution* was by far the toughest challenge of this pipeline project. While the 610 km pipeline from the Draupner platform to the nearshore area was basically conventional subsea pipeline engineering and installation, the shore approach and landing of the pipeline on the main land was a highly unconventional task. The reason for this was that the entire shore area, including the islands, the tidal inlets and channels and the tidal flats, had - and still has - status as a national park area with strong restrictions on human activities within this area.

Due to the national park status of the area this part of the pipeline project was a highly sensitive environmental issue. The finally selected routing and installation conditions for the pipeline through the coastal area were established on the basis of extensive studies of the wave, current and sediment transport characteristics in the area. In addition the routing and installation of the pipeline was the result of a long process where political authorities played an important role and in which environmental organisations and public opinion were strongly engaged. Questions were raised and had to be handled and given qualified answers on a continuous basis throughout the whole project period. In addition the project planning and pipeline engineering had to go on in order to establish a shore approach and landfall solution for the pipeline that was fully satisfactory from a technical and economic point of view.

Basically all tidal inlets and estuaries on the German North Sea Coast were studied at the feasibility stage of the project. The studies concluded with Accumer Ee as the recommended location for shore approach routing and landing of the pipeline.

Throughout the entire engineering, planning and construction period of the project the use of computerized *Coastal Hydrodynamic Models* for the actual coastal area proved to be a highly applicable means of handling the engineering requirements and above all giving answers to the environment related questions that were raised. The following sections will focus on the establishment and qualification of these models followed by presenting some key issues from the final engineering period of the project illustrating the application of these models.

Establishing and Qualification of Coastal Models

Mathematical models used in building up coastal models for simulation of current and waves will not be discussed here nor will the various numerical methods that are applicable for the same purpose. Descriptions are available in the literature and reference is made to these. Coastal models are commercially available at Research Institutes specializing in Coastal Hydrodynamics.

The approach in practical applications of coastal modelling to the pipeline project should be discussed and agreed with the actual coastal engineering group. Normally the following steps will be included:

- Coastal engineering group to be selected and established with responsibility for the modelling task. Preferrably the group should consist of coastal engineers and modelling specialists with relevant experience
- Group to be informed about the pipeline project, the planned pipeline routing and the actual engineering challenges
- Define actual area to be modelled in discussions with the coastal engineering group
- Seabed bathymetry data covering the model area to be collected and implemented in the models. Seabed survey data along the pipeline route will normally be available within the pipeline project.
- Data to be applied at the outward boundaries to be collected and implemented. The environmental design data basis established for the pipeline project will normally be used together with additional data as required.
- External “global” models, f. ex. a model of the North Sea basin, may be considered
- Testing the model for operational criteria, i.e. numerical stability, reference case simulations, etc.
- Calibration of models against relevant physical model data - or preferrably - against full scale data
- Validation of models against prototype case data. Level of accuracy of the models for prototype applications to be established

When the models thus are concluded to be valid, with an agreed level of accuracy, they are ready to be used for engineering purposes.

Calibration and Validation of the Europeipe 1 Models

The Europeipe 1 project started work to establish Coastal Models for use in the final engineering of the shore approach solution as soon as the landing location for the pipeline, the Accumer Ee, was decided. Delft Hydraulics was contracted for the work.

Bathymetry data of high quality were available. In addition up to date bathymetrical and geotechnical data were collected in pipeline route surveys performed by the project. Historical syrvey data were also provided by German Authorities and included in the data basis for the coastal modelling work.

Coastal models for simulation of waves, current and tidal levels were established as described above. The work started from existing models where mathematical formulations and numerical schemes were already worked out, tested and operational for other coastal applications. Data defining the external boundaries, the islands, the tidal inlets and the seabed for the defined area was introduced.

Wave model features were

- wave growth by wind action
- dissipation by wave braking and bottom friction
- directional spreading in incident and generated wave fields
- wave refraction by uneven sea bed

Results from application of the wave model across the sand bar area is shown in Figure 4. The model clearly illustrating the effect of the sand bar area on waves propagating from the sea across the and inwards through the tidal inlet.

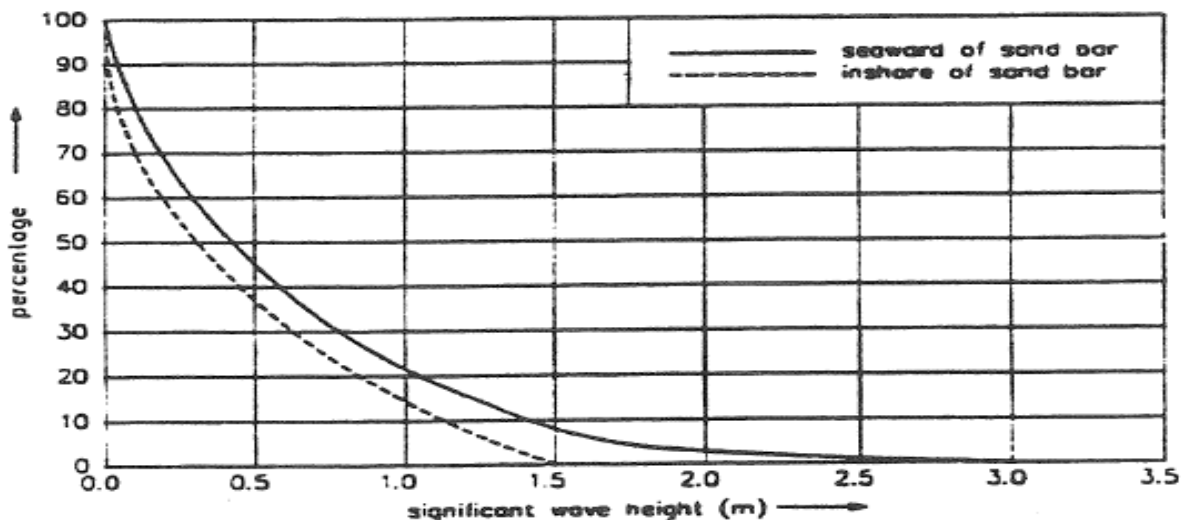


Figure 4. Wave propagation across sand bar area. Europe 1 wave model

Current model features were

- convective accelerations
- earth's rotation
- water level gradients
- momentum exchange due to eddy viscosity
- bed friction
- wind effect

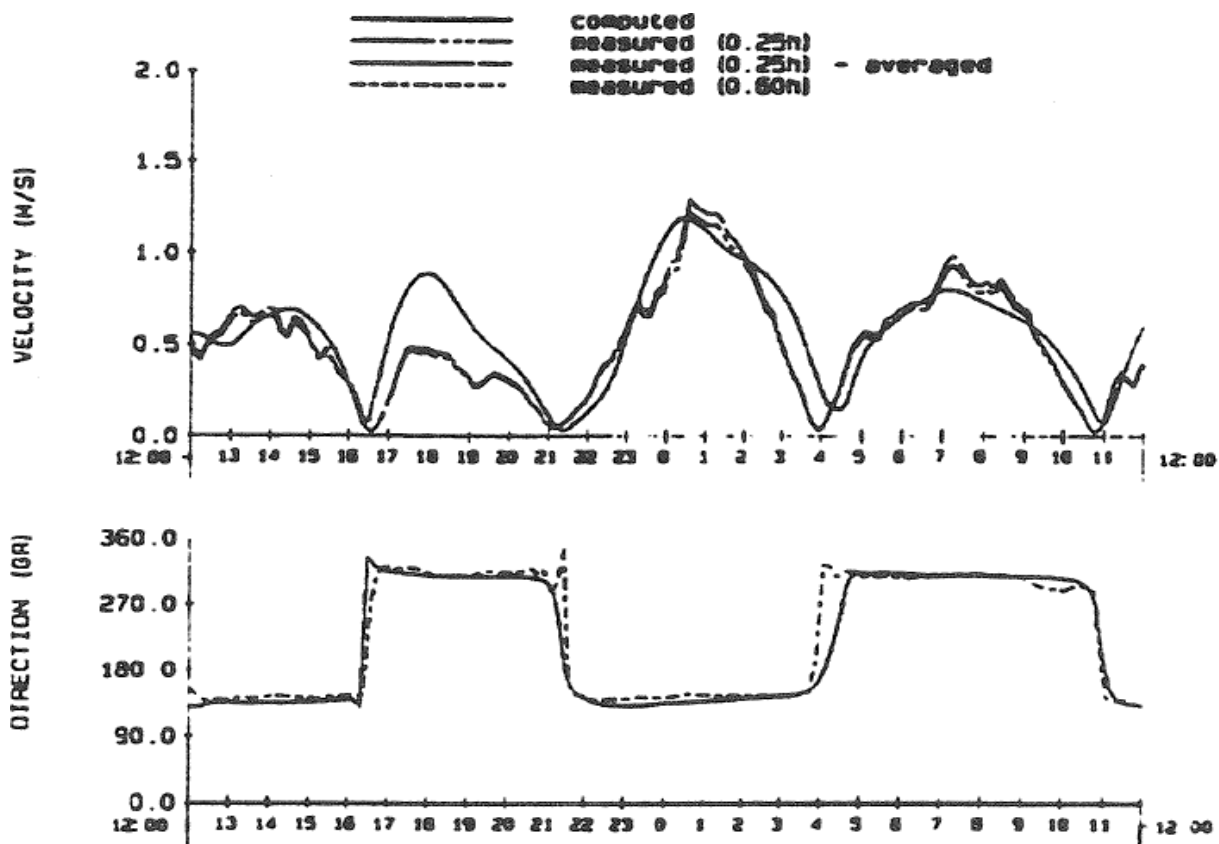


Figure 5. Comparison of Flow Model and Prototype Current Measurements

A *development scheme* for testing, calibration and validations of the models was established. An essential part of this scheme was a program for collection of data on currents (magnitude and direction), water levels and wind (magnitude and direction) by field measurements in the prototype area for calibration and validation purposes.

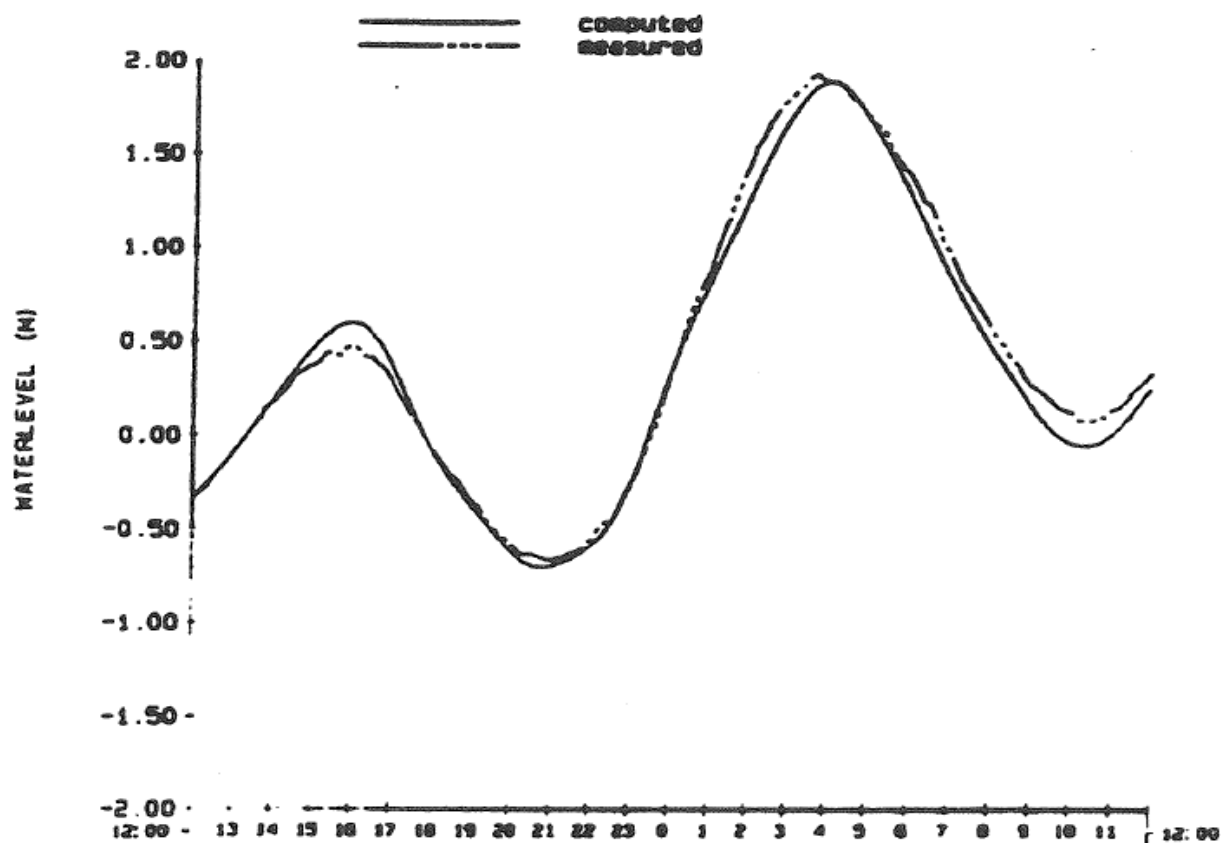


Figure 6. Comparison of Flow Model and Prototype Water Level Measurements

The results from the Current Model validation test are shown in Figures 5 and 6 above. The test was to simulate current velocity and direction plus water level at a selected point in the middle of the pipeline route in the Accumer Ee inlet over a period of 24 hours and compare simulations with the prototype measurements at the same point. It appears from Figure 5 that flow directions and change of direction in time are well reproduced by the model. The current velocity simulation shows some anomaly in the 1700 to 2100 hrs outflow. However, for the other three outflows and inflows over the actual test period the model reproduced also the current velocity well.

The water level simulations shown in Figure 6 are seen to compare very well with the prototype measurements both in magnitude and time wise. The current model was concluded to be valid for application in the final engineering of the Europeipe 1 project.

Engineering Applications of the Europeipe 1 Coastal Models

Offshore pipelay barges are not able to operate in shallower waters than about - 15 m. Therefore pipeline installation for the shore approach part of the route had to be performed by a special flat bottom barge built for this purpose. However, even this barge needed deepening

of the seabed along the shallowest part of the route which was in the sand bar area. Opening an access channel for the flat bottom barge by dredging along this part was necessary for the realisation of the project.

The access channel raised several questions from the authorities, like

- Would the access channel change the flow conditions in the tidal inlet and thereby cause navigation problems for the fishing and public transportation boats?
- Would the access channel cause changed wave and current exposure of the islands and possibly destabilize their nearby coastline?

A technical issue related to the access channel was the rate of natural sediment backfilling of it and the need for maintenance dredging.

A favourable feature of computerized coastal models is the ease with which a modified lateral boundary or locally changed seabed can be implemented. This was done with the access channel followed by running the models to simulate the effect of the access channel on the wave and current fields. The following Figures 7 and 8 illustrate such runs.

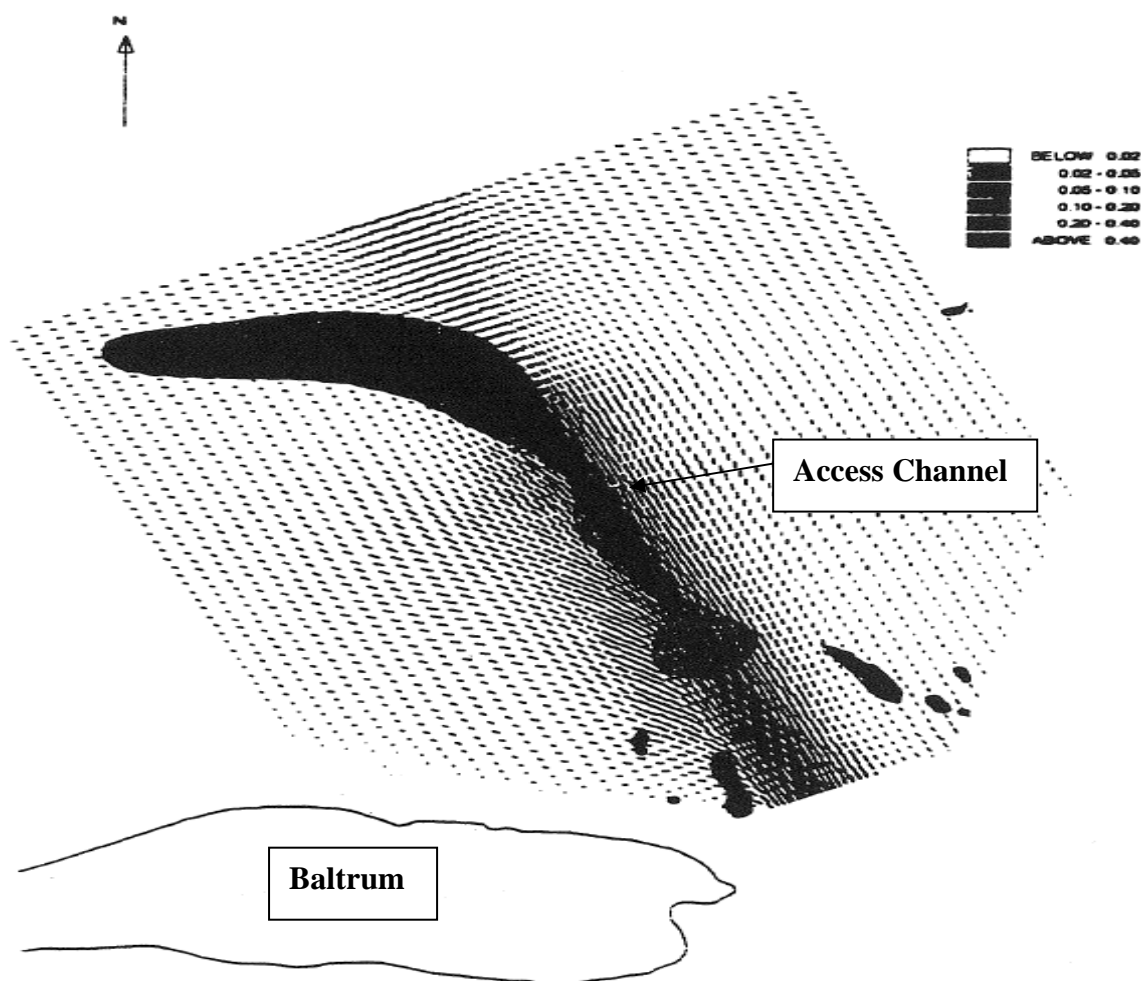


Figure 7. Modified Current Field by the Access Channel. Shaded Areas: Increased Velocity During Ebb Flow

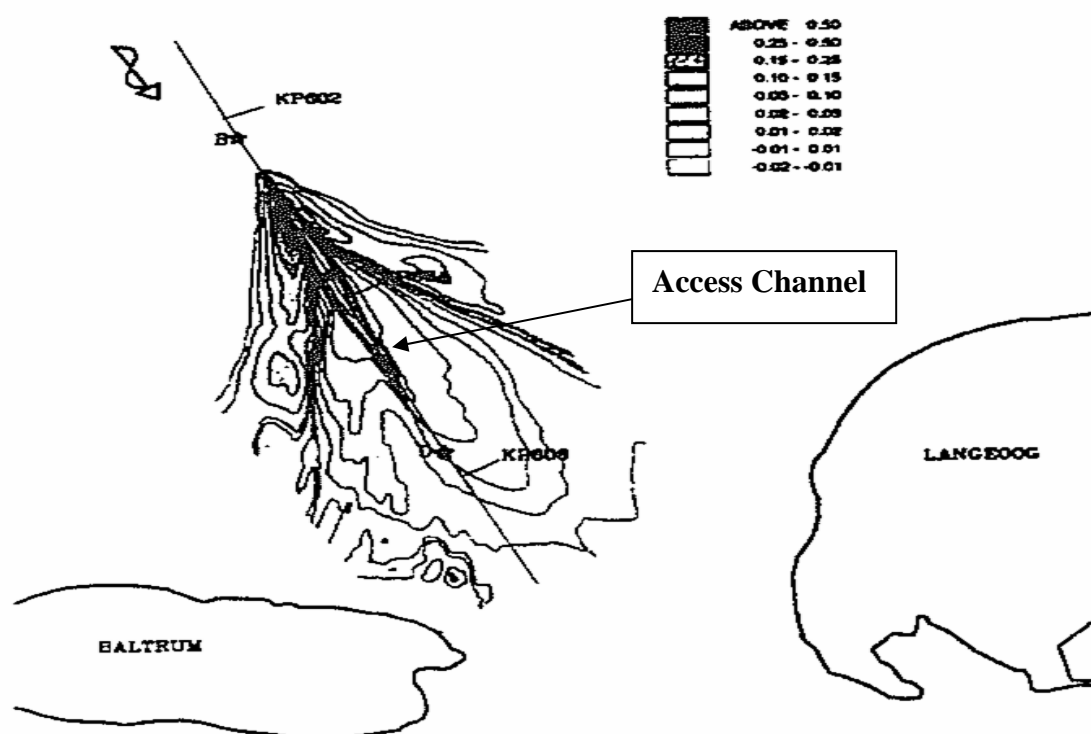


Figure 8. Access Channel Effect on Wave Field, NW Storm. Shaded Areas: Higher Waves

The application of coastal models on the access channel provided information on

- the extent and field of influence by the access channel on both currents and waves
- quantitative data on increase or decrease factor on wave or current conditions at specific locations, including the beaches of the neighbouring islands
- data basis for access channel sedimentation evaluations

Coastal Morphology. Determination of Pipeline Trench Depth

Another key question in the engineering of an acceptable and safe pipeline solution in the coastal area was that of the trenching depth of the pipeline along the shore approach route. The historical bathymetry data showed clearly that the seabed changed over time as a result of seabed scour and sedimentation processes.

These long term morphological changes were studied systematically on the basis of the mentioned historical data, the morphological data basis (MDB). The number of historical bathymetric surveys was not high enough to provide a solid basis for normal statistical methods. However, within its statistical limitations the basis provided highly useful information. The pipeline needed to be trenched to a certain depth in order not to be uncovered and later appear with free spanning sections. Also with respect to the existing boat traffic in the area uncovered pipeline sections were not acceptable. Thus one main objective of the morphological studies was to establish a necessary and acceptable trench depth, i.e. the

pipeline installation depth. The concluded trench depth along the entire shore approach route is shown in Figure 9.

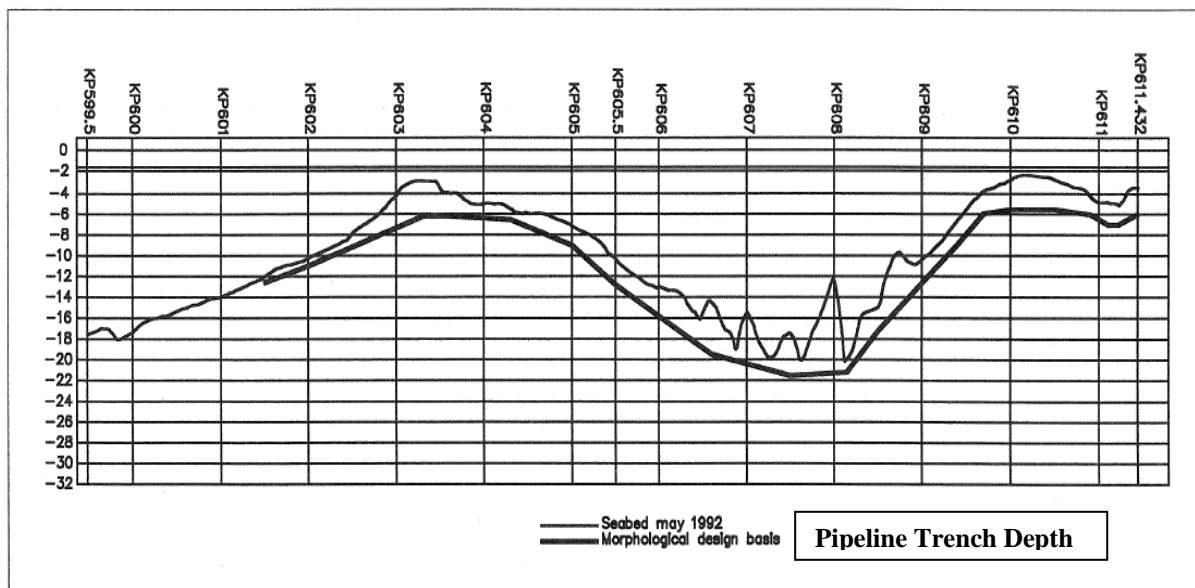


Figure 9. Application of Morphological Design Basis. Shore Approach Pipeline Trench Depth

The application of Coastal Modelling technique in the Europipe 1 shore approach engineering work obviously saved the project from great difficulties in obtaining acceptance for the pipeline shore approach solution by the German authorities. What the consequences would have been to the project of not having such modelling tools available for the engineering work is not easily assessed. However, it seems rather likely that the project would have experienced a significant extension of the project schedule and associated costs. The importance of the models to the success of the Europipe 1 project was fully acknowledged by all parties involved:

*“It was concluded that the wave and flow models were an indispensable tool for good and effective pipeline and **authority engineering** in the Accumer Ee tidal inlet.”*

NORFRA – A PIPELINE ENGINEERING CHALLENGE

Project Characteristics

The *NorFra* pipeline- now renamed *Franpipe*, *Norfra* will be used here - is a 42 inch trunkline transporting gas of export quality from Norway to France, starting at the Draupner platform in the North Sea and landing at Dunkerque, located on the North Sea coast of France at the eastern end of the English Channel, Figure 1. It was engineered and built in the mid 1990es and was set in operation in 1997. Thus the Norfra pipeline project followed directly after Europipe 1. The application of Coastal Modelling was then an established method, with Europipe 1 as the reference case. And the method came into use also for Norfra, as the following sections will show. While the Europipe 1 was primarily an environmental and authority challenge for the shore approach area, the NorFra was a pipeline engineering challenge in the nearshore area.

The pipeline route follows a straight southward line from Draupner up to the British sector line and follows this sector line until entering the English Channel. From here it follows the same corridor as the Zeepipe 1 pipeline until heading straight for Dunkerque, Figure 10.

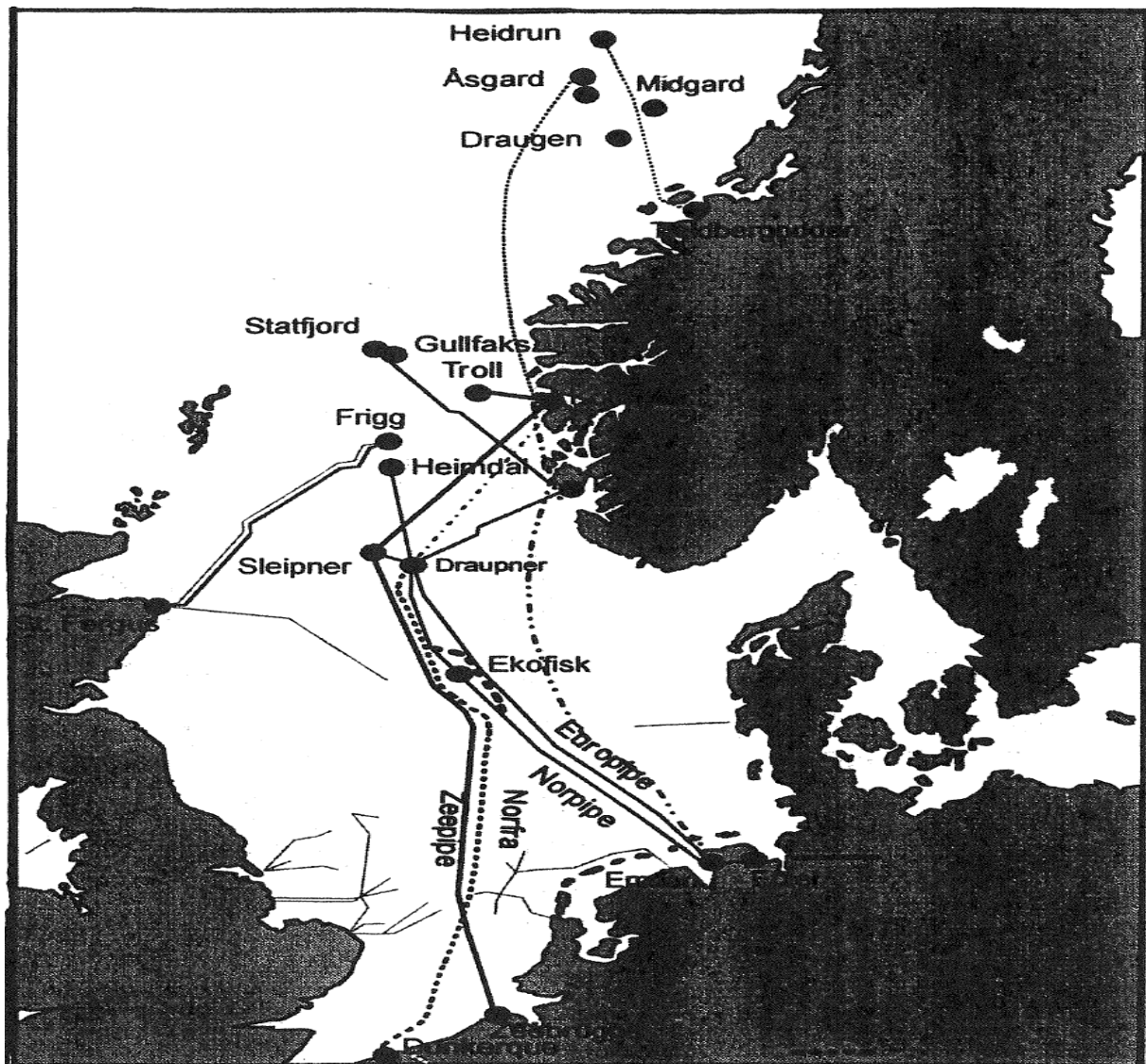


Figure 10. Norfra pipeline route

Nearshore Challenge

The *Nearshore area* is here the part of the route which is in the English Channel. The entire nearshore seabed area is dominated by large sand banks, Figure 11. The pipeline stability and installation solution was established based on conventionally established wave and current data for the nearshore area. This solution challenged the project by giving a designed pipeline submerged weight, necessary for pipeline stability, exceeding the capacity of the lay barge. As a consequence a modified pipeline installation concept, was engineered. In parallel to this a coastal modelling study was contracted to *Laboratoire National d'Hydraulique*, a branch institute of Electricite' de France (EDF), located at Chatou, Paris.

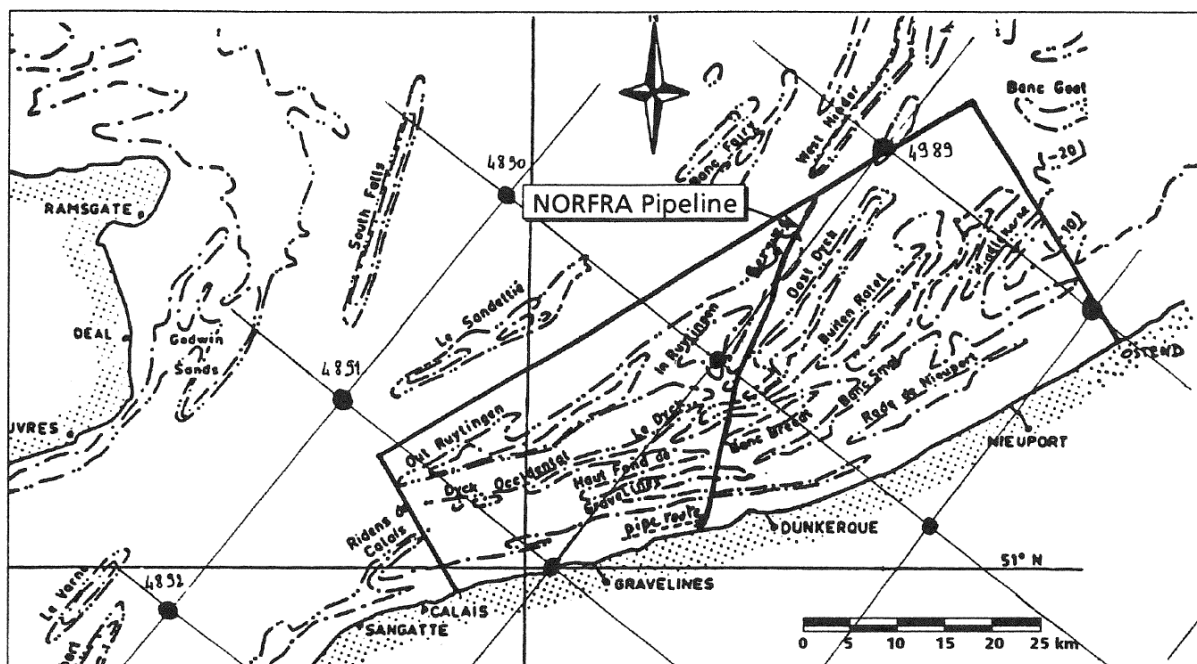


Figure 1. Nearshore area covered by model

Figure 11. Norfra Nearshore Area and Model Extension

Wave and current models were established, calibrated and validated with the Europe 1 studies as reference. Validation results are shown in Figure 12.

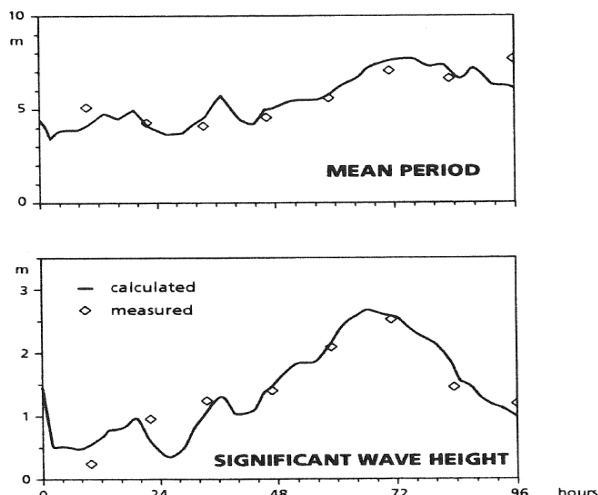


Figure 3. Wave model validation

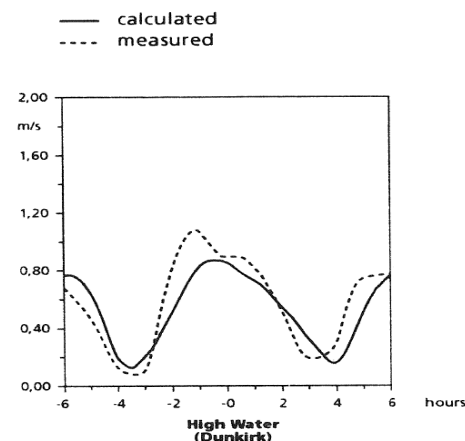


Figure 4. Current model validation

Figure 12. Validation of Wave and Current Models for NorFra nearshore area

Both wave and current actions in the area are important. Thus validation of both models were considered equally important for the engineering applications.

Engineering applications

The NorFra application of the coastal models was exclusively for establishing a continuous and locally applicable set of design values on waves and current for pipeline stability design. Again the shallowest parts of the sand banks had to be trenched for access of the shallow water lay barge. And again the access channels were conveniently included in the computerized models for engineering application, Figure 13. As can be seen the actual sand bank crossings are typically 2 - 3 km in length and 10 - 15 m in height. The shallowest parts are going up to about 5 - 6 m water depth.

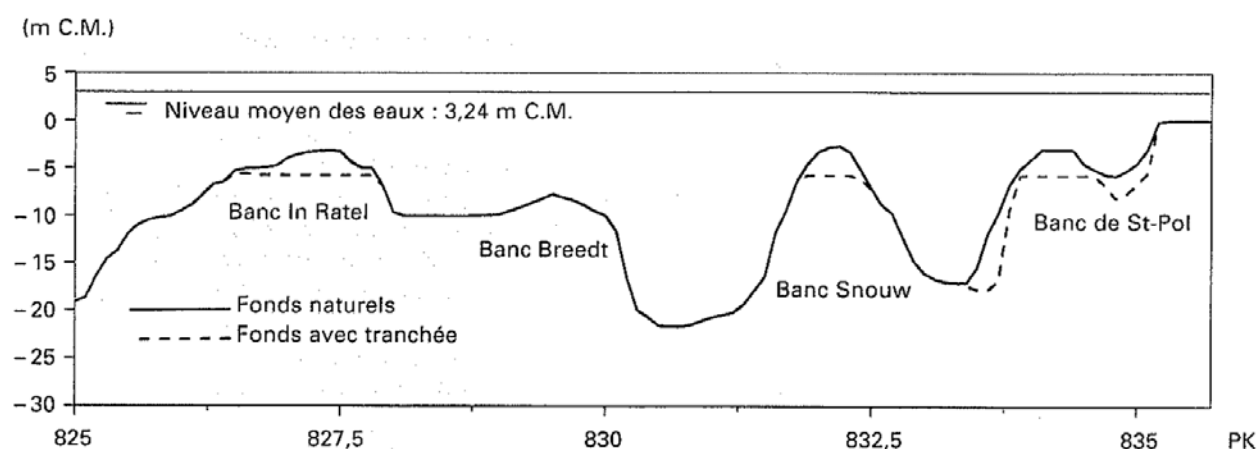


Figure 13. Nearshore Pipeline Route Profile with trenched Laybarge Access Channels

The effect of coastal modelling application to this extreme case of pipeline stability design is clearly illustrated by the resulting requirements for concrete coating thicknesses on the pipeline along the nearshore route, as shown in Table 1 below.

Concrete Coating	Design Approach	
	Conventional	Coastal Modelling
WT (mm)	160 - 190	90

Table 1. Coastal Modelling Results on NorFra Nearshore Pipeline Stability Design

The project concluded that a concrete coating thickness of 90 mm was sufficient along the entire nearshore and shore approach route. With this re-established pipeline stability design the pipeline was layable by the conventional shallow water laybarge method which also was a project conclusion based on the modelling results.

Final Remarks on Coastal Modelling Applications

The application of coastal modelling technique to the NorFra nearshore engineering proved to be a powerful method that led directly to the required pipeline stability solution. The NorFra case also illustrates the weakness of the conventional methods used in establishing the *design data basis* for offshore pipelines. The methods are established for offshore conditions where

the applications are fully valid. However, in complex areas such as seen in the Europipe 1 shore approach and NorFra nearshore areas the method fails. Data on waves and currents collected by measurements offshore normally are representative for a relatively wide area. This is not the case in shore approach and nearshore areas such as those we have dealt with here. The real wave and current conditions in these areas show strong local variations reflecting the extreme topographical variations of the seabed and the shoreline. The coastal modelling technique handles this complexity.

A second aspect of the application of coastal modelling technique for engineering purposes is illustrated by both the Europipe 1 and the NorFra cases. Coastal models are also *engineering tools* by their ability to include any type of seabed modifications or built in structures directly as part of the actual models. This calls for strong involvement, preferably with the main responsibility for the modelling task, by the project engineer(s) in the study team, in cooperation with the design data basis engineers and the coastal modelling specialists. This way of organising the work was applied in both of the above pipeline projects and is recommended for future projects.

TROLL OIL PIPELINE 1

Pipeline Route

A third case of successful application of coastal engineering to a pipeline project is that of the Troll Oil Pipeline 1 (*TOR1*) Project. This is a 16 inch pipeline for transport of oil from the Troll B platform in the Norwegian Trench to the Mongstad refinery, North of Bergen. The Mongstad refinery is located on the Southern side of Fensfjorden some 15 km inwards from the fjord mouth. The TOR 1 pipeline was engineered and built in the mid 1990s.

The pipeline route starts at 300 m water depth at the Troll field, crosses the Norwegian Trench and follows the Eastern Slope up to the sill of Fensfjorden at about 240 m depth. From the sill area the route descends into the deeper parts of Fensfjorden via a steep sloping section down to a maximum depth of 540 m. The sloping route section is at the same time characterized by highly irregular seabed bathymetry. It has the character of a submerged steep and rocky valley. The further part of the route towards Mongstad is on relatively flat fjord bottom 350 m - 400 m deep before entering the refinery area through a drilled landfall tunnel.

It was clear at an early stage of the TOR 1 project that the steep, narrow and irregular part of the pipeline route in the outer part of Fensfjorden presented a tough challenge to the project. Engineering and installing the pipeline along this section was beyond experience in any pipeline project to that date.

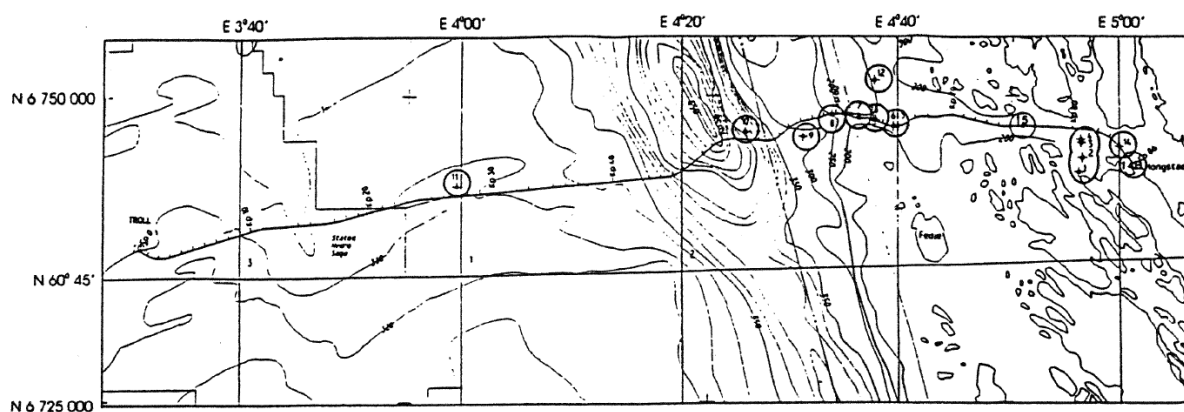


Figure 14. TOR 1 Pipeline Route from Troll to Mongstad

Engineering Approach

The approach taken was by entering into development activities and studies on critical areas of pipeline engineering identified by the project such as:

- mapping technology for deep and complex seabed areas
- pipeline free span design criteria
- seabed conditions for supporting structures
- pipeline installation along the most complex part of the route

Design criteria for pipeline free spans hardly existed at the time. An ambitious program to establish the necessary technological basis for a safe and reliable pipeline design along the complex route section was initiated. DNV's pipeline unit was engaged on the structural design and the coastal engineering group of Sintef was contracted on establishing the current design basis. It was a clear conclusion from DNV's work on the free span design criteria that

the current velocity was the most important single parameter contributing to the value of the design or “safety” factors for the free spans.

A program of current measurements along the route was part of the coastal engineering work. Figure 15 shows the current measurement setup along the route. The measurement program also included sea water density measurements.

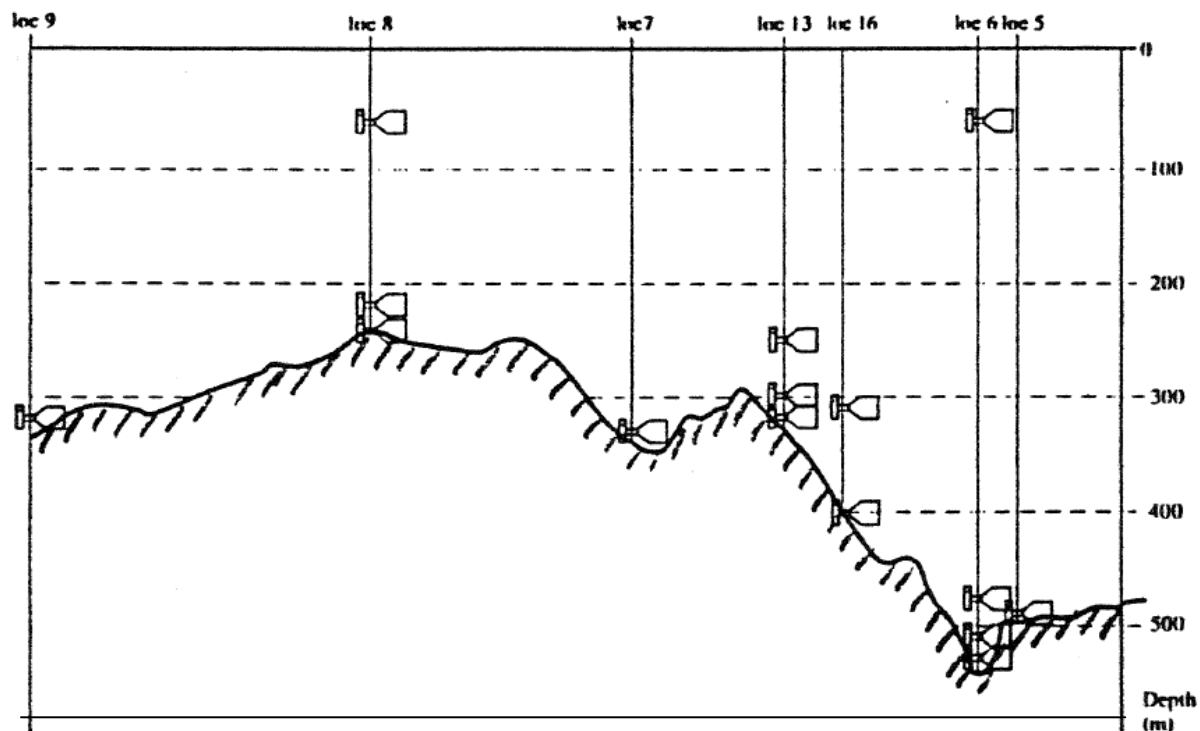


Figure 15. Vertical Profile of Route Section along Fjord Sill and irregular steep Slope showing Current Field Measurements Setup

The measured current measurements were surprisingly high and showed an occurrence pattern that was not expected. In order to understand the generation and behaviour of the near seabed currents it was decided to study the fjord oceanographic system in a physical model. The special rotating flow basin operated by the coastal engineering group was used. This facility is set up to simulate also the flow effect from the Earth’s rotation. Figure 16 shows the basic

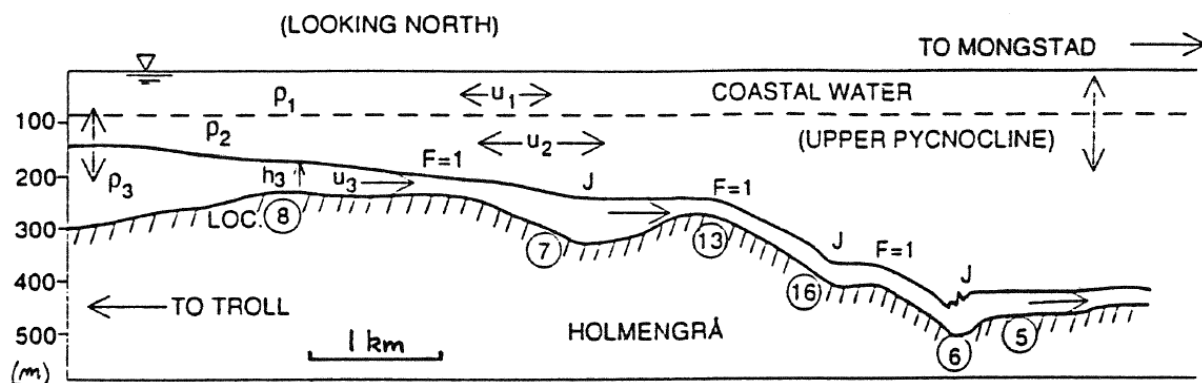


Figure 16. Longitudinal Section of simplified 3-layer flow with sill overflows

flow system that was modelled. The model results were checked against field measurements as shown in Figure 17.

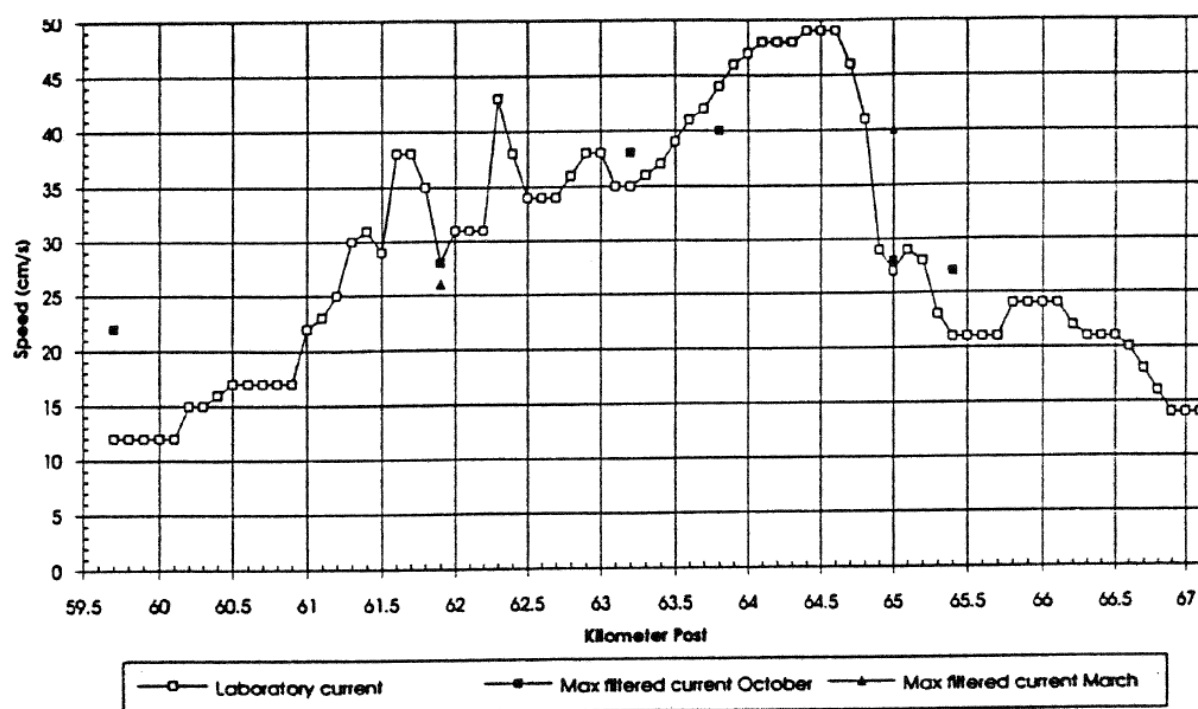


Figure 17. Comparison of Laboratory data with non-tidal bottom currents along the pipeline

The above physical coastal modelling work is published in the paper by Per Erik Bjerke et al, at the OMAE conference in Copenhagen, 1995. The work on the free span design for the TOR 1 project also triggered a major research program on establishing an industry (DNV) guideline with design criteria for pipeline free spans, the MULTISPAN project.

Final Remarks on Physical Modelling for Coastal Engineering Applications

The physical flow modelling was a success and provided the needed basis for interpretation and use of the current data in designing the free spans that occurred in multitude along this section of the TOR 1 route. The testing facilities represent a highly specialized type of coastal engineering services and is essential for handling a complex project such as the TOR 1.

COASTAL ENGINEERING IN PIPELINE CODES

Coastal engineering is a specialized engineering field and the knowledge of the field is not widespread within the pipeline industry. The applications to the Europe 1 and NorFra pipelines were recognized within the companies and other parties involved. Thus the engineering method applied for Europe 1 has been implemented in the Coastal Management Standards for The Netherlands.

It is noticeable that the DNV pipeline standard DNV-OS-F101 has taken in an Appendix F: *Requirements for Shore Approach and Onshore Sections*. However, coastal engineering applications are not mentioned. There is obviously plenty of room for further improvements

of pipeline codes in this respect and for the coastal engineers in the future to see this as a challenge.

REFERENCES

1. Berge, J. O.: *North Sea Pipelines - Pushing the Technology Front*. Proc. ISOPE, Seoul, 2005
2. Bijker, R., Chen, Z. and Moshagen, H.: *Morphology and Pipeline Design Through a Tidal Inlet. The Europipe Case*. Proc. OMAE, Houston, Texas, 1994
3. Bjerke, P. E., Moshagen, H., Røed, L. P., Eidnes, G. and McClimans, T.: *Troll Oil Pipeline: Current Measurements and Modelling. Data Basis for Free Soan Design*. OMAE; Copenhagen, 1995
4. Collberg, L., Moshagen, H. and Gjertveit, E.: *New International Pipeline Codes – Did they Meet the Expectations?* Proc. ISOPE, Honolulu, 2003
5. Latteux, B., Marcos, F. and Peltier, E.: *Le Gasoduc NorFra a l'Approche de Dunkerque: L'Ingenierie Cotiere a la Rescousse pour un "Atterage" en Douceur!* EDF-DER, EPURE No. 58, 1998
6. Moe, H., Gjevik, B. and Ommundsen, A.: *A High Resolution Tidal Model for the Coast of Møre and Trøndelag, Mid-Norway*. Norwegian Journal of Geography, Vol. 57, Oslo 1951, ISSN 0029
7. Moshagen, H. and Bijker, R.: *Europipe Pipeline Shore Approach. Environmental Design Basis*. Proc. ISOPE, Osaka, 1994
8. Moshagen, H., Torbjørnsen, B., Strass, P., Latteux, B. and Venturi, M.: *The NorFra Pipeline. Challenging Shore Approach Handled by Coastal Dynamics Modelling*. Proc. ISOPE, Honolulu, 1997
9. Moshagen, H., Gjertveit, E., Lund, S. and Verley, R.: *New International Standard for Offshore Pipelines*. Proc. ISOPE; Montreal, 1998
10. Moshagen, H., Verley, R., Bruschi, R. and Solemsli, O.: *The MULTISPAN Project. Project Background and Summary*. OMAE, Yokohama, 1997
11. Thorbjørnsen, B., Dale, H., Eldøy, S. and Mercanti, M.: *The Norfra Pipelione Shore Approach. Engineering, Environmental and Construction Challenges*. Proc. ISOPE, Honolulu, 1997

STABILITY AGAINST WAVES AND CURRENTS OF GRAVEL RUBBLE MOUNDS OVER PIPELINES AND FLAT GRAVEL BEDS

*Øivind A. Arntsen, Alf Tørum and Colin Kuester
Norwegian University of Science and Technology, Trondheim, Norway.*

INTRODUCTION

For different reasons oil/gas pipelines or parts of oil/gas pipelines have to be covered with rubble mounds. The question is then what the size of the stones/gravel in the mound should be to withstand waves and currents of the area. Typical design significant wave heights and mean wave periods for North Sea conditions are $H_s \approx 10 - 15$ m and $T_m \approx 10 - 15$ s. Typical pipeline diameters are $d = 20 - 40$ inches and typical height of the mound could be up to $(h-h_c) = 1.5 - 2.0$ m. Typical slopes of the mound are $\text{tg}\beta = 1:2 - 1:3$ and typical mean stone "diameter" in the mound has been $D_{50} = 50 - 100$ mm for North Sea wave and current conditions for water depth $h = 40 - 70$ m. In order to obtain more information on the stability of gravel mounds over pipelines, laboratory tests in a wave/current flume have been carried out and are summarized herein. In addition data from other similar investigations elsewhere are discussed. A brief analysis of the stability of a flat gravel bed subjected to irregular waves has also been included, using the concept of the statistical distribution of the bed shear stress.

NOMENCLATURE

$a_\delta(t)$	bed orbital displacement of water particles	$R_w = u_{\delta m} A_{\delta m} / \nu$	near bed wave Reynoldsnumber
A	damage area	$S = A/D_{n50}$	non-dimensional damage on a gravel or rock structure
$A_{\delta m}$	orbital amplitude of wave motion at the bed	t	time
B	width of mound berm	T_m	mean wave period
D	sieve grain size diameter	U	background current speed
d	pipe diameter	$u_* = \sqrt{\tau_b / \rho_w}$	friction velocity
$D_{n50} = (W_{50} / \rho_s)^{1/3}$	grain diameter for which 50% of the grains by mass are finer	$u_{\delta m}$	orbital amplitude of horizontal particle velocity at sea bed
D_p	sieve grain diameter for which $p\%$ of the gravel/stones are smaller	W_{50}	50% of the stones are heavier than W_{50}
f_g	grain gradation factor	z_0	$= k_s/30$ for rough turbulent flow; $= \nu/(9u_*)$ for smooth turbulent flow.
f_w	wave friction factor in $\tau_b = \frac{1}{2} \rho_w f_w u_\delta^2$	ρ_s	mass density of the gravel/stones
g	acceleration of gravity ($= 9.8 \text{ m/s}^2$)	ρ_w	mass density of the water
H	wave height	Δ	$= \rho_s / \rho_w - 1$
h	water depth around the mound	Φ	phase angle
h_c	water depth above the mound	β	angle of sloping bed to the horizontal
H_s	significant wave height	ε	small parameter
k_c	wave number calculated using h_c as depth	ν	kinematic viscosity of water
k_s	$= 2.5D_{50}$, sand roughness	$\theta = \tau_{bm} / (\rho_w g \Delta D_{n50})$	Shields mobility parameter
$M_p = u_{\delta m}^2 / (g \Delta D_{n50})$	a mobility parameter	σ	standard deviation of measured data
N	number of waves	τ_b	bed shear stress
$N_s = H / (\Delta D_{n50})$	stability number	τ_{bm}	maximum bed shear stress under a wave
P	probability of non-exceedence	τ_{cr}	threshold bed shear stress
$R_s = k_s u_* / \nu$	bed roughness Reynolds number	τ_p	bed shear stress for which $p\%$ of the stresses in a random sea is less

PREVIOUS WORK

There have been some previous studies on the stability of near-bed gravel structures and bed gravel protection. It has been customary to use a non-dimensional damage S to define the damage on a gravel or rock structure.

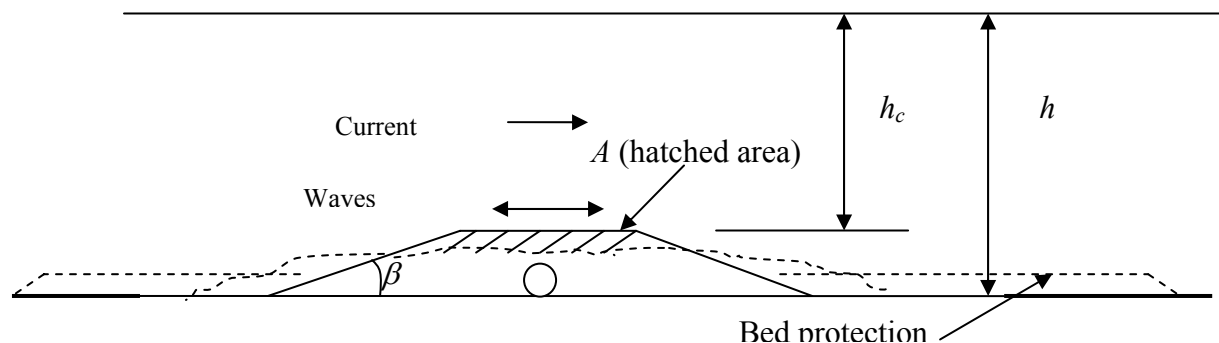


Figure 1. Definition sketch showing damage A to the mound.

With reference to Figure 1, S is defined as:

$$S = \frac{A}{D_{n50}^2} \quad (1)$$

where A is the damage area, $D_{n50} = (W_{50}/\rho_s)^{0.333}$. Typical test slopes have been $1:10 < \text{tg}\beta < 1:1$.

Vidal et al. (1998), (2002), (2007) carried out laboratory as well as full scale tests on near bed structures and sewage outfall protection structures exposed to waves. They analyzed their test data in different ways: Damage vs. a stability number $N_s = (H/\Delta D_{n50})$, damage vs. Morison force, damage vs. a mobility parameter $\theta = \tau_{bm}/(\rho g \Delta D_{n50})$, where the maximum sea bed shear stress τ_{bm} was calculated using Eq. (5). In the analysis of their first tests, (1998) and (2002), they used the water particle velocity on the top of the mound, calculated using linear wave theory as if the water depth was h_c . In their (2007) paper they found the water particle velocity above the mound using a numerical model and applied the maximum water particle velocity at the rear edge of the mound when calculating the mobility parameter.

Lomonaco et al. (2003) discuss further the water particle velocity above the mound. Based on field measurements they recommend that the water particle velocities as obtained from linear wave theory and with the water depth equal to the water depth above the mound are enhanced by a factor 1.41.

Lomonaco (1994) carried out tests on the stability of gravel mounds of different heights, in relation to water depth, and shape. He analyzed his data in different ways similar to Vidal et al. Lomonaco included also current in some of his tests.

Van Gent and Wallast (2001) carried out similar tests and in the same wave flume as Lomonaco (1994) on the stability of gravel mounds. They also analyzed their data in different ways, but arrived at the recommendation that the damage S should be set equal to:

$$S = 0.2 M_p^3 N^{0.5} \quad (2)$$

where $M_p = \frac{u_{\delta m}^2}{g\Delta D_{n50}}$ is a mobility parameter where $u_{\delta m} = \frac{\pi H_s}{T_m} \frac{1}{\cosh(k_c h_c)}$, and where k_c is the wave number calculated using linear wave theory with wave period equal to T_m and local water depth equal to h_c . The number of waves was typically $N = 2000$.

Figure 2 shows van Gent and Wallast's results for all their tests, including currents and some of Lomonaco (1994) data. Eq.(2) is also included in Figure 2. van Gent and Wallast stated that the influence from the current can be neglected when $U/u_{\delta m} < 2.2$ for $0.15 < M_p < 3.5$.

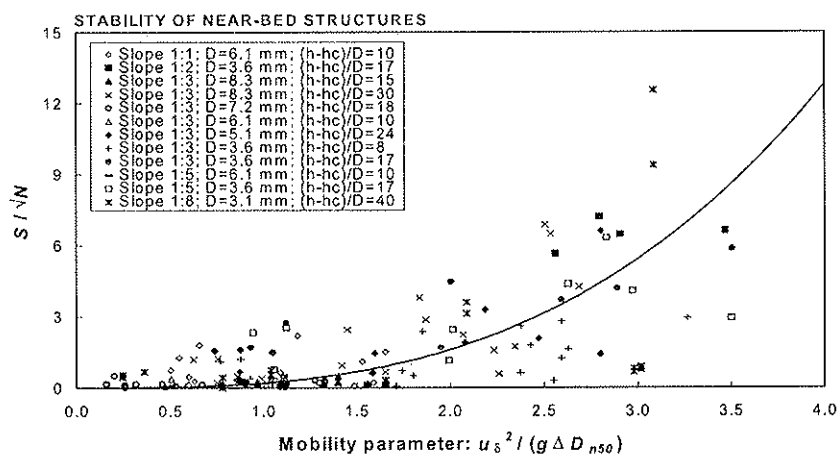


Figure 2. S/\sqrt{N} as a function of the mobility parameter M_p . Tests with and without a current. After van Gent and Wallast (2001).

It is noted that there is inherent scatter of the data. This is normally the case when testing the stability of granular material (breakwaters etc), but it could also reflect an improper model for the analysis. It is also noted that for small values of the mobility parameter (less than 1.0) Eq. (1) could under-predict the damage.

It is this method of van Gent and Wallast (2001) that is recommended in the newly published rock manual CIRIA, CUR, CETMEF (2007). The following is quoted from this manual, with referenced equation and figures from this present paper:

“Eq. (2) is the best fit on the measured values from model tests. Spreading exists around the predicted values, see Figure 2. The difference between the predictions of S/\sqrt{N} and existing data are characterized by a standard deviation of $\sigma = 1.54$ for conditions with waves only and $\sigma = 1.58$ for conditions with waves in combination with a current.” --- “A way to take the spreading into account for design purposes is by using an additional factor, α , with a value of $\alpha = 3.0$ in Eq.(2)” giving:

$$\frac{S}{\sqrt{N}} = \alpha \cdot 0.2 \cdot M_p^3 = 0.6 \cdot M_p^3 \quad (3)$$

As for mounds covering oil and gas pipelines the acceptable damage S should be rather low, $S < 50$ or $S/\sqrt{N} \approx 1.0$ assuming $N = 2000$. Hence the results for small values of the mobility parameter are of main interest. Eqs. (2) and (3) may not be adequate for the lower range of the mobility parameter M_p . This issue will be addressed later.

TESTS AT NTNU (2007)

Test set-up

In view of the diverging results from previous investigations it was decided to carry out additional tests and analysis at NTNU on the stability of rock mounds over pipelines in fairly deep water. The objective of the investigation was to arrive at improved design tools for the design of “near-bed-structures”. The results of the tests may be a basis for probabilistic or performance design analysis of gravel fill over pipelines. However, such analysis has not been carried out within this project.

Details of the tests and data analysis are found in Tørum, Kuester and Arntsen (2008). The tests were carried out in a wave/current flume shown schematically in Figure 3. The flume is 26.5 m long, 0.60 m wide and 0.70 m deep. The water depth during the tests was 0.50 m. At one end is a wave generator capable of generating regular and irregular waves. At the opposite end is a parabolic “beach” to absorb wave energy and create as little wave reflections as possible in the flume. Three wave gauges were positioned in the flume to measure the surface elevation at three points.

A 50-cm diameter return pipe, a flow impeller, and the various connections at either end created a circulation flow in the flume/pipe system. With a flume water depth of 0.5 m, this system is capable of producing a current up to 60 cm/s. Currents were measured by an Acoustic Doppler Velocity meter. The given current U in this paper is a cross-sectional average without waves.

The setup for these tests included two model mounds tested concurrently. They were spaced approximately 5 meters apart near the centre of the flume, with one wave gauge before the first mound, one between the mounds, and one after the second. The mounds were built trapezoidal in section, with heights of $(h-h_c) = 5$ cm and flat tops $B = 7.5$ cm wide. The first mound had slopes of $\text{tg}\beta = 1:3$ and the second mound has slopes of $\text{tg}\beta = 1:2$. The profiles of the mounds were measured with a laser system, guided on a track above at various cross-sections. The ratio of the mound crest height and the water depth, $(h-h_c)/h$, is $5/50 = 0.1$. Coarse sand with sieve diameter $D_{50} = 1.9$ mm with gradation factor $f_g = D_{85}/D_{15} \approx 3.1$ was used as mound material. D_{50} corresponds approximately to $1.2 \cdot D_{n50}$. The mass density of the stones was measured to $\rho_s = 2800$ kg/m³.

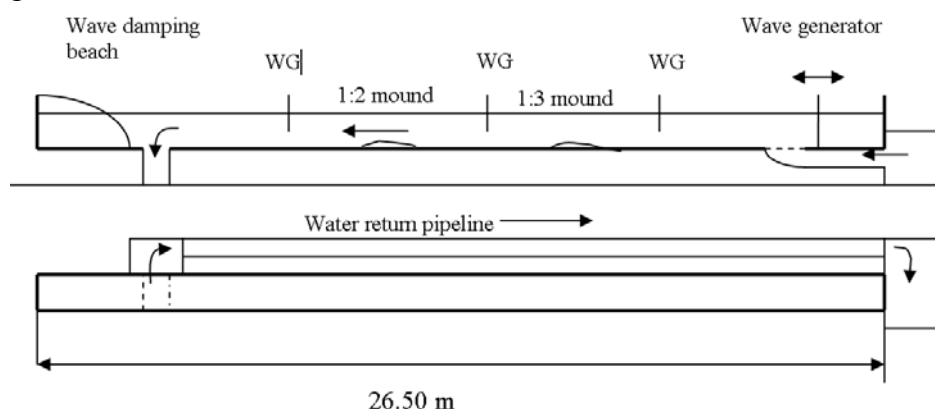


Figure 3. The wave/current flume, elevation and plan view, schematically shown. The mounds were located 5 m apart. WG = wave gauge

ANALYSIS RESULTS AND DISCUSSIONS

Analysis of mound data

The data analysis was performed to compare the data obtained in these tests to the data obtained by van Gent and Wallast (2001). It was noted that damage occurred only when a current was present, except one test. This is somewhat contradictory to the statement of van Gent and Wallast (2001) that the current had no significant influence on the damage. The damage parameter S/\sqrt{N} vs. the mobility parameter M_p is shown in Figures 4. Data from van Gent and Wallast (2001) tests are also included in Figure 4. Eq. (3) is also shown in the same figure. In Figure 5 data for the “No current” cases are shown. The Lomonaco (1994) data are for Structures No. 4 and 6 with height 0.05 and 0.125 m respectively.

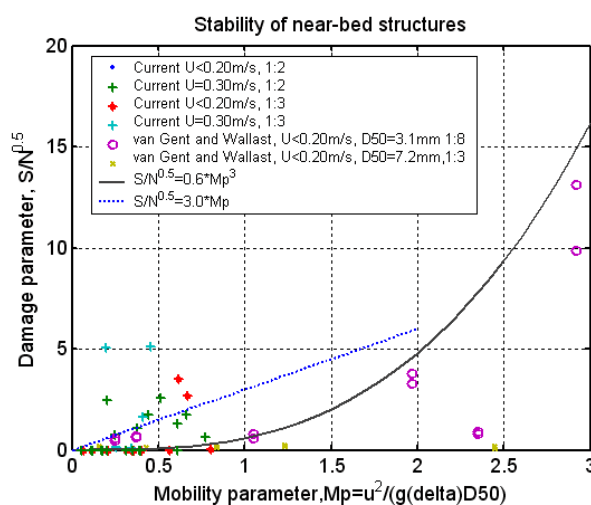


Figure 4. Damage as function of the mobility parameter. The damage parameter is S/\sqrt{N} (van Gent and Wallast's definition). Own data and data from van Gent and Wallast (2001).

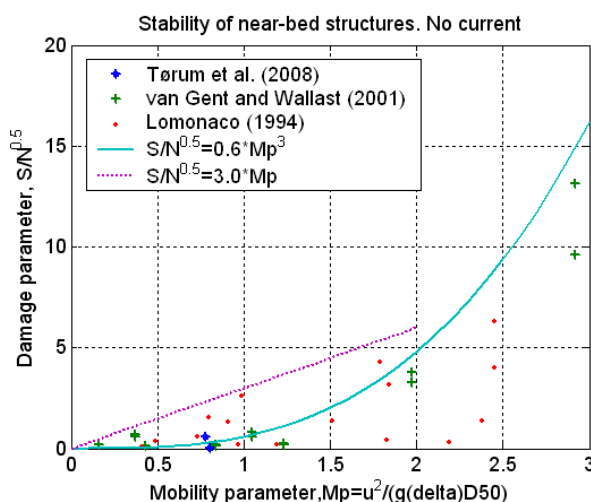


Figure 5. Damage as function of the mobility parameter. The damage parameter is S/\sqrt{N} (van Gent and Wallast's definition). No current. Own data and data from Lomonaco (1994) and from van Gent and Wallast (2001).

The tests with rather high velocity, $U = 30$ cm/s, show a rather high damage. This is because the current alone is then nearly able to move the stones. The waves will then tend to stir up the grains and the current is then more easily able to move them. The ratio of the current velocity U and the wave induced water particle velocity amplitude $u_{\delta m}$ is then $U/u_{\delta m} = 2.41$ and is outside the range where van Gent and Wallast stated that the influence from the current is negligible. Also, as shown in Table 1 (see later), $U/u_{\delta m} = 2.41$ is much higher than will be the case for “deep” North Sea conditions. Hence for “deep” North Sea design conditions the test results with the high velocities can be discarded. Tests with $U = 50$ cm/s showed considerable damage with the current alone.

It is interesting to note the significant differences of van Gent and Wallast’s results for slope $\text{tg}\beta = 1:8$, $D_{50} = 3.1$ mm and slope $\text{tg}\beta = 1:3$, $D_{50} = 7.2$ mm. This is an indication that the analysis method should be revisited.

Several other data was included by van Gent and Wallast (2001), cf. Figure 2. An upper bound for damage when $M_p < 1.0 - 1.5$ is given by

$$\frac{S}{\sqrt{N}} = 3.0M_p \quad (4)$$

Eq. (4) is also shown in Figures 4 and 5. Note that the mobility parameter is defined solely from wave parameters and that current parameters are not included in its definition.

Another aspect that may be of interest is to consider the wave induced water particle displacement amplitude $A_{\delta m}$ vs. grain diameter D_{50} , $A_{\delta m}$ vs. mound width B , and the current velocity U vs. wave induced particle velocity amplitude $u_{\delta m}$ for model and prototype conditions. This has been done as shown in Table 1 for two tests and for a prototype condition. Van Gent and Wallast (2001) states that the influence of the current can be neglected when $U/u_{\delta m} < 2.2$ for $0.15 < M_p < 3.5$. This would be the case for the prototype condition shown in Table 1. For Test 17 with a ratio $U/u_{\delta m} = 2.41$ it was seen that the damage was not acceptable because of the high current velocity. Test 16 and the prototype conditions come in this case closest to each other with respect to $U/u_{\delta m}$, $A_{\delta m}/D_{50}$ and $A_{\delta m}/B$. However, it is not exactly known how important this issue is with respect to the stability.

Table 1. Model vs. prototype. Width of berm = B . $B_{\text{model}} = 0.075$ m, $B_{\text{prototype}} = 2.0$ m.

	H_s (m)	T_m (s)	$u_{\delta m}$ (m/s)	U (m/s)	$U/u_{\delta m}$	$A_{\delta m}$ (m)	$A_{\delta m}/D_{50}$	$A_{\delta m}/B$
Model								
Test 16	0.093	1.40	0.148	0.1	0.67	0.033	17.4	0.44
Test 17	0.078	1.38	0.124	0.3	2.41	0.027	14.2	0.36
$D_{50} = 1.9\text{mm}$								
Prototype	10.6	10.7	1.39	0.90	0.64	2.38	31.7	0.79
$h = 40$ m, $D_{50} = 75$ mm								

Analysis and discussion of the flat bed case

Lomonaco (1994) included tests on the stability of gravel/stones on a flat bed. This case is almost similar to the case with a protection of the sea bed on either side of the mound, cf. Figure 1. The analysis of this flat bed stability data are, for “Waves only” cases, carried out in view of the statistical distribution of the wave shear stresses at the bottom, Myrhaug (1995).

The maximum shear stress on the sea bed under waves is expressed as:

$$\tau_{bm} = \frac{1}{2} \rho_w f_w u_{\delta m}^2 \quad (5)$$

Myrhaug (1995) deals with bottom friction beneath random waves. The waves are described as a stationary Gaussian narrow-band random process. According to Myrhaug, the bed orbital displacement is under this assumption given as:

$a_{\delta}(t) = A_{\delta m}(\varepsilon t) \cos[\omega t + \Phi(\varepsilon t)]$, and the bed orbital velocity as:

$$u_{\delta}(t) = \frac{da(t)}{dt} = u_{\delta m}(\varepsilon t) \sin\left[\omega t + \Phi(\varepsilon t) - \frac{\pi}{2}\right] + O(\varepsilon); \text{ where } u_{\delta m}(\varepsilon t) = \omega A_{\delta m}(\varepsilon t)$$

and $\omega = 2\pi/T$, t is time, Φ is a phase angle and ε is a small parameter. Myrhaug (1995) used the following relations for the friction factor f_w and where herein the different flow regimes are defined according to Madsen and Wood (2002):

$$\text{Laminar flow (i.e. } R_w = u_{\delta m} A_{\delta m} / \nu < 2000): \quad f_w = 2R_w^{-0.5} \quad (6)$$

$$\text{Smooth turbulent (i.e. } R_w > 2000 \text{ and } R_s = k_s u_* / \nu < 3.3): \quad f_w = 0.0450 R_w^{-0.175} \quad (7)$$

$$\text{Rough turbulent (i.e. } R_w > 2000 \text{ and } R_s = k_s u_* / \nu > 3.3): \quad f_w = 1.39 \left(\frac{A_{\delta}}{z_0} \right)^{-0.52} \quad (8)$$

Myrhaug found that the statistical distribution of the maximum shear stress, τ_{bm} , under each wave cycle followed a Weibull probability distribution function, with different values of parameters for laminar flow, smooth flow and turbulent flow:

$$\text{Laminar flow:} \quad P_{\tau_{bm}}(\xi) = 1 - \exp(-\xi^2); \quad \xi = \frac{\tau_{bm}}{\rho_w u_{*L}^2} \geq 0, \quad (9)$$

$$\text{Smooth turbulent flow:} \quad P_{\tau_{bm}}(\xi) = 1 - \exp(-\xi^{1.212}); \quad \xi = \frac{\tau_{bm}}{\rho_w u_{*S}^2} \geq 0, \quad (10)$$

$$\text{Rough turbulent flow:} \quad P_{\tau_b}(\xi) = 1 - \exp(-\xi^{1.35}); \quad \xi = \frac{\tau_{bm}}{\rho_w u_{*R}^2} \geq 0, \quad (11)$$

$$\text{Where } u_{*L}^2 = \frac{1}{2} \cdot 2R_{rms}^{-0.175} u_{rms}^2; \quad u_{*S}^2 = \frac{1}{2} \cdot 0.0450 R_{rms}^{-0.175} u_{rms}^2; \quad u_{*R}^2 = \frac{1}{2} \cdot 1.39 \left(\frac{A_{rms}}{z_0} \right)^{-0.52} u_{rms}^2$$

in which A_{rms} is the root-mean-square value of the water particle excursion at the bottom, u_{rms} the root-mean-square value of the near bed water particle velocity amplitudes and $R_{rms} = u_{rms} \cdot A_{rms} / \nu$ is the Reynolds number at the bottom for irregular waves. The rms-values are related to the zeroth moments of the amplitude and velocity spectral densities, respectively. Note that the distribution of the shear stress for the laminar case is a Rayleigh distribution.

In the derivations of the statistical distributions of the shear stress it has been assumed that the flow conditions are laminar, smooth or rough for all the waves in the considered sea state. However, this may not be the case, especially for laboratory conditions. The flow may be laminar for the smallest waves, smooth for intermediate waves and rough for the largest waves.

The critical shear stress τ_{cr} , i.e. the stress beyond which the stones start to move, is given in Soulsby and Whitehouse (1997) and Soulsby (1997) as mean value throughout a large range of D_* -values, including only current, only waves and a combination of waves and currents acting simultaneously with the formula:

$$\theta_{cr} = \frac{0.24}{D_*} + 0.055[1 - \exp(-0.020D_*)] \quad (12)$$

where $\theta_{cr} = \tau_{cr} / (\rho_w g \Delta D)$ is the critical Shields parameter and $D_* = \left[\frac{g \Delta}{\nu^2} \right]^{1/3} D$, where ν is the kinematic viscosity of the water.

Lomonaco (1994) used stones with $D_{50} = 4.34$ mm for the flat bed case. The critical shear stress, for these stones according to the Eq. (12) is $\tau_{cr} = 3.6$ N/m². D_{50} has been used as D in Eq. (12) and the value of D_* is then $D_* \approx 95$. It should be remembered that τ_{cr} is obtained from test data on the start of movement of the sand/stone grains and that there is scatter in the data. Examining the Shields diagrams shown in Soulsby and Whitehouse (1997) for $D_* \approx 95$ for the “only wave case” gives a minimum, mean and maximum critical shear stress of $\tau_{cr,min} = 4.2$ N/m², $\tau_{cr,mean} = 6.2$ N/m² and $\tau_{cr,max} = 9.1$ N/m².

The statistical distribution of the bed shear stresses in this case is carried out under the assumption that the flow is “rough, turbulent”. Closer examinations showed this was the conditions in this case for the largest waves. Figure 6 shows the calculated statistical distribution of the shear stresses for one of the test conditions of Lomonaco (1994), flat base case. The $\tau_{cr,min}$, $\tau_{cr,mean}$ and $\tau_{cr,max}$ is also marked in Figure 6. Similar statistical distributions have also been calculated for other of Lomonacos’s test cases.

The statistical distribution of the shear stresses is obtained under the assumption that the Rayleigh distribution applies for the wave heights and that the wave spectrum is narrow. As often done in coastal engineering the calculation has been assumed to be valid also for a JONSWAP spectrum with a γ -factor = 2.2.

The maximum shear stress will depend on the maximum wave height. The ratio of the maximum wave height to H_s , H_{max}/H_s vs. H_s for Lomonaco (1994) tests are shown in Figure 7. The ratio H_{max}/H_s is fairly low, which frequently is seen from tests in wave flumes and wave basins. One reason for this is probably limitations in capability of wave generators to generate the larger waves. Assuming that the wave heights are Rayleigh distributed the probability that the maximum wave height is not exceeded during the Lomonacos’s tests can be calculated. It is then assumed that the same probability applies for the shear stress also. Based on this

assumption the damage parameter S/\sqrt{N} vs. τ_{\max} has been plotted as shown in Figure 8. τ_{90} , e.g. the 90% probability of not being exceeded has, somewhat arbitrary, also been plotted for Lomonacos's flat base case. τ_{90} is close to what might be designated the significant shear stress, $\tau_s \approx \tau_{87}$. The minimum, mean and maximum critical shear stresses are also marked in Figure 8.

For the lowest damage value, $S/\sqrt{N} = 0.04$, the calculated maximum shear stress does not exceed the critical shear stress. However, as mentioned, there is some uncertainty on the value of the critical shear stress. According to the calculations τ_{cr} is exceeded for quiet many of the waves, some 8%, for the highest damage values, $0.4 < S/\sqrt{N} < 0.6$, Figure 8. If a damage $S = 50$ or $S/\sqrt{N} = 1.10$ for $N = 2000$, is accepted, the flat bed structures tested by Lomonaco are considered to be stable.

This approach to stability considerations of flat bed stone structures represents a new approach and should be further explored to obtain a relation between S/\sqrt{N} and τ_{\max} or τ_{90} or some other fracture of τ , both for the flat bed and for the mound case. For a mound some "new" critical Shields parameter, $\theta_{cr,mound}$, should be obtained.

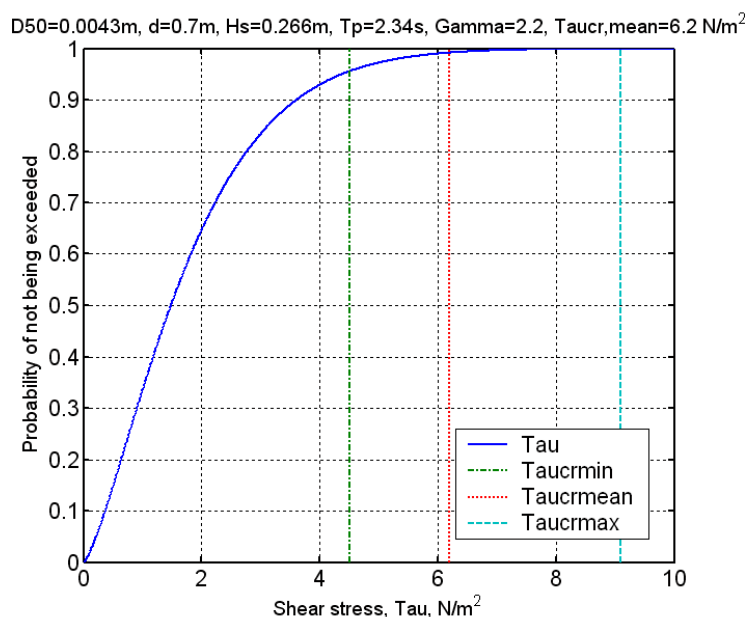


Figure 6. Lomonaco (1995) flat bed case. Probability of not exceeding a certain shear stress.

$h = 0.70$ m, $H_s = 0.266$ m, $T_p = 2.34$ s, JONSWAP wave spectrum with $\gamma = 2.2$. $\tau_{cr,min} = 4.2$ N/m², $\tau_{cr,mean} = 6.2$ N/m² and $\tau_{cr,max} = 9.1$ N/m².

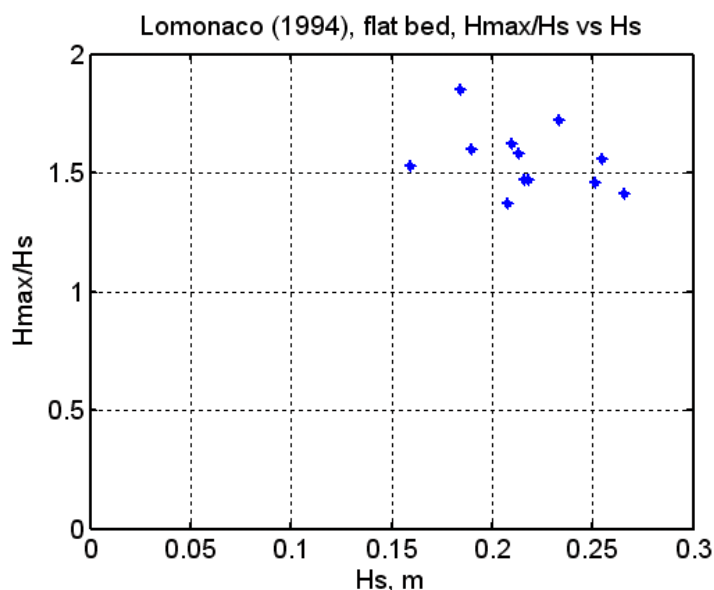


Figure 7. Ratio H_{\max}/H_s vs H_s during Lomonaco's tests, flat bed case.

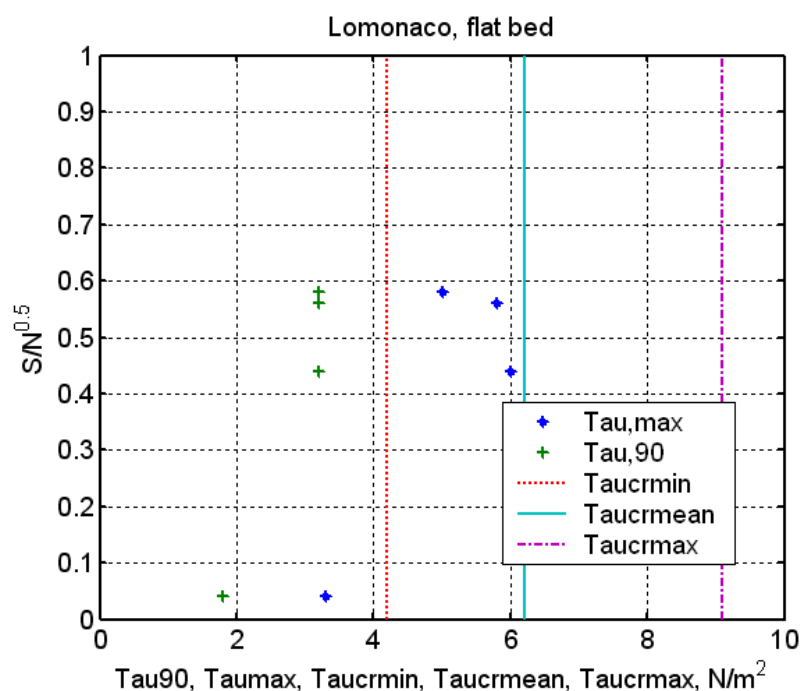


Figure 8. Lomonaco (1994), flat bed case. The damage parameter S/\sqrt{N} vs τ_{90} and τ_{\max} . $\tau_{\text{cr,min}} = 4.2 \text{ N/m}^2$, $\tau_{\text{cr,mean}} = 6.2 \text{ N/m}^2$ and $\tau_{\text{cr,max}} = 9.1 \text{ N/m}^2$.

CONCLUSIONS

Tests on the stability against waves of granular material (breakwaters, near bed structures, sand beds, sand bed protections et.) show inherent test results scatter. The scatter is due to several factors e.g. variation of the stone size, stone orientation, wave and current turbulence, observation procedures. Stability calculation methods are mainly based on some average value of the test results. Normally no safety factor is used on this average value approach. This may be because traditionally this approach has been taken for breakwaters and there has been tradition

for accepting some repair damage on rubble mound breakwaters. However, newer approaches have been to carry out probabilistic analysis of performance of structures, including mound structures, to actions from waves and currents, ISO 21650 (2007).

Mounds

It is recommended that the damage of homogenous mounds with slopes in the range $\text{tg}\beta < 1:2 - 1:3$ over pipelines is calculated for small damage values as follows:

$$S = 3.0 \cdot M_p \cdot \sqrt{N} \quad \text{for } M_p < 1.0 - 1.5$$

It remains to decide what the acceptable damage is. Vidal et al. (1998) recommended that a mound over a sewage outfall should be designed for $M_p < 0.06$ giving $S = 3.0$. The sewage outfall pipeline had fairly large stones, $W_{50} = 123, 386$ and 700 kg, placed in two layers. A rock mound over a pipeline with a crest width of $B = 2$ m and $D_{n50} = 0.10$ m means that there are on the average approximately $B/D_{n50} = 2.00/0.10 = 20$ stones across the crest width. With $S = 50$ and $S = 100$ it means that approximately 2.5 and 5 layers of the stones will be removed respectively or 0.25 m and 0.50 m. The mound will probably cover the pipeline with at least 0.50 m. A damage of $S = 50$ should probably be acceptable.

It is recommended that “Acceptable damage” is therefore set to $S = 50$.

In general it is noted that in calculations of the stability of granular materials (mound breakwaters, mounds over pipelines etc.) exposed to waves the calculation formulas are based on some mean values of test results. Further probability of damage analysis should include the inherent scatter of test results and the uncertainty of wave climates at the location under consideration.

The scatter in the test results especially for low mobility parameters, the important range for gravel mounds over pipelines in “deep” water, induces uncertainties in the design basis. Improved kinematics of the waves when passing over a mound should be used in future work on the stability of pipeline mounds, and may be a better understanding of the interaction of the water and the stones on the mound, may be by a “new” shear stress concept.

Analysis of results of surveys (profiles) of existing mounds over pipelines with documentation of wave conditions between survey periods may also be useful.

Flat bed

A new approach to investigate the stability of flat bed stone protection layers has been outlined. This approach has been based on work by Myrhaug (1995) on the statistical distribution of wave induced shear stresses. Further experimental work should be carried out to obtain improved stability criteria. The same approach should probably be taken for mounds also. But then a “mound Shields number” should be established.

ACKNOWLEDGEMENTS

The Authors thank ConocoPhillips for the financial support to build the water current system in the wave flume. The Valle Scandinavian Scholarship and Exchange Program at the University of Washington, Seattle, USA, are acknowledged for providing a scholarship for Colin Kuester to stay at NTNU. The Authors also acknowledge fruitful discussions with Professor Dag Myrhaug, NTNU.

REFERENCES

- CIRIA, CUR and CETMEF. 2007: *The Rock Manual. The use of rock in hydraulic engineering.* (2nd edition). C83, CIRIA, London.
- ISO 21650. 2007: Actions from waves and currents on coastal structures. *International Standard*, First edition, 2007-10-15.
- Kuester, C. 2007: *Waves and currents on near-bed structures. Data summary report.* Norwegian University of Science and Technology, Department of Civil and Transport Engineering/Valle Scandinavian Scholarship and Exchange Program. June 2007.
- Lomonaco, P. 1994: *Design of rock cover for underwater pipelines.* MSc-thesis International Institute for Infrastructural, Hydraulic and Environmental Engineering, Delft Technological University, Delft, The Netherlands.
- Lomonaco, P., Vidal, C., Losada, I.j. and Mendez, F.J. 2003: Wave height, pressure and velocity CDF's (*cumulative distribution function*) around rubble protections for submarine outfalls. *Proceedings of the conference Coastal Structures 2003*, 26 – 30 August 2003, Portland, Oregon, USA. American Society of Civil Engineers (ASCE).
- Madsen, Ole S. and Wood, William. 2002. Sediment Transport Outside the Surf Zone In: *Coastal Engineering Manual, Part III, Coastal Sediment Processes, Chapter III-6, Engineer Manual 1110-2-1100*, U.S. Army Corps of Engineers, Washington, DC.
- Myrhaug, D. 1995: Bottom friction beneath random waves. *Coastal Engineering*, 24 pp 259 – 273, 1995.
- Myrhaug, D., Holmedal, L.E., Simons, R.R. and MacIver, R.D. 2001: Bottom friction in random waves plus current flow. *Coastal Engineering*, 43 pp 75 – 92, (2001).
- Soulsby, R.L. and Whitehouse, R.J.S. 1997: Threshold of sediment motion in Coastal Environments. Proc. *Combined Australasian Coastal Engineering and Ports Conference*, Christchurch, 1997.
- Soulsby, R.L. 1997: *Dynamics of marine sands.* Publisher Thomas Telford, London, UK.
- Tørum, A., Kuester, C. and Arntsen, Ø.A. 2008: *Stability against waves and currents of rubble mounds over pipelines.* Norwegian University of Science and Technology, Department of Civil and Transport Engineering, Report no. BAT/MB-R1/2008. Under preparation.
- Van Gent, M.R.A. and Wallast, I 2001: *Stability of near-bed structures and bed protections. Analysis of physical model tests with waves and currents.* Delft Cluster report DC030204H3804, Delft Hydraulics, December 2001, Delft, The Netherlands.
- Van Gent, M.R.A. and Wallast, I. 2002: Stability of near-bed structures under waves and currents. *Proceedings of the 28th International Coastal Engineering Conference*, 7 – 12 July 2002, Cardiff, Wales, Great Britain. World Scientific Publishing Co. Pte Ltd.
- Vidal, C., Losada, I., Martin, F.L. 1998: Stability of near-bed rubble mound structures. *Proceedings of 26th International Conference on Coastal Engineering*, 22 – 26 June 1998, Copenhagen, Denmark. ASCE.
- Vidal, C., Lomonaco, P. and Martin, F.L. 2002: Prototype analysis of stability of rubble mound protections for submarine outfalls. *Proceedings of the 28th International Coastal Engineering Conference*, 7 – 12 July 2002, Cardiff, Wales, Great Britain. World Scientific Publishing Co. Pte Ltd.
- Vidal Pascual, C., Lopez Mera, F. and Losada, I. 2007: Stability analysis of low-crested and submerged rubble mound breakwaters: Relation between flow characteristics and measured damage and stability formulae for low-crested and submerged breakwaters. *Proceedings of the international conference on Coastal Structures 2007*, 1 – 5 July 2007, Venice, Italy.

KEYWORDS

Pipeline, waves and currents, rubble mound, stability, bed shear stress, laboratory experiments.

STOCHASTIC AND DYNAMIC APPROACHES TO SEABED BOUNDARY LAYER AND SEDIMENT DYNAMICS UNDER IRREGULAR WAVES PLUS CURRENT

*Dag Myrhaug and Lars Erik Holmedal
Department of Marine Technology
Norwegian University of Science and Technology
NO-7491 Trondheim, Norway*

ABSTRACT

In real situations, ocean waves are random of nature; this affects the boundary layer flow and wave-current induced sediment transport. The paper is organized as follows. Section 1 gives an introduction containing an overview of the topic. In Section 2 the background of a stochastic method is given together with three recent examples of application for random waves; the bedload sediment transport caused by boundary layer streaming; the erosion and deposition of mud, and the mobile layer thickness in sheet flow. Section 3 deals with the bedload sediment transport and associated ripple migration rates under random waves plus current using Monte Carlo simulations of parameterized models. Section 4 gives examples of results of suspended sediment transport under random waves plus current using a classical dynamic sediment diffusion model in combination with a dynamic turbulent boundary layer model. A Summary is given in Section 5.

INTRODUCTION

The complexity of the phenomena associated with the flow over sandy seabeds in the combined action of waves and currents is well known. Suspended sediment concentrations over sandy seabeds in shallow and intermediate water depths, i.e. in coastal zones and on continental shelves, occur predominantly as a result of the combined action of waves and currents. The waves are the principal cause of the entrainment of the sediments, which are diffused into the flow by turbulent processes, and subsequently transported by the current. The combination of waves and currents, and sediment transport affect many engineering applications. Wave-current-sediment interaction considerations are included in scour and erosion studies for seabed pipelines and other near seabed structures. This interaction is also important in developing models for predicting the movement of sediments on the seabed in combined action of waves and currents, and the resulting coastal evolution.

The wave-current-sediment interaction has been investigated theoretically and experimentally by many researchers for several decades. The subject is treated in the books by Fredsøe and Deigaard (1992), Nielsen (1992), and Soulsby (1997). Theory and experiments show generally that the effect of adding currents to waves is to enhance the bedload and sediment suspension, as well as causing sediment transport.

Previous studies of bottom friction beneath random waves have been undertaken by, among others, Madsen (1994); Simons et al. (1994, 1996); Myrhaug (1995); Myrhaug et al. (1998, 2001); Mathiesen and Madsen (1999); Samad (2000); Holmedal et al. (2000, 2003); Myrhaug and Holmedal (2002, 2003, 2005); Myrhaug et al. (2004) as well as Tanaka and Samad (2006). Madsen (1994) gave explicit wave friction factor formulas for spectral wave-current boundary layer flow. The formulas were obtained using a time-invariant eddy viscosity model based on the concept of an equivalent sinusoidal wave having the same near-bed orbital velocity amplitude and excursion amplitude as the *rms* value of the wave spectrum. Laboratory experiments studying the bed boundary layer under random waves plus current were carried out by Simons et al. (1994, 1996) and by MacIver and Simons in 1998 (see Myrhaug et al. (2001)). All these measurements were

performed in the basin at the UK Coastal Research Facility allowing for waves having an angle of attack on the current. Myrhaug (1995) showed that if the free surface elevation is assumed to be stationary Gaussian narrow-band process, the bed shear stress maximum for waves alone is Weibull distributed. This approach was successfully compared with estimates of bed shear stresses under random waves from field measurements near the seabed in the Strait of Juan de Fuca, Washington State, and at EDDA, North Sea, in Myrhaug et al. (1998). The Myrhaug (1995) approach was extended by Myrhaug et al. (2001) to weak wave-current interactions. Mathiesen and Madsen (1999) investigated the bottom roughness for spectral waves and current. Their experiments show that sinusoidal and spectral wave-current bottom boundary layer flow over a fixed rippled bed can both be characterized by a single bottom roughness when used in conjunction with a representative equivalent wave. Samad (2000) and Tanaka and Samad (2006) investigated laminar and smooth turbulent flow characteristics in the bed boundary layer under irregular waves. They performed systematic experimental investigations as well as computations using a $k - \varepsilon$ model. Shear stress amplitudes under random waves plus current have been calculated by Holmedal et al. (2000) using Monte Carlo simulations of Soulsby's (1997) parameterized wave-current friction factor formulas valid for sinusoidal waves plus current. Holmedal et al. (2003) used a dynamic eddy viscosity ($k - \varepsilon$) model to investigate the seabed boundary layer under random waves plus current. Myrhaug and Holmedal (2002) extended Myrhaug et al. (2001) approach to calculate the bottom friction in nonlinear random waves plus current flow near a rough bed in the lower near-bed excursion amplitude to bed roughness range. Myrhaug and Holmedal (2003) used a similar approach to calculate the laminar bottom friction beneath nonlinear random waves. Myrhaug and Holmedal (2005) investigated the effect of boundary layer streaming on the seabed shear stresses, beneath random waves, for laminar flow and smooth turbulent flow, while Myrhaug et al. (2004) did the same for rough turbulent flow.

Previous studies of bedload transport rate under random waves have been undertaken by Myrhaug and Holmedal (2001), Holmedal and Myrhaug (2004) as well as Myrhaug et al. (2004). The first reference calculated analytically the bedload transport rate under random second order Stokes waves using a simple bedload formula by Damgaard et al. (1996) for each individual wave component. The second reference calculated the flat bed bedload transport rate under random waves plus current using Monte Carlo simulations of Soulsby's (1997) parameterized wave-current friction formulas combined with his bedload transport formula valid for sinusoidal waves plus current. The third reference investigated the effect of streaming on the bedload sediment transport rate beneath random waves and compared the magnitude of this effect with that caused by second order asymmetric waves as determined by Myrhaug and Holmedal (2001).

Previous studies of sediment suspension and sediment transport over a flat bed for random waves have been undertaken by, among others, Zyserman and Fredsøe (1988), Ribberink and Al-Salem (1994), Deigaard et al. (1999) and Holmedal et al. (2004). Zyserman and Fredsøe (1988) investigated the mean suspended sediment transport due to irregular waves plus current using a model based on the momentum-defect boundary layer model of Fredsøe (1984). Ribberink and Al-Salem (1994) used a Jonswap spectrum to generate random Stokes second-order oscillations in an oscillating water tunnel. The net sediment transport rate due to the wave asymmetry was investigated, and vertical time-averaged profiles of sediment concentrations were given for a range of wave parameters. Deigaard et al. (1999) predicted the net sediment transport under wave groups and bound long waves, using a one-dimensional mixing length model in conjunction with a sediment diffusion model. Both the effect of streaming and mass drift were included. Holmedal et al. (2004) investigated the sediment suspension under sheet flow conditions beneath random waves plus current using a classical dynamic sediment diffusion model in conjunction with a dynamic turbulent boundary layer model.

Field studies have also been made; reviews are given in Grant and Madsen (1986) and Myrhaug et al. (1995); the second reference gave a review of the measurements made to that date. The second reference also included an extensive analysis of North Sea data; here time series of near-bed velocities, estimated seabed shear stresses and suspended sediment concentrations were given. Furthermore, sea bed ripples before and after storms were investigated. From two different measurements after storms, with similar physical conditions, it appeared that sediment transport had taken place only for one of the measurements. This exemplifies the complexity of field measurements; mechanisms not captured by the measurement equipment can take place. The earlier mentioned work of Myrhaug et al. (1998) also contained comparisons between the Myrhaug (1995) parametric model and the North Sea measurements. Trowbridge and Agrawal (1995) represent the first detailed field measurements of the sea bed boundary layer. Employing a profiled Laser Doppler Velocimeter deployed on a tripod, they were able to measure velocities as close as 0.5 cm above the sand bottom. These measurements were carried out at the Field Research Facility in Duck, North Carolina, USA, operated by the U.S. Army Corps of Engineers Waterways Experiment Station. Foster et al. (2000) presented field measurements of velocity and suspended sediments in the near-shore wave bottom boundary layer. The measurements were carried out during the period 14th to 23th of August, 1994, at the Army Corps of Engineers Field Research Facility in Duck, North Carolina, USA. These observations were the first surf zone measurements of the wave boundary layer structure, the moveable bed elevation, as well as the vertical structure of suspended sediments. It was found that the boundary layer under significant sediment response exhibits a more rapid mixing of momentum than predicted from simple eddy viscosity models.

STOCHASTIC METHOD WITH EXAMPLES OF APPLICATION

Background

The present method is based on the following assumptions: (1) the free surface elevation $\zeta(t)$ is a stationary Gaussian narrow-band random process with zero expectation described by the single-sided spectral density $S_{\zeta\zeta}(\omega)$, and (2) the formulas for bottom friction, bedload transport, mobile layer thickness in sheet flow, erosion and deposition of mud for regular waves are valid for irregular waves as well.

The second assumption implies that each wave is treated individually, and that memory effects are neglected. The accuracy of this assumption has been justified by Samad (2000) (see also Tanaka and Samad (2006)) for laminar and smooth turbulent boundary layer flow. They found good agreement between the measured bed shear stresses (laminar and smooth turbulent) under irregular waves and simulations of bed shear stresses based on individual wave formulas. For rough turbulent flow the validity of this approach was confirmed for seabed shear stresses by Holmedal et al. (2003) for high values of A/z_0 (≈ 30000). Time-series of seabed shear stresses were obtained by using a standard high-Reynolds number ($k - \varepsilon$) model; the waves were generated using a Jonswap frequency spectrum with a peakedness factor of 3, and linear potential theory was applied to evaluate the time-series of near-bed wave orbital displacement and velocity. Characteristic statistical values of the resulting seabed shear stress amplitude deviated less than 20% from those obtained by the Monte Carlo simulation method by Holmedal et al. (2000). The Holmedal et al. (2000) method is essentially based on the same two assumptions upon which the present approach is based. Regarding the second assumption that each wave is treated individually, Holmedal et al. (2003) concluded for large values of A/z_0 that the main reason for the fair agreement obtained between the Monte Carlo simulations and ($k - \varepsilon$) model predictions is the good description of the wave friction factor for individual waves. This appears to be much more important than violating the assumption of independent individual waves. Since the bottom friction, bedload transport,

mobile layer thickness in sheet flow, erosion and deposition formulas for mud are essentially based on the bed friction factors for laminar, smooth turbulent and rough turbulent flow, the assumption of treating each wave individually seems reasonable.

The narrow-band assumption is generally considered to be a better approximation at the seabed than at the surface, since most of the higher frequencies near the seabed are filtered away because of the linear wave dispersion relationship. It should also be noted that the Holmedal et al. (2003) results included both memory effects and the effect of finite bandwidth of the wave process. Thus, based on the results referred to above, this also justifies that the narrow-band assumption is reasonable for practical application. More details are given in Holmedal et al. (2003). More discussion of the accuracy of the narrow-band assumption will also be given below.

Based on the present assumptions, the time-dependent near-bed orbital displacement $a(t)$ and velocity $u(t)$, are both stationary Gaussian narrow-band processes with zero expectations. For a narrow-band process the waves are specified as a “harmonic” wave with cyclic frequency ω and with slowly varying amplitude and phase. Then, for the first order, W is related to A by $W = \omega A$. It follows from the narrow-band assumption that the near-bed orbital displacement amplitude, A , the near-bed orbital velocity amplitude, W , and the linear wave height, H , are Rayleigh-distributed with the cumulative distribution function (*cdf*) given by $P(\hat{x}) = 1 - \exp(-\hat{x}^2)$; $\hat{x} = x / x_{rms} \geq 0$ where x represents A , W or H , and x_{rms} is the *rms* value of x representing A_{rms} , W_{rms} or H_{rms} . Moreover, for a narrow-band process the wave frequency ω is taken as the mean zero-crossing frequency for the near-bed orbital displacement ω_z , i.e. $\omega = \omega_z = W_{rms} / A_{rms}$. This result is valid for a stationary Gaussian random process. Note that for a finite-band process this zero-crossing frequency of $a(t)$ at the bed generally will be smaller than zero-crossing frequency of $\zeta(t)$ at the surface due to greater attenuation of high frequencies; this means that the high wave frequency components will not reach the bottom. However, for a narrow-band process these zero-crossing frequencies will be equal, since there is only one frequency present.

Let y represent the response variable of interest, i.e. the bottom friction, bedload transport, etc. which is a function of the flow variables; say A and W . A consequence of the narrow-band assumption is that $A = W / \omega = W / \omega_z = \hat{W} A_{rms}$ where $\hat{W} = W / W_{rms}$, and thus the nondimensional response variable $\hat{y} = y / \bar{y}_{rms}$ is given by $\hat{y} = \hat{y}(\hat{W})$; \bar{y}_{rms} is the response quantity defined in terms of the characteristics flow variables. Now the *cdf* of \hat{y} follows by transformation of random variables when $\hat{W}(\hat{y})$ is known by utilizing that the probability density function of \hat{y} is obtained by $p(\hat{y}) = p(\hat{W}) |d\hat{W} / d\hat{y}|$ and that \hat{W} is Rayleigh-distributed. For the cases considered here $\hat{y} = \hat{W}^\gamma$, $\gamma > 0$ and thus the *cdf* of \hat{y} becomes $P(\hat{y}) = 1 - \exp(-\hat{y}^\beta)$; $\hat{y} \geq 0$, $\beta = 2/\gamma$, i.e. \hat{y} is Weibull-distributed. For known *cdf* the characteristic statistical values can be calculated. Often it is of interest to compare the results from a stochastic approach with those of a deterministic approach, i.e. representing the irregular waves by an equivalent sinusoidal wave. The deterministic approach is obtained by replacing the wave-related quantities by their *rms*-values in the regular wave formulas.

EXAMPLES OF APPLICATION

Bedload sediment transport caused by boundary layer streaming beneath random waves

The steady streaming under sinusoidal waves is caused by the non-uniformity of the wave boundary layer resulting from spatial changes of the orbital velocities. This wave-induced current is due to the

vertical velocities generated within the bottom boundary layer under progressive waves, which are not exactly out of phase with the horizontal velocities, leading to a non-zero time-averaged bed shear stress. The steady streaming for a laminar wave boundary layer was determined by Longuet-Higgins (1956). Based on this work the streaming-related time-averaged bed shear stress can be expressed in terms of the wave friction factor and the wave number (see e.g. Nielsen, 1992). The purpose of this example is to investigate the effect of streaming on the bedload sediment transport rate beneath random waves, and to compare the magnitude of this effect with that of second order wave asymmetry determined by Myrhaug and Holmedal (2001). The asymmetric wave motion gives a non-zero net sediment transport in the direction of wave propagation. The present results should be taken as valid for flows over flat rough beds with $A/z_0 \gtrsim 900$, for which the momentum transfer is dominated by turbulent processes, leading to streaming in the direction of wave propagation. The results for the bedload transport rate are particularly relevant to shingle and coarse sand, where all or at least most of the sediment transport takes place as bedload. It should be noted that two second order effects are considered; streaming is a second order effect of linear waves; second order wave asymmetry as a property of second order waves. Streaming under second order waves, which is not considered here, would imply including terms of similar or smaller magnitude.

The bedload transport caused by streaming is calculated using the Soulsby (1997) formulas for bedload transport by regular waves plus current. The reason is that the wave motion, with the effect of streaming included, can be modelled by waves plus a weak current caused by streaming. This corresponds to the wave-dominated situation for co-linear waves plus current.

The ratio between the effect of second order wave asymmetry and the effect of streaming in a given water depth from intermediate to shallow water (for $\pi/10 \leq \bar{k}h \leq 1.2$) versus $\bar{k}h$ is shown in Fig. 1. Overall it appears that the second order wave asymmetry effect is nearly an order of magnitude larger than the streaming effect in shallow water, while the two effects are approximately of the same order of magnitude in intermediate water. However, both effects are much smaller in intermediate than in shallow water. It should be noted that confidence in the results can only be supported by measurements or simulations by random waves. More details are given in Myrhaug et al. (2004).

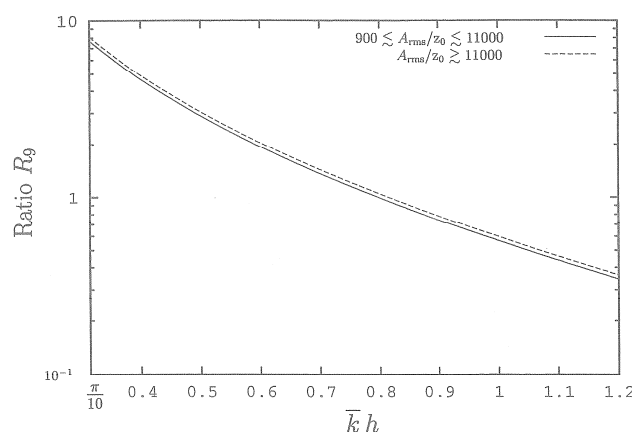


Figure 1 - The ratio between the effect of second order wave asymmetry and the effect of streaming in a given water depth versus $\bar{k}h$; \bar{k} is associated with ω_z determined from $\omega_z^2 = g\bar{k} \tanh \bar{k}h$ (from Myrhaug et al. (2004)).

Erosion and deposition of mud beneath random waves

Clays and silt are referred to as mud, where fine to medium clay has $d_{50} = 0.001$ mm, and coarse silt has d_{50} up to 0.06 mm (Soulsby, 1997). The movement of mud within coastal and estuarine waters might have large economical and ecological impact in the development of new engineering works and maintenance of existing installations, e.g. related to necessary routine dredging required for ports' accessibility to shipping. The capability to predict the movement of mud is also crucial to understand the distribution of certain pollutants adsorbed to mud as cohesive sediments are often contaminated nowadays. It appears that organic (pcb's, etc.) and inorganic (heavy metals, etc.) pollutants adhere easily to the clay particles and organic material of the sediments. Further details on the background and complexity as well as reviews of the problems are given in Whitehouse et al. (2000) and Winterwerp and van Kesteren (2004).

Physically erosion and deposition take place simultaneously (similar as for sand); more discussion is found in Winterwerp and van Kesteren (2004). However, the present approach based on treating the erosion and deposition to take place independently, is the one most frequently used. One should note that although the flow conditions over mud beds most likely are in the laminar or smooth turbulent flow regime (Whitehouse et al. (2000), p. 52), rough turbulent flow is included in the formulation in order to make it complete.

The application of the stochastic method is shown with examples using data for field conditions, demonstrating how engineering assessments of the mean erosion and the mean deposition rates of mud beneath random waves can be made. The examples represent laminar (deposition) and smooth turbulent (erosion) flow conditions, and it appears that a stochastic approach should be used for deposition, while the deterministic method is an adequate approximation to the stochastic method for erosion. However, other examples might give other results regarding whether a deterministic or a stochastic method should be used. Comparisons with data are required before a conclusion regarding the validity of this approach can be given. More results are given in Myrhaug et al. (2006).

Mobile layer thickness in sheet flow beneath random waves

Under large random waves over a flat bottom wave or current induced seabed ripples are washed out, such that a layer of high sediment concentration is developed in the vicinity of the bed, i.e. a sheet flow layer with a thickness of the order of mm to cm depending on how it is defined, i.e. as the erosion depth or the sheet flow layer thickness.

The sheet flow layer is defined as the layer where concentrations are so high that intergranular forces and sediment-flow interaction forces are important. The erosion depth and the sheet flow layer thickness represent two characteristic parameters for transport processes in oscillatory sheet flow. Sheet flow transport is important in the surf zone even in moderate wave conditions, and the associated high concentrations play an important role for erosion, sedimentation and morphology as well as for the design of coastal structures. Under severe wave conditions sheet flow may occur in intermediate water depths where e.g. buried pipelines and foundations of structures may be exposed since part of the sediments are transported. Sheet flow conditions might also have ecological implications since the suspension of sediments might directly affect life in the ocean in several ways; for example by hindering settling of plankton which benthic vertebrates feed on, causing a cut in the population, and thus affecting the food chain. Moreover, highly turbid water might negatively impact fish to feed, as well as reducing their reproduction rate. The suspended sediments also play an important role in spreading and transport of pollutants, since it affects the upper bottom sediment layer which is brought into suspension.

Following Dohmen-Janssen (1999) (see also Dohmen-Janssen et al. (2001) and O'Donoghue and Wright (2004)), the erosion depth (δ_e) is defined as the distance between the top of the non-moving sand bed at zero velocity and the top of the bed at maximum velocity; the sheet flow layer thickness (δ_s) is defined as the distance between the top of the non-moving sand bed at maximum velocity and the level where the time-average concentration becomes equal to 8 vol% (see Fig. 2). For a concentration of 8 vol% the distance between particles is on the average equal to the grain diameter. Studies of sheet flow under sinusoidal waves have found that the ratio between the maximum thickness of the mobile layer in a wave cycle and the median sand grain size diameter is proportional to the maximum Shields parameter in a wave cycle; the Shields parameter is the dimensionless bottom shear stress.

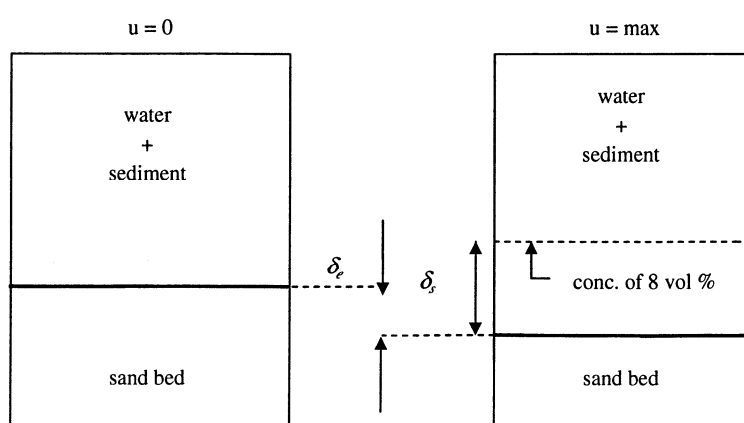


Figure 2 – Definitions of erosion depth (δ_e) and sheet flow layer thickness (δ_s) (reproduced from Dohmen-Janssen (1999, Fig. 2.8) and Dohmen-Janssen et al. (2001, Fig. 2)).

Application of the stochastic method shows that sheet flow conditions are achieved every 18-80 days (based on the critical Shields parameter for sheet flow of 0.8 and 1.0, respectively) at the seafloor of the Ekofisk location in the central North Sea at a water depth of 70 m. The seafloor consists mainly of fine sand with median grain size diameter $d_{50} = 0.20$ mm. These results are obtained by applying the Myrhaug and Hansen (1997) long-term distribution of seabed shear stresses beneath random waves. Moreover, for a sea state corresponding to a 100 year return period at the Ekofisk location with significant wave height $H_s = 15$ m and mean zero-crossing wave period $T_z = 12.3$ s, it was found that $\delta_e = 5$ mm and $\delta_s = 23$ mm.

For shallower flow conditions at a water depth $h = 15$ m with $H_s = 5$ m, $T_z = 8.9$ s and $d_{50} = 0.20$ mm it was found that $\delta_e = 10$ mm and $\delta_s = 44$ mm.

It should be noted, however, that the sheet flow layer thickness will also depend on the erosion/accretion pattern resulting from divergence of the sediment transport rate under non-uniform conditions, as well as on bedform migration, which both could cause a larger thickness. It should also be noted that confidence in the results can only be supported by measurements or simulations for random waves. More results are given in Myrhaug and Holmedal (2007).

Bedload transport under irregular waves plus current from Monte Carlo simulations of parameterized models with application to ripple migration rates observed in the field

The bedload transport rate under random waves plus current has been predicted for a large range of wave-current conditions. A parameterized model valid for regular waves plus current has been used in Monte Carlo simulations, assuming the wave amplitudes to be Rayleigh distributed. This model is described in details in Holmedal and Myrhaug (2004).

In order to investigate the applicability of the present approach, comparisons with field measurements by Amos et al. (1999) have been made. In these field measurements bed state, ripple migration and bedform transport of fine sand were recorded with time-lapse photography on Sable Island Bank, the Scotian Shelf, Canada.

Figure 3 (left part) shows contours of measured ripple migration rates, from the measurements by Amos et al. (1999). The figure is a partial reproduction from Amos et al. (1999, Fig. 3) and is displayed here in order to give a complete description of the measured ripple migration process. The contours are plotted against the near-bed current velocity U_b (m/s) and the mean deviation of the near-bed wave velocity amplitude, W_{md} (m/s) which here is related to W_{rms} by $W_{md} = 1.25\sqrt{2}W_{rms}$. The whole thick line represents the limit for ripple breakoff for wave formed ripples; the dashed lines show the contours of ripple migration rate by Amos et al. (1999). Below the breakoff limit ripple migration increases with the flow. Above the breakoff limit ripple migration may either increase or decrease and ripples degrade. The breakoff region represents a transition from low to high sediment transport rates, marking the onset of saltation and suspension. Since the bedload prediction is based on the skin-friction shear stress, and since the estimated ripple migration rate is only related to the bedload, the physical behaviour at and above the ripple breakoff limit can not be captured by the present model. In the present model the ripple migration increases with the flow; no ripple breakoff is predicted. Since the region between 10^{-3} mm/s and the ripple breakoff limit essentially represents bedload transport alone, a comparison with the present model is feasible in this region. Thus the contours 10^{-3} mm/s and 10^{-2} mm/s are compared with predictions.

Figure 3 (right part) shows a comparison between predicted and measured contours of the ripple migration rate in the feasible region where the sediment transport takes place as bedload. The axes, the measured contours (dashed lines) as well as the ripple breakoff limit are the same as in the left part of Fig. 3, but the contours which do not represent bedload have been removed for the sake of clarity. The whole thin lines represent the estimated ripple migration rate contours corresponding to the measured ones. It appears that the predictions capture the qualitative behaviour of the ripple migration rates with one exception: For small U_b the curvature of the predicted contours is positive, while that of the measured contours is negative. Overall, the ripple migration rate is surprisingly well predicted, except for stronger currents, where the ripple migration is underpredicted. More details are given in Holmedal and Myrhaug (2004).

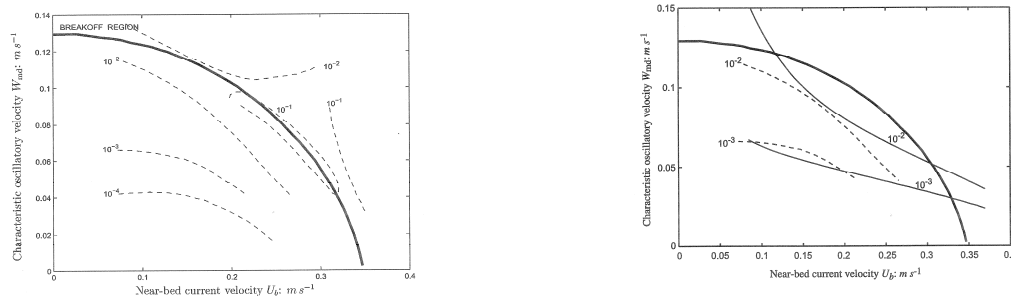


Figure 3 - Left part: contours of ripple migrations rates (dashed lines) and ripple breakoff region (whole thick line). The ripple migration rates are given in mm/s. Field measurements by Amos et al.(1999). Right part: Comparisons between predicted (whole thin line) and measured (dashed lines) ripple migration rate contours (mm/s) in the bedload regime. The whole thick line represents the ripple breakoff region. The averaged sea bed roughness is evaluated from $z_0 = 2.5d_{50}/30$ (from Holmedal and Myrhaug (2004)).

SEDIMENT SUSPENSION UNDER SHEET FLOW CONDITIONS: RANDOM WAVES PLUS CURRENT

The suspended sediment concentration under large random waves alone as well as under large random waves plus current has been examined by a classical dynamic sediment diffusion model in conjunction with a dynamic turbulent boundary layer model based on the linearized boundary layer equations with horizontally uniform forcing. The turbulence closure is provided by a high Reynolds number $k-\varepsilon$ model. This model is described in details in Holmedal et al. (2004). Under such conditions wave or current induced sea bed ripples are washed out, such that a sheet flow and a suspension layer of high sediment concentration exist.

Figure 4 shows time series of suspended sediment concentrations under random waves obtained from a Jonswap spectrum, at six elevations ranging from 0.1 cm to 3 cm above the theoretical bed; the outer wave velocity is included below the abscissa. The phase lags of the sediment concentrations can be observed by following the local maxima within wave half-cycles. For the largest individual waves, suspended sediments prevail after each individual wave half-cycle; this can be seen by following the sediment concentration nearest the bed, denoted with the solid line in Fig. 4. Physically this might be explained by the late decay of turbulent eddies after being generated, causing sediments to remain in suspension as the near-bed flow reverses. When large individual wave half-cycles are followed by larger wave half-cycles, as happens in wave groups, sediments are accumulated in the suspension layer. This is clearly seen in Fig. 4 under the wave group given in the time interval 850-900 seconds. This pumping-up of sediments under large wave groups has been observed both in field and laboratory measurements.

The most common situation at sea is the simultaneous presence of random waves and current, and hence it is of practical interest to investigate the resulting suspended sediment concentration. Now the near-bed velocity is taken as the random near-bed wave velocity superposed on a steady current at the elevation 0.5 m above the sea bed. The shift in wave frequency due to the current is disregarded here, since this is significant only for very strong currents.

The mean vertical sediment flux profiles have also been predicted from random waves plus current and from an equivalent wave plus current. The agreement is surprisingly good; for all cases the sediment flux obtained from the equivalent wave approach differs less than about 30 percent from the sediment flux obtained from the random wave approach. The largest difference occur near the

bed; in most of the vertical range the difference between the equivalent wave approach and the random wave approach, is less than about 10 percent. Overall, this strongly supports the equivalent wave concept for predicting sediment fluxes over a range of wave-current parameters. More details are given in Holmedal et al. (2004).

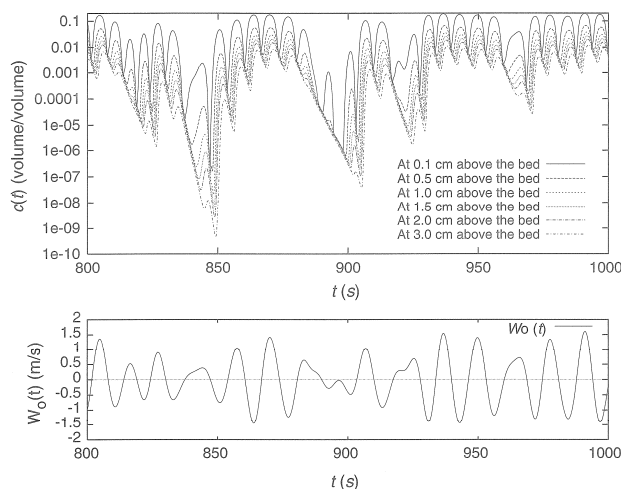


Figure 4 - Predicted time series of the sediment concentration, at six elevations above the bed. The outer velocity W_0 is included below the abscissa. Realizations of random waves are obtained from a parameterized Jonswap spectrum as described in details in Holmedal et al. (2003). Here the sea state is characterized by a significant wave height of 12 m and a peak period of 13.86 s; the water depth is 40 m. The median grain diameter d_{50} is 0.21 mm and is related to the bed roughness by $z_0 = d_{50}/12$. The settling velocity of the sediments is 0.026 m/s (from Holmedal et al. (2004)).

SUMMARY

The effect of the random nature of ocean waves on the bottom boundary layer flow and the near-bed wave-current induced sediment transport has been addressed by giving examples from three different approaches. Although there is lack of experimental data for random waves to compare with, the obtained results appear to be physically sound.

The results obtained by using a classical sediment diffusion model in combination with a dynamic turbulent boundary layer model, support the application of an equivalent wave to predict mean sediment concentrations, mean sediment fluxes, as well as the total sediment transport under sheet flow conditions.

Moreover, the predictions by using Monte Carlo simulations of parameterized models capture the qualitative behaviour of the ripple migration rates in a wide range of wave-current conditions. The ripple migration rate is fairly well predicted, except for stronger currents, where the ripple migration is underpredicted. This shows the capacity of the present simple engineering model to predict the bed load transport in the ocean.

The results by the stochastic method for the bedload sediment transport caused by streaming; the mobile layer thickness in sheet flow; and the erosion and deposition of mud are based on idealized conditions and, as such, the results should be taken as a first approximation. Confidence in the results can only be supported by measurements of simulation for random waves. However, e.g. to separate the streaming effects in experiments are both difficult and challenging; two-dimensional simulations for random waves are also demanding.

REFERENCES

- Amos, C.L., Bowen, A. J., Huntley, D.A., Judge, J. and Li, M.Z. 1999. Ripple Migration and Sand Transport Under Quasi-Orthogonal Combined Flows on the Scotian Shelf, *Journal of Coastal Research* 15 (1), 1-15.
- Damgaard, J.S., Stripling, S. and Soulsby, R.L. 1996. Numerical modeling of coastal shingle transport, Report TR4. Wallingford, UK: HR Wallingford.
- Deigaard, R., Jacobsen, J.B. and Fredsøe, J. 1999. Net sediment transport under wave groups and bound long waves, *J. Geophys. Res.* 104 (C6), 13559-13575.
- Dohmen-Janssen, C.M. 1999. Grain size influence on sediment transport in oscillatory sheet flow. Phase-lags and mobile-bed effects, PhD Thesis, Delft University of Technology, The Netherlands.
- Dohmen-Janssen, C.M., Hassan, W.N. and Ribberink, J.S. 2001. Mobile-bed effects in oscillatory sheet flow, *J. Geophys. Res.* 106 (C11), 27103-27115.
- Foster, D.L., Beach, R.A. and Holman, R.A. 2000. Field observations of the wave bottom boundary layer, *J. Geophys. Res.* 105 (C8), 19631-19647.
- Fredsøe, J. 1984. Turbulent boundary layer in wave-current motion, *J. of Hydraulic Eng.* ASCE, 110, 1103-1120.
- Fredsøe, J. and Deigaard, R. 1992. Mechanics of Coastal Sediment Transport, *World Scientific*, Singapore.
- Grant, W. D. and Madsen, O.S. 1986. The continental-shelf bottom layer, *Ann. Rev. Fluid Mech.* 18, 265-305.
- Holmedal, L.E. and Myrhaug, D. 2004. Bedload transport under irregular waves plus current from Monte Carlo simulations of parameterized model with application to ripple migration rates observed in the field, *Coastal Eng.* 51, 155-172.
- Holmedal, L.E., Myrhaug, D. and Eidsvik, K.J. 2004. Sediment suspension under sheet flow conditions beneath random waves plus current, *Cont. Shelf Res.* 24, 2065-2091.
- Holmedal, L.E., Myrhaug, D. and Rue, H. 2000. Seabed shear stresses under irregular waves plus current from Monte Carlo simulations of parameterized models, *Coastal Eng.* 39, 123-147.
- Holmedal, L.E., Myrhaug, D. and Rue, H. 2003. The sea bed boundary layer under random waves plus current, *Cont. Shelf Res.* 23(7), 717-750, err., 1035.
- Longuet-Higgins, M.S. 1956. The mechanics of the boundary layer near the bottom in a progressive wave, *Proc. 6th Int. Conf. Coastal Eng.*, ASCE, Miami, 184-193.
- Madsen, O.S. 1994. Spectral wave-current bottom boundary layer flows, *Proc. 24th Int. Conf. Coastal Eng.*, ASCE, Kobe, Japan, 384-398.
- Mathiesen, P.P. and Madsen, O.S. 1999. Waves and currents over a fixed rippled bed 3. Bottom and apparent roughness for spectral waves and currents, *J. Geophys Res.* 104(C8), 18447-18461.
- Myrhaug, D. 1995. Bottom friction beneath random waves, *Coastal Eng.* 24, 259-273.
- Myrhaug, D. and Hansen, E. H. 1997. Long-term distribution of seabed shear stresses beneath random waves, *Coastal Eng.* 31, 327-337.
- Myrhaug, D. and Holmedal, L.E. 2001. Bedload sediment transport rate by nonlinear random waves, *Coastal Eng. J.* 43(3), 133-142.
- Myrhaug, D. and Holmedal, L.E. 2002. Bottom friction in nonlinear random waves plus current flow, *Proc. 18th Int. Conf. Coastal Eng.*, ASCE, Cardiff, Wales, 1, 545-556.
- Myrhaug, D. and Holmedal, L.E. 2003. Laminar bottom friction beneath nonlinear random waves, *Coastal Eng. J.* 45, 49-61.
- Myrhaug, D. and Holmedal, L.E. 2005. Bottom friction caused by boundary layer streaming beneath random waves for laminar and smooth turbulent flow, *Ocean Eng.* 32, 195-222.
- Myrhaug, D. and Holmedal, L.E. 2007. Mobile layer thickness in sheet flow beneath random waves, *Coastal Eng.* 54, 577-585.

- Myrhaug, D., Holmedal, L.E., Simons, R.R. and MacIver, R.D. 2001. Bottom friction in random waves plus current flow, *Coastal Eng.* 43, 75-92.
- Myrhaug, D., Holmedal, L.E. and Rue, H. 2004. Bottom friction and bedload sediment transport caused by boundary layer streaming beneath random waves, *Applied Ocean Res.* 26, 183-197.
- Myrhaug, D., Holmedal, L.E. and Rue, H. 2006. Erosion and deposition of mud beneath random waves, *Coastal Eng.*, 53, 793-797.
- Myrhaug, D., Slaattelid, O.H. and Lambrakos, K.F. 1998. Seabed shear stresses under random waves: Predictions versus estimates from field measurements, *Ocean Eng.* 25, 907-916.
- Myrhaug, D., Slaattelid, O.H., Soulsby, R.L. and Lambrakos, K.F. 1995. Measurements and analysis of flow velocity and sediment concentration at the sea bed, *Appl. Mech. Rev.* 48(9), 570-587.
- Nielsen, P. 1992. Coastal bottom boundary layers and sediment transport, *World Scientific*, Singapore.
- O'Donoghue, T. and Wright, S. 2004. Flow tunnel measurements of velocities and sand flux in oscillatory sheet flow for well-sorted and graded sands, *Coastal Eng.* 51 (11-12), 1163-1184.
- Ribberink, J.S. and Al-Salem, A.A. 1994. Sediment transport in oscillatory boundary layers in cases of rippled beds and sheet flow, *J. Geophys. Res.* 99 (C6), 12707-12727.
- Samad, M.A. 2000. Investigation of bottom boundary layer under irregular waves, PhD-Thesis Department of Civil Engineering, Tokohu University, Aoba, Sendai, Japan.
- Simons, R.R., Grass, T.J. and Tehrani, M.M. 1994. Bottom shear stresses under random waves with a current superimposed, *Proc. 24th Int. Conf. Coastal Eng., ASCE*, Kobe, Japan, 565-578.
- Simons, R.R., MacIver, R.D. and Saleh, W.M. 1996. Kinematics and shear stresses from combined waves and longshore currents in the UK coastal research facility, *Proc. 25th Int. Conf. Coastal Eng., ASCE*, Orlando, USA.
- Soulsby, R.L. 1997. Dynamics of marine sands, *Thomas Telford Publications*.
- Tanaka, H. and Samad, M.A. 2006. Prediction of instantaneous bottom shear stress for smooth turbulent bottom boundary layers under irregular waves, *J. Hydraulic Res.* 44(1), 94-106.
- Trowbridge, J.H. and Agrawal, Y.C. 1995. Glimpses of wave boundary layer, *J. Geophys. Res.* 100 (C10), 20729-20743.
- Whitehouse, R., Soulsby, R., Roberts, W. and Mitchener, H. 2000. Dynamics of estuarine muds, *Thomas Telford*, London, UK.
- Winterwerp, J.C. and van Kesteren, W.G.M. 2004. Introduction to the physics of cohesive sediment in the marine environment, Elsevier, Amsterdam, The Netherlands.
- Zyserman, J.A. and Fredsøe, J. 1988. Numerical simulation of concentration profiles of suspended sediment under irregular waves. Inst. of Hydrodynamics and Hydraulic Engng, Technical University of Denmark, Progress Report 68, pp. 15-26.

KEYWORDS: Random waves plus current; Streaming; Sheet flow; Sediment transport; Turbulence; Stochastic processes.

EXPERIMENTAL INVESTIGATIONS OF THE EFFICIENCY OF ROUND-SECTIONED HELICAL STRAKES IN SUPPRESSING VORTEX INDUCED VIBRATIONS

Raed Lubbad¹

¹*Norwegian University of Science and Technology (NTNU), Trondheim, Norway*

ABSTRACT

Vortex Induced Vibrations (VIV) may cause great damage to deep-water risers. Helical strakes are used as a mitigating measure to suppress these vibrations. The purpose of this paper is to verify the efficiency of round-sectioned helical strakes in suppressing VIV. It is believed that round-sectioned helical strakes more readily can be mounted on risers for intervention and maintenance compared to sharp-edged strakes that may have to be welded onto the risers.

Systematic experimental investigations including twenty eight configurations of round-sectioned helical strakes were tested in an attempt to find an optimal strake configuration. The experiments were performed in a steady flow flume, with an elastically mounted rigid circular cylinder of 50 cm length and 5 cm outer diameter. The test cylinder was spring-supported in both the in-line and cross-flow directions. The measurements were limited to map the displacement of the cylinder. The smooth cylinder was tested and used as a reference case. Lastly, the experiment investigated the effects on the cylinder's response of restraining the motion of the test cylinder in the in-line direction.

The optimum configuration for the tested round-sectioned helical strakes reduces the amplitude of oscillation relative to the smooth cylinder by 95.6 % in the cross-flow direction, and by 96.9 % in the inline direction. The main features of this optimum configuration are manifested by the number of starts (3), the pitch ($5D$) and the diameter of strake ($0.15D$), respectively where D is the outer diameter of the test cylinder and starts refer to the number of individual strakes used.

INTRODUCTION

Marine risers are essential for the offshore petroleum industry. Risers are used for drilling of sub sea wells and for well intervention and also for the flow of well fluids to production facilities at the surface. Furthermore, export risers take the processed fluids to storage, to loading terminals or to pipelines leading to shore facilities. The importance of proper design of marine risers is coming into sharper focus of the oil companies as they venture into deeper water. The costs of well intervention and well maintenance are also increasing with depth and slim line intervention from simple support vessels would make well intervention economic in many instances where hiring of a large rig or a drill ship may be economically prohibitive causing wells to produce less efficiently than required.

A major concern in the development of deep-water risers is Vortex Induced Vibrations (VIV) of risers subjected to large deep-water ocean currents. These vibrations increase the drag forces acting on the riser and they may cause fatigue damage. Therefore, it is of utmost importance to accurately predict such vibrations and to have dependable method by which to suppress them when necessary. Blevins (1990) suggests four options to suppress VIV. Namely by increasing the reduced damping, avoiding resonance, using streamlined cross sections, and by adding vortex suppression devices. Zdravkovich (1981), and Jones and Lamb (1993) classify the vortex

suppression devices into the following three categories: Surface protrusions (Topographic devices), Shrouds and Nearwake stabilisers (Wake devices). According to Jones and Lamb (1993), helical strakes are the most successful topographic devices. The edge of these strakes causes the flow separation to occur at the strake while the helical shape disturbs the axial correlation of the vortices which reduces the global lift force. Helical strakes are simple, reliable and omni-directional. Their use involves some disadvantages however, mostly related to handling problems during the installation and amplification of drag coefficient when the riser is not vibrating.

This paper is based on a master thesis at NTNU, Lubbad (2006). The main bulk of this paper is presented also in Lubbad et al. (2007). The paper presents experimental data on the response of circular cylinders, fitted with round-sectioned helical strakes, in a steady uniform current. The analysis of the experimental data shall determine the efficiency of round-sectioned helical strakes and decide upon the optimal design of these strakes.

The motivation for the present work is very much of practical nature. The innovation of a new spinning machine initiated the current study (Norwegian Patent Application Number P5256NO). This machine has the potential to fit ropes helically to the riser during the installation phase which helps overcoming the handling problems of the ordinary sharp-edged helical strakes. The circular strakes (e. g. ropes) can be spun onto the riser when it leaves the surface vessel and can be spun off the riser at the bottom when the riser is about to enter a well. It is also believed that ropes more easily can be fixed to flexible risers as compared to sharp-edged strakes. The circular strakes (e.g. ropes) may also be applied to riser bundles and to smaller risers strapped piggyback onto carrier risers.

DESCRIPTION OF THE EXPERIMENTS

The Test Rig

A purpose designed rig was constructed in order to test the VIV response of an elastically mounted rigid circular cylinder. The rig was designed to have low structural damping and mass ratio, and it allowed the test cylinder to oscillate in the cross- flow as well as the in-line directions. Due to its good stiffness / weight ratio, aluminum was chosen as the building material for both the rig and the test cylinder. Table 1 summarizes the properties of the rig, while Fig. 1 shows a schematic presentation of the elevation and the side views of this experimental apparatus.

The experimental apparatus was equipped with four sensitive force gauges in order to track the horizontal and vertical positions of the test cylinder. The locations of these gauges are shown in Fig. 1. Similar rigs have been used by many different researchers in the field of flow induced vibrations. It is believed that it was first introduced in Moe and Overvik (1982).

Table 1: The properties of the test rig.

External diameter of the test cylinder	0.05 m
Length of the test cylinder	0.5 m
The equivalent stiffness of the springs of the test rig in the in-line direction	791 N/m
The equivalent stiffness of the springs of the test rig in the cross-flow direction	244 N/m
Natural period of oscillation for the test rig in water without the test cylinder (in-line direction)	0.30 s
Natural period of oscillation for the test rig in water without the test cylinder (cross-flow direction)	0.83 s

Natural period of oscillation for the test rig in water with the test cylinder (in-line direction)	0.60 s
Natural period of oscillation for the test rig in water with the test cylinder (cross-flow direction)	1.046 s
Mass of the test cylinder in air (including the end plates and the fittings)	1.53 kg
Mass ratio of the test rig in the cross-flow direction (without the added mass)	4.62
Mass ratio of the test rig in the in-line direction (without the added mass)	2.66
Relative damping ratio in the cross-flow direction for the test rig in water without the cylinder	1.1%
Relative damping ratio in the in-line direction for the test rig in water without the cylinder	2.8%

The Steady Current Flume

A new tank was built for the purpose of this study at the Harbour and Coastal Laboratories at NTNU. The tank (12 m × 0.7 m × 1.2 m) was designed to generate a steady flow by circulating the water inside the tank. After many trials, an almost uniform current was obtained in the tank by using perforated plates and pipe grids at various locations. The obtainable current velocity was limited due to the height of the tank walls, and the maximum velocity was approximately 47 cm/s. An Acoustic Doppler Velocity meter (ADV) was used to measure the mean current velocity and to estimate the turbulence intensity.

As indicated in Fig. 1, the vertical arms of the test rig are oscillating in separate channels in order to reduce the damping of the rig. The width of these side channels, w , is 6.5 cm. Moreover, the test cylinder is placed horizontally in the tank at a depth of 25 cm while the total water depth is 50 cm. The cylinder is connected to the vertical arms through gaps in both of the internal walls. The dimension of the gaps is 7 cm × 14 cm.

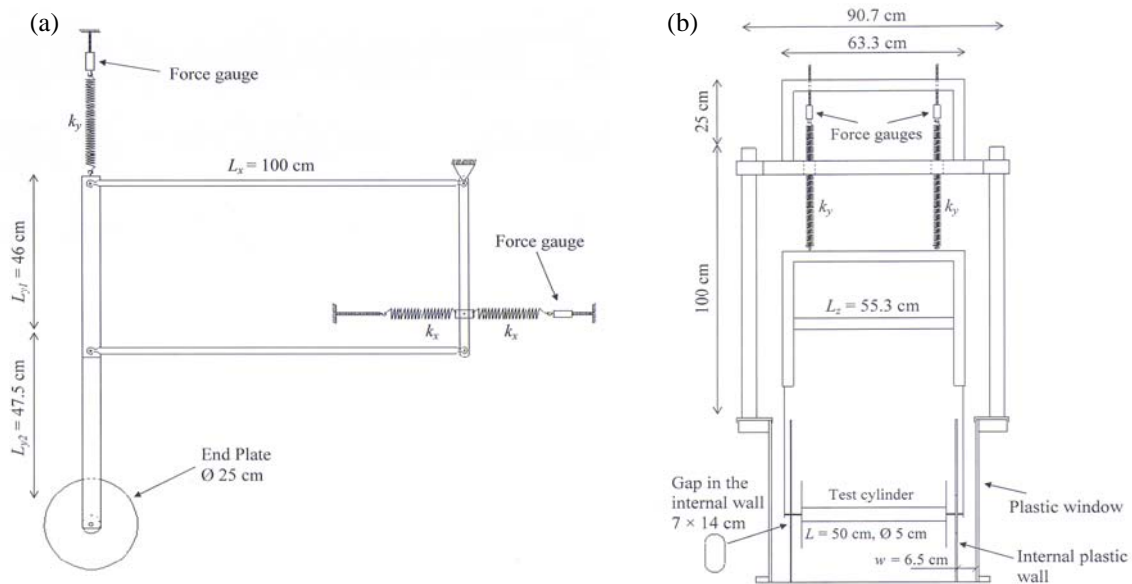


Figure 1: A schematic presentation of the rig used in the present study: (a) elevation (front) view, (b) side view.

Types of the Experiments Conducted

During the testing period, different types of experiments were conducted as follows:

- Decay tests in air and water for the rig with and without the test cylinder. The decay tests in water without the test cylinder were used to calculate the structural damping, since their contribution to damping covers all the damping except the contribution from the hydrodynamic forces on the cylinder.
- VIV tests with different configurations of the test cylinder.

The Different Configurations of the Test Cylinder

The smooth cylinder was tested and used as a reference case, i.e. the rest of the configurations were compared to it. The configurations of a cylinder with round-sectioned helical strakes are defined by the number of starts, diameter of the strake and the pitch of the strake (the pitch is defined as the distance along the cylinder axis that is needed to complete one full turn of the strake). Table 2 presents the configurations of round-sectioned strakes that were tested while Fig. 2 shows an actual picture of the ropes (cables) that were used in the tests.

Table 2: The tested configurations of cylinders with round-sectioned helical strakes.

	$d/D: 0.06$	0.08	0.1	0.15	0.20
Pitch/ D : 2.5			- 3 starts - 1 start		
3.5				- 3 starts	
5	- 3 starts - 1 start	- 3 starts - 1 start	- 3 starts - 2 starts - 1 start	- 3 starts - 2 starts - 1 start	- 3 starts - 1 start
5.5				- 3 starts	
6.5				- 3 starts	
8				- 3 starts	
10	- 3 starts - 1 start	- 3 starts - 1 start	- 3 starts - 1 start	- 3 starts - 1 start	- 3 starts - 1 start

where d is the strake diameter and D is the test cylinder diameter

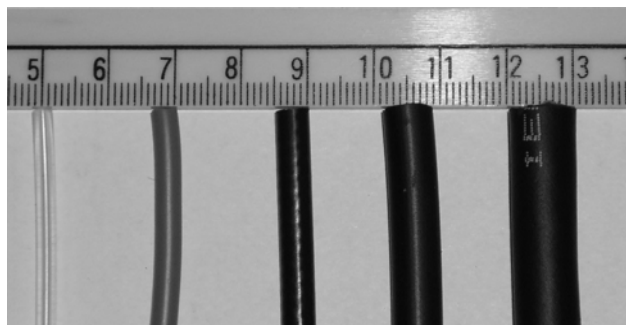


Figure 2: A picture of the cables that were used as helical strakes during the tests.

Some tests were run, in which oscillations in the cross flow direction only were permissible (One Degree of Freedom, 1DOF). The results of these tests were useful to check the sensitivity of the results.

The methodology of the tests

A complete test series consisted of 15 tests. Within each test series, the current velocities were increased in steps from 4.7 cm/s obtained in the first test, up to 47 cm/s achieved in the last test. The Reynolds number varied from $2.4 \cdot 10^3$ to $2.4 \cdot 10^4$. Hence, the whole test series was located in the subcritical flow regime. The range of reduced velocities in the cross-flow and in-line

directions was 1 to 10 and 0.57 to 5.7, respectively. These reduced velocities were calculated as $U_r = U/(f \cdot D)$ where U_r is the reduced velocity, U is the flow velocity, D is the diameter of the test cylinder and f is the natural frequency of oscillation of the test cylinder in still water.

The procedures in each test were:

- Setting the propeller carriage to the right value.
- Waiting until the current in the tank reached the required velocity (ADV was used to monitor the current velocity 16 cm upstream the center of the cylinder).
- Interfering with the motion of the cylinder. In other words, excite it if it was not moving, or stop it if it was vibrating.
- Waiting until the cylinder reached an equilibrium state (dynamic/static equilibrium).
- Starting the data acquisition. The sampling frequency was 100 Hz and the acquisition period was 60 s during each test.

Beside the VIV tests, decay tests were performed as much as possible to control the damping parameter. All decay tests were carried out by exciting a displacement and letting the test cylinder oscillate freely until it returns to the rest position.

THE EXPERIMENTAL RESULTS

Analysis Method

A Matlab subroutine was developed to analyse the time series obtained from the tests. This subroutine is able to locate the peaks in any time series as shown in Fig. 3. Then the amplitude ratio of the response, (A/D) , is calculated as $(Y_{p-p}/2D)_{mean}$, where Y_{p-p} is the peak to peak value of the response and D is the diameter of the test cylinder.

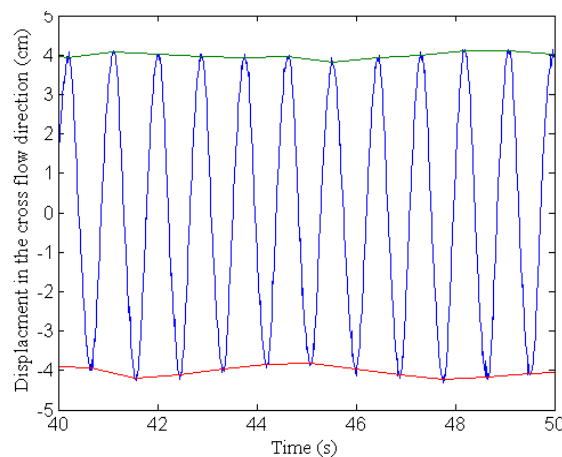


Figure 3: The locations of the peaks in the time series.

By performing the same analysis for the complete test series, the response of the cylinder can be plotted versus the reduced velocity.

Results

Fig. 4 shows the response of a smooth cylinder in the cross flow, CF, and the inline, IL, directions. Table 3 illustrates the maximum amplitude of oscillation in the lock-in range, $(A/D)_{max}$, of the test cylinder fitted with the different configurations of round-sectioned helical strakes (in Table 3, the test cylinder oscillates simultaneously in the in-line and cross flow directions).

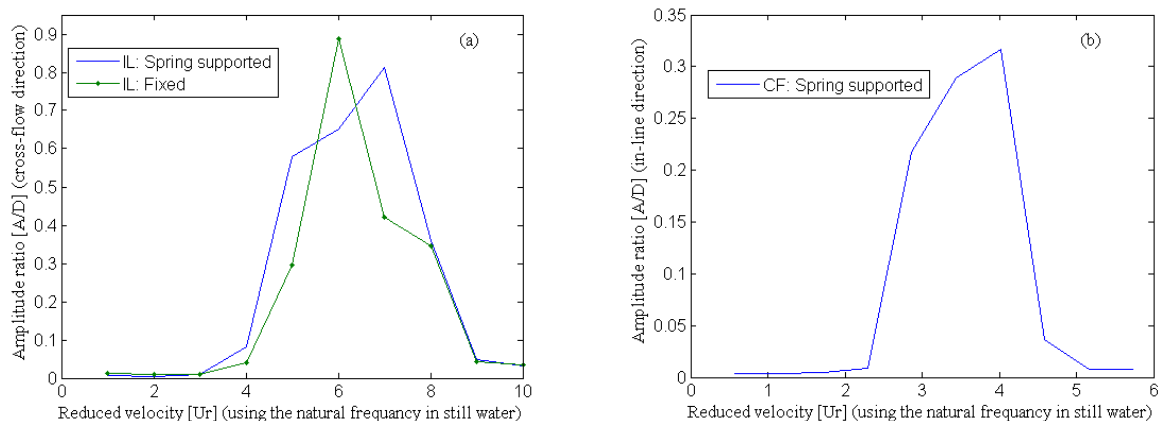


Figure 4: The response of smooth cylinder versus reduced velocity, (a) CF, (b) IL.

Table 3: Maximum amplitude of oscillation found at the different number of starts.

Maximum amplitudes of oscillation in the cross-flow direction $[(A_y/D)_{\max}]$				Maximum amplitudes of oscillation in the in-line direction $[(A_x/D)_{\max}]$			
d/D	1 start	2 starts	3 starts	d/D	1 start	2 starts	3 starts
Pitch = 2.5D				Pitch = 2.5D			
0.10	0.891	-	0.533	0.10	0.232	-	0.075
Pitch = 3.5D				Pitch = 3.5D			
0.15	-	-	0.040	0.15	-	-	0.013
Pitch = 5D				Pitch = 5D			
0.06	0.935	-	0.730	0.06	0.261	-	0.168
0.08	0.908	-	0.579	0.08	0.253	-	0.097
0.10	0.881	0.687	0.431	0.10	0.246	0.130	0.052
0.15	0.861	0.563	0.036	0.15	0.206	0.091	0.010
0.20	0.756	-	0.023	0.20	0.178	-	0.009
Pitch = 5.5D				Pitch = 5.5D			
0.15	-	-	0.030	0.15	-	-	0.011
Pitch = 6.5D				Pitch = 6.5D			
0.15	-	-	0.026	0.15	-	-	0.012
Pitch = 8D				Pitch = 8D			
0.15	-	-	0.030	0.15	-	-	0.013
Pitch = 10D				Pitch = 10D			
0.06	0.861	-	0.557	0.06	0.242	-	0.111
0.08	0.813	-	0.457	0.08	0.228	-	0.073
0.10	0.866	-	0.437	0.10	0.246	-	0.048
0.15	0.807	-	0.103	0.15	0.205	-	0.011
0.20	0.845	-	0.021	0.20	0.191	-	0.008
Statistical properties of $(A_y/D)_{\max}$				Statistical properties of $(A_x/D)_{\max}$			
Minimum	0.756	0.563	0.023	Minimum	0.178	0.091	0.009
Maximum	0.935	0.687	0.73	Maximum	0.261	0.13	0.168
Average	0.857	0.625	0.269	Average	0.226	0.111	0.047
Standard deviation	0.050	0.088	0.265	Standard deviation	0.027	0.028	0.049

Where d is the diameter of the strake and D is the test cylinder diameter.

Fig. 5 demonstrates the response of two configurations of round-sectioned helical strakes where the test cylinder was once allowed to oscillate simultaneously in the in-line and cross flow

directions (Two Degrees of Freedom, 2DOF) and thereafter the in-line motion of the cylinder was restrained (1DOF). The two configurations have 3 starts and $10D$ pitch while the strake diameter varies from $0.08D$ to $0.1D$.

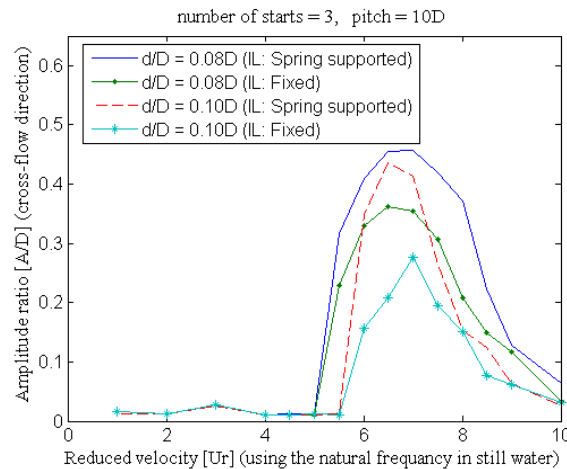


Figure 5: The effect of restraining the in-line motion of the test cylinder.

DISCUSSION

Fig. 4 shows the response of a smooth cylinder. The most important information obtained from this figure is presented in Table 4.

Table 4: Summary of the results of a smooth cylinder test.

The information	(2DOF)		(1DOF)	
	cross flow	inline	cross flow	inline
The range of reduced velocities at which the lock-in occurs (roughly)	4 - 9	2.9 - 4.6	4 - 9	-
The reduced velocity associated with the maximum oscillation amplitude	7	4.1	6	-
The maximum oscillation amplitude in the lock-in range, $(A/D)_{\max}$	0.81	0.32	0.89	-

The literature provides ample data that present information about VIV of elastically-mounted smooth rigid circular cylinders. Table 5 summarizes the predicted characteristics of the lock-in range of a smooth cylinder in the cross-flow direction. Halse (1997) discusses the in-line oscillation of a smooth circular cylinder and he reports from the literature that the amplitude of the in-line oscillations is about one-tenth of that in the cross-flow direction. Besides, two instability regions are distinguished in the in-line direction. King (1977) finds the range of the first instability region to be $1.5 < U_r < 2.5$, and the range of the second instability region to be $2.7 < U_r < 3.8$.

The comparison between the experimental results presented in Table 4 and the literature information suggests:

1. In the cross flow direction, the observed range of oscillations as well as the location of the oscillations' maximum amplitude in the lock-in range agrees well with the predicted values. Moreover, preventing in-line cylinder motions did not influence the range of the cross flow vibrations, but it did affect the amplitudes of the oscillation in the lock-in range.

2. It was impossible to distinguish two in-line instability regions in our experiments. Furthermore, the obtained maximum amplitudes of oscillation were higher than the maximum amplitudes presented in the literature. The available information about in-line oscillation is quite limited, however, and most of it is based on experiments where the cylinder motion is restrained to oscillate only in the in-line direction.

Table 5: Characteristics of the lock-in range of a smooth cylinder in the cross-flow direction.

Reference	Characteristic considered	Value
King (1977)	The range of reduced velocities at which the lock-in occurs	4.5 - 10
	The reduced velocity associated with the maximum oscillation amplitude	6.5 - 8
Currie et al. (1972)	The range of reduced velocities at which the lock-in occurs	4.5 - 10
	The reduced velocity associated with the maximum oscillation amplitude	7
Griffin et al. (1975)	$\left(\frac{A_y}{D}\right)_{\max} = \frac{1.29\gamma}{\left[1 + 0.43(2\pi \cdot S^2 \cdot K'_s)\right]^{3.35}}$	1.045
Sarpkaya (1978)	$\left(\frac{A_y}{D}\right)_{\max} = \frac{0.32\gamma}{\left[0.6 + (2\pi \cdot S^2 \cdot K'_s)^2\right]^{0.5}}$	0.407
Iwan and Blevins (1974)	$\left(\frac{A_y}{D}\right)_{\max} = \frac{0.07\gamma}{(1.9 + K'_s)S^2} \left[0.3 + \frac{0.72}{(1.9 + K'_s)S}\right]^{1/2}$	0.923
Where A_y is the amplitude of the cross-flow vibrations, D is the cylinder diameter, S is Strouhal number for a vibrating cylinder at maximum amplitude of vibration, K_s is the stability parameter, K'_s is the stability parameter included the added mass, and γ is a dimensionless mode factor. The test rig used in our experiments had the following values: $K_s = 0.55$, $K'_s = 0.6$, $S = 0.2$ and $\gamma = 1$.		

For the test cylinder fitted with round-sectioned helical strakes, the ranges of instability of the 1DOF and 2DOF systems are quite the same. However, it appears that the amplitudes of oscillation of the 1DOF cylinders are lower than those of 2DOF cylinders, see Fig. 5. The information presented in Fig. 5 includes only two configurations of round-sectioned helical strakes, therefore it is necessary to conduct more tests in order to confirm the conclusions drawn based on this figure.

The results presented in Table 3 allow us to discuss the efficiency of round-sectioned helical strakes. The following comments are drawn from this table:

- The configurations with 2 starts were tested twice and the results were intermediate between the results of 1 start and 3 starts.
- The standard deviation of the measured values of $\left(\frac{A}{D}\right)_{\max}$ for the configuration with 1 start is small (0.05, 0.02 in cross-flow and in-line directions, respectively). This means that varying the strake pitch and/or the strake diameter does not highly influence the efficiency of such a configuration.

- The maximum value of the measured values of $(A/D)_{\max}$ for the configuration with 3 starts is less than the Minimum value of $(A/D)_{\max}$ for the configuration with 1 start. This is valid in the cross-flow as well as the in-line direction.

Figs. 6 and 7 show the maximum amplitudes of the oscillations as a function of the number of starts. The pitch of the strakes in Fig. 6 is $5D$ while the pitch in Fig. 7 is $10D$.

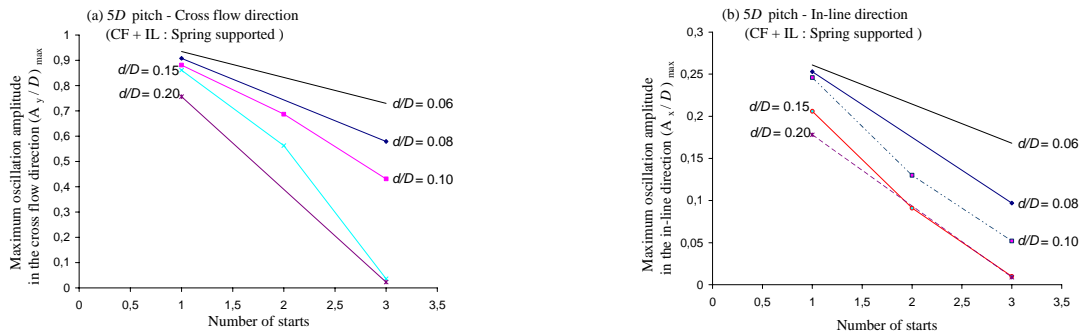


Figure 6: $(A/D)_{\max}$ as a function of number of starts at strake pitch of $5D$, (a) CF, (b) IL.

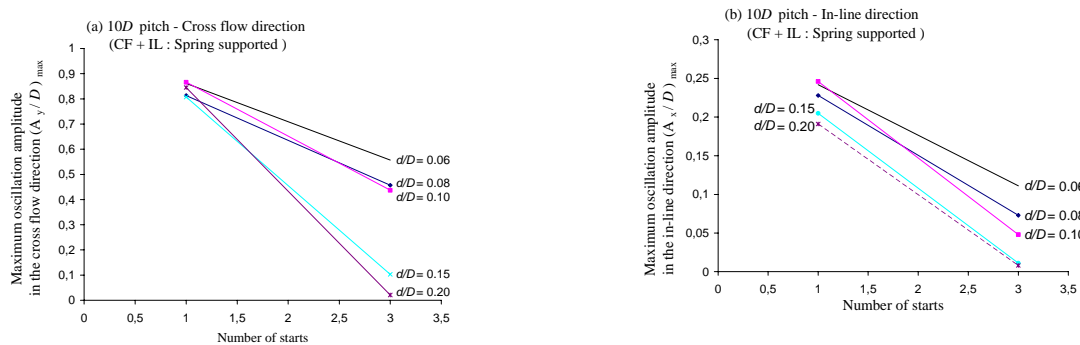


Figure 7: $(A/D)_{\max}$ as a function of number of starts at strake pitches of $10D$, (a) CF, (b) IL.

From the above discussion and figures, it is clear that regardless of the strake diameter and pitch, the configuration with 3 starts is the most efficient among the tested configurations in reducing the amplitude of vibration in both the cross-flow and the in-line directions.

For a configuration with 3 starts, Fig. 8 shows the maximum amplitude of oscillation as a function of both the strake diameter and the strake pitch.

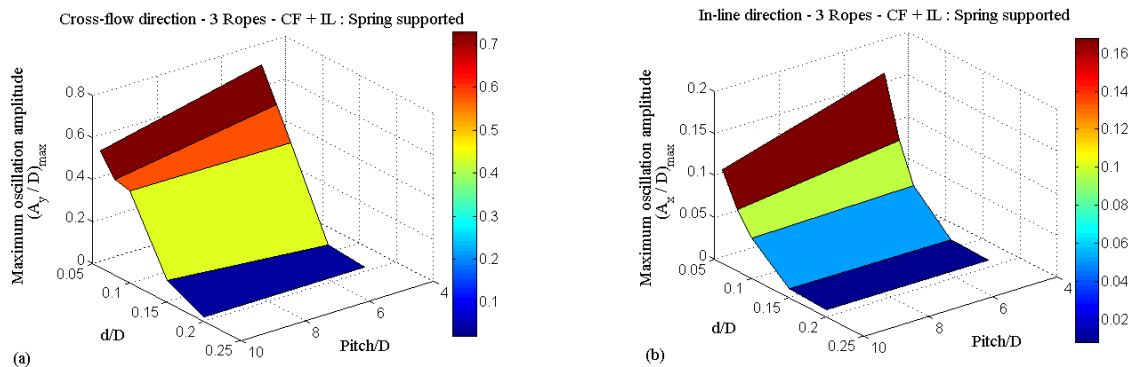


Figure 8: $(A/D)_{\max}$ as a function of the strake's diameter and the strake pitch (a) CF, (b) IL.

The most important observations from Fig. 8 are:

- For $d/D < 0.1$, a strake pitch of $10D$ seems to be better than those with $5D$. However, the overall efficiency in reducing $(A/D)_{\max}$ is still quite low.
- For $d/D > 0.1$, a strake pitch of $5D$ is better than $10D$ for suppressing motions in the cross-flow direction, while the in-line motions were approximately equal.
- $(A/D)_{\max}$ decreases with increasing strake diameter for all strake pitches for the in-line and cross-flow motions. Fig.9 shows the relationship between the strake diameter and $(A/D)_{\max}$ for 3 starts and a $5D$ pitch configuration.

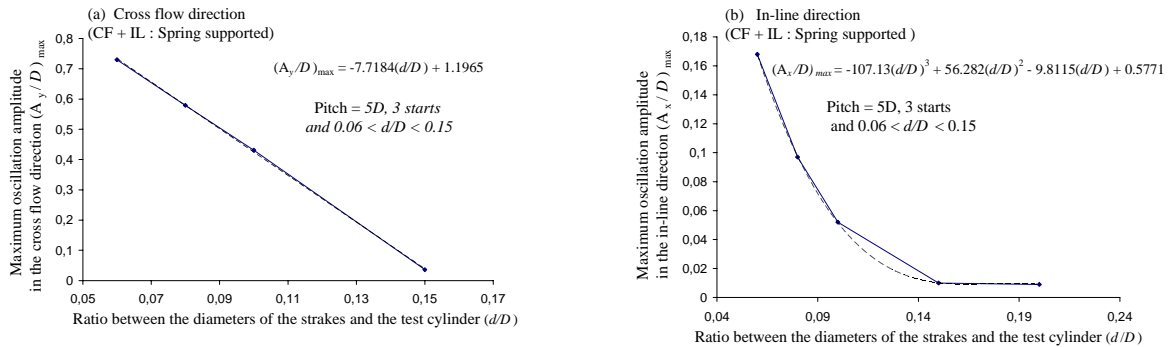


Figure 9: The relationship between $(A/D)_{\max}$ and the diameter of the strakes for 3 starts and $5D$ pitch configuration, (a) CF, (b) IL.

Summing up, the most efficient configuration of round-sectioned helical strakes among the tested configurations is a configuration with:

- 3 starts
- Strake pitch = $5D$
- Strake diameter = $0.20D$

A rope diameter of $0.20D$ may cause some handling problems especially when considering the possibility to spin the strakes on at the site. Therefore, a rope diameter of $0.15D$ is probably preferable. Table 6 compares the efficiency of $0.20D$ and $0.15D$ rope diameters.

Table 6: Comparison of the efficiency of $0.20D$ and $0.15D$ rope diameters to suppress VIV.

Ratio of the maximum amplitude of oscillation to that of a smooth cylinder $\frac{(A/D)_{\max}}{(A/D)_{\text{smooth cylinder}}}$		
Rope diameter	Cross-Flow direction	In-line direction
$0.15D$	0.044	0.031
$0.20D$	0.028	0.028

From Table 6 is seen that a rope diameter of $0.15D$ reduces the amplitude of the oscillations relative to the smooth cylinder by 95.6% in the cross-flow direction, and by 96.9% in the inline direction. These results are absolutely satisfactory and far better than those for a rope diameter of $0.10D$. Thus the selected configuration of round-sectioned (ropes) helical strakes is:

- 3 starts
- Strake pitch = $5D$
- Strake diameter = $0.15D$

Fig. 10 shows a picture of the test cylinder fitted with the selected optimum round-sectioned helical strakes.

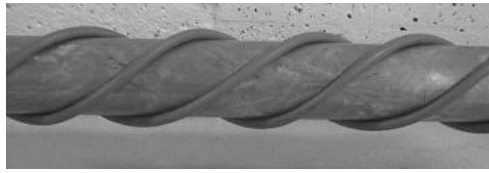


Figure 10: Picture of the test cylinder fitted with the optimum round-sectioned helical strakes.

The effects of varying the strake pitch on the amplitude of oscillation of the selected configuration of round-sectioned helical strakes are tested. Fig.11 plots the strake pitch versus the percentage reduction of the vibration amplitude relative to the smooth cylinder. From the figure it is obvious that the efficiency of the optimum strake configuration is reduced significantly when the strake pitch reaches $10D$. However, over the range of strake pitch from $3.5D$ to $8D$ the efficiency is approximately constant (from 95.1% to 96.8%). We thus conclude that it is not necessary to install the round-sectioned helical strakes very accurately with respect to the strake pitch. This eases the application of round-sectioned helical strakes to temporary risers (for example intervention risers and coiled tubing risers).

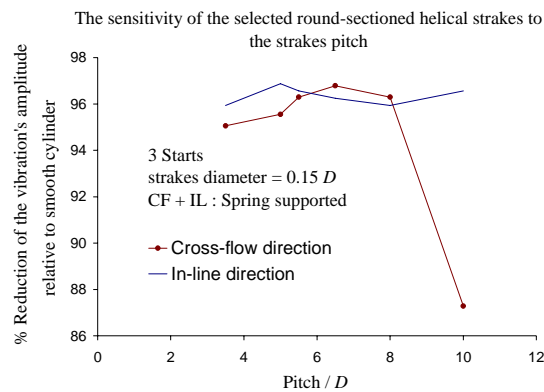


Figure 11: Strake pitch versus the percentage reduction of the vibration's amplitude relative to smooth cylinder.

The ratio of the cross-flow to the in-line natural frequencies of the test cylinder may have some effects on the efficiency of the selected configuration of round-sectioned helical strakes. Currently Adimas Pribadi is testing these effects as a part of his master work at the department of civil and transport engineering at NTNU. Some of Adimas preliminary results are shown in Fig. 12.

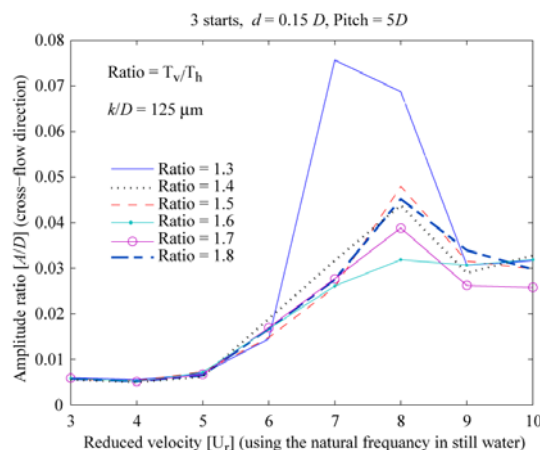


Figure 12: the effects of (T_v/T_h) on the efficiency of the selected optimum configuration.

In figure 12, the ratio between the cross-flow natural period of the test cylinder and the in-line natural period, (T_v/T_h) , is varied from 1.3 to 1.8 and the test cylinder has a surface roughness of $k/D = 125 \mu\text{m}$. The figure shows that the overall efficiency of the selected configuration of round-sectioned helical strakes remains in acceptable level.

Weaver (1961) carried out different experiments in order to determine the optimum number, size, and pitch of *helical weirs strakes*. It was found that the best configuration was three or four starts, $8D$ to $16D$ pitch and $0.094D$ strake height. Woodgate and Maybrey (1959) carried out tests to determine the optimum design of *sharp edged rectangular strakes*. They found that the best configuration consisted of three starts, $5D$ pitch and $0.09D$ height ($0.12D$ height for less damped structures, i.e. marine risers). Ruscheweyh (1972) confirmed that the optimal pitch for *sharp edged strakes* is within the range of $4D$ to $5D$. Wilson and Tinsley (1989) recommended a three starts sharp edged strake of $0.1D$ height and 60° helix angle from the cylinder axis. According to Jones and Lamb, 1993, the optimum design of *flexible sharp edged strakes* is three or four starts, $12D$ pitch and $0.1D$ height.

By reviewing the literature, it is evidence that the optimum design of round-sectioned helical strakes presented in this paper is in a reasonable agreement with the optimum configurations of other geometry helical strakes that are reported in the literature.

Tørum (1995) used an experimental set-up like the one used in the present work. He found that the turbulence length scale was approximately in the order of 1 cylinder's diameter. Mathiesen (1995) analysed full scale turbulence in the ocean. His turbulence length scale results show considerable scatter but they seem to be in order of several cylinder diameters (full scale cylinder's diameter is assumed to be in the range between 0.5 to 1 m). This difference between the prototype and the model turbulence length scales may have some effects on the relevance of the laboratory data.

Under prototype conditions risers may experience flows at supercritical Reynolds number. Since the present experiments are all conducted at subcritical Reynolds number, the validity of the present conclusions is less certain.

CONCLUSIONS

The following list shows the conclusions from the present study.

1. The response of an elastically mounted rigid circular cylinder to VIV depends on whether it is fixed or spring-supported in the in-line direction. Generally, the ranges of instability of 1DOF and 2DOF systems are the same. However, the amplitudes of oscillations in the lock-in range are certainly different. For cylinders with strakes it appears that the amplitudes of oscillation of the 1DOF cylinders are lower than those of the 2DOF cylinders.
2. The maximum amplitude of the in-line response of a smooth cylinder was found to be larger than the values reported in the literature. Additionally, it was impossible to identify two instability regions as expected from previous work. The reason for that is probably due to the interaction between cross-flow and in-line oscillations (2DOF system).

3. One-start round-sectioned helical strakes (helical strakes using one rope) is not efficient in reducing VIV. This is valid for all strake pitches and diameters tested. The simplest explanation for this finding is that one rope is insufficient to create three-dimensional flow over the whole length of the cylinder. This allows two-dimensional vortices to shed from different parts of the cylinder in a sufficient manner as to enhance the oscillations.
4. The main finding in this paper about the round-sectioned helical strakes is that three-starts, $5D$ pitch and $0.15D$ strake diameter appears to be the optimum configuration. It reduces the amplitude of oscillation relative to the smooth cylinder by 95.6 % in the cross-flow direction, and by 96.9 % in the inline direction.
5. The efficiency of the abovementioned optimum round-sectioned helical strakes is not very sensitive to the pitch of the strakes. . Nearly the same optimum performance has been obtained with pitches ranging from $3.5D$ to $8D$.

ACKNOWLEDGMENTS

The author expresses his thanks to the master programme in Coastal and Marine Civil Engineering for providing the possibility to study in Norway. The author would like to express thanks to Gustav Jakobsen for preparing the test flume and for all assistance during the testing. Thanks to Statoil ASA for providing the funding for the experimental work and finally thanks to Adimas Pribadi for providing some of his preliminary results to this publication.

REFERENCES

- Blevins, R.D. (1990): Flow-induced vibration (Second ed.), New York, USA, Van Nostrand Reinhold, 451 p.
- Currie, I.G., Hartlen, R.T., and Martin, W.W. (1972): The response of circular cylinders to vortex shedding, IUTAM-IAHR symposium in flow-induced structural vibrations, Karlsruhe, Germany, pp. 128-142.
- Griffin, O.M., Skop, R.A. and Ramberg, S.E. (1975): The resonant, vortex-excited vibrations of structures and cable systems, Proceedings of the Offshore Technology Conference, Paper No. 2319, Houston, Texas.
- Halse, K.H. (1997): On vortex shedding and prediction of vortex-induced vibrations of circular cylinders, Dr.Ing thesis, Dept. of Marine structures, Norwegian University of Science and Technology (NTNU), Trondheim, Norway.
- Iwan, W.D. and Blevins R.D. (1974): A model for vortex-induced oscillation of structures, Journal of Applied Mechanics, vol. 41, pp. 581-586.
- Jones, G.S. and Lamb, W.S. (1993): The suppression of vortex induced vibration in marine risers. Trans IMarE, vol. 105, Part 5, pp 197-209.
- King, R. (1977): A review of vortex shedding research and its application, Ocean Engineering, vol. 4, pp. 141-171.
- Lubbad, R. (2006): Flow Induced Vibrations of Risers – Effect of Helical Strakes, Master thesis, Norwegian University of Science and Technology (NTNU), Trondheim, Norway.
- Lubbad, R., Løset, S., Gudmestad, O., Tørum, A. and Moe, G. (2007): Vortex Induced Vibrations of Slender Marine Risers, Effects of Round-Sectioned Helical Strakes, The 17th International Offshore and Polar Engineering Conference ISOPE, Lisbon, Portugal.
- Mathiesen, M. (1995): MULTISPAN new seabed flow characteristics in Macro-roughness areas. Analysis of current data. SINTEF NHL report no. STF60 F94044 to Statoil and Norske Agip A/S, Trondheim, Norway.
- Moe G. and Overvik, T. (1982): Current Induced Motions of Multiple Risers, BOSS-82, Behaviour of Offshore Structures, Proceedings, Vol 1, pp 618-639

- Ruscheweyh, H. (1972): Tip effect on vortex excited oscillation of a model stack with and without efflux stream, Symposium On Flow Induced Structural Vibrations, Karlsruhe, W. Germany, Suppl., 101-103.
- Sarpkaya, T. (1978): Fluid forces on Oscillating cylinders, Journal of the Waterway, Port, Coastal and Ocean Division of ASCE, Vol. 104, No. WW4, pp. 275-290.
- Tørum, A. (1995): MULTISPAN vortex induced vibrations tests, SINTIF, report no. STF60 F95109, xx, 117p, Trondheim, Norway.
- Weaver, W. (1961): Wind-induced vibrations in antenna members, Proc. Am. Soc. Civ. Eng., J. Eng. Mech. Div., vol. 87, pp. 141-165.
- Wilson, J.E. and Tinsley, J.C. (1989): Vortex load reduction; experiments in optimal helical strake geometry for rigid cylinders, Journal of Energy Resources Technology, vol. 3, pp. 72-76.
- Woodgate, L. and Maybrey, J.F.M. (1959): Further experiments on the use of helical strakes for avoiding wind excited oscillations of structures of circular or nearly circular section, Natl. Phys. Lab. (U.K.), Aero Rep. 381.
- Zdravkovich, M.M. (1981): Review and classification of various aerodynamic and hydrodynamic means for suppressing vortex shedding, Journal of Wind Engineering and Industrial Aerodynamics, vol. 7, pp. 145-189.

**Session E:
CHALLENGES IN COLD CLIMATE**

SOME CHALLENGES RELATED TO THE PETROLEUM INDUSTRY IN COLD WATERS

Sveinung Løset
Norwegian University of Science and Technology

INTRODUCTION

The basics of offshore oil and gas developments in Arctic regions are essentially the same as in other offshore areas, however, the low winter temperatures, the presence of ice and icing and some offshore permafrost as well as the darkness and remoteness make the work here more challenging than in most other locations where hydrocarbons are extracted.

Ice can impose large actions on rigs, platforms and production vessels and may create gouges in the sea floor, which can affect pipeline integrity. Ice can also impede access by supply ships and tankers, and create difficulties for personnel evacuation. The influence of ice will usually require customised solutions to the engineering and operations of offshore oil and gas systems.

ICE ACTIONS

Exploration and production of hydrocarbons in ice-infested waters are quite demanding with respect to design and operations. Two types of ice actions - global loads and local pressures - are quite important for the selection of structure and design. In both cases the selection of structure is important. Basically this is affected by:

- Water depth (floater or GBS)
- Metocean conditions (sea state and ice features)
- Required deck capacity of structure

The ice feature is very decisive. For instance, in case of icebergs drifting into the actual waters, statistics are especially required on mass and drift velocity. If the momentum exceeds what is manageable with ice management, the structure must either be designed to withstand the loads/pressures that may be exerted, or it should be possible to disconnect the structure. In case of disconnection, the shut-down/disconnection time must be within the warning time given by the ice management system. Further, what should the structure geometry be in the water line? Should the ice-exposed surfaces be vertical or upward/down sloping? Should the floater be ship-shaped or like an omni-directional buoy?

The estimation of ice actions have been discussed for many years. With respect to sea ice the major uncertainty is connected to estimation of loads from ice ridges. The keels, often treated as a Mohr-Coulomb material, can extend to a depth 20 m plus depending on location. First-year sea ice ridges may exert severe loadings on a moored structure and the keel imposes a risk for the sub surface system. Thus NTNU has a special focus on loads/pressures from ridges and we carry out field surveys and ice tank testing to study the processes involved, see Fig. 1.

For vertical faced structures it is also well-known that the global pressure $p_G = p_G(v, u_w, K_w)$ depends on ice velocity v , and the waterline displacement u_w , which is a function of the waterline stiffness K_w of the structure (Kärnä et al., 2008). Analyses of laboratory data indicate that the global load on a narrow structure may increase by 50 % if a stiff model structure is substituted with a compliant structure.

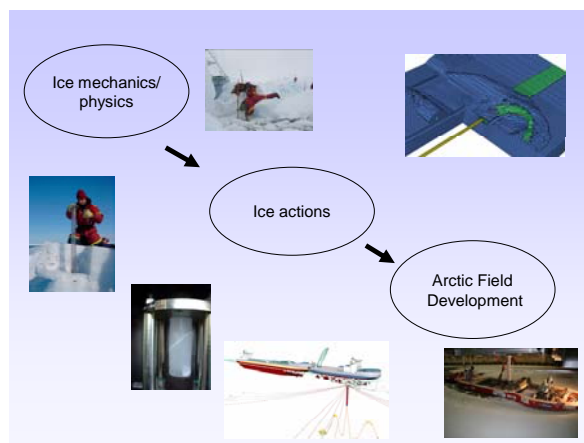


Fig. 1. Sketch indicating research involved in estimation of loads/pressures from level ice and ridges.

New information on ice loads has recently been compiled in the design standard S471-04. This standard does not recognize the earlier experimental findings showing that the external quasi-static global load as well as the local pressures on a compliant structure may be significantly higher than for a stiff structure. This may also be affected by moorings.

OFFLOADING OF HYDROCARBONS

Produced hydrocarbons need to be exported to the market either via pipeline or by tankers. An overview of some concepts for offloading in ice is presented in Bonnemaire et al. (2007), see Fig. 2. The concepts are grouped into: 1) A variety of fixed terminal designs, 2) Loading behind a GBS structure 3) Tandem loading from a fixed tower or moored vessel, 4) Single anchored vessels and 5) Sub surface moored vessels. There are various obstacles connected to all these concepts such as ice drift and drift changes in addition to loads and dynamics. A special promising concept is the Arctic Tandem Offloading Terminal (ATOT) consisting of a moored icebreaker with a tanker in

the wake of the icebreaker, see lower right corner in Fig. 1 (Breivik et al., 2007).

ARCTIC CLIMATE CHANGE

Global warming may affect many coastal communities adversely:

- Severe coastal erosion will be a governing problem as rising sea level and a reduction in sea ice allow higher waves and storm surges to reach the shore.
- Along some arctic coastlines, thawing permafrost weakens coastal lands, adding to their vulnerability.
- The risk of flooding in coastal wetlands is projected to increase, with impacts on society and natural ecosystems.

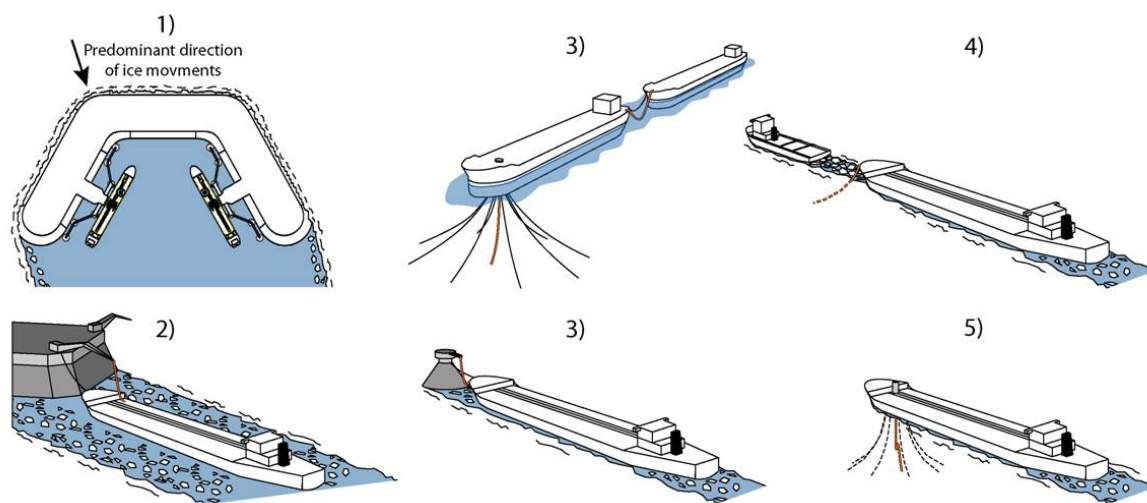


Figure. 2. Offloading concepts for operations in the Arctic. 1) Terminal with pronounced ice drift direction, 2) Loading from a Gravity Base Structure, 3) Tandem loading from a production vessel and a loading tower, respectively 4) Single anchored vessel with ice management and a sub surface solution.

REFERENCES

- Aksnes, V., B. Bonnemaire, S. Løset and C. Lønøy. 2008. Model Testing of the Arctic Tandem Offloading Terminal – Tandem Mooring Forces and Relative Motions between Vessels. *Proceedings of the 19th International Symposium on Ice (IAHR)*, Vancouver, Canada, July 6 to 11, 2008, Vol. x, pp. xx-xx.
- Bonnemaire, B., T. Lundamo, K.U. Evers, S. Løset and A. Jensen. 2008. Model Testing of the Arctic Tandem Offloading Terminal – Mooring Ice Loads. *Proceedings of the 19th International Symposium on Ice (IAHR)*, Vancouver, Canada, July 6 to 11, 2008, Vol. x, pp. xx-xx.
- Breivik, K., B. Bonnemaire, S. Løset, J. Høvik, K. Riska, O. Ravndal, S.I. Eide and A. Jensen. 2007. Arctic Tandem Offloading Terminal – *Offshore Loading in Ice Covered Waters*, DOT Conference, Stavanger, 10 p.
- Kärnä, T., F. Guo, S. Løset and M. Määttänen. 2008. Small-scale data on magnification of ice loads on vertical structures. *Proceedings of the 19th International Symposium on Ice (IAHR)*, Vancouver, Canada, July 6 to 11, 2008, Vol. x, pp. xx-xx.
- S471-04. *General requirements, design criteria, the environment, and loads*. Canadian Standards Association. February 2004. 416 p.

See Coast 2008 homepage for extras. <http://www.ivt.ntnu.no/bat/english/coast2008/>

NUMERICAL SIMULATION AND FAILURE MODE ANALYSIS OF ICE DRIFT ON ARRANGEMENTS OF ICE PROTECTION PILES

A. Gürtner¹, I. Konuk¹ and S. Løset¹

*Norwegian University of Science and Technology (NTNU),
Department for Civil and Transport Engineering, Trondheim, Norway*

ABSTRACT

Ice Protection Piles (IPPs) may be employed as an ice protection measure in shallow water to reduce ice loads on offshore structures. This paper presents a numerical study on ice drift on IPPs, where the main focus is directed towards investigating the influence of the pile-to-pile spacing and accordingly the exerted ice forces. The Computational Cohesive Element Model (CCEM) is developed using finite elements discretization in combination with cohesive elements and cohesive zone model (CZM) for fracture. The creation and successive treatment of new surfaces together with multiple contacts characterizes the CCEM. The model is implemented into the Finite Element Program LS-DYNA. The presented method is employed to investigate ice interaction on arrangements of multiple piles. The simulations show that the pile-to-pile spacing alters the ice failure.

INTRODUCTION

Ice Protection Piles (IPPs) are used to protect shallow water field developments from the hazards of drifting ice. Piles are installed in close vicinity to the structure which is to be protected. The piles then pre-fracture the approaching ice before interacting with the structure of concern and thus lower the resistance capacity required. Semi-ice resistant or ice-strengthened platforms may thereby be employed in ice infested areas. IPPs were successfully employed in the Northern Caspian Sea to protect a drilling barge (Evers et al., 2001).

Due to active pre-fracturing of the approaching ice sheet by the existence of IPPs, ice rubble forms and may eventually lead to initiating a grounded ice rubble field. Ice forces acting on the structure to be protected may diminish if the rubble gets sufficiently grounded onto the sea floor (Marshall et al., 1989). Wide openings between neighbouring piles allow for significant ice bypassing, whereas narrow spacing may lead to the desired ice rubble accumulation but in turn increase construction costs. The pile-to-pile spacing is hence a significant parameter to investigate. Gürtner and Berger (2006) presented results of ice model tests to address the question of varying pile spacing. Apart from IPPs, the investigation of the pile-to-pile distance which allows for ice bypassing is considered to be a classical ice-engineering problem. However, ice interaction with multiple cylindrical piles has been devoted limited attention in the literature compared to investigations of ice interaction on a single pile. Copious researchers studied ice indentation on a single vertical pile with the endeavour to empirically define ice force based on effective pressure and the influence of aspect ratios, i.e. the ratio of pile diameter to ice thickness (e.g. Korzhavin, 1962; Schwarz, 1970; Hirayama 1974; Sodhi and Morris, 1984). Ice load estimates on structures consisting of multiple cylindrical piles are based on adding the force estimate for one individual pile over the total number of piles in the structure or arrangement,

whereupon reduction factors to account for interference effects, effects of non-simultaneous failure and effects of ice jamming are employed (ISO, 2007, p. 178). However, the effect of multiple piles of a structure to constrain the downstream flow of ice and thereby initiate ice rubble accumulations, culminating into ice jamming, has been paid little attention to. The failure mechanism evolves with time from ice crushing and splitting on individual vertical contact surfaces to bridging between neighbouring piles, whereupon ice jamming is initiated (Gürtner and Berger, 2006). In shallow water, grounding of ice may become evident if ice drift onto the initial ice jam persists over time. The common apprehension is that the ratio of pile-to-pile distance (centre to centre), l , to the pile diameter, D , represents the governing factor for determining whether or not the piles allow for bypassing of ice. This in turn implies multiple piles can be considered as mutual independent for large l . The optimal range of influence l , where no interference between neighbouring piles occurs, has by several researchers, based on model scale investigations, been defined as $l = 6D$ (e.g. Timco, 1986; Toyama and Yashima, 1994; Gürtner and Berger, 2006). Kato and Sodhi (1983) on the other hand concluded that for two cylindrical structures no interference of the neighbouring structure occurs for $l = 5D$. Evers and Wessels (1986) found a convergence limit of $l = 7.3D$ for a four-legged offshore structure in model scale. In actual fact, there is likely some influence of pile spacing on pile loads and ice stresses, and ice fracture pattern as well. Therefore, potential ice jamming may occur for ranges of pile spacing larger than discussed in the literature. The main parameters that influence the ice and IPP interaction process are ice sheet thickness, ice floe size and geometry, ice drift speed, ice properties (temperature etc.), and pile structural characteristics (e.g. number of piles, stiffness, and damping). It is very unlikely that a simple linear relationship between l and D will be able to encapsulate such a complex process. However, it may be possible to derive such a formula associated with a certain small change on ice loads of piles (adequate for engineering purposes) and very small chance of jamming for a limited range of ice floe sizes, ice thicknesses, and a range of pile stiffness's. Such a study or the determination of validity ranges for linear aspect ratio formulas is beyond the scope of this paper.

In the present paper a numerical modelling exercise is presented to investigate the ice failure modes involved and accordingly which pile-to-pile spacing is sufficient to minimize ice bypassing. The numerically obtained results will be compared to aforementioned model test observations of Gürtner and Berger (2006). This paper presents a novel approach in which we combine the explicit Finite Element Method (FEM) with non-linear fracture mechanics in a Computational Cohesive Element Model (CCEM) to numerically simulate ice interactions. In the present approach plastic properties of the ice co-exist with fracture properties. This is virtually achieved by including cohesive elements (CE) into the existing computational finite element grid of the ice. The commercial FEM software LS-DYNA (LSTC, 2006) is utilized to solve the mentioned boundary value problem. After elucidating on the implementation of cohesive elements and their physics, we present the application of this new approach to the analysis of ice interaction on arrangements of multiple piles where l varies from $2D$ to $8D$.

NUMERICAL METHODOLOGY AND PROBLEM FORMULATION

The numerical methodology herein employed is based on the Cohesive Zone Model (CZM) of Dugdale (1960) and Barrenblatt (1962). Since the early attempts to characterize fracture in steel, this method has found vast application in dynamic fracture of both brittle and ductile materials (e.g. Chowdhury and Narasimhan, 2000; Ruiz et al. 2000). Typical problems solved by the CZM

concerns the simulation of single cracks, crack branching, and fracture during dynamic impact in a varying range of materials (Song et al., 2007). The CZM is implemented into the commercially available explicit finite element code LS-DYNA (LSTC, 2006). Grtner et al. (2008) showed the applicability of the CZM to simulated ice rubble accumulation on an ice barrier and accordingly exerted ice forces. The implementation of the CZM manifests itself in the discretization of the bulk ice mass with cohesive elements along all internal element boundaries (Fig. 1). The thickness of the cohesive elements is minimal but finite. While the bulk ice elements account for stress and strain, the cohesive elements account for fracture properties such as traction and separation. Due to the fact that fracture is explicitly accounted for in the present methodology, cracks may nucleate, propagate and possibly branch to form discrete ice fragments without any assumptions on pre-existing cracks. Besides accounting for fracture *per se*, the present cohesive element model also accounts for the post-cracking behaviour. That is, new surfaces, which are created within the bulk ice mass, are tracked in a consistent mechanics framework and are allowed to subsequently interact.

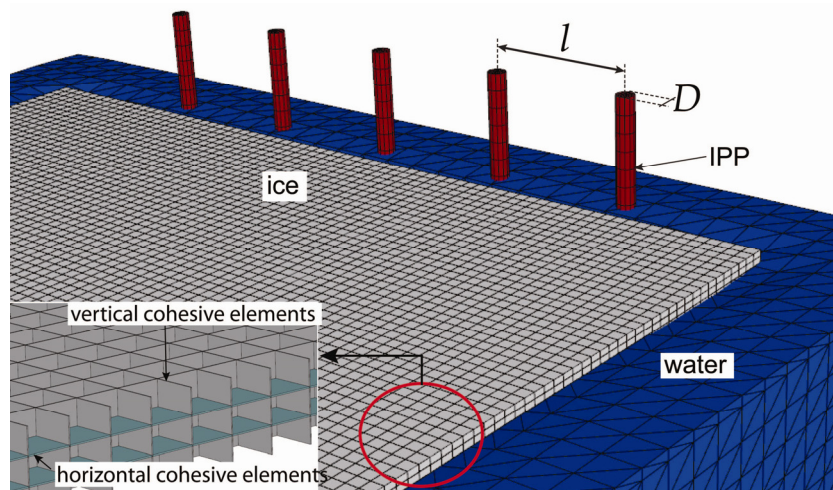


Figure 1. Set-up of the computational boundary value problem with rigid piles of diameter D , a 1.5×1.5 m ice sheet with cohesive elements (here partly submerged) and water (Eulerian mesh).

The implementation of cohesive elements into a conventional finite element discretization relies upon a cohesive element law which defines the traction (stress), T , versus separation (displacement), u . The cohesive law adopted in this paper is similar to the traction-separation law presented by Tvergaard and Hutchinson (1992), as shown in Fig. 2. The area under the traction-separation curve equals the fracture energy and the dissipated energy is hence used to advance a crack within the medium. The utilized traction-separation law should be regarded as a phenomenological characterization of the Fracture Process Zone (FPZ) ahead of the crack tip, where at the critical displacement, u_c , the surfaces in the FPS are considered to separate. Anisotropy with regard to fracture is handled by assigning distinct properties for vertical and horizontal cohesive elements, respectively. To describe the stress-strain relationship of the bulk ice mass an isotropic, elasto-plastic constitutive law is utilized in this paper. A finite element discretization with in-plane edge length of 20 mm is chosen for the ice sheet covering 1.5×1.5 m. This is considered to be sufficient in a trade-off between numerical accuracy and computation time.

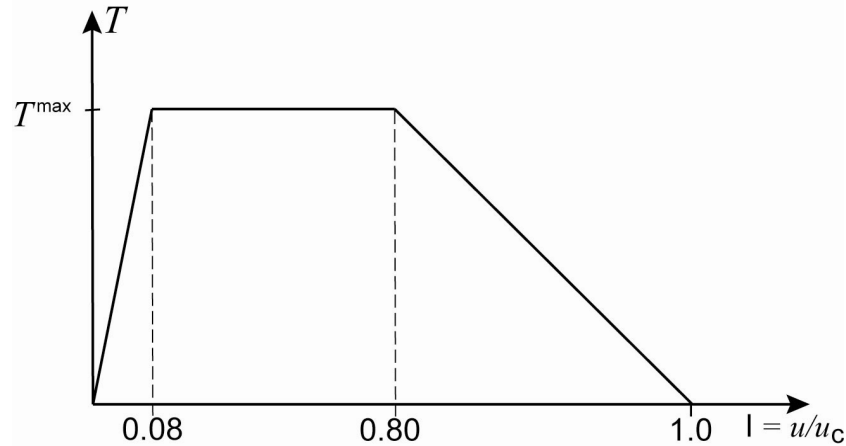


Figure 2. Constitutive relation of the vertical cohesive elements by means of a normalized traction-separation law for mode-I fracture according to Tvergaard and Hutchinson (1992).

The numerical boundary value problem presented in Fig. 1 resembles the described model test set-up of Gurtner and Berger (2006), though the present investigations are carried out at the scale of the physical model test. Opposed to physical test conditions, the IPPs are modelled as being rigid, since the stiffness and damping of the model IPPs were not determined in the tests. The structural responses' influence on the ice failure process is therefore discarded, even though its influence on measured ice forces is seen to be large (Fig. 3 a). Pile dynamics infer a snap-back condition where energy, due to interaction, initially is stored and then suddenly released. This sudden release of energy is associated with the pile impacting the ice and accordingly resulting in high load peaks of short duration, as seen in Fig. 3 a). The considered pile-to-pile distances are $2D$, $4D$, $6D$ and $8D$. As in the model tests, the IPPs impact the stationary ice sheet of 31 mm thickness, which is constrained from moving at the outer boundaries, by a constant velocity of 0.125 m/s. The IPPs diameter is 30 mm, giving an aspect ratio of approximately unity. Interface forces of the centre pile within an arrangement are separably measured and may be compared to the total force on the arrangement. Due to the complexity of the problem at hand, the first stage of simulations concerns the water to be modelled as an elastic foundation. With this set-up both the mesh density and pile-to-pile distance variations are investigated. At the final stage of verification studies, the complete multi-material model will be simulated to investigate the upstream ice rubble initiation. This involves the water being explicitly modelled by a true Eulerian grid, where the material flows through a mesh fixed in space and, consequently, results in correct buoyancy forces for the floating ice sheet together with inertia and damping terms. Ice submergence and up-lift are hence consistently modelled.

Calibration of the numerical model with regard to the exerted ice forces was achieved by investigating the model test run $l = 6D$, where no interference of the IPPs could be observed. Fig. 3 a) shows the ice force on one individual IPP and accordingly a statistical estimate of the maximum force. The highest force peaks were due to dynamic interaction, which is beyond the scope of this paper. Fig. 3 b) shows the simulated ice force history. It can be seen that the maximum attained ice force is approximately of the same magnitude as the statistical ice force of 193 N resulting from the physical model tests. Tab. 1 defines the material properties used in the present study. The properties are selected to match the density, Poisson's ratio and elasticity modulus from model tests, whereas fracture properties are directly derived from calibration. It is

worth mentioning that the influence of pile dynamics results in total force release after attaining peaks, whereas the simulated ice force history is not seen to drop to zero but fluctuates around a static force component. It is however seen that the chaotic nature of the ice force is preserved. The influence of pile dynamics on the exerted ice force should however be investigated in future.

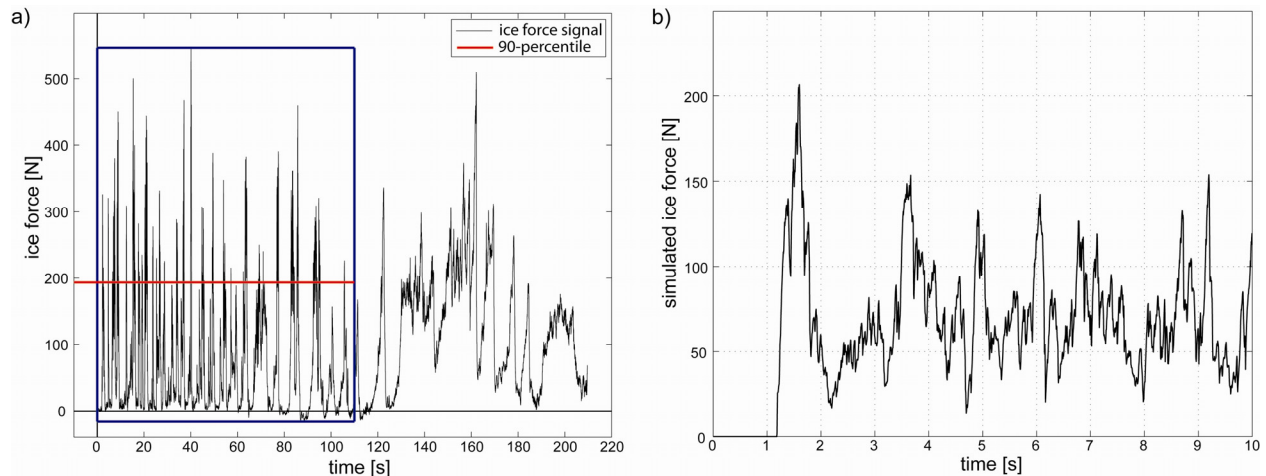


Figure 3. a) Model test ice force on IPP with $l = 6D$, blue box defines the time at which minimal interference was observed and red line accordingly refers to 90%-tile of the ice force; and b) simulated ice force on rigid pile arrangement with $l = 6D$.

Table 1. Material properties for ice with cohesive elements and a mesh edge length of 20 mm.

	Value
<u>Bulk material properties:</u>	
Density, ρ	900 kg/m ³
Modulus of elasticity, E	280 MPa
Poisson's ratio, ν	0.3
Yield stress, σ_y	1.8 kPa
<u>Vertical cohesive element properties:</u>	
Peak traction, T	65 kPa
Max separation, δ_c	95 μm
Energy release rate normal, G_{norm}	~ 5.4 N/m
Energy release rate tangential, G_{tang}	~ 30 N/m
<u>Horizontal cohesive element properties:</u>	
Peak traction, T	71 kPa
Max separation, δ_c	200 μm
Energy release rate normal, G_{norm}	~ 12 N/m
Energy release rate tangential, G_{tang}	~ 19 N/m

RESULTS

Ice drift onto arrangements of IPPs are simulated to investigate the effect of various pile-to-pile spacing on ice bypassing, as well as to investigate the exerted ice force. Fig. 4 shows the simulated outcome of ice drift onto a narrow spaced arrangement and alternatively onto a wide spaced arrangement. The difference in failure mode leading to ice bypassing may be appreciated. Whereas the piles of arrangement $l = 2D$ are seen to be mutually dependent, piles of arrangement

$l = 8D$ act as individual piles. In general, simulations show that for $l \geq 6D$ ice bypassing takes place. Fig. 5 shows accordingly the different stress fields in the ice of the two respective arrangements in Fig. 4 at the initial stage of interaction. For $l = 2D$ (Fig. 5 a) the stress field is seen to be continuously distributed within the ice mass, whereas the stress field for $l = 8D$ (Fig. 5 b) develops separately from the neighbouring piles.

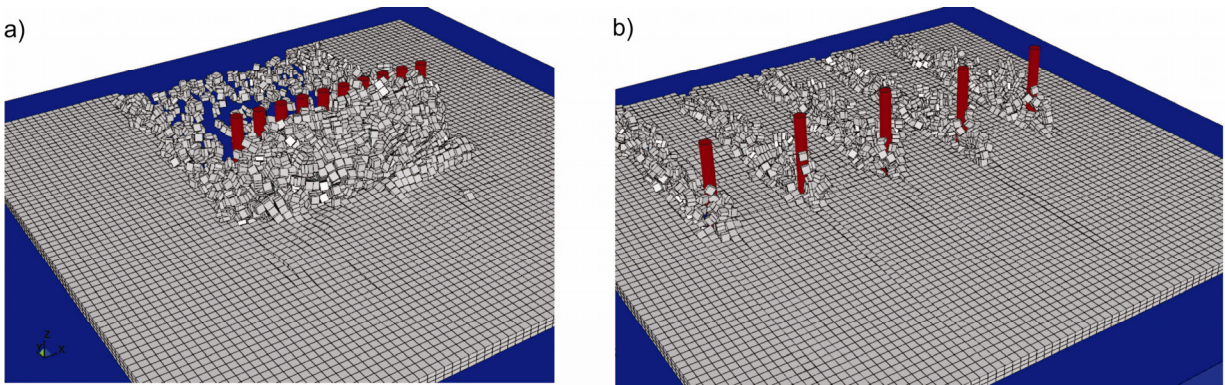


Figure 4. Failure mode comparison; a) ice accumulation upstream the IPPs for $l = 2D$; and b) no mutual influence of IPPs for $l = 8D$.

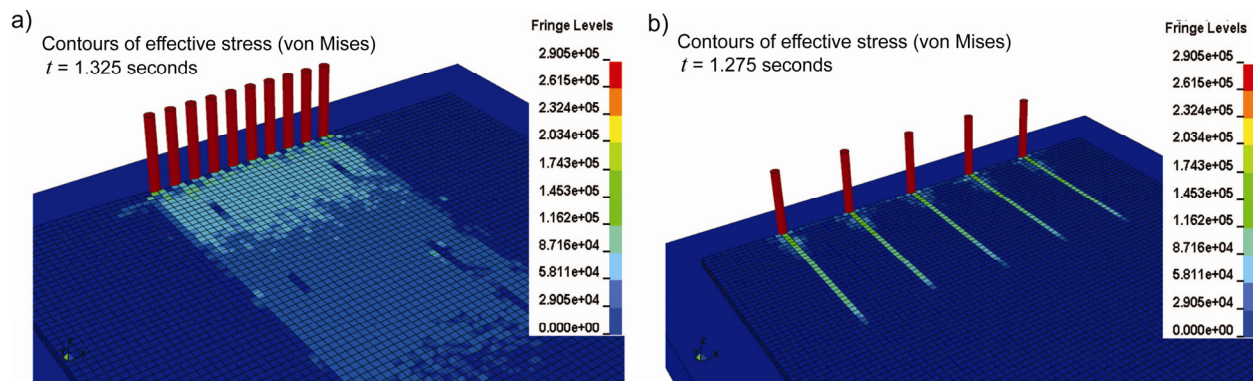


Figure 5. Comparison of the effective stress field in the ice; a) for $l = 2D$; and b) for $l = 8D$.

Ice forces on the centre piles within each arrangement are continuously measured throughout the indentation simulation. Fig. 6 compares the horizontal ice forces histories of the arrangements considered in this study. Fig. 6 a) and b) show a weak increasing trend due to increased upstream ice rubble accumulation with time. High frequency components of the ice force also appear to be damped by the existence of upstream ice rubble (Fig. 6 a). The maximum ice force within 9 seconds of interaction is seen to vary between the different arrangements and for $l = 4D$ the exerted ice force attains a maximum of 247.7 N. The mean ice force on the respective IPPs is also depicted in Fig. 6. The mean ice force increases due to the presence of upstream ice rubble. Fig. 7 compares the horizontal ice force on the centre pile within an arrangement with the total exerted force on all piles divided by the number of piles in an arrangement. It is seen that this average forces are correlated but are seen to be of higher magnitude.

The dependence on mesh size is studied in Fig. 8. The initial calibration was achieved with an in-plane mesh size edge length of 20 mm. The mesh size study concerns the reduction of the mesh edge length to 14 mm, that is, under half the diameter of the piles. The materials properties are

kept constant (Tab. 1). The reduction of mesh size influences the exerted ice force levels in the sense that the loads are lower. Due to computational limitations only 4.5 seconds were simulated. Visual observations show that ice bypassing is still restricted for $l = 2D$.

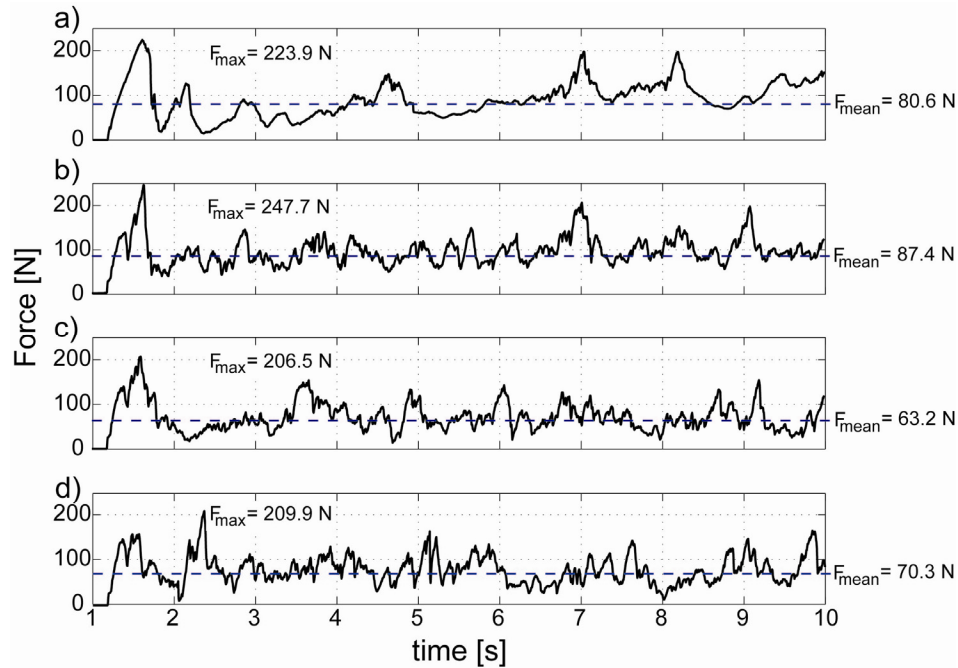


Figure 6. Simulated horizontal ice force on centre pile within each arrangement;
a) $l = 2D$; b) $l = 4D$; c) $l = 6D$ and d) $l = 8D$.

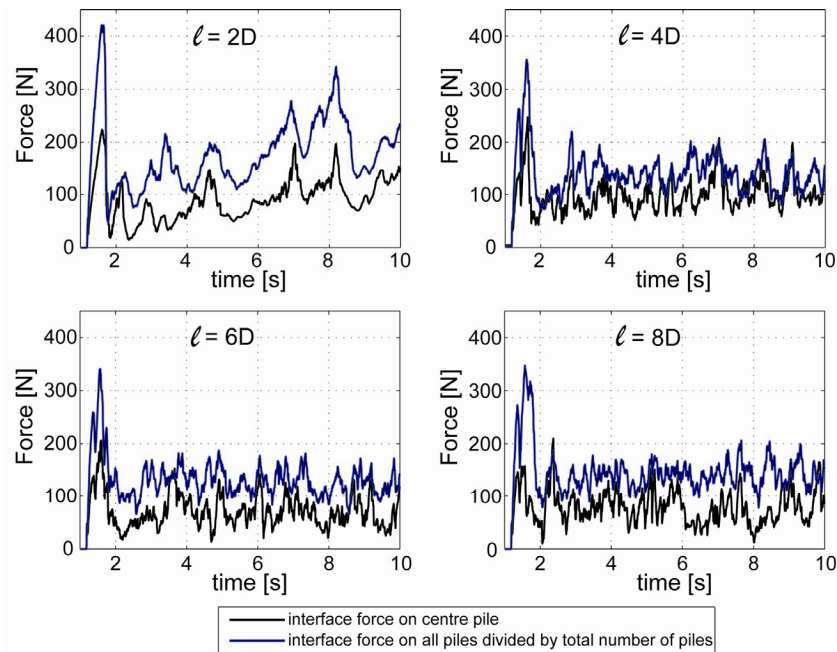


Figure 7. Comparison of simulated ice force on a single centre pile versus the total force on all piles divided by the number of piles within the arrangements, i.e. average force.

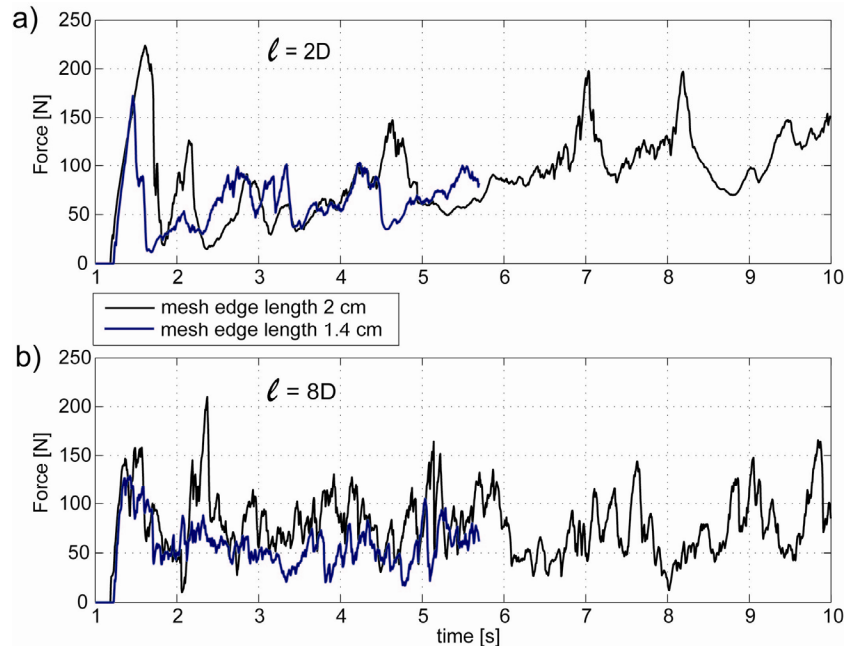


Figure 8. Mesh size dependence on simulated exerted ice forces.

DISCUSSIONS

This modelling exercise devoted much focus on the analysis of the pile-to-pile distance. Concerning IPPs alone, the optimal spacing may influence the construction costs. For multi-legged offshore structures, such as conventional steel jackets, the question of optimal leg spacing arises from the need to allow for ice bypassing, as ice jamming may increase the exerted forces onto the structure, as seen in the increasing trend of the ice force in Fig. 6 a) and b). Earlier recommendations of, for instance $l = 6D$, built solely on model scale observations. Computational methods may aid to investigate the problem more thoroughly and provide a consistent method for extrapolations.

For an ice thickness of 30 mm the simulated failure mode presented in Fig. 4 is seen to coincide with physical tests in the ice model test basin, shown in Fig. 9. However, from visual model tests it is apparent that ‘ice bridging’ between two piles is seen to form the starting point of accelerated ice accumulations (Gürtner and Berger, 2006). It is therefore postulated that the pile-to-pile distance for which no interference of neighbouring piles takes place also depends on the ice thickness. To test the above hypothesis, the ice thickness of the initial boundary value problem was increased to 62 mm and 93 mm, i.e. two-times and three-times the initial ice thickness of 31 mm, respectively. Fig. 10 illustrates the simulation results. Opposed to interaction with thinner ice, interference between the piles appears now to be the case. It is hence strongly recommended to take into concern the ice thicknesses (and its properties) as a parameter for the design of multi-legged offshore structures and not solely base the design on a linear relationship between l and D .



Figure 9. Difference in ice failure mode on $l = 2D$ (left) and $l = 8D$ (right) observed during physical model testing.

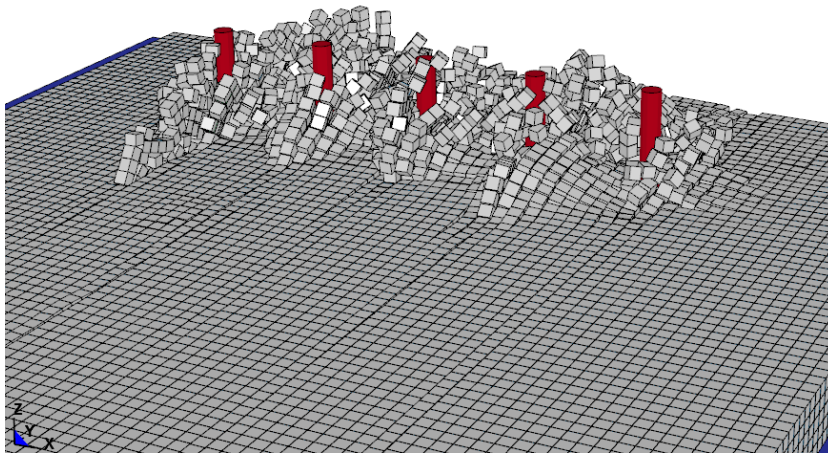


Figure 10. Simulation of ice failure mode of a thick (93 mm) ice sheet interacting with IPPs with a pile-to-pile spacing of $l = 6D$.

Ice forces recorded in Fig. 6 show that the initial force peak is significant. That is, the energy to break the ice is at maximum when the ice is intact. This is particularly the case for the average force presented in Fig. 7. The high initial pile forces observed in this case are somewhat associated with the artificial ice floe geometry, i.e. rectangular shape, with flat contact area. In reality, no ice floe will have a straight face and thus will not contact all of the piles at the same time. The initial load on the arrangement of IPPs may therefore be approximated by using the initial load on a single pile. Owing to the non-simultaneous exceedance of maximum ice load on individual piles, Afanasyev and Afanasyev (1990) found an average decrease in ice load by the increase of the number of piles. The present study cannot confirm this finding as the average force is seen to be of higher magnitude than the force of an individual pile (Fig. 7). As mentioned above, it is likely that both the number of piles as well as the relationship between the floe size (and geometry) to the IPP width will influence the loads in addition to other factors related to the ice properties. This kind of study is beyond the scope of this paper. The higher loads observed on the piles near the ends in our model are likely due to the boundary conditions imposed on the sides of the ice floe. In reality (and to a certain extent in the experiments) ice floe will be finite and floe edges will be stress free or have different stress conditions.

The simulated ice drift velocity onto the IPPs was held constant at $v = 0.125$ m/s in the above investigations. To investigate the influence of the indentation velocity on the exerted ice force, the base case velocity of $v = 0.125$ m/s was first decreased to one half (Fig. 11 a) and thereafter increased to the double (Fig. 11 c) to simulate ice drift on IPPs with $l = 6D$. As in the initial studies, the aspect ratio is approximately unity. Note that only the indentation velocity is varied, whereas all material parameters are kept constant. Fig. 11 compares the exerted ice forces on the centre pile of arrangement $l = 6D$ for different indentation velocities. A significant dependence of the ice force on the indentation velocity may be observed. Force peaks, which are comparable in magnitude to the initial force peak, are seen to occur frequently for $v = 0.250$ m/s (Fig. 11 c), whereas the initial force peak is governing for lower velocities. The magnitude of the maximum force is seen to be slightly dependent on the indentation velocity. Furthermore, the ice force histories' general dependence on the rate of interaction is noteworthy. The mean ice force appears to increase with increasing velocity. For $v = 0.250$ m/s (Fig. 11 c) the ice force approaches a more random process than what could be observed for lower velocities. Capturing the rate dependence of indentation is of particular concern for dynamic ice-structure interactions, not of concern in the present study. However, the CCEM may be a tool to investigate dynamic ice-structure phenomenon in future.

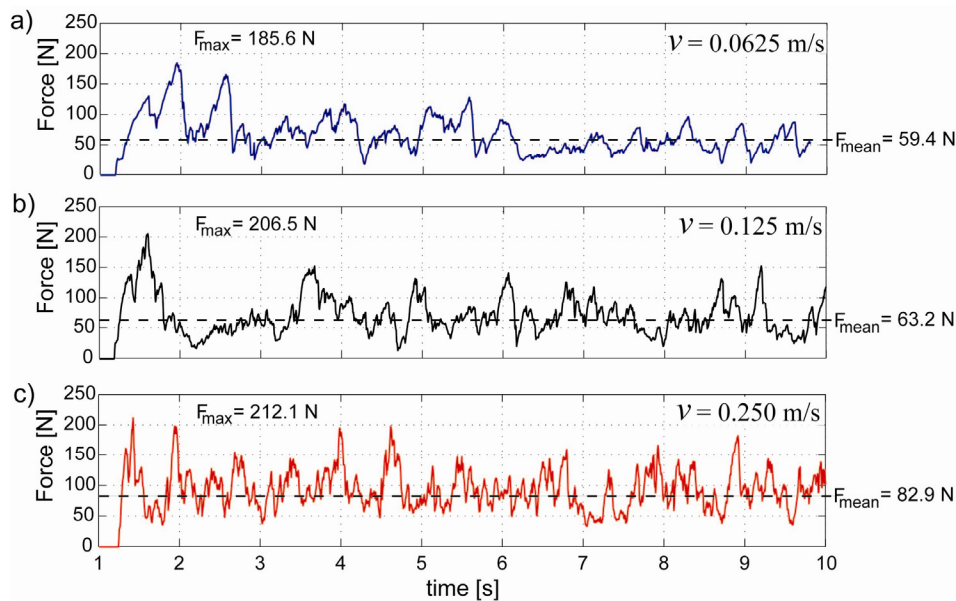


Figure 11. Ice force dependence on indentation velocity for centre pile of arrangement $l = 6D$; a) $v = 0.0625$ m/s; b) $v = 0.125$ m/s (base case) and c) $v = 0.250$ m/s.

As already outlined in the introduction, the boundary value problems analysed so far are solved by considering the water being simplified by an elastic foundation to save computation time. However, this simplification leads to broken ice which is constrained in the vertical direction upstream the IPPs. In case of intensive ice rubble accumulation taking place and pieces of ice getting submerged, a realistic accumulation process cannot be simulated with sufficient accuracy by applying an elastic foundation. Therefore, ice drift on IPPs with $l = 2D$ is solved in a multi-material model with water being explicitly modelled by an Eulerian mesh, as depicted in Fig. 1. Due to buoyancy, the ice sheet becomes free floating. Fig. 12 compares the simulated ice forces on IPPs with $l = 2D$ for elastic foundation and water, respectively. The initial peak force is

reduced compared to the simulation with elastic foundation which attributes to a less constrained ice and therefore less force needed to deflect it. The trend of an increasing ice force with increasing ice rubble accumulations establishes faster in the simulation with water. Fig. 13 a) depicts a snap-shot of the ice breaking process and Fig. 13 b) accordingly the contours of the effective stress field in the ice sheet. Boundary effects on the sides may be observed. It was earlier postulated that these boundary effects are the cause of increased average simulated ice forces on IPPs. Fig. 14 shows a sequence of the simulated bending failure process in the midsection of the ice sheet. Bending and buckling together with ice submergence are seen to be naturally accommodated by the buoyancy of the water. Due to the fact that no *a priori* failure modes are assumed, the observed bending failure of the ice sheet is a direct outcome of the simulations. Although computational costs are high, the multi-material model involving ice, water and IPPs is seen to be more realistic and physically correct than what can be achieved by simplified elastic foundations.

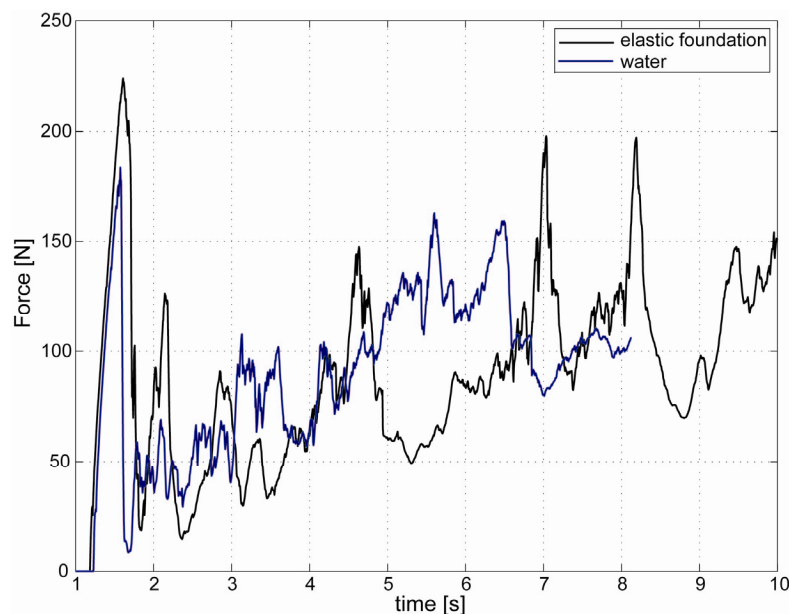


Figure 12. Comparison of simulated ice force on IPPs with $l = 2D$ with a) elastic foundation; and b) water.

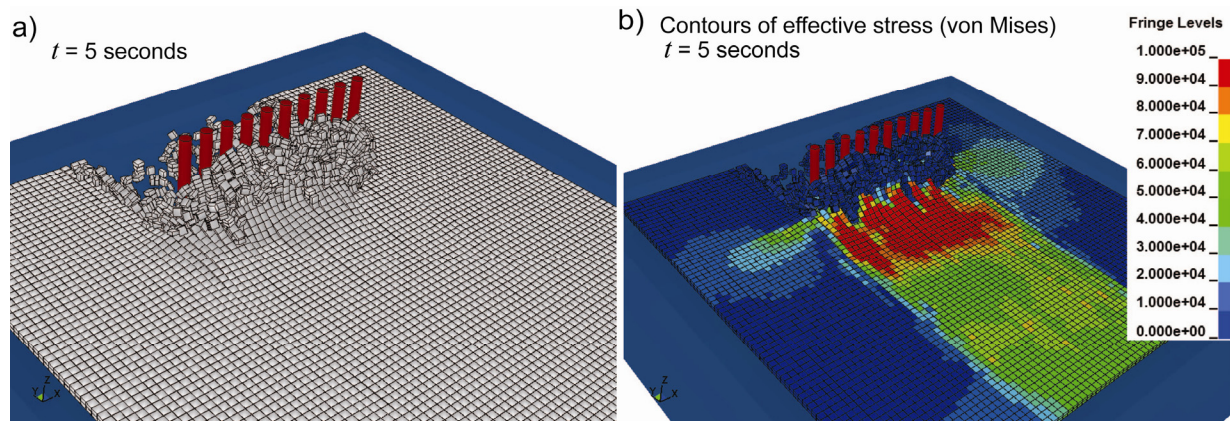


Figure 13. Simulation of ice drift on $l = 2D$ with water; a) failure mode and b) effective stress contours.

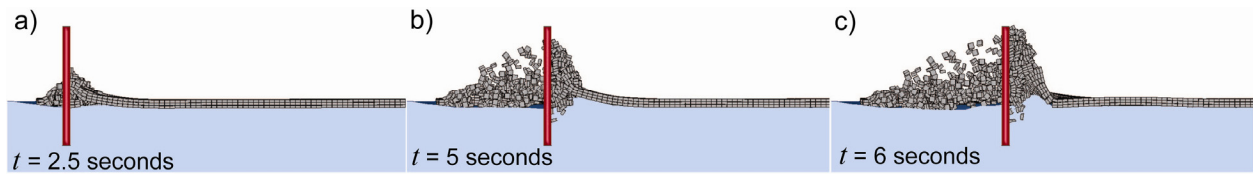


Figure 14. Side view into midsection of successive bending failure at a) $t = 2.5$ s; b) $t = 5$ s; and c) $t = 6$ s.

CONCLUSIONS

Ice drift on arrangement of multiple IPPs has been numerically simulated by means of a CCEM. The simulations are compared to earlier conducted model tests on IPPs. It was shown that the CCEM is a methodology which enables modelling of ice structure interaction with focuses on both visual appearance and exerted ice forces. The simulated results compare well with physical experiments. There exist today no other restriction for the application of the CCEM other than significant CPU-time required for solving the boundary value problem.

The CCEM provides a consistent methodology for simulating ice-structures interactions in which fracture nucleation and propagation are a natural outcome of the simulation. Due to the macroscopic nature of the investigation, we do not account for the detailed representation of the fracture process zone ahead of the crack tip, although this may be achieved with a sufficiently fine mesh. As shown in this study, the mesh size becomes a property of the ice and standard convergence studies on mesh size are hence not applicable for the CCEM.

ACKNOWLEDGEMENTS

The author's express their gratitude to the PETROMAKS program, the Research Council of Norway, to NTNU's PetroArctic project and to StatoilHydro for funding this study.

REFERENCES

- Afanasyev, V.P. and Afanasyev, S.V. (1990): Drifting Ice Forces on Offshore Piles. Proceedings of the 1st European Offshore Mechanics Symposium, Trondheim, Norway, pp. 521- 526.
- Barrenblatt, G.I. (1962): The Mathematical Theory of Equilibrium of Cracks in Brittle Fracture. Advances of Applied Mechanics, Vol. 7, pp. 55-129.
- Chowdhury, S.R. and Narasimhan, R. (2000): A cohesive Finite Element Formulation for Modelling Fracture and Delamination in Solids. Sadhana Academy Proceedings in Engineering Sciences, Vol. 25, No. 6, pp. 561-587.
- Dugdale, D.S. (1960): Yielding of Steel Sheets Containing Slits. Journal of Mechanics and Physics of Solids, Vol. 8, pp. 100-104.
- Evers, K.-U., Spring, W., Foulkes, J., Kühnlein, W., Jochmann, P. (2001): Ice Model Testing of an Exploration Platform for Shallow Waters in the North Caspian Sea. Proceedings of the 16th International Conference on Port and Ocean Engineering under Arctic Conditions (POAC), Vol. 1, pp. 254-264.
- Evers, K.U. and Wessels, E. (1986): Model Test Study of Level Ice Forces on Cylindrical Multilegged Structures. Polartech '86. VTT Symposium 71, International Offshore Navigation Conference and Exhibition. Vol. 3, pp. 251- 275.

- Gürtner, A. and Berger, J. (2006): Results from Model Testing of Ice Protection Piles in Shallow Water. Proceedings of the 25th International Conference on Offshore Mechanics and Arctic Engineering, OMAE2006-92100.
- Gürtner, A., Konuk, I., Gudmestad, O.T., and Liferov, P. (2008): Innovative Ice Protection for Shallow Water Drilling Part III – Finite Element Modelling of Ice Rubble Accumulation. Proceedings of the 27th International Conference on Offshore Mechanics and Arctic Engineering, OMAE2008-57915 (accepted paper).
- Hirayama, K. (1974): An Investigation of Ice Loads on Vertical Structures. The University of Iowa, Ph.D. thesis, 152p.
- ISO (2007). Petroleum and natural gas industries - Arctic offshore structures, ISO TC 67/SC 7 N. International Organization for Standardization.
- Kato, K. and Sodhi, D.S. (1983): Ice Action on Pairs of Cylindrical and Conical Structures. CRREL Report 83-25, Hanover, N.H., USA, September 1983, 42p.
- Korzhasin, K.N. (1962): Ice action on engineering structures. Novosibirsk, 202p. (in Russian)
- LSTC (2006): LS-DYNA Theory Manual. Livermore Software Technology Corporation, John O. Hallquist (ed.), Livermore, California, USA.
- Marshall A.R., Frederking R.M., Sayed M., Nadreau J.P., Croasdale K.R. and Jordaan I.J. (1989): Measurements of Force Transmission through Grounded Ice Rubble. Proceedings of the 10th International Conference on Port and Ocean Engineering under Arctic Conditions, Luleå, Sweden, Vol. 1, pp. 575-584.
- Ruiz, G., Ortiz, M. and Pandolfi, A. (2000): Three-Dimensional Finite Element Simulation of the Dynamic Brazilian Tests on Concrete Cylinders. International Journal for Numerical Methods in Engineering, Vol. 48, No. 7, pp. 963-994.
- Schwarz, J. (1970): Treibeisdruck auf Pfähle, Mitteilung des Franzius-Institutes für Grund- und Wasserbau der Technischen Universität Hannover, Hannover 1970 (in German).
- Sodhi, D. and Morris, C.E. (1984): Ice Forces on Rigid, Vertical, Cylindrical Structures. CRREL Report 84-33. 47 p.
- Song, J.-H., Wang, H. and Belytschko, T. (2007): A Comparative Study on Finite Element Methods for Dynamic Fracture. Computational Mechanics, DOI: 10.1007/s00466-007-0210-x (*in press*).
- Timco, G.W. (1986): Ice Forces on Multi-Legged Structures. Proceedings of the IAHR Symposium on Ice, Iowa City, Iowa, USA, 1986, Vol. II, p. 321-337.
- Toyama, Y. and Yashima, N. (1994): Model –Tests of Multi-Legged Structures in Continuous and Broken Ice. Proceedings of the 4th International Offshore and Polar Engineering Conference, Osaka, Japan, April 10-15, 1994. Vol. 2, pp. 565-571.
- Tvergaard, V. and Hutchinson, J.W. (1992): The Relation between Crack Growth Resistance and Fracture Process Parameters in Elastic-Plastic Solids. Journal of Mechanics and Physics of Solids, Vol. 40, pp. 1377-1397.

ICEBERG TOWING: ANALYSIS OF FIELD EXPERIMENTS AND NUMERICAL SIMULATIONS

Aleksey Marchenko^{1,2} and Christian Ulrich³

¹⁾ *The University Centre in Svalbard (UNIS), Spitsbergen, Norway*

²⁾ *Norwegian University of Science and Technology (NTNU), Trondheim, Norway*

³⁾ *Hamburg University of Technology (TUHH), Germany*

ABSTRACT

Experiments on icebergs towing in the Barents Sea in 2004 and 2005 are analyzed. A mathematical model of iceberg towing is developed to simulate the tension in the towing rope by the towing with one branch and two branches rope. Numerical simulations demonstrate that monotonic increasing of ship propulsion causes numerous hitches of rope tension following with few minutes interval between successive hitches. Peak tensions of the rope created by the hitches can exceed the rope strength. Rotational mode of iceberg motion is constructed and investigated. It is shown that iceberg rotation during the towing increases rope tension significantly in comparison with the towing without iceberg rotation.

INTRODUCTION

The towing of icebergs by ships is used to prevent iceberg impacts on offshore structures and communication lines. The experience of icebergs towing was accumulated during several tens of years on the Canadian Shelf, where numerous icebergs produced by Greenland glaciers drift to the South by the East Greenland current. Glaciers on Franz Josef Land, Svalbard and Novaya Zemlya are the sources of icebergs in the Barents Sea. Barents Sea icebergs are much smaller than Greenland icebergs. Nevertheless the mass of Barents Sea icebergs can be sufficiently big (up to several millions of tons) to create damage of ships and offshore platforms (Løset and Carstens, 1996). In 2003 more than hundred icebergs were observed around the Shtokman Gas Deposit area. Horizontal sizes of icebergs from Novaya Zemlya and Franz Josef Land are varied from several tens to several hundreds meters (Zubakin et al., 2006).

The experimental towings of the iceberg reported here were carried out in the Barents Sea near the northern Novaya Zemlya in the April of 2004 and 2005 in research cruises of RV "Mikhail Somov". In both experiments the towing was carried out by poly-steel rope composed from seven patterns of 110 m length. The rope was deployed around the iceberg and then fastened by the double-bit bollard on the ship stern.

Mean diameter of the iceberg in 2004 was estimated as 32 m, and its mean draft was about 11 m (Fig. 1a). The iceberg mass was estimated to 8000 tons. The iceberg was drifting on the open water partially covered by very thin ice - nilas. The towing rope was deployed around the iceberg by a small boat. The towing was occurred during 40 minutes with a mean speed of 0.8 m/s (Marchenko and Gudoshnikov, 2005). The photograph of the towing is shown in Figure 1a. During the towing parts of the rope connected to the ship with length about 200 m hanged in the

air, while the other parts were floating on sea or ice surface. The iceberg towing was undertaken in calm conditions without surface waves and strong winds.

The mean diameter of the iceberg in 2005 was about 80 m, and its draft exceeded 40 m (Fig. 1b). The iceberg mass was estimated to 200000 tons. The iceberg was partially frozen in the edge of an ice floe, which thickness was about 40 cm near the iceberg. Other floes were floating around the iceberg. Ice free water from one side of the iceberg gave possibility to moor the ship to the iceberg for one day period to study its properties. On the second day the rope was removed from the ship on the iceberg surface and then deployed around the iceberg manually.

The towing took place on the second day in conditions of sufficiently strong wind up to 20 m/s without surface waves. During the towing almost all rope between the ship and the iceberg hanged in the air, and only its small parts were floating on water surface near the iceberg. The rope length between the ship stern and the iceberg is estimated as 450 m. After approximately 30 minutes of the towing the ship was decelerated due to the approach of a floe in front of the ship. In this time iceberg rotation was observed visually from the ship due to the depression of the tension in one branch of the towing rope (Fig. 2a). Another branch of the rope had sufficiently strong tension keeping significant part of the rope above water surface. After 10-15 minutes the ship accelerated and the rope was broken (Fig. 2b). The situation of the rope break up is explained in Fig. 3.

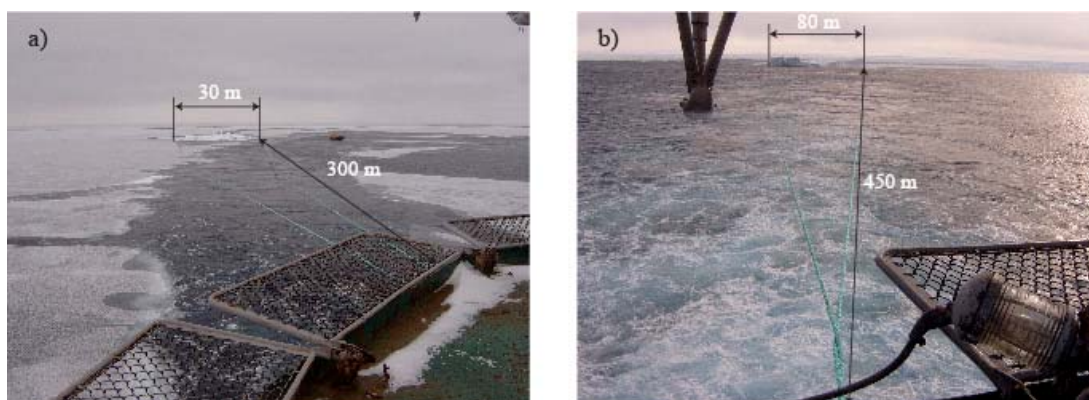


Figure 1 - Iceberg towing in 2004 (a) and 2005 (b).

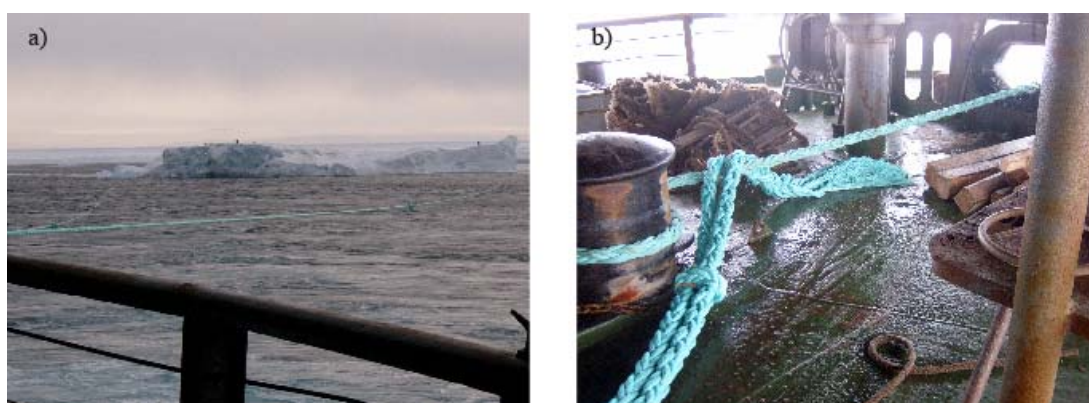


Figure 2 - The depression of the tension in left branch of the rope created by ship deceleration and iceberg rotation (a). Broken towing rope (b).

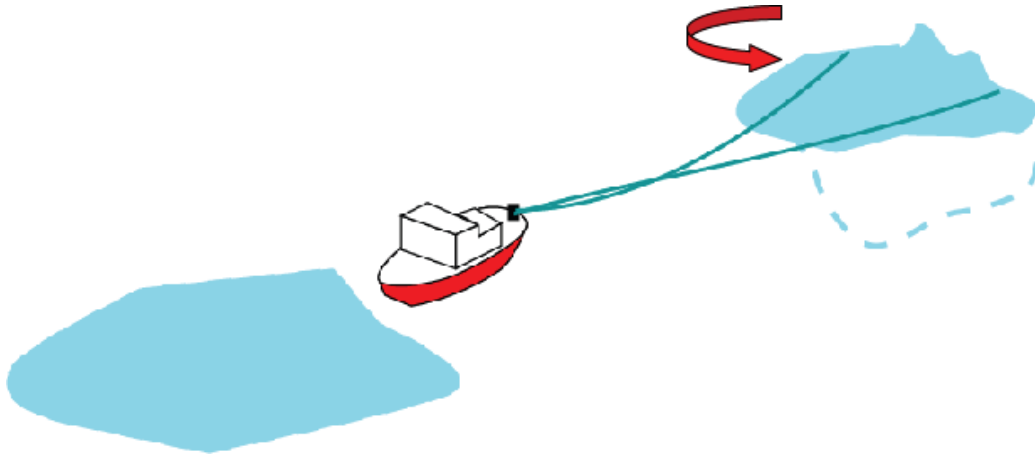


Figure 3 - Iceberg rotation caused by ship deceleration.

FORMULAS FOR THE CALCULATION OF ROPE TENSION

It is assumed that gravity, tension and inertial forces determine the motion of the rope. The force balance at the rope is expressed as follows

$$\frac{W}{g} \mathbf{a} = \frac{d}{ds} \boldsymbol{\sigma} + \mathbf{W} \quad (1)$$

where $\mathbf{W} = (0, -W)$ is the weight of the rope of unit length, $\boldsymbol{\sigma}$ is the rope tension, \mathbf{a} is the rope acceleration, and ds is infinitesimal length of the rope (Fig. 4). The rope tension is written as $\boldsymbol{\sigma} = \sigma \boldsymbol{\tau}$, where $\boldsymbol{\tau}$ is unit tangential vector to the rope. Using Frenet formulas equation (1) is written as follows

$$\frac{W}{g} \mathbf{a} = \frac{d\sigma}{ds} \boldsymbol{\tau} - \sigma k \mathbf{n} + \mathbf{W}, \quad (2)$$

where \mathbf{n} is unit normal vector to the rope and $k = \eta_{,xx} (1 + \eta_x^2)^{-3/2}$ is the rope curvature. It is assumed that the rope shape is described by equation $z = \eta(x, t)$.

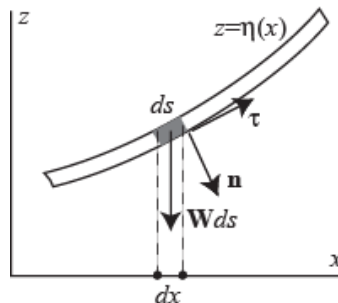


Figure 4 - Scheme of forces applied to extended rope.

In steady case the integration of the projection of equation (2) on τ -direction leads to the formula $\sigma = \sigma_0 + W\eta$. The projection of (2) on \mathbf{n} -direction is reduced to the equation

$$\sigma \frac{d^2\eta}{dx^2} = W \sqrt{1 + \left(\frac{d\eta}{dx}\right)^2} \quad (3)$$

Let us perform the solution of equation (3) as $\eta = \eta_0 + \delta\eta$, where η_0 is the solution of equation

$$\sigma_0 \frac{d^2\eta}{dx^2} = W \quad (4)$$

Assuming that the rope is fixed at $z = H_s$ by $x = 0$ and at $z = 0$ by $x = A$ we find

$$\eta_0 = \frac{W}{\sigma_0} \left(\frac{x^2}{2} - Ax \right) + H_s \quad (5)$$

If the rope is floating by $x > A$, then the tension σ_0 is found from the condition $d\eta/dx = 0$ by $x = A$ as (Marchenko and Gudoshnikov, 2005)

$$\sigma_0 = \frac{WA^2}{2H_s} \quad (6)$$

From (6) follows that $WH_s \ll \sigma_0$ and consequently $W\eta \ll \sigma_0$, when $A \gg \sqrt{2H_s}$. This inequality is typically occurred for the towing of icebergs, when the distance A is about the distance between the ship and the body (200-500 m) and H_s is free board of the ship (5-10 m). It means also that $\eta_x \ll 1$. Therefore further $\eta = \eta_0$ is assumed.

The length of the rope above the water surface is calculated with formula when

$$l_{0A} = \int_0^A \sqrt{1 + \eta_x^2} dx \quad (7)$$

Substituting the expression from formula (6) into (7) we find

$$l_{0A} = \frac{\sigma_0}{2W} \left(\frac{WA}{\sigma_0} \sqrt{1 + \left(\frac{WA}{\sigma_0}\right)^2} + \operatorname{arcsinh}\left(\frac{WA}{\sigma_0}\right) \right) \quad (8)$$

With using Taylor series this expression is simplified with accuracy to high order terms as follows

$$l_{0A} = A \left(1 + \frac{2}{3} \frac{H_s^2}{A^2} \right) \quad (9)$$

Expressing the rope length as $l_r = l_{0A} + X - A$, where X is the coordinate of rope fastening at the iceberg (Fig. 5), we find

$$A = \frac{2}{3} \frac{H_s^2}{l_r - X} \quad (10)$$

After substitution of formula (10) into formula (6) the rope tensions is expressed as

$$\sigma_0(l_r, X) = \frac{2}{9} \frac{WH_s^3}{(l_r - X)^2} \quad (11)$$

In steady solution the rope tension is in a balance to the rope weight. The influence of rope inertia becomes important when $W\partial^2\eta/\partial t^2 \approx g\sigma_0\partial^2\eta/\partial x^2$. Using formula (6) one finds the ratio between representative time (T) and length scale (L) of nonstationary perturbations as $T = LA^{-1}\sqrt{2H_s/g}$. Assuming $L = A$ and $H_s = 7$ m we estimate $T = 1.2$ s.

THE ESTIMATION OF ROPE TENSION

Visual analysis of the photographs of the rope during the towing in 2005 has shown that both branches of the towing rope with length about 450 m hanged in the air. Substituting in formula (6) numerical values

$$W = 25 \text{ Nm}^{-1}, \quad A = 450 \text{ m}, \quad H_s \approx 7 \text{ m}. \quad (12)$$

we estimate the tension in each branch of the rope as $\sigma \approx 36.9$ T. Therefore the total force applied to the iceberg by the ship was about $2\sigma \approx 73.8$ T. This load is closed to critical tension of the rope $\sigma_{cr} \approx 80$ T. Thus the rope would be broken if this load would be applied to one branch of the rope.

Iceberg rotation due to ship acceleration created the depression of the left branch of the rope (Fig. 2a). When ship was accelerated most of the load became applied to the right branch of the rope. It can be the reason for the break up of towing rope in 2005.

EQUATIONS OF ICEBERG MOTION UNDER THE TOWING

Let us consider model iceberg with the shape of vertical cylinder with radius R and draft H (Fig. 5). The equation of momentum balance describing iceberg motion under the towing is written as follows

$$M_i \frac{d\mathbf{v}_i}{dt} = \mathbf{F}_{wi} + \mathbf{T}, \quad \frac{d\mathbf{x}_i}{dt} = \mathbf{v}_i \quad (13)$$

where M_i is iceberg mass, $\mathbf{v}_i = (v_{i,x}, v_{i,y})$ is the vector of iceberg velocity in the horizontal plane (x, y) , \mathbf{F}_{wi} is the force applied to the iceberg by the water, \mathbf{T} is the force applied to the iceberg by the rope, and vector $\mathbf{x}_i = (x_i, y_i)$ shows the location of iceberg centre mass at the plane (x, y) .

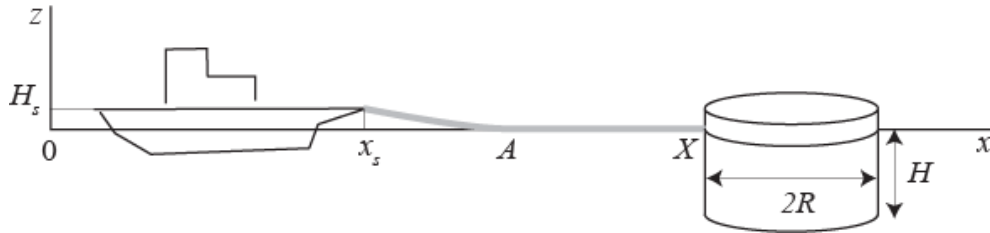


Figure 5 - The scheme of cylindrical iceberg towing.

The force \mathbf{F}_{wi} is equal to a sum of the force due to added mass effect and form drag

$$\mathbf{F}_{wi} = M_{ad} \frac{d(\mathbf{v}_w - \mathbf{v}_i)}{dt} + \rho_w C_d S_i |\mathbf{v}_w - \mathbf{v}_i| (\mathbf{v}_w - \mathbf{v}_i) \quad (14)$$

where $M_{ad} = \pi \rho_w R^2 H$ is added mass of the iceberg, \mathbf{v}_w is mean horizontal water velocity in the vicinity of the iceberg, ρ_w is water density, C_d is form drag coefficient, $S_i = 2RH$ is the effective area of vertical cross-section of submerged part of the iceberg.

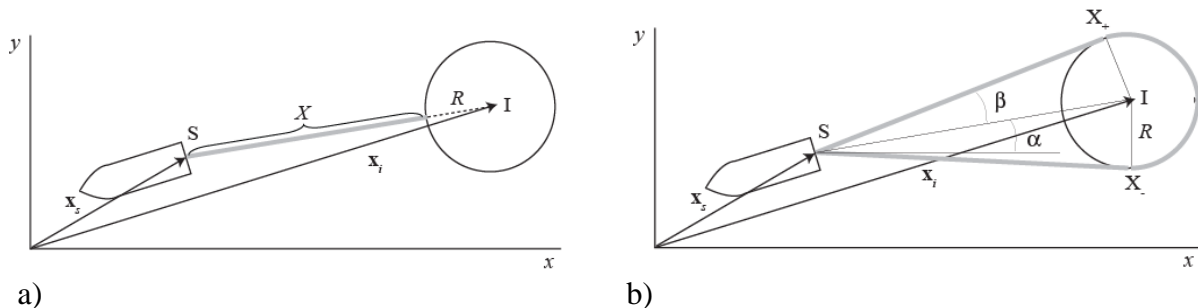


Figure 6 - Iceberg towing with one rope branch (a) and with two branch rope (b).

The vector of rope tension by iceberg towing with one rope branch (Fig. 6a) is calculated by formulas

$$\mathbf{T} = \mathbf{e}_{IS} \sigma_0(l_r, X), \quad \mathbf{e}_{IS} = \frac{\mathbf{x}_s - \mathbf{x}_i}{X_{IS}}, \quad X_{IS} = |\mathbf{x}_s - \mathbf{x}_i| \quad (15)$$

The value of σ_0 is calculated with formula (11), where $X = X_{IS} - R$. Vector $\mathbf{x}_s = (x_s, y_s)$ is associated with the coordinates of fastening point of the rope at ship stern.

The vector of rope tension by iceberg towing with two branches of the rope (Fig. 5b) is calculated by formulas

$$\begin{aligned} \mathbf{T} &= \mathbf{T}_+ + \mathbf{T}_- & (16) \\ \mathbf{T}_\pm &= T_\pm (\cos \alpha_\pm, \sin \alpha_\pm), \quad T_\pm = \sigma_0(l_\pm, X), \quad X = \sqrt{X_{IS}^2 - R^2}, \quad X_{IS} = |\mathbf{x}_s - \mathbf{x}_i| \\ \alpha_\pm &= \alpha \pm \beta, \quad \alpha = \arcsin \frac{y_s - y_i}{X_{IS}}, \quad \beta = \arcsin \frac{R}{X_{IS}} \end{aligned}$$

Rope length l_+ between points S and X_+ and rope length l_- between points S and X can be different.

The conservation of angular momentum of the iceberg is written as follows

$$I_i \frac{d^2 \varphi}{dt^2} = R(T_- - T_+) \quad (17)$$

where I_i represents the iceberg's inertia and φ is the angle of iceberg rotation around its vertical axes.

Five equations (13) and (17) together with formulas (14), (15) and (16) form closed system of ordinary differential equations for the finding of unknown functions $x_i(t)$, $y_i(t)$, $v_{i,x}(t)$, $v_{i,y}(t)$ and $\varphi(t)$, when functions $x_s(t)$ and $y_s(t)$ are given. In the other case equations (12) and (16) have to be completed by equations describing the ship motion.

SIMULATIONS OF ICEBERG TOWING WITH ONE BRANCH ROPE

Let us consider iceberg towing in calm water ($\mathbf{v}_w = 0$) in the direction of x -axis with one branch rope when the ship motion is described by equations

$$M_s \frac{dv_s}{dt} = F_{ws} - T + P, \quad \frac{dx_s}{dt} = v_s \quad (18)$$

where $M_s = 15000$ t is the ship mass, v_s and x_s are the velocity and the location of the ship, P is the power of ship propulsion and T is rope tension calculated with formula (15). The force applied to the ship by the water is defined as follows

$$F_{ws} = -\rho_w C_s S_s |v_s| v_s \quad (19)$$

where drag coefficient $C_s = 0.003$ and the area of wetted surface of the ship hull is $S_s = 1000 \text{ m}^3$. The ship propulsion is defined by formula

$$P = -\rho_w C_s V_s^2 \tanh^2(5t/t_s) \quad (20)$$

where t_s is the time of ship acceleration to the speed V_s in the case when rope tension is absent ($T = 0$).

Results of numerical simulations computed with $M_i = 200000 \text{ t}$, $M_{ad} = M_i / 2$, $H_s = 7 \text{ m}$, $W = 45 \text{ N/m}$, $l_r = 450 \text{ m}$, $S_i = 3200 \text{ m}^2$ and $C_i = 0.6$ are shown in Fig. 7.

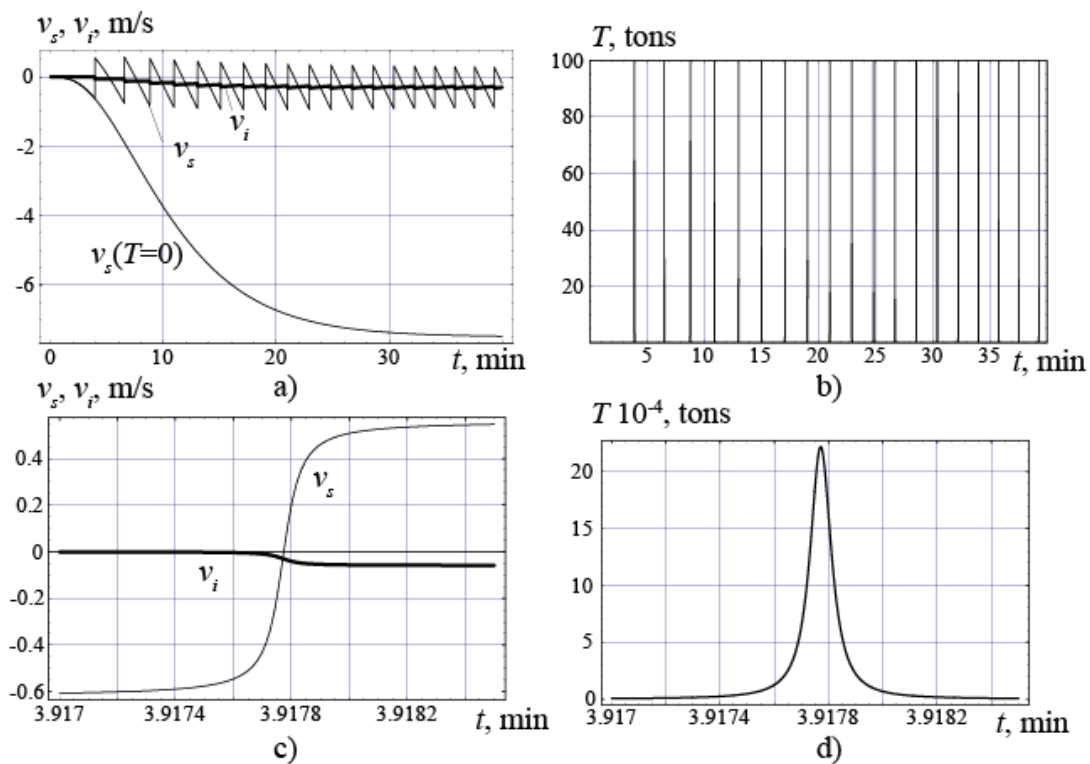


Figure 6 - Velocities of ship and iceberg (a,c). Vertical lines show the times of peak tension of the rope (b). Rope tension in the vicinity of local maxima (d).

The line marked by $v_s(T = 0)$ in Fig. 7a shows ship velocity versus the time if the ship would be accelerated by the propulsion (20) with $T = 0$. Ship velocity increases to 7.5 m/s during 30 min. Lines v_s and v_i show the speeds of the ship and the iceberg during the towing. Since the iceberg mass is much bigger than the ship mass the iceberg motion looks more monotonic in comparison with ship motion. The ship speed is changed from negative to positive values due to the influence of the rope tension. Each change of the sign of the ship velocity is created by the hitch of the rope. Vertical lines in Fig. 7b show the times of rope hitches. The time interval between two successive hitches is about few minutes. Peak tensions of the rope decrease with the time.

Ship speed and iceberg speed in the vicinity of the first hitch of the rope is shown in Fig. 7c versus time. In the moment of peak tension the iceberg and the ship move in opposite directions. Fig. 7d shows rope tension versus the time in the vicinity of the first hitch of the rope. One can see that peak value of the tension is very high and it is realized in very short time about 0.001 s, when the rope inertia can be of importance.

ROTATIONAL MODE OF ICEBERG MOTION

Rotational mode of iceberg motion is described by equations (17) and (16). Equations (13) are satisfied with assumptions $dx_s/dt = 0$ and $dx_i/dt = 0$. In this case the points X_+ and X_- are fixed in the space and the sum of rope length $l_{r,-}$ between points S and X_- and rope length $l_{r,+}$ between points S and X_+ is a constant

$$l_{r,+} + l_{r,-} = 2L \quad (21)$$

Temporal variations of $l_{r,-}$ and $l_{r,+}$ are related to angular velocity of the iceberg as follows

$$\frac{dl_{r,+}}{dt} = -R \frac{d\varphi}{dt}, \quad \frac{dl_{r,-}}{dt} = R \frac{d\varphi}{dt} \quad (22)$$

Absolute values of the rope tensions T_+ and T_- determined by formulas (11) and (16) are expressed as follows

$$T_+ = \frac{C}{(l_{r,+} - c)^2}, \quad T_- = \frac{C}{(l_{r,-} - c)^2} \quad (23)$$

where $C = 2WH_s^3/9$ and $c = |SX_-| = |SX_+|$.

Substituting formulas (21)-(23) in equation (17) we find

$$I_i \frac{d^2 l}{dt^2} = -R^2 C \left(\frac{1}{(2L - l - c)^2} - \frac{1}{(l - c)^2} \right), \quad l = l_{r,+} \quad (24)$$

Equations (24) is integrated once by time after its multiplication on dl/dt . Let us introduce new dimensionless variables $n \in (-1,1)$ and t' by formulas

$$n = \frac{l - L}{l_0 - L}, \quad t' = t 2R \sqrt{\frac{C\beta}{I_i(1 - \alpha^2)}}, \quad \beta = \frac{L - c}{(L - l_0)^4}, \quad \alpha^2 = \left(\frac{L - c}{L - l_0} \right)^2 \quad (25)$$

where $l = l_0$ when $dl/dt = 0$. Since $l_0 > c$, constant $\alpha > 1$. The value of constant α is increased with the increasing of the initial length of the rope l_0 when the distance c is fixed. Integrating equation (24) by the time and substituting dimensionless variables we find

$$\frac{dn}{dt'} = \sqrt{\frac{1-n^2}{\alpha^2-n^2}}, \quad T = 4 \int_{-1}^0 \sqrt{\frac{\alpha^2-n^2}{1-n^2}} dn \quad (26)$$

where T is dimensionless period of the solution. When $\alpha \gg 1$ the solution of (26) has period $2\pi\alpha$ and it is approximated by the formula $n = \sin(t/\alpha)$. Therefore the period of angular oscillations is increased with the increasing of constant α or the initial rope length l_0 . Phase diagram of the solution and period T versus constant α are shown in Fig. 8. One can see that maximal angular velocity of iceberg rotation (it is proportional to dn/dt') is increased with the decreasing of constant α or the initial rope length l_0 .

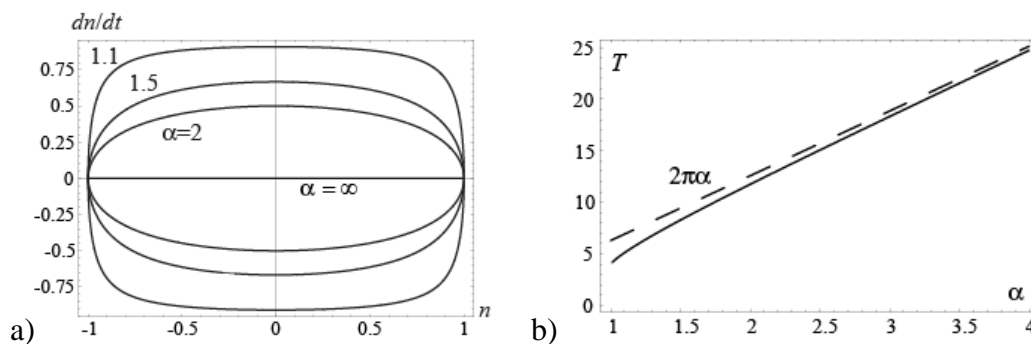


Figure 8 - Phase diagram of periodical solutions of equation (26) constructed with different values of α (a) and dimensionless period T versus constant α (b).

THE INFLUENCE OF ICEBERG ROTATION ON ROPE TENSION

In this simulation the ship motion is given as fixed input value. A towing in calm water ($\mathbf{v}_w = 0$) with two branch rope is considered. The calculations have been carried out with $M_i = 200000 \text{ t}$, $M_{ad} = M_i/2$ (no added mass for the rotation), $H_s = 7 \text{ m}$, $W = 45 \text{ N/m}$, $S_i = 3200 \text{ m}^2$ and $C_i = 0.6$.

The initial conditions for the simulations were related to the equilibrium towing in the direction of x -axis with the velocities $v_i = v_s = 0.1 \text{ m/s}$. For these velocities the rope tension was calculated as $10\,000 \text{ N}$ for each branch. When the ship accelerates from the initial 0.1 m/s up to 0.2 m/s in 320 s , we can observe four hitches in the rope with the peak tension of $3.5 \cdot 10^5 \text{ N}$ (Fig. 9a). To simulate the influence of iceberg rotation to the peak tensions, we induce a tension of $1.26 \cdot 10^5 \text{ N}$ to one rope branch right at the beginning of the ship's acceleration. This scenario represents a rotated iceberg which experiences an increasing of tensions in both rope branches due to ship's acceleration. The maximum peak tension is $9.6 \cdot 10^5 \text{ N}$ is shown in Fig. 9b. This maximum value occurs at the branch of the rope with the lower initial tension. Comparing Fig. 9a and Fig. 9b we conclude that iceberg rotation increases peak tension of the rope approximately in two times.

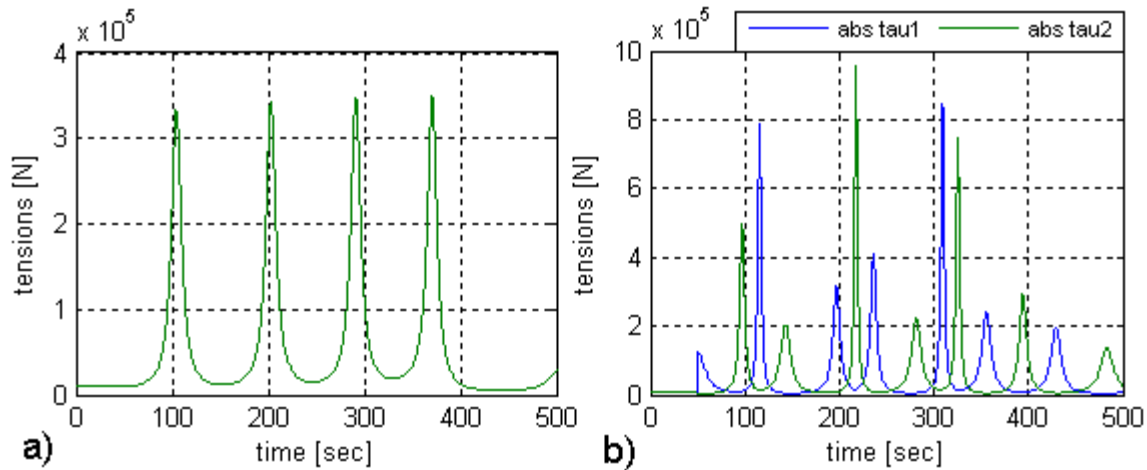


Figure 9 - Peak tensions of both rope branches; a) shows the tension due to ship's acceleration without iceberg rotation; b) displays the scenario of ship's acceleration when the iceberg has some initial rotation.

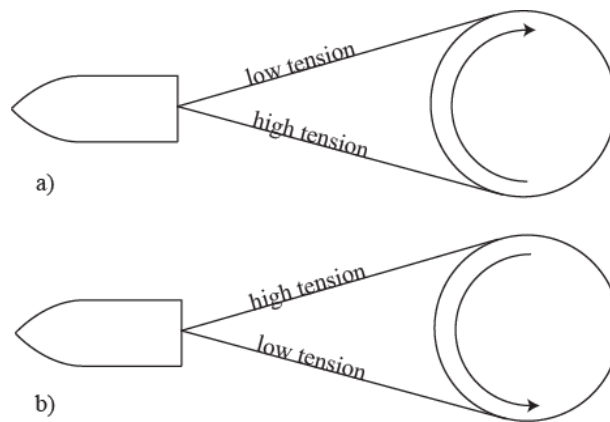


Figure 10 - Scheme of iceberg rotation in initial time of the towing (a) and after the peak tension in the branch with low initial tension (b).

The scheme of iceberg rotation during the towing is shown in Fig. 10. In initial time the tension in one rope branch is higher than in the other rope branch (a). It creates clockwise iceberg rotation until the tension in the second rope branch reaches its peak value. After that the iceberg starts to rotate in counter clockwise direction (b).

CONCLUSIONS

Iceberg towing by a ship and towing rope is accompanied by the hitches of the rope tension following successively with few minutes interval. These hitches can lead to the break up of the towing rope. Small acceleration in initial period of the towing will reduce peak tensions of the rope. Peak values of rope tension computed for the case of iceberg towing with two branches rope are smaller than those values computed for the towing with one branch rope.

There is rotational mode of iceberg motion under the towing with two branches rope. This mode can be excited due to the change of towing direction or due to unequal tension in rope branches in initial time. Iceberg rotation can increase peak values of rope tensions significantly. This effect created the break up of the rope in iceberg towing experiment in the Barents Sea in 2005.

ACKNOWLEDGEMENTS

The work was supported by the PetroArctic project funded by PETROMAKS, the Research Council of Norway. I would like to thank Prof. Sveinung Løset for his comments, and Prof. Gennadii Zubakin and Dr. Yuri Gudoshnikov for cooperation during the fieldwork.

REFERENCES

- Løset, S, and T. Carstens (1996): Sea ice and icebergs in the Western Barents sea in 1987. Cold Reg. Sci. Techn., Vol. 24, N4, pp. 323-340.
- Marchenko, A. and Yu.. Gudoshnikov (2005): The influence of surface waves on iceberg towing. Proc. of 18th Int. Conference on Port and Ocean Engineering under Arctic Conditions (POAC'05), Vol. 2, Clarkson University, Potsdam, NY, pp.543-553.
- Zubakin, G.K., Shelomentsev, A.G., Onshuus, D.K., Eide, L.I. and I.V.Buzin (2005): Distribution of icebergs in the Barents Sea based on archived data and observations of 2003. of 18th Int. Conference on Port and Ocean Engineering under Arctic Conditions (POAC'05), Vol. 2, Clarkson University, Potsdam, NY, pp.575-583.

KEYWORDS

Iceberg towing, iceberg motion, rope tension

HYDROLOGICAL CHARACTERISTICS OF THE STRAIGHT SEPARATING BRAGANZAVÅGEN FROM SVEABUKTA IN VAN MIJEN FJORD

Aleksey Marchenko^{1,2}, Ivar Langen³ and Aleksey Shestov^{1,4}

¹*The University Centre in Svalbard, Longyearbyen, Norway*

²*The Norwegian University of Science and Technology, Trondheim*

³*University of Stavanger, Stavanger, Norway*

⁴*Moscow Institute of Physics and Technology, Moscow, Russia*

ABSTRACT

The paper describes measurements of sea current, water pressure and sea temperature below the ice in a narrow and very shallow area of Van Mijen fjord on Spitsbergen in the winter season 2008. The experimental setup consists of a 3D acoustic Doppler velocimeter and temperature and pressure sensors. Based on filed data mean current velocities, tidal amplitudes, Reynold stresses, water – ice drag coefficients and turbulent heat fluxes are calculated. The maximal heat fluxes to ice bottom reached 10 W/m^2 obtained during rising tides. The calculated mean values of the drag coefficients vary between 0.003 and 0.004. The collected data shows the existence of water velocity oscillations directed transversally to the fjord axis and water pressure at bottom with periods multiples of 12.5 min at low tide.

INTRODUCTION

The natural environment of large areas on the Arctic shelf is characterized by small water depth, long ice season, strong winds, low air temperatures, tides with current velocities up to 1 m/s and water level variations about 1 m, regions with seasonal permafrost and variable river runoff, among others factors. Estimates of design loads on arctic offshore structures are carried out using actual field data. Overestimates of design loads lead to a significant increase of the costs for the construction of engineering structures, while underestimates can cause catastrophic results.

Penetration of tidal currents in shallow water regions covered by ice creates high shear stresses in the water and therefore causes stronger sediment transport during an ice season. This effect was studied in several rivers (Hains and Zabilansky, 2004), where seabed scours created near bridge piers by the current in winter time were larger than in summer time. The influence of tidal currents on sediment transport in Arctic coastal zones is not well studied phenomenon. Zubov (1944) wrote about significant decreasing of tidal amplitudes in the mouth of several rivers flowing into the White Sea in winter time in comparison to ice free season. Voinov (1999) demonstrated delay of tidal phase in ice season in the Kara Sea.

The influence of sea currents on the level ice is realised by drag force existing due to the transfer of liquid particles momentum to the ice bottom. Since water molecular viscosity is very small, the momentum transfer in natural conditions is mainly related to the production of vorticity in ice adjacent layer, and water currents below the ice is turbulent. Since the bottom surface of drifting sea ice is not level, total drag force can be decomposed into turbulent drag force and form drag force. Form drag force depends on the amount of ice ridges per unit area of sea ice and their geometrical sizes, while turbulent drag depends mainly on the area covered by the level ice. The bottom of land fast ice is smooth. Therefore the influence of water currents on land fast ice is related mainly to turbulent drag force. The drag force creates internal ice stresses in land fast ice and can cause its break up. Direct measurements of turbulent drag forces at the bottom of drifting ice were carried out in (Langleben, 1980; McPhee, 2007; Gorbatsky and Marchenko, 2007)

Filed observations of the landfast sea ice near Point Barrow, Alaska, recorded vertical displacements of several centimetres amplitude and periods of the order of 600 s (Bates and Shapiro, 1980) prior to a large ice push episode. Further, over about 5 years of nearly continuous radar observations of near shore ice motion in that area, similar oscillations were always observed to occur for at least several hours before the start of movement of the landfast ice or adjacent pack ice. This suggests that oscillations of the ice within some range of periods and amplitudes are a precursor to ice motion and could be useful in providing warning of potential hazards to offshore or coastal installations and operations, and to hunting parties moving over the ice. Marchenko et al (2002) demonstrated theoretically that the excitation of long surface waves with period about 600 s is possible due to the transfer of floes momentum into the water under their relative displacements and ice ridges build up induced by wind drag force. Smirnov et al. (2004) measured oscillating tilts of floating drilling platform frozen in sea ice in Ob Bay with period of 12-15 min. The oscillations were observed together with low frequency oscillations of water level due to semidiurnal tide. The existence of the oscillations was related to the excitation of natural modes of water oscillations in the local basin under the influence of tides and atmosphere pressure perturbations.

The present paper is related to the study of sea currents below the ice in very shallow area of Van-Mijen fjord separating Braganzavagen from Sveabukta. The amplitude of semidiurnal tide is determined by incoming tide from the Greenland Sea, and it is almost the same over a year. In winter time Van Mijen fjord is covered by ice with mean thickness up to 1m. Therefore peak value of tidal currents in winter time should be stronger in comparison with ice free season. We have measured velocities, temperature and pressure in several locations. These data gave us possibility to calculate turbulent drag force, drag coefficients and turbulent heat fluxes to the ice bottom. We also found high frequency oscillations of all measured parameters.

LOCATION OF THE FIELD STUDY

The region of the field study from January to April 2008 is characterised by shallow water depth, a tidal variability from 0.5 m at neap to 1.8 m at spring tides, an ice cover with thicknesses up to 1 m, and a modest river runoff from Braganzavågen. Typically, ice covers the sea surface from the end of January to the end of June in the Van Mijen fjord. The region of the field study is shown in Figure 1. The mean depth across the fjord varies from 1 to 3 meters over the tidal cycle. There is very shallow water in the central part of the fjord where the ice can be grounded at low tide. Ice drilling has shown that the seabed soil was frozen when the ice was grounded, and it was not frozen when a water layer with a thickness of a few centimetres was observed below the ice.



Figure 1 – Aerial photograph and map of the study region.

Snow thickness on the ice surface was measured from 10 to 40 cm with variations up to 20 cm across the fjord during the period in 2008. The ice thickness was about 1 m near the beach and about 50 cm in the middle part of the fjord in March. In April ice thickness in the middle part of the fjord was increased to 80 cm. The shape of ice surface cross the fjord was reconstructed by the measurements of the distance from seabed to ice surface in 13 holes drilled through the ice on March 12. Each of 3 series of 13 measurements has been done within 0.5 hour with crossing of the fjord by snow scooter. The shape of ice is shown in Figure 2 a,b,c. One can see that absolute value of the slope angle of ice surface reaches 0.02. In the middle part of the fjord the ice is grounded in low tide. In high tide ice surface is blown up in three places. In low tide ice surface is depressed in the left part of the fjord.

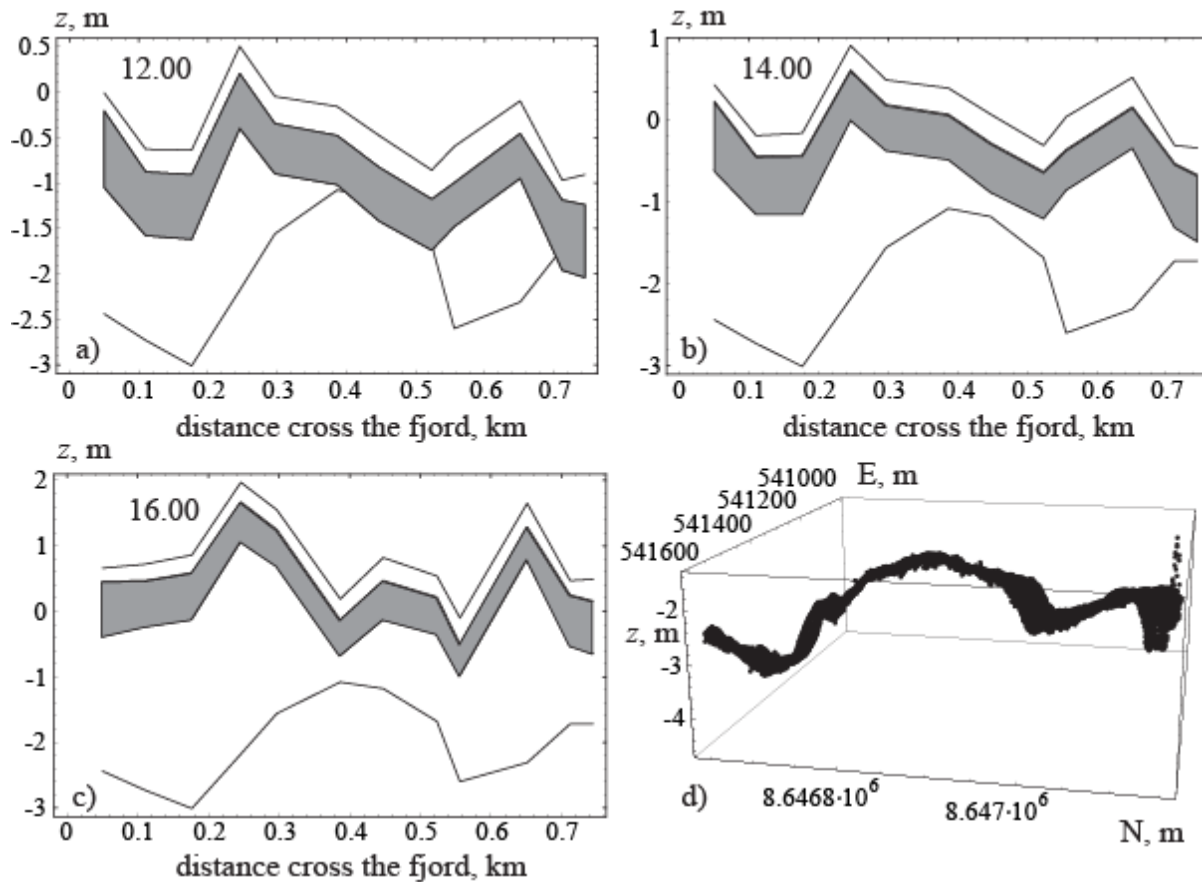


Figure 2. Ice thickness (grey regions), snow thickness on the ice (white regions) and distance from sea bottom to ice surface measured at 13 locations over the fjord in different times on March 12, 2008 (a,b,c). Seabed profile measured in geological survey from the ship in summer time (d).

Figure 3a shows variations of water pressure measured at sea bed in two locations from different sides of the shallow part in the middle of the fjord in different times using temperature and pressure recorder SBE-39. Figure 3b shows ice bottom profiles shown in Figure 2 all together. One can see that water pressure variations and displacements of ice bottom vary cross the fjord.

EXPERIMENTAL SETUP

The 3D sea current velocity relative to the ice (\mathbf{v}_{wi}) was measured in a 2 cm^3 volume by a SonTek 5-MHz ADVOcean Probe (Acoustic Doppler Velocimeter) mounted on the sea ice with a tripod. The mounting allowed us to lift the ADV up and down at half-meter intervals down to 3 m below the ice. The probe was located 18 cm from the acoustic transmitter. The sampling rate was chosen

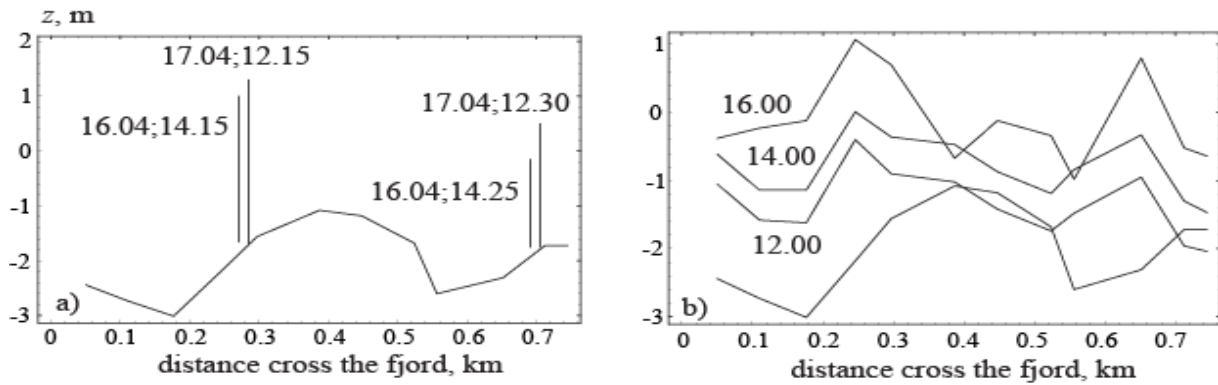


Figure 3. Vertical lines show water pressure measured at the seabed in two locations in different times (a). Ice bottom profiles shown in Figure 2 (b).

from 1 to 25 Hz at several geographical locations. Measurements of the temperature (T) and the pressure (P) were carried out using 1 Hz sampling with an SBE-39 recorder (1) mounted with the ADV. Another SBE-39 recorder (2) was placed on the seabed below the ADV to measure bottom temperature and water depth. The scheme of measurements is shown in Figure 4. ADV data are recorded on a recorder located in ADV canister. The operating temperature should be higher than -5°C . Therefore the canister was put inside an insulated box with heater taking energy supply from a generator. SBE-39 data recorder is located inside SBE body

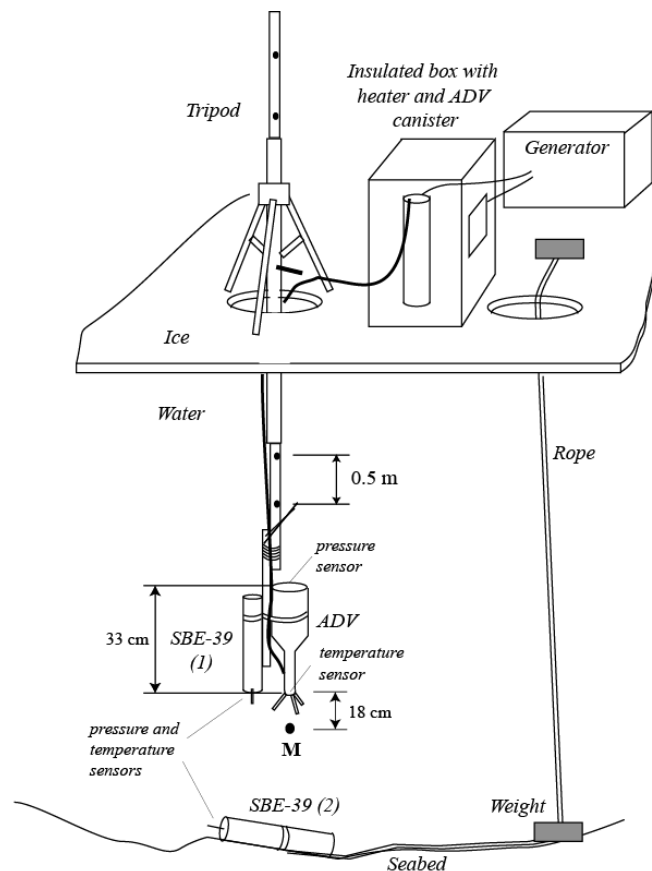


Figure 4. Scheme of water velocity measurements with ADV and temperature and pressure with SBE-39 recorders.

DATA PROCESSING

ADV and SBE data were used to calculate vertical turbulent heat fluxes in the water below the ice by the formula

$$\mathbf{F} = \rho_w c_{v,w} \langle \mathbf{v}'_{wi,z} T' \rangle \quad (1)$$

where ρ_w and $c_{v,w}$ are the density and the specific heat capacity of the water, respectively. Velocity (\mathbf{v}') and temperature (T') fluctuations are calculated as follows

$$\begin{aligned} \mathbf{v}_{wi,j} &= \langle \mathbf{v}_{wi} \rangle + \mathbf{v}'_{wi,j}, \quad \mathbf{v}_{wi} = (v_{wi,x}, v_{wi,y}, v_{wi,z}) \\ \langle \mathbf{v}_{wi} \rangle &= \sum_{j=1}^N \mathbf{v}_{wi,j} [\omega(t_2 - t_1)]^{-1}, \quad T = \langle T \rangle + T', \quad \langle T \rangle = \sum_{j=1}^N T_j [\omega(t_2 - t_1)]^{-1} \end{aligned} \quad (2)$$

where $\mathbf{v}_{wi,j}$ and T_j are the values measured in the time $t = t_j$ ($t_j \in (t_1, t_2)$), N is the number of samples per burst, and ω is the sampling rate.

ADV data were used also to calculate the Reynolds stresses on the lower water by the formulas

$$\sigma_{xz} = -\rho_w \langle v'_{wi,x} v'_{wi,z} \rangle, \quad \sigma_{yz} = -\rho_w \langle v'_{wi,y} v'_{wi,z} \rangle \quad (3)$$

Then the water – ice drag coefficients ($C_{w,x}$ and $C_{w,y}$) are calculated from

$$\sigma_{xz} = -\rho_w C_{w,x} \sqrt{\langle v_{wi,x} \rangle^2 + \langle v_{wi,y} \rangle^2} \langle v_{wi,x} \rangle, \quad \sigma_{yz} = -\rho_w C_{w,y} \sqrt{\langle v_{wi,x} \rangle^2 + \langle v_{wi,y} \rangle^2} \langle v_{wi,y} \rangle \quad (4)$$

According to well known solution describing turbulent boundary layer near the wall in a steady current the current velocity has logarithmic profile near the wall and turbulent drag force applied to the wall is directed along the current, i.e. $C_{w,x} = C_{w,y} = C_w$. Assuming logarithmic law for the distribution of water velocity near the wall we find formula

$$C_{w,1} = \omega C_{w,z}, \quad \omega = [\ln(z/z_0) / \ln(1/z_0)]^2 \quad (5)$$

connecting the values of drag coefficients $C_{w,1}$ and $C_{w,z}$, when vector of mean velocity $(\langle v_{wi,x} \rangle, \langle v_{wi,y} \rangle)$ in formula (4) is measured at the distance 1 m and z m from the wall. The value of ω is varied from zero to 1 when z is changed from 0 to 1 m and becomes larger than 1 when $z > 1$ m. Hydrodynamic roughness z_0 is smaller than 0.02 m typically.

RESULTS OF MEASUREMENTS

Since ADV and SBE-39 are fastened by the tripod the point of measurements moves with ice surface due to the tidal variations of water level in the fjord. Measurements have been carried out at several locations across the fjord. Three of them are shown in Figure 5 by points A, B and C. Measurements at points A, B and C have been carried out on April 2-3, April 8-9 and February 14-15 respectively in 2008. Points A and B were located on 50 m and 100 m distance from the beach. Point C was located close to the shallow water region in the middle part of the straight. Water

depth in point A was about 1.7 m at low tide and 2.5 m at high tide. Water depth in points B was 1.5 m at low tide and more than 3 m at high tide. Water depth in point C varied from 2 m to 3 m over the tidal cycle. Compass diagrams in Figure 5 show the directions of mean velocities of tidal currents over the time of measurements which was about two cycles of semidiurnal tide. In all cases measured currents are reversal. In points B and C the current is directed along the axis of the fjord. In point A the current is directed along the soil bank in transversal direction to the axis of the fjord.

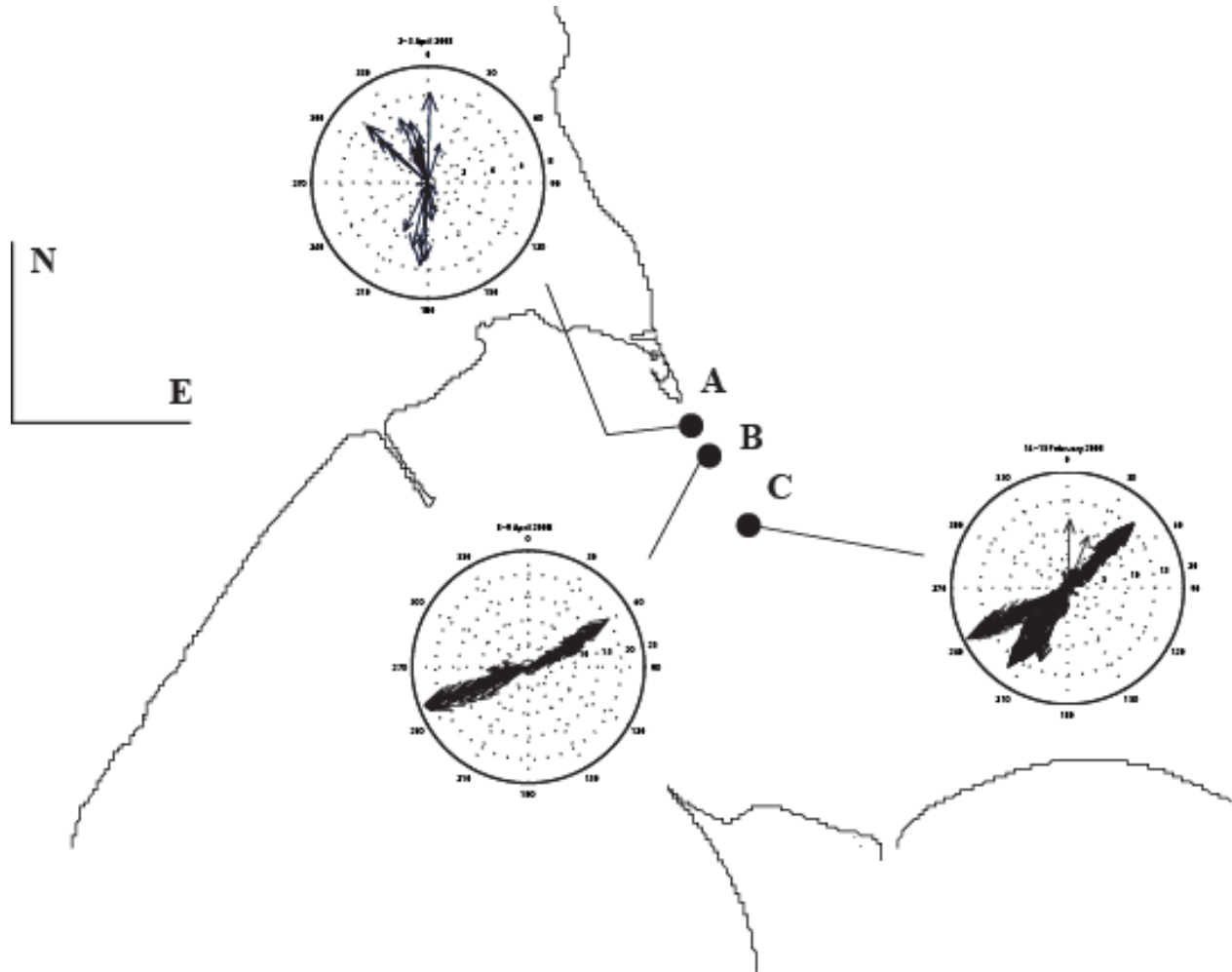


Figure 5. Locations of ADV and SBE measurements are shown by points A, B and C. Directions of mean velocities measured over tidal cycle are shown by black arrows.

Figure 6 shows that water pressure at the bottom is varied in the same phase as water temperature measured by SBE-39(1), while the variation of seabed temperature measured by SBE-39 (2) has phase shift about 2 hours relatively the bottom pressure. When water level is increased the temperature of upper layers of water is higher than the bottom temperature. At high tide both temperatures became equal and almost the same. Maximal temperature gradient about $0.03\text{ }^{\circ}\text{C}$ per 0.5 m was measured one hour later after the low tide. Comparing Figures 6 a and b we conclude that temperatures measured with SBE-39 (1) and SBE-39(2) were the same in the beginning of the measurements with SBE-39(1) when the point of measurements (Figure 4) was very close to the bottom. Then difference between temperatures measured with SBE-39(1) and SBE-39(2) increases.

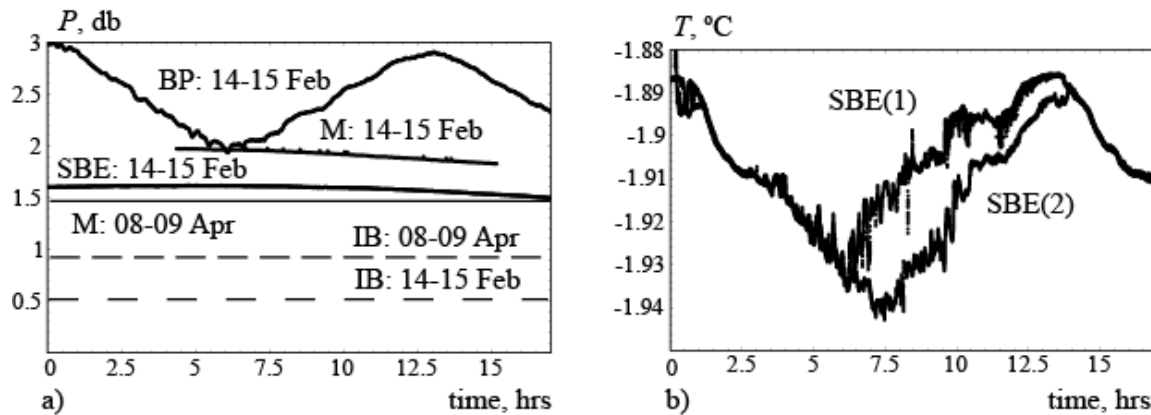


Figure 6. (a) Water pressures at sea bottom and at point M of ADV measurements on February 14-15. Water pressure of ice bottom is shown by line IB: 14-15 Feb. Water pressure at the level of SBE-39 (1) measurements is shown by line SBE: 14-15 Feb. Water pressures at ice bottom and point M of ADV measurements on April 08-09 are shown by lines IB: 08-09 Apr and M:08-09 Apr. (b) Water temperatures measured with SBE-39 (1) and SBE-39 (2) on February 14-15. The time is calculated from 19:00 on February 14.

Figure 7a shows oscillating part δP of water pressure at the bottom measured from the moment of lowest tide at $t \approx 6$ h on Figure 6. One can see 4 oscillations of water pressure with period about 25 min measured in first 100 min. Then 6 oscillations with period about 100 min are well visible. The amplitude of 25 min oscillations is about 0.04 db. Similar oscillations of water pressure at the bottom were observed on all records in the region shown in Figure 5. Figure 7b shows oscillations of eastern v_E and northern v_N components of water velocity at low tide. High frequency oscillations with period about 12.5 min are well visible on the graphs. Components v_E and v_N has opposite signs and almost the same amplitudes. Therefore water particles moves in transversal direction to the fjord axis by these waves.

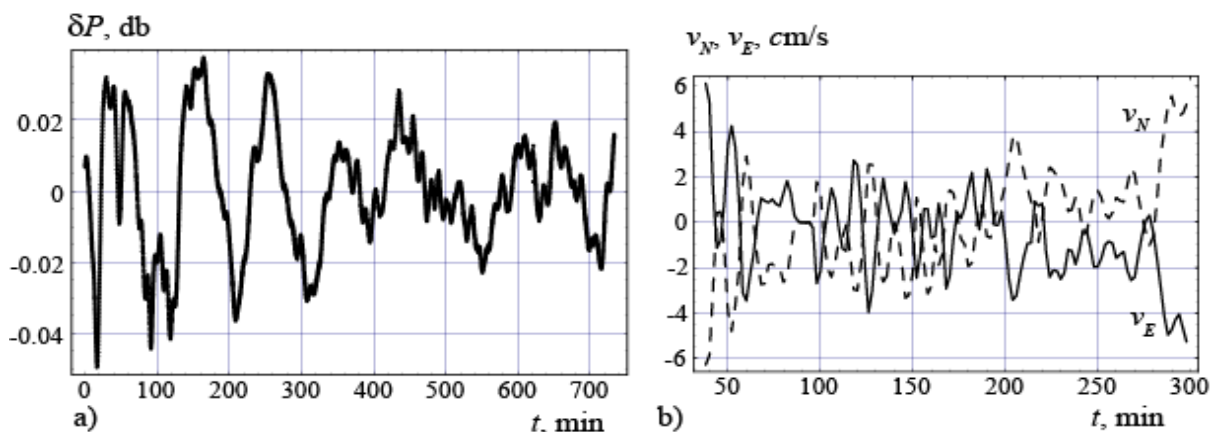


Figure 7. High frequency oscillations of water pressure perturbation δP (a) and eastern v_E and northern v_N components of water velocity (b) on February 14-15. The time is calculated from 00:40 on February 15.

Figure 8 shows three components of water velocity measured in the point C. Low velocities correspond to the low tide. The point M of ADV measurements is located almost at the bottom in low tide (Figure 6a) and ADV measures water velocities at the distance about several centimetres from the bottom. According to Figure 6a point M of ADV measurements is located closer to sea bottom than to the ice bottom during all time of the measurements. It explains negative value of calculated Reynolds stresses, drag coefficients and heat fluxes.

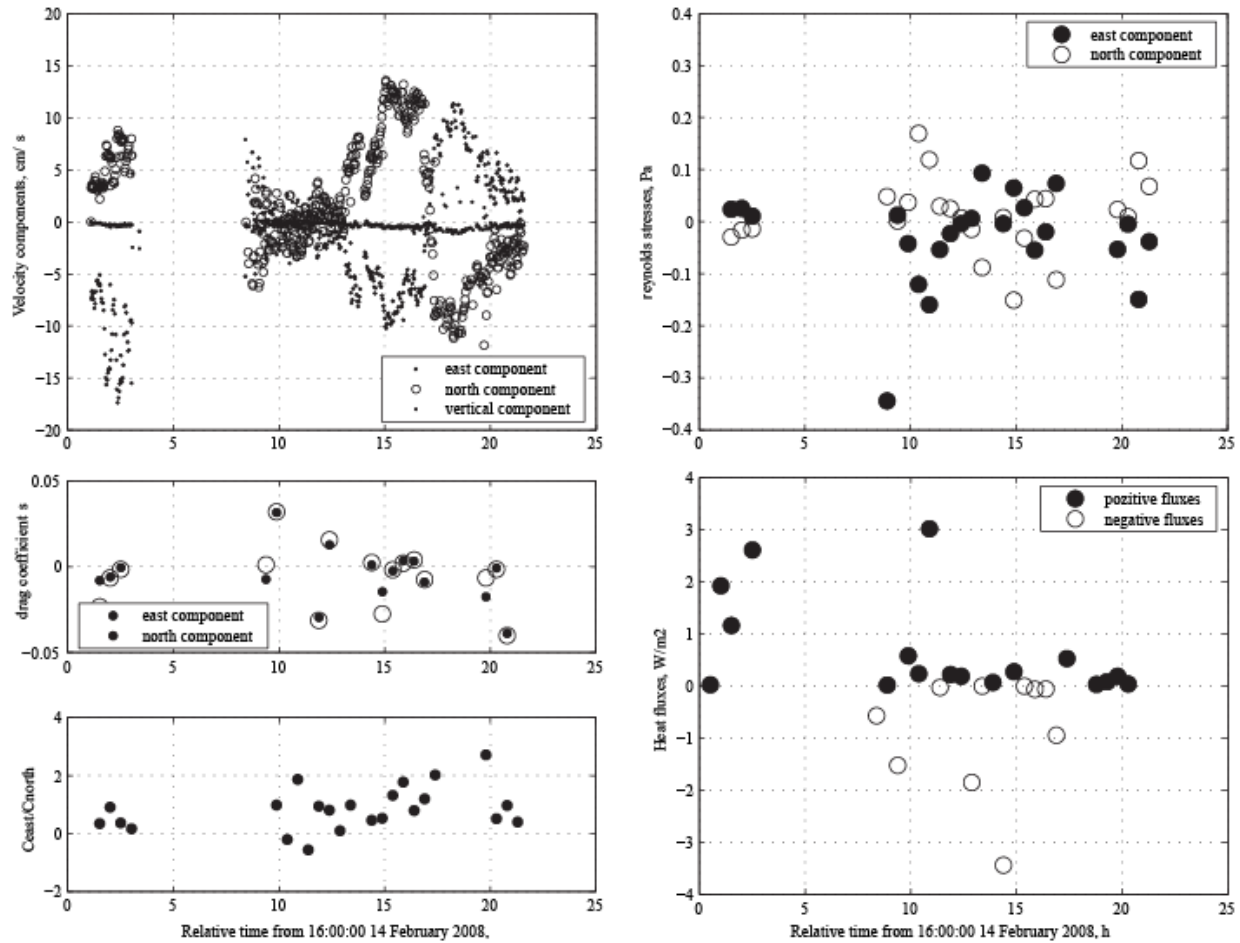


Figure 8. Mean velocities of sea current versus the time measured at point C on February 14-15, 2008. Calculated Reynolds stresses, drag coefficients, ratio of drag coefficients and heat fluxes versus time.

Figure 9 shows three components of water velocity measured in the point B. Low velocities correspond to the low tide. Black dots show the time and the amplitude of high and low tides according to tidal tables for the tide near Longyearbyen. From Figure 6a follows that the point M of ADV measurements is located at the distance about 0.5 m from the ice bottom. One can see that Reynolds stresses are parallel to mean velocities of tidal current below the ice. Mean value of drag coefficients are about 0.0025 and the ratio of the coefficients is about 1 when water current velocities are sufficiently high. When the velocity is smaller than 1 m/s the dispersion of calculated drag coefficient is increased. Assuming $C_{w,0.5} = 0.0025$ we find with formula (5) $C_{w,1} = 0.0037$ when $z_0 = 0.02$ m, and $C_{w,1} = 0.0031$ when $z_0 = 0.002$ m. Mean heat fluxes calculated over the tidal cycle (~ 12 hours) each 3 hours are 0.47 W/m^2 , -0.01 W/m^2 , 0.19 W/m^2 and 0.09 W/m^2 . Total heat flux to the ice bottom over the tidal cycle is estimated as 0.16 W/m^2 .

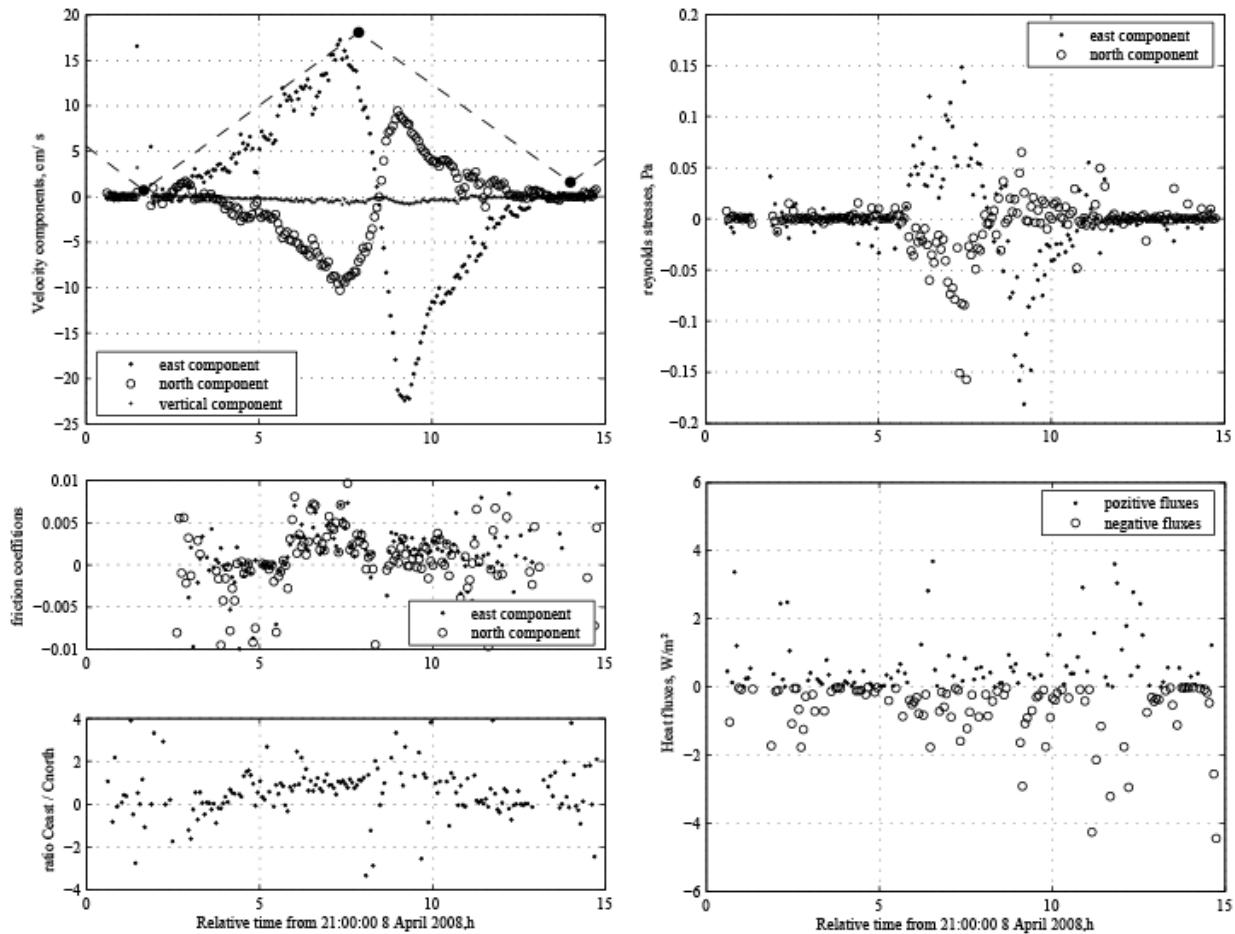


Figure 9. Mean velocities of sea current versus the time measured in the point B on April 08-09, 2008. Calculated Reynolds stresses, drag coefficients, ratio of drag coefficients and heat fluxes versus the time.

CONCLUSIONS

At each location we measured well-defined variations of water velocities, temperature and pressure related to semi-diurnal tides. Maximal values of water velocities averaged over a few minutes reached 1 m/s. They were observed during several tens of minutes. Mean values of maximal velocities vary from 20 to 40 cm/s depending on the location of the measurements. In all measurements over the cycle of semidiurnal tide the currents change direction at high tide.

Temperature variations during a tidal cycle reached several hundredths of a centigrade. The vertical gradient of the temperature varies over a tidal period. Maximal heat fluxes to the ice bottom reached 10 W/m^2 and were obtained during rising tides. Mean values of heat fluxes over the tidal cycle was found about 0.1 W/m^2 .

The direction of the Reynolds stresses in general coincides with the direction of the mean water velocity. Calculated mean values of the drag coefficients vary from 0.003 to 0.004. They are about the same as the value of 0.004 recommended for large scale modeling of ice cover dynamics (Langleben, 1980).

The water pressure at the bottom is almost sinusoidal in time. The dependence on time of the water velocity measured at certain distance from the ice bottom is more complicated, because of the point of measurement was located within boundary layer near sea bottom at low tide.

REFERENCES

- Bates, H.F. and Shapiro, L.H. 1980. Long-period gravity waves in ice-covered sea. *J. Geophys. Res.* 85(2): 1095–1100
- Gorbatsky, V.V. and Marchenko, A.V. 2007 On the influence of turbulence in ice adjacent layer on water-ice drag forces and heat fluxes in the Barents Sea. *Recent development of Offshore Engineering in Cold Regions*. Yue (ed), POAC-07, Dalian, China, June 27-30, 2007, Dalian University Press, Dalian, ISBN 978-7-5611-3631-7, 648-659.
- High, D., and Zabilansky, L. 2004. *Laboratory test of scour under ice: data and preliminary results*. ERDC/CRREL TR-04-9, Hanover, New Hampshire, 174 pp.
- Langleben, M.P. 1980. Water drag coefficient at AIDJEX, Station Caribou. *Sea ice processes and models*, R.S.Pritchard (ed.), University of Washington Press, Seattle, 464-470.
- Marchenko, A., Makshtas A., Shapiro L. 2002. On the excitation of shelf-edge waves due to self-, induced oscillations of ice floes. *Ice in the Environment: Proceedings of the 16th IAHR International Symposium on Ice*, Dunedin, New Zealand 2nd–6th December 2002. International Association of Hydraulic Engineering and Research: 35-43.
- McPhee, M.G. 2007. The ISPOL Upper Ocean Physics Project. *Deep Sea Res.* (in press)
- Smirnov, V.N., Korostelev, V.G. and Shibakin, S.L., 2004. Oscillations of drilling platform caused by ice cover and wind impact. *Proceedings of the 17th IAHR International Symposium on Ice*, St Petersburg, Russia, 21-25 June. International Association of Hydraulic Engineering and Research. Vol 2, 132 -138
- Voinov, G.P. 1999. *Tidal phenomena in the Kara Sea*. St.-Petersburg. Izd. Russian Geographical Society, 109 pp.
- Zubov, N.N. 1944. *Arctic Ice*. Moscow. Izd. Gkavsevmorputi. 360 pp. (in Russian)

KEYWORDS

Hydrological data, sea ice, waves, measurements, drag coefficient, heat flux

AUTHORS INDEX

	Page
Arntsen, Øivind A.	181
Athanassoulis, G. A.	84
Belibassakis, K. A.	84
Brevik, Iver	96
Burcharth, Hans F.	140
Dalrymple, Robert A.	29
De Padova, Diana	29
Debernard, Jens Boldingh	118
Einarsrud, Kristian Etienne	96
Fouques, Sebastien	17
Fylling, Ivar	108
Gansel, Lars	130
Gerostathis, Th. P.	84
Gürtner, Arne	222
Holmedal, Lars Erik	193
Konuk, Ibrahim	222
Kuester, Colin	181
Langen, Ivar	247
Losada, Iñigo J.	13
Lubadd, Raed	205
Løset, Sveinung	220 222
Marchenko, Aleksey	235 247
Massel, Stanislaw R.	2
McClimans, Thomas A.	130 152
Moshagen, Hermann	163
Mossa, Michele	29
Myrhaug, Dag	130 193
Petrillo, Antonio F.	29
Røed, Lars Petter	118
Shestov, Aleksey	247
Solaas, Frøydis	108
Stansberg, Carl Trygve	17
Testik, Firat Y.	141
Tørum, Alf	40 181
Ulrich, Christian	235
Young, D. Morgan	141

KEYWORDS INDEX

	Page
arctic	40 220
bed shear stress	181
bottom model	108
breakwater	40 140 141
bubble curtain	152
Climate change	118
coastal engineering	40 163
cold waters	220
design	140 163
drag	130 247
Eulerian Approach	17
fjord	152
fluid viscosity	29
harbours	40
heat flux	247
helical strakes	205
historical review	40
hydrological data	247
ice	222 247
iceberg	235
irregular waves	2 17
jetty	108
laboratory experiments	181 205
Lagrangian approach	17
marine risers	205
marine vegetation	83
measurements	247
microbubbles	152
mixing	152
modelling	2
multiphase plumes	96
Norway	40
numerical methods	29
numerical models	118
numerical simulation	222
panel program.	108
particle number	29
physical modelling	29
piles	222
pipeline	40 163 181
PIV	130
plumes	96
porous cylinder	130
random waves	193
reflection coefficient	141
regular waves	29
rope tension	235
rubble mound	181
safety	140
scour	141
sediment transport;	193
sheet flow	193

KEYWORDS INDEX (cont)

	Page
ship motions	108
SPH	29
stability	181
stochastic processes	193
stormsurges	118
streaming	193
tankers	108
TKE	130
turbulence	96 193
variable bathymetry	84
velocity defect	130
vertical breakwater	141
VIV	205
water depth	108
water waves	2 83 84 118 141 247
wave-current-seabed interaction	84
waves on currents	84 181 193

COASTAL TECHNOLOGY – Coast 2008

International workshop celebrating
Professor Alf Tørum's 75th birthday

29-30 May 2008, Trondheim, Norway

PROCEEDINGS

